

AO-A188 852

PIEZOELECTRIC POLYMER TACTILE SENSOR ARRAYS FOR
ROBOTICS(U) AIR FORCE INST OF TECH WRIGHT-PATTERSON AFB
OH SCHOOL OF ENGINEERING D G PIROLO DEC 87

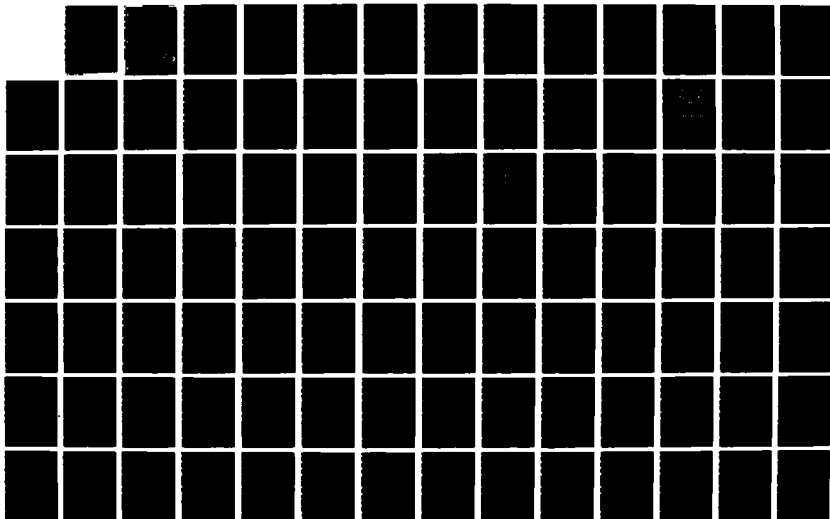
1/3

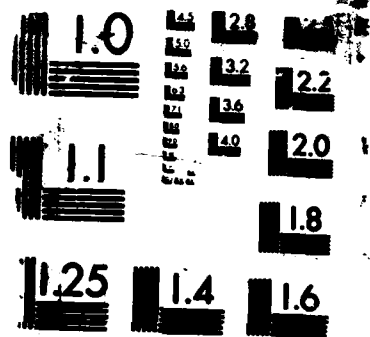
UNCLASSIFIED

AFIT/GE/ENG/87D-52

F/G 17/11

NL





MICROCOPY RESOLUTION TEST CHART

AD-A188 852

DTIC FILE COPY



PIEZOELECTRIC POLYMER TACTILE SENSOR

ARRAYS FOR ROBOTICS

THESIS

David G. Pirolo, B.S.E.
Captain, USAF

AFIT/GE/ENG/87D-52

DTIC
ELECTE
FEB 10 1988
S D E

DEPARTMENT OF THE AIR FORCE
AIR UNIVERSITY

AIR FORCE INSTITUTE OF TECHNOLOGY

Wright-Patterson Air Force Base, Ohio

THIS DOCUMENT HAS BEEN APPROVED
FOR PUBLIC RELEASE AND CITE AS

RR 9

4 044

AFIT/GE/ENG/87D-52

PIEZOELECTRIC POLYMER TACTILE SENSOR

ARRAYS FOR ROBOTICS

THESIS

David G. Pirollo, B.S.E.
Captain, USAF

AFIT/GE/ENG/87D-52

DTIC
ELECTE
S FEB 10 1988 D
E

Approved for public release; distribution unlimited

PIEZOELECTRIC POLYMER TACTILE SENSOR ARRAYS
FOR ROBOTICS

THESIS

Presented to the Faculty of the School of Engineering
of the Air Force Institute of Technology
Air University

In Partial Fulfillment of the
Requirements for the Degree of
Master of Science in Electrical Engineering



David G. Pirolo, B.S.E.
Captain, USAF

December 1987

Accession For	
NTIS GRA&I	<input checked="checked" type="checkbox"/>
DTIC TAB	<input type="checkbox"/>
Unannounced	<input type="checkbox"/>
Justification	
By _____	
Distribution/	
Availability Codes	
Dist	Avail and/or Special
A-1	

Approved for public release; distribution unlimited

Preface

The purpose of this study was to design, fabricate, and evaluate the performance of piezoelectric polymer tactile sensor arrays (PPTSAs). The fundamental performance goal for these PPTSAs was to have nondestructive, passive devices which are capable of providing valuable information to a robotic's controller when physical contact is made with an object of interest. These tactile devices are of particular interest to those who fabricate robots which must avoid mechanical damage and electrical discharge with an object while performing a particular task.

The PPTSAs were fabricated from the piezoelectric polymer polyvinylidene fluoride (PVDF). PVDF provided the nondestructive and passive power element to the PPTSAs. Fabrication techniques were developed to handle the temperature and chemical limitations of PVDF. Each of the PPTSAs consisted of a 5 x 5 array of discrete sensor elements.

I thank the numerous individuals who provided me with assistance during this study. First and foremost, I thank my thesis advisor, Maj E. Kolesar, for his writing skills, technical knowledge, guidance, patience, and continual support. I also thank the other members of my thesis committee, Maj D. Kitchen, Dr. M. Kabrisky, and Col C. Hatsell for their support. I owe a special thanks to Mr. W. Kingery and Mr. J. Thompson of the 4950th Test Wing and Mr.

D. Via of the Avionics Laboratory for their priceless experimental assistance. A word of thanks goes to AFIT's technical staff for providing support, equipment, and assistance in times of need. They were outstanding.

I thank the vendors who provided very valuable technical information and materials during this thesis. The most important vendor was Solvay Technologies, Inc (609 Fifth Avenue, New York, NY 10017). The president of Solvay Technologies, Dr. G. Gerliczy, provided numerous samples of PVDF film and invaluable technical information. Mrs. D. Kehrhahn, Mr. G. McGraw, and Mr. V. Chatingy of the Pennwalt Corporation (Kynar Piezo Film Department, P.O. Box 799, Valley Forge, PA 19482) were an excellent source of PVDF related articles and information.

Finally, I wish to thank the most important person in my life, my wife Julie, for her love, understanding, and support during this study.

Table of Contents

	Page
Preface	ii
List of Figures	vii
List of Tables	xv
Abstract	xvii
I. Introduction	1.1
Background	1.1
Problem Statement	1.2
Scope	1.2
Summary of Current Knowledge	1.2
Approach	1.4
Sequence of Presentation	1.9
II. Background	2.1
Piezoelectric Effect	2.1
Historical Perspective	2.1
Microscopic Origin	2.3
Macroscopic Origin	2.10
Nonpiezoelectric Materials	2.15
Piezoelectric Materials	2.18
Polyvinylidene Flouride (PVDF)	2.22
Advantages and Disadvantages	2.25
Physical Properties of PVDF	2.26
Piezoelectric Activity	2.28
Orientation Dependence	2.34
Temperature Dependence	2.36
Piezoelectric PVDF Film Manufacturers	2.36
Inducing the Piezoelectric Effect	
in Polyvinylidene Fluoride	2.37
Orientation Techniques	2.39
Poling Techniques	2.42
Tactile Sensors	2.47
Human Tactile Sensing	2.48
Robotic Tactile Sensing	2.50
Tactile Sensor Designs	2.52
Summary	2.54

III.	Experimental Designs, Fabrication, Poling, and Testing	3.1
	Sensor Designs	3.1
	The Square Pad Design	3.7
	The Stripe Design	3.10
	Sensor Fabrication Procedures	3.12
	Thermal Poling	3.15
	The Thermal Poling Arrangement	3.16
	The Thermal Poling Procedure	3.17
	Evaluation Procedures	3.20
	Electrode-Structure Fabrication	
	Process Evaluation Procedure	3.20
	Electrode-Structure Dimension	
	Evaluation Procedure	3.21
	Stripe Electrode Impedance	
	Evaluation Procedure	3.24
	Piezoelectric Activity	
	Evaluation Procedure	3.26
	Piezoelectric Activity	
	Measurement Arrangement	3.29
	Piezoelectric Activity	
	Measurement Procedure	3.31
	Reducing the Piezoelectric	
	Activity Measurement Data	3.33
	Summary	3.37
IV.	Experimental Data	4.1
	Electrode-Structure Fabrication	
	Process Evaluation Data	4.1
	Piezoelectric Activity Measurement Data	4.10
	Summary	4.17
V.	Discussion and Analysis	5.1
	Electrode-Structure Fabrication	
	Process Evaluation	5.1
	Piezoelectric Activity Evaluation	5.8
	Examining the Collected Data	5.9
	Data Analysis	5.16
	Interpreting the Data	5.17
	Comparing the Design Configurations ..	5.18
	Comparing the PVDF Film Thicknesses ..	5.22
	Comparing the Electrode-Structure	
	Fabrication Processes	5.23
	Effects of Thermal Poling	5.23
	Summary	5.26

VI.	Conclusions and Recommendations	6.1
	Conclusions	6.1
	Recommendations	6.3
Appendix A:	Procedure for Fabricating the High Resolution Plate Masks	A.1
Appendix B:	Procedure for Fabricating Evaporation Masks	B.1
Appendix C:	Procedure for Evaporating Aluminum Electrode Patterns on the Unmetallized PVDF film	C.1
Appendix D:	Procedure for Etching the Electrode Structures from the Commercially Metallized PVDF Film	D.1
Appendix E:	Procedure for Final Assembly of a Stripe Design Piezoelectric Polymer Tactile Sensor Array	E.1
Appendix F:	Procedure for Final Assembly of a Square Pad Design Piezoelectric Polymer Tactile Sensor Array	F.1
Appendix G:	Photocopies of the High Resolution Plate and Evaporation Masks	G.1
Appendix H:	Thermal Poling Chamber	H.1
Appendix I:	Computer Programs	I.1
Appendix J:	Piezoelectric Activity Data Plots	J.1
	Bibliography	BIB.1
	Vita	VITA

List of Figures

Figure	Page
1.1 The Principal Crystalline Phases: (a) Non-piezoelectric Alpha-Phase and (b) Piezoelectric Beta-Phase.	1.5
2.1 Electric Dipole.	2.4
2.2 Scalar Electric Potential and Vector Electric Field.	2.5
2.3 Crystal With and Without a Center of Inversion. (a) A Crystal with a Center of Inversion Exhibits No Piezoelectric Effect. (b) A Crystal Lacking a Center of Inversion Exhibits the Piezoelectric Effect.	2.7
2.4 A Phenomenological Crystal (a) Unstressed and (b) Stressed.	2.9
2.5 Rectangular Coordinate System Used in Crystallography.	2.12
2.6 Three Common Stresses Found in Stressed Materials: (a) Compressional, (b) Extensional, and (c) Shear.	2.14
2.7 Strains in the x, y, and z Directions.	2.16
2.8 Schematic Dipiction of the Two Most Common Crystalline Chain Conformations of PVDF: (a) Alpha-Form PVDF and (b) Beta-Form PVDF.	2.27
2.9 Sphere with Spontaneous Polarization Dispersed in an Isotropic Matrix.	2.29
2.10 High Field Poling.	2.44
2.11 Schematic Drawing of Wang and Von Seggern's Poling Arrangement.	2.44
2.12 Schematic Drawing of the Current Limiting Poling Arrangement.	2.45
2.13 Corona Poling.	2.46
2.14 Simple Tactile Sensor.	2.53

2.15	Complex Tactile Sensor.	2.53
3.1	Electrode Structure of the Square-Pad Configuration.	3.3
3.2	Electrode Structure of the Stripe Configuration.	3.3
3.3	A Cross-Sectional Diagram of the Square-Pad Design.	3.7
3.4	The Square-Pad Design Electrode Pattern.	3.9
3.5	The Conductor Pattern for the Square-Pad Design.	3.10
3.6	A Cross-Sectional Diagram of the Stripe Design.	3.11
3.7	The Stripe Electrode Design.	3.11
3.8	Schematic of the Thermal Poling Arrangement.	3.16
3.9	Drawing of an Installed Stripe Design PPTSA in the Poling Chamber.	3.18
3.10	Drawing of an Installed Square-Pad Design PPTSA in the Poling Chamber.	3.18
3.11	Electrode Structure Numbering System for the Stripe Design Configurations.	3.23
3.12	Electrode Structure Numbering System for the Square-Pad Design Configurations.	3.23
3.13	Showing where the Measurements were Taken Between the Main Stripe Electrodes.	3.24
3.14	Identification of the Stripe Electrodes for the Impedance Measurements.	3.25
3.15	Diagram Showing the Six Configurations that were Measured.	3.27
3.16	Schematic of the Piezoelectric Activity Measurement Arrangement.	3.29
3.17	A Drawing Illustrating the Technique Used to Apply a Load to a Discrete Sensor.	3.30
3.18	Sequence of Events Accomplished to Perform a Measurement Cycle.	3.32

3.19	An Example of Five Measurements Having a Consistent Uniform Pattern.	3.33
3.20	An Example of a Data Set of Six Measurements that has Gross Irregularities.	3.34
3.21	An Example of a Graph with the Input and Computed Data Points that are Associated with the DELTA.BAS Computer Program.	3.35
2.22	Points that Formed a Transient Response Curve, Like Those Shown, were Omitted From the Input Point Selection Process.	3.36
4.1	Response of Four Measurements for the PPTSA #13 Configuration. These Measurements were for the Corner Sensor and 100 Gram Load.	4.14
4.2	Response of Four Measurements for the PPTSA #13 Configuration. These Measurements were for the Corner Sensor and 200 Gram Load.	4.14
4.3	Response of Five Measurements for the PPTSA #13 Configuration. These Measurements were for the Corner Sensor and 500 Gram Load.	4.15
4.4	Response of Five Measurements for the PPTSA #13 Configuration. These Measurements were for the Corner Sensor and 700 Gram Load.	4.15
4.5	Response of Six Measurements for the PPTSA #13 Configuration. These Measurements were for the Corner Sensor and 1,000 Gram Load.	4.16
4.6	Response of Five Measurements for the PPTSA #13 Configuration. These Measurements were for the Corner Sensor and 1,500 Gram Load.	4.16
5.1	The Radii of Evaporation-Formed Corners Spanned 8 to 16 Microns.	5.6
5.2	The Radii of Photolithographic-Formed Corners Spanned 1 to 3 Microns.	5.6
5.3	Examples of (a) Detectable and (b) Undetectable System Drift.	5.10
5.4	Example of the Adverse Effect a Parasitic Capacitance had on a Measurement.	5.12
5.5	Schematic of the Center Sensor of the PPTSA #8 Configuration.	5.13

5.6	Example of a Measurement with a Dip.	5.14
5.7	Examples of Spikes Occuring at (a) the Application of a Load and at (b) the Removal of a Load.	5.15
5.8	A Load Machine Relay Changing States Would Occasionally Cause Two Slight Transients. (a) The First Change of State Would Increase the Voltage and (b) the Second Change of State Would Decrease the Voltage.	5.16
5.9	Linear Least Squares Curve Fit for the PPTSA #2 Configuration.	5.19
5.10	Linear Least Squares Curve Fit for the PPTSA #4 Configuration.	5.19
5.11	Linear Least Squares Curve Fit for the PPTSA #6 Configuration.	5.20
5.12	Linear Least Squares Curve Fit for the PPTSA #8 Configuration.	5.20
5.13	Linear Least Squares Curve Fit for the PPTSA #13 Configuration.	5.21
5.14	Linear Least Squares Curve Fit for the PPTSA #15 Configuration.	5.21
5.15	The Sequence of Three Measurements for the PPTSA #4 Configuration as the X4 Stripe Electrode was Fracturing.	5.24
5.16	A Scanning Electron Microscope Picture of the Break in the X4 Stripe Electrode of the PPTSA #4 Configuration.	5.25
5.17	A Picture of the Burned Hole in the Number 11 Discrete Sensor of the #13 Configuration.	5.27
C.1	Schematic of the Evaporation Mask, PVDF Film, and Glass Plate Sandwich	C.2
E.1	Mounting the Copper Foil Tape to the Electrode Stripes.	E.2
F.1	A Process for Final Assembly of a Square-Pad Design Piezoelectric Polymer Tactile Sensor Array.	F.2
G.1.	Photocopies of the Stripe Design PPTSA High Resolution Plate Masks.	G.2

G.2.	Photocopies of the Evaporation Masks for (a) the Stripe Design PPTSAs that have an Inner Electrode Spacing of 500 Microns and (b) the Stripe Design PPTSAs that have an Inner Electrode Spacing of 750 Microns.	G.3
G.3.	Photocopies of the High Resolution Plate Masks for the Square-Pad Design PPTSAs that have an Inner Electrode Spacing of 500 Microns.	G.4
G.4.	Photocopies of the High Resolution Plate Masks for the Square-Pad Design PPTSAs that have an Inner Electrode Spacing of 750 Microns.	G.5
G.5.	Photocopies of the High Resolution Plate Masks for the Square-Pad Design PPTSA Conductor Patterns.	G.6
G.6.	Photocopies of the Evaporation Masks for the Square-Pad Design PPTSA Electrode Structures. ...	G.7
H.1	Drawing of the Thermal Poling Chamber.	H.1
H.2	Drawing of the Upper Chamber Assembly.	H.2
H.3	Drawing of the Lower Chamber Assembly.	H.3
H.4	Drawing of a Protective Housing.	H.4
H.5	Drawing of the Electrode Assembly.	H.5
J.1	Response of Six Measurements for the PPTSA #2b Configuration. These Measurements were for the Center Sensor and 100 Gram Load.	J.2
J.2	Response of Five Measurements for the PPTSA #2b Configuration. These Measurements were for the Center Sensor and 200 Gram Load.	J.2
J.3	Response of Five Measurements for the PPTSA #2b Configuration. These Measurements were for the Center Sensor and 500 Gram Load.	J.3
J.4	Response of Five Measurements for the PPTSA #2b Configuration. These Measurements were for the Center Sensor and 700 Gram Load.	J.3
J.5	Response of Four Measurements for the PPTSA #2b Configuration. These Measurements were for the Center Sensor and 1,000 Gram Load.	J.4

J.6	Response of Four Measurements for the PPTSA #2b Configuration. These Measurements were for the Center Sensor and 1,500 Gram Load.	J.4
J.7	Response of Four Measurements for the PPTSA #2b Configuration. These Measurements were for the Corner Sensor and 100 Gram Load.	J.5
J.8	Response of Four Measurements for the PPTSA #2b Configuration. These Measurements were for the Corner Sensor and 200 Gram Load.	J.5
J.9	Response of Five Measurements for the PPTSA #2b Configuration. These Measurements were for the Corner Sensor and 500 Gram Load.	J.6
J.10	Response of Six Measurements for the PPTSA #2b Configuration. These Measurements were for the Corner Sensor and 700 Gram Load.	J.6
J.11	Response of Four Measurements for the PPTSA #2b Configuration. These Measurements were for the Corner Sensor and 1,000 Gram Load.	J.7
J.12	Response of Five Measurements for the PPTSA #2b Configuration. These Measurements were for the Corner Sensor and 1,500 Gram Load.	J.7
J.13	Response of Five Measurements for the Poled PPTSA #2b Configuration. These Measurements were for the Center Sensor and 100 Gram Load.	J.8
J.14	Response of Five Measurements for the Poled PPTSA #2b Configuration. These Measurements were for the Center Sensor and 200 Gram Load.	J.8
J.15	Response of Five Measurements for the Poled PPTSA #2b Configuration. These Measurements were for the Center Sensor and 500 Gram Load.	J.9
J.16	Response of Five Measurements for the Poled PPTSA #2b Configuration. These Measurements were for the Center Sensor and 700 Gram Load.	J.9
J.17	Response of Four Measurements for the Poled PPTSA #2b Configuration. These Measurements were for the Center Sensor and 1,000 Gram Load.	J.10
J.18	Response of Four Measurements for the Poled PPTSA #2b Configuration. These Measurements were for the Center Sensor and 1,500 Gram Load.	J.10

- J.19 Response of Four Measurements for the Poled PPTSA
#2b Configuration. These Measurements were for
the Corner Sensor and 100 Gram Load. J.11
- J.20 Response of Five Measurements for the Poled PPTSA
#2b Configuration. These Measurements were for
the Corner Sensor and 200 Gram Load. J.11
- J.21 Response of Four Measurements for the Poled PPTSA
#2b Configuration. These Measurements were for
the Corner Sensor and 500 Gram Load. J.12
- J.22 Response of Five Measurements for the Poled PPTSA
#2b Configuration. These Measurements were for
the Corner Sensor and 700 Gram Load. J.12
- J.23 Response of Six Measurements for the Poled PPTSA
#2b Configuration. These Measurements were for
the Corner Sensor and 1,000 Gram Load. J.13
- J.24 Response of Five Measurements for the Poled PPTSA
#2b Configuration. These Measurements were for
the Corner Sensor and 1,500 Gram Load. J.13
- J.25 Response of Five Measurements for the PPTSA #13
Configuration. These Measurements were for the
Center Sensor and 100 Gram Load. J.14
- J.26 Response of Five Measurements for the PPTSA #13
Configuration. These Measurements were for the
Center Sensor and 200 Gram Load. J.14
- J.27 Response of Five Measurements for the PPTSA #13
Configuration. These Measurements were for the
Center Sensor and 500 Gram Load. J.15
- J.28 Response of Five Measurements for the PPTSA #13
Configuration. These Measurements were for the
Center Sensor and 700 Gram Load. J.15
- J.29 Response of Five Measurements for the PPTSA #13
Configuration. These Measurements were for the
Center Sensor and 1,000 Gram Load. J.16
- J.30 Response of Four Measurements for the PPTSA #13
Configuration. These Measurements were for the
Center Sensor and 1,500 Gram Load. J.16
- J.31 Response of Five Measurements for the Poled PPTSA
#13 Configuration. These Measurements were for
for the Center Sensor and 100 Gram Load. J.17

- J.32 Response of Six Measurements for the Poled PPTSA
 #13 Configuration. These Measurements were for
 the Center Sensor and 200 Gram Load. J.17
- J.33 Response of Four Measurements for the Poled PPTSA
 #13 Configuration. These Measurements were for
 the Center Sensor and 500 Gram Load. J.18
- J.34 Response of Five Measurements for the Poled PPTSA
 #13 Configuration. These Measurements were for
 the Center Sensor and 700 Gram Load. J.18
- J.35 Response of Four Measurements for the Poled PPTSA
 #13 Configuration. These Measurements were for
 the Center Sensor and 1,000 Gram Load. J.19
- J.36 Response of Seven Measurements for the Poled
 PPTSA #13 Configuration. These Measurements were
 for the Center Sensor and 1,500 Gram Load. J.19
- J.37 Response of Six Measurements for the Poled PPTSA
 #13 Configuration. These Measurements were for
 the Corner Sensor and 100 Gram Load. J.20
- J.38 Response of Six Measurements for the Poled PPTSA
 #13 Configuration. These Measurements were for
 the Corner Sensor and 200 Gram Load. J.20
- J.39 Response of Six Measurements for the Poled PPTSA
 #13 Configuration. These Measurements were for
 the Corner Sensor and 500 Gram Load. J.21
- J.40 Response of Six Measurements for the Poled PPTSA
 #13 Configuration. These Measurements were for
 the Corner Sensor and 700 Gram Load. J.21
- J.41 Response of Seven Measurements for the Poled
 PPTSA #13 Configuration. These Measurements were
 for the Corner Sensor and 1,000 Gram Load. J.22
- J.42 Response of Seven Measurements for the Poled
 PPTSA #13 Configuration. These Measurements were
 for the Corner Sensor and 1,500 Gram Load. J.22

List of Tables

Table	Page
2.1 Common Piezoelectric Crystals	2.8
2.2 Material Property Symbols and Definitions	2.13
2.3 The Electromagnetic Coupling Coefficient for a Select Group of Piezoelectric Crystals	2.23
2.4 Theory Compared to Experiment for the Piezoelectric Constant 'e'.....	2.32
2.5 Calculated Fractional Contributions for the Piezoelectric Constant 'e'.....	2.33
2.6 Comparison of Parameters of Poled Uniaxially Oriented and Biaxially Oriented PVDF	2.35
2.7 Draw Ratio Versus Piezoelectric Constant d_{33}	2.36
2.8 Typical Properties of the KYNAR Material	2.38
2.9 Principal Properties for the Solef Material	2.40
2.10 Dielectric Data for Different Orientation Techniques	2.42
3.1 The 16 Sensor Configurations Formulated	3.6
3.2 The Eight Electrode Structures Measured	3.22
3.3 The Six Configurations Measured	3.27
4.1 Sensor Spacing Measurement Data for the Stripe Design Configurations	4.2
4.2 Sensor Spacing Measurement Data for the Square-Pad Design Configurations	4.3
4.3 Thickness of the Aluminum Electrode Structures for the Configurations Fabricated Using the Evaporation Process	4.6
4.4 Stripe Electrode Impedance Data	4.7
4.5 Piezoelectric Activity Measurement Data	4.11
5.1 Electrode Structure Dimension Error Data for the Stripe Design Configurations	5.3

5.2	Electrode Structure Dimension Error Data for the Square-Pad Design Configurations	5.5
5.3	Linear Least Squares Curve Fit Coefficients for the Measured Piezoelectric Activity Data	5.18

Abstract

This study resulted in the design and fabrication of 16 piezoelectric polymer tactile sensor arrays (PPTSAs) for robotics. Six of these PPTSAs were evaluated for piezoelectric activity. Two of the six were thermal poled and evaluated again for piezoelectric activity. Each PPTSA contained a 5 x 5 array of identical, (3 mm x 3 mm) discrete sensors. Polyvinylidene fluoride (PVDF) was the piezoelectric polymer used in the study. The PVDF was in two film thicknesses (25 and 40 microns) and in two forms (unmetallized and vendor metallized). The PVDF film had inherent chemical and temperature limitations. Two electrode-structure fabrication processes were developed to accommodate these limitations.

PIEZOELECTRIC POLYMER TACTILE SENSOR ARRAYS FOR ROBOTICS

I. Introduction

Background

One of the most promising applications of robotic research is its utility for refueling aircraft in a hazardous environment. In order to accomplish this task, it is necessary to first locate the refueling port on the aircraft, and then connect the pump's nozzle without causing mechanical damage or electrical discharge. This critical location and positioning task may be accomplished with or without human assistance, depending upon the sensors and computational power involved.

A fundamental step towards solving this problem is to develop tactile sensor arrays that will provide information to the robotic's controller when physical contact is made with an object of interest. Ultimately, the sensor will be configured as a planar array and have graduated sensitivity levels. This spatial configuration will yield information to discern an object's shape.

Problem Statement

The purpose of this thesis was to design and fabricate 16 piezoelectric polymer tactile sensor array (PPTSA) configurations from two selected designs. The polyvinylidene fluoride (PVDF) polymer was the piezoelectric material of choice. PVDF was selected because it has the highest piezoelectric activity of all known polymers (Kawai, 1969:975-976), and it possesses several physically desirable characteristics (flexibility, durability, and chemical resistance) (Lovinger, 1983:1115).

Scope

The project was restricted to the design and the fabrication of 16 PPTSA configurations. Six of the configurations were evaluated for piezoelectric activity. Two of the six configurations were thermally poled and evaluated again for changes in the piezoelectric activity.

Summary of Current Knowledge

Piezoelectric materials have the ability to develop an electric charge proportional to an applied mechanical stress, or conversely, a physical strain proportional to an applied electric field. This electrical-to-mechanical and converse relationship that occurs in these materials is called piezoelectricity. Cady (Cady, 1964:177) defined piezoelectricity as follows:

A piezoelectric crystal may be a crystal in which 'electricity of electric polarity' is produced by pressure; or, more briefly, as one that becomes electrified on squeezing; or as one that becomes deformed when in an electric field. The first two definitions express the direct piezoelectric effect, while the third expresses the converse piezoelectric effect.

At the atomistic or microscopic level, electric dipoles created in piezoelectric materials under mechanical stress are the basic element of the piezoelectric effect. Electric dipoles form because the piezoelectric material's crystal-line structure lacks a center of inversion. Under stress, the crystal symmetry of the material becomes distorted and the electric dipoles are created. Although it is convenient to understand piezoelectricity at the atomistic level, no one has been able to exactly predict the piezoelectric activity of a material.

Typically, piezoelectricity in materials is described at the macroscopic level. The piezoelectric properties of a material are described in terms of directionally-sensitive piezoelectric coefficients (such as stress, strain, voltage, and charge).

Although piezoelectricity occurs in a select group of single crystals without any conditioning process, ceramics and polymers need a conditioning process to make them piezoelectric (KYNAR Piezo Film Department, 1983:29; Jaffe and others, 1971:1-4). Ceramics are made piezoelectric using a conditioning process called poling (Jaffe and

others, 1971:1). The poling process causes the randomly aligned crystallites in a material to become preferentially aligned, and thus, make the material piezoelectric. Polymers use mechanical stretching and a subsequent poling processes to make them piezoelectric (Lovinger, 1983:1115). Mechanical stretching imparts limited piezoelectric activity in a polymer (Gerliczy and Betz, 1984:6).

Piezoelectric polymers, like PVDF, combine the best characteristics of polymeric materials, such as small mass, flexibility, simple processing, large piezoelectric coefficients, significant bandwidth, and linear output over a wide dynamic range (Lovinger, 1983:1115; Pedotti and others, 1984:163). PVDF is a semi-crystalline, high-molecular weight polymer whose monomer formula is $(CH_2-CF_2)_n$ (KYNAR Piezo Film Department, 1983:26). The polymer is approximately 50 percent crystalline and 50 percent amorphous. The principal crystalline phases shown in Figure 1.1 are the nonpolar alpha- and the polar beta-phases (KYNAR Piezo Film Department, 1983:27). High piezoelectric response is associated with the polar beta-phase.

Approach

The general approach consisted of designing and fabricating 16 PPTSA configurations. Six of these configurations were evaluated for piezoelectric activity. Two of the six evaluated configurations were thermally poled and evaluated again for changes in the piezoelectric activity. This study

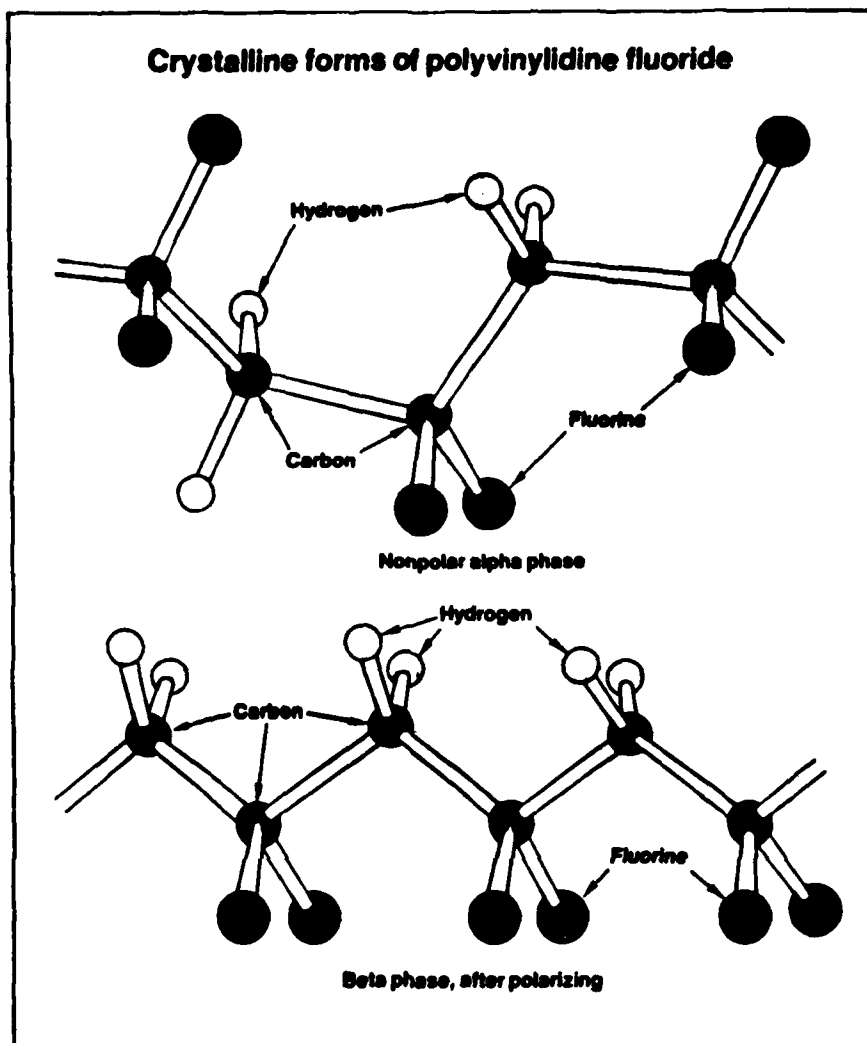


Figure 1.1. The Principal Crystalline Phases: (a) Non-piezoelectric Alpha-Phase and (b) Piezoelectric Beta-Phase (Carlisle, 1986:4).

was based on several variations included in the selected designs. Through a common evaluation process, the advantages and the disadvantages of the electrode-structure fabrication processes, the PPTSA designs, and the thermal poling process was revealed.

Each of the two selected designs consisted of a 5 x 5 array of discrete sensor elements, but they differed in their design and method of fabrication. One design, called the stripe design, used two orthogonal sets of five parallel electrode stripes. One set of stripes was patterned on one surface of the PVDF, and the second set was positioned on the opposite surface, but was rotated 90 degrees with respect to the first set. The second design, called the square-pad patterned design, had two different electrode patterns on the surfaces of the PVDF film. The upper surface consisted of a homogeneous and continuous common electrode ground plane, and the lower surface had 25 discrete square electrodes arranged in a 5 x 5 matrix. Both designs were fabricated to approximate the size of an adult's fingerprint.

The fabrication parameters involved two sensor designs (stripe and square-pad), two PVDF film thicknesses (25 and 40 microns), two sensor element spacings (500 and 750 microns), and vendor metallized and unmetallized PVDF film. Two electrode-structure fabrication processes were generated to account for the vendor metallized and unmetallized PVDF film used. Sixteen unique PPTSA configurations were fabricated.

This research effort was partitioned into six phases. The first four phases consisted of fabricating 16 unique PPTSAs from vendor poled PVDF film, and were

organized according to the ease of PPTSA fabrication. In the fifth phase, an electrode-structure fabrication process evaluation, and a piezoelectric activity evaluation were performed. The sixth phase involved thermally poling two configurations and a second piezoelectric activity evaluation. A description of each of the six phases follows:

1. Phase I. Four stripe design PPTSA configurations were fabricated from the vendor's unmetallized PVDF film in this phase. These PPTSAs were the simplest to fabricate. Since these were the first PPTSAs fabricated, the first samples were made individually to optimize the process variables. A thermal evaporation electrode-structure fabrication process was used to realize stripe electrodes on the unmetallized PVDF film. The identifying PPTSA number, film thickness, and element spacing of the configurations in this phase were:

1. 25 micron thick film, 500 micron element spacing
2. 25 micron thick film, 750 micron element spacing
3. 40 micron thick film, 500 micron element spacing
4. 40 micron thick film, 750 micron element spacing

2. Phase II. Four square-pad design PPTSA configurations were fabricated from the vendor's unmetallized PVDF film in this phase. The thermal evaporation electrode-structure process was used to realize the square-pad and ground plane electrodes on the PVDF film. The identifying

PPTSA number, film thickness, and element spacing of the configurations in this phase were:

5. 25 micron thick film, 500 micron element spacing
6. 25 micron thick film, 750 micron element spacing
7. 40 micron thick film, 500 micron element spacing
8. 40 micron thick film, 750 micron element spacing

3. Phase III. Four stripe design PPTSAs were fabricated from the vendor's aluminum metallized PVDF film in this phase. A photolithographic process was used to define the electrode stripes from the aluminum film that was on the surfaces of the metallized PVDF film. The identifying PPTSA number, film thickness, and element spacing of the configurations in this phase were:

9. 25 micron thick film, 500 micron element spacing
10. 25 micron thick film, 750 micron element spacing
11. 40 micron thick film, 500 micron element spacing
12. 40 micron thick film, 750 micron element spacing

4. Phase IV. Four square-pad patterned PPTSA configurations from the vendor's aluminum metallized PVDF film were fabricated in this phase. The photolithographic process was used to form the electrode ground planes and square electrode pads from the aluminum film that was on the surfaces of the metallized PVDF film. The identifying PPTSA number, film thickness, and element spacing of the configurations in this phase were:

13. 25 micron thick film, 500 micron element spacing
14. 25 micron thick film, 750 micron element spacing
15. 40 micron thick film, 500 micron element spacing
16. 40 micron thick film, 750 micron element spacing

5. Phase V. This phase involved an electrode-structure process evaluation and a piezoelectric activity evaluation. The electrode-structure process evaluation consisted of two parts. In the first part, a dimensional error analysis was performed on the electrode structures that were fabricated using the two electrode-structure fabrication processes (evaporation and photolithographic). The purpose of this analysis was to determine how the fabricated structures compared to the design specifications. The performance of the stripe electrodes was determined in the second part. The piezoelectric activity evaluation was used to determine the relative piezoelectric activity of the PVDF film in six of the PPTSA configurations.

6. Phase VI. Two of the six PPTSA configurations from the previous phase were thermally poled and evaluated in this phase. The two configurations consisted of one stripe and one square-pad design configuration. A piezoelectric activity evaluation was performed on these two configurations after they were thermally poled.

Sequence of Presentation

A chronological order is used to present the flow of the thesis. The thesis consisted of five main sections: the background, the experimental designs and procedures, the

experimental data collection, the discussion and analysis, and the conclusions and recommendations.

The background information for the thesis is presented in Chapter II. This chapter discusses and summarizes the piezoelectric effect theory, how to induce the piezoelectric effect in polymers, and the concept of tactility as it relates to robotics. These subjects were determined crucial for understanding how piezoelectric polymer tactile sensor arrays for robotics are synthesized. The bulk of the material in this chapter was extracted from the literature.

The experimental designs, sensor fabrication procedures, thermal poling procedure, and evaluation procedures are described in Chapter III. The instrumental interfaces, equipment, and materials used in the various thesis procedures are discussed.

Chapter IV contains the experimental data. The data from the electrode-structure fabrication process evaluation and the piezoelectric activity evaluation are presented.

Finally a discussion and analysis section is presented in Chapter V. The data from the two evaluations are examined, discussed, and analyzed.

Chapter VI contains conclusions drawn from the discussion and analysis chapter. This chapter also provides recommendations for future studies.

The appendices contain supplemental material. The numerous fabrication procedures are Appendices A through F.

inclusive. Photocopies of the high resolution plates were placed in Appendix G. A sketch of the thermal poling chamber is included in Appendix H. The computer programs that were used in the data analysis are contained in Appendix I. Appendix J contains several graphs of piezoelectric activity data.

II. Background

Constructing piezoelectric polymer tactile sensor arrays for robotics requires an understanding of the piezoelectric effect, how to induce piezoelectricity in polymers, and the concept of tactility as it applies to robotics. This chapter covers the piezoelectric effect (history and origin), the properties of the polymer, polyvinylidene fluoride, the different methods of inducing the piezoelectric effect in polyvinylidene fluoride (stretching and poling), and the concept of tactility.

Piezoelectric Effect

This section presents a historical overview concerning the piezoelectric effect and the microscopic and macroscopic theory behind this effect. The history subsection explains that this effect was discovered more than 100 years ago; and that it no longer applies solely to crystals, but also includes ceramics and polymers. The microscopic theory subsection explains why piezoelectricity occurs in piezoelectric materials. The macroscopic theory subsection describes the derivation of the direct and converse piezoelectric effect equations.

Historical Perspective. In 1880, Pierre and Jacques Currie discovered that some crystals, when compressed in particular directions, produced positive and negative charges on certain portions of a crystal's surface (Cady,

1964:2-3). The charges produced were proportional to the applied pressure and disappeared when the pressure was removed. This discovery is known today as the direct piezoelectric effect. The piezoelectric effect was observed in crystals, such as quartz, rochelle salt, and tourmaline.

In the year following the Curries' discovery, Lippmann postulated the application of thermodynamic principles to reversible processes involving electric quantities (Cady, 1964:4). As a consequence, Lippmann postulated the converse piezoelectric effect. Before the end of 1881, the Curries also experimentally verified this effect.

By 1894, Duheim, Pockels, and Voight advanced the quantitative formulation of the piezoelectric theory (Cady, 1964:5). They combined elements of elastic tensors and electric vectors with the geometrical aspects of crystals to explain why 20 of the 32 crystal classes possessed the piezoelectric effect.

In 1916, Langevin conceived the idea of using quartz crystals underwater for emitters and receivers (Cady, 1964:5-6). In his experiment, one quartz crystal was excited with a high frequency signal, and he used another crystal to detect the emitted vibrations. Using the 'echo method', he was also able to determine the locations of objects.

The first piezoelectric ceramics were introduced in the early 1940's (Jaffe and others, 1971:1-4). Since piezoelec-

tric ceramics are generally isotropic in nature, they are not piezoelectric (Seippel, 1983:123). A ceramic is generally considered isotropic because it has the same properties regardless of the direction of measurement (Seippel, 1983:123). The polar axes of the individual crystallites in ceramics are randomly oriented with respect to each other. Piezoelectric properties are induced in ceramics using a poling process (Jaffe and others, 1971:1). The poling process uses an intense electric field and an elevated temperature to cause the polar axes of the crystallites to align and make the ceramics anisotropic. The crystallites will remain favorably aligned as the temperature is reduced to room temperature, at which the electric field is removed.

In 1969, Kawai discovered that polyvinylidene fluoride (PVDF) could be poled to a piezoelectric activity level not previously achieved with any other polymer (Kawai, 1969:975-976). He demonstrated that PVDF has the highest piezoelectric activity of all known polymers.

Microscopic Origin. This section explains the microscopic origin of piezoelectricity. Electric dipoles created under mechanical stress are shown to be the basic element of the piezoelectric effect. These electric dipoles are associated with a scalar electric potential and a vector electric field.

From electromagnetics, the electric dipole is an entity composed of two opposite charges of equal magnitude ($+q$ and

$-q$) which are separated by a distance l , as depicted in Figure 2.1 (Kraus, 1984:35). The vector electric dipole moment (\vec{p}) is (Kraus, 1984:35):

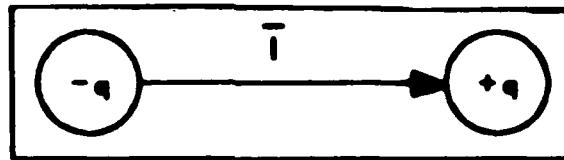


Figure 2.1. Electric Dipole (Kraus, 1984:35).

$$\vec{p} = q\vec{l} \quad (\text{C-m}) \quad (2.1)$$

where \vec{l} is the vector distance measured from the negative charge ($-q$) toward the positive charge ($+q$). The dipole moment (\vec{p}) is defined to be the product of the positive charge and the vector distance.

The vector electric polarization (\vec{P}) is the net electric dipole moment per unit volume, and is given by:

$$\vec{P} = \sum_{i=1}^N \vec{p}_i \quad (\text{C/m}^2) \quad (2.2)$$

where N is the number of electric dipole moments per unit volume. The value for polarization is highly dependent on the orientation of the individual electric dipole moments unless they all lie in the same direction.

An electric scalar potential (V) and a vector electric field (\vec{E}) from electrostatics can be associated with the

electric dipole moment (Kraus, 1984:35-36). Referring to Figure 2.2, the electric scalar potential of the electric dipole is:

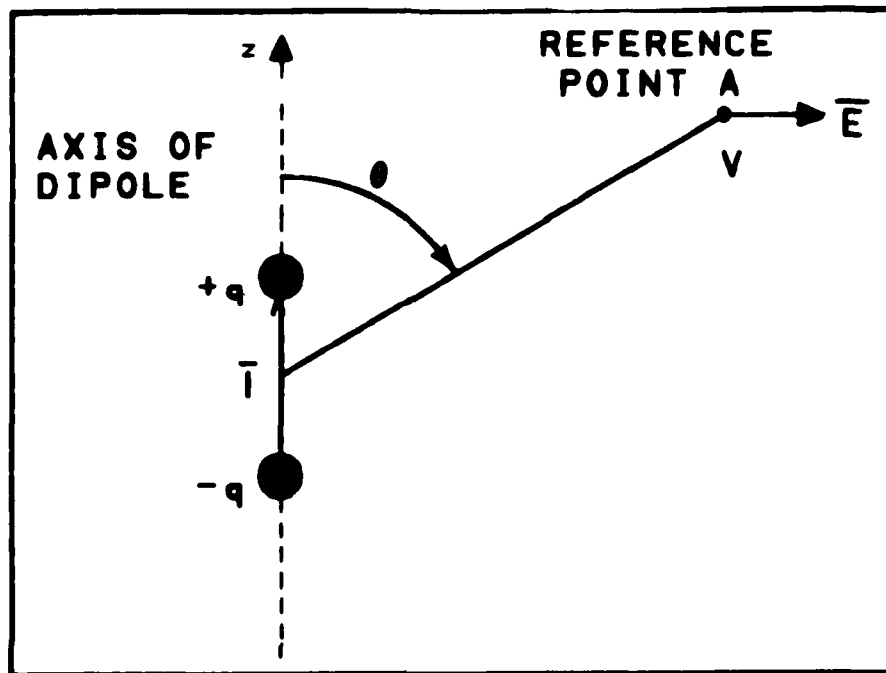


Figure 2.2. Scalar Electric Potential and Vector Electric Field (Kraus, 1984:35).

$$V = ql \cos(\theta) / 4\pi\epsilon r^2 \quad (V) \quad (2.3)$$

where

- ql = magnitude of the electric dipole moment (C-m),
- θ = angle measured from the z-axis (degrees),
- $\epsilon = \epsilon_0 \epsilon_r$ is the permittivity of the material (F/m),
- ϵ_0 = permittivity of vacuum (F/m),
- ϵ_r = relative permittivity, and
- r = distance from the center of the dipole to the reference point A (m).

The gradient of the scalar electric potential is the vector electric field (Kraus, 1984:36). The vector electric field (\vec{E}_s) in spherical coordinates at the reference point A for the dipole moment is:

$$\vec{E}_s = (ql / 4\pi\epsilon r^3) [\hat{r} 2 \cos(\theta) + \hat{\theta} \sin(\theta)] \quad (\text{V/m}) \quad (2.4)$$

where

\hat{r} = unit vector in the r direction

$\hat{\theta}$ = unit vector in the θ direction.

Since crystallographers use the rectangular coordinate system, it is appropriate to express the vector electric field in rectangular coordinates. The vector electric field in rectangular coordinates is:

$$\begin{aligned} \vec{E}_r = (ql / 4\pi\epsilon r^3) & \\ & [\hat{x} 3 \cos(\theta) \sin(\theta) \sin(\phi) \\ & + \hat{y} 3 \cos(\theta) \sin(\theta) \cos(\phi) \\ & + \hat{z} 3 \cos^2(\theta)] \quad (\text{V/m}) \quad (2.5) \end{aligned}$$

where

\hat{x} = unit vector in the x direction

\hat{y} = unit vector in the y direction

\hat{z} = unit vector in the z direction.

ϕ = angle measured from the x-axis (degrees).

Stressed crystals that display a net (directional) polarization are piezoelectric. The reason these crystals

develop a polarization is because they lack a center of inversion, and the crystal symmetry becomes distorted under stress. Figure 2.3 illustrates two crystals, one with a center of inversion and one without a center of inversion.

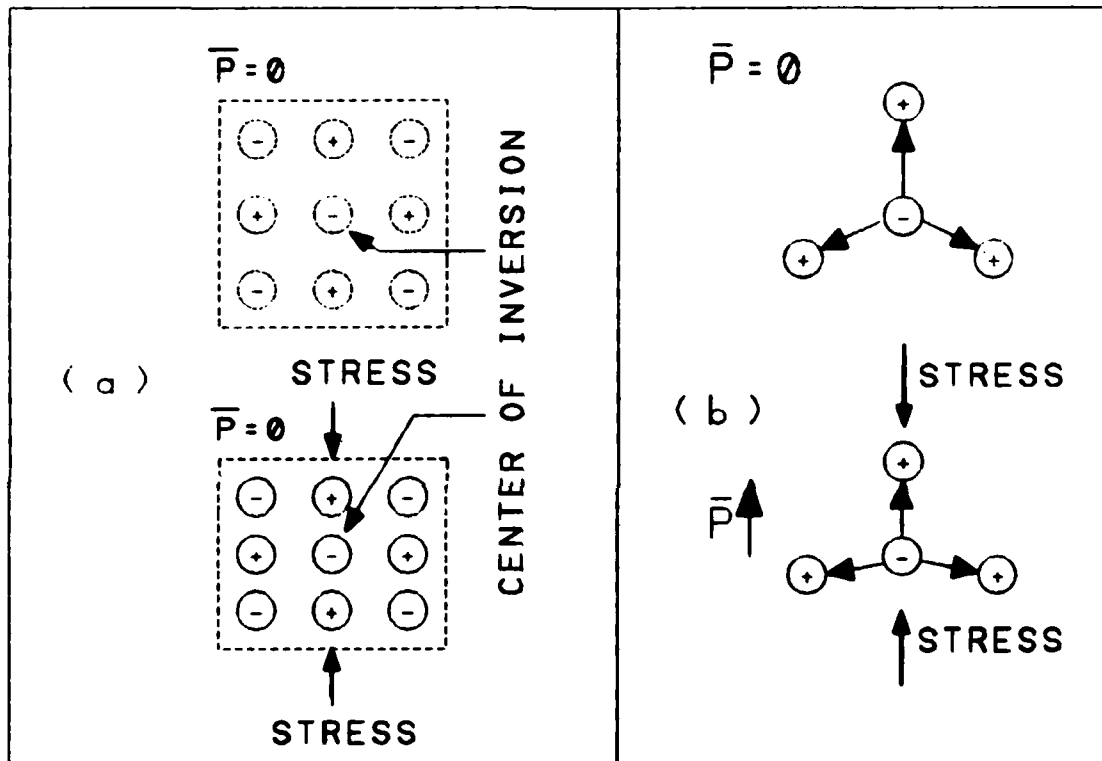


Figure 2.3. Crystals With and Without a Center of Inversion. (a) A Crystal with a Center of Inversion Exhibits No Piezoelectric Effect. (b) A Crystal Lacking a Center of Inversion Exhibits the Piezoelectric Effect (Omar, 1975:407).

The crystal with the center of inversion maintains a symmetrical charge distribution, even under stress, and does not produce a net polarization. However, the symmetrical charge distribution in the crystal that lacks a center of inversion produces a net polarization when stressed. The

associated electric scalar potential and electric field are created when a net polarization is produced.

Twenty of the 32 crystal classes are noncentrosymmetric (Omar, 1975:407-408). However, not all noncentrosymmetric crystals are good piezoelectric crystals, as illustrated in Table 2.1.

Table 2.1
Common Piezoelectric Crystals (Omar, 1975:407)
(in Decreasing Value of Piezoelectric Strength)

Crystal (Chemical Formula)	Relative Piezoelectric Strength
Rochelle Salt ($\text{NaKC}_4\text{H}_4\text{O}_6 - 4\text{H}_2\text{O}$)	Very Strong
Ammonium Dihydrogen Phosphate ($\text{NH}_4\text{H}_2\text{PO}_4$)	Strong
Potassium Dihydrogen Phosphate (KH_2PO_4)	Moderate
Alpha-Quartz (SiO_2)	Weak

The effect distortion has on a crystal can be illustrated with an example. A phenomenological piezoelectric crystal illustrated in Figure 2.4 possesses symmetry with respect to the negative charge before a stress is applied. The positive charges are positioned every 120° with respect

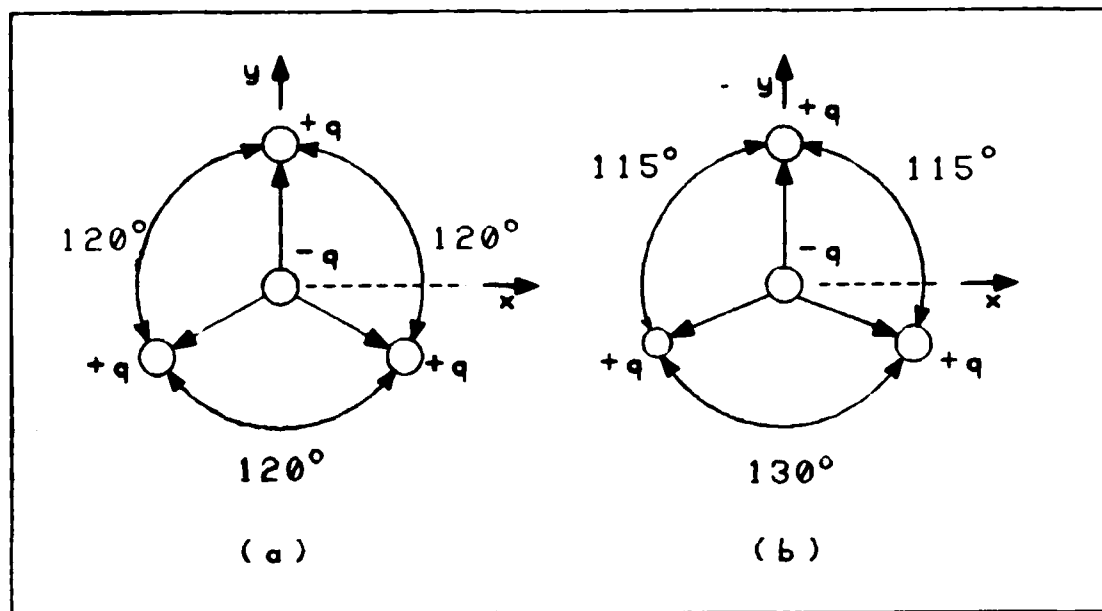


Figure 2.4. A Phenomenological Crystal (a) Unstressed and (b) Stressed.

to the negative charge. If the distance between the negative and positive charges is 5 units, the electric dipole moments are:

$$\begin{aligned}\bar{p}_1 &= \hat{x} [(0.0)q] + \hat{y} [(+5.0)q] \\ \bar{p}_2 &= \hat{x} [(-4.3)q] + \hat{y} [(-2.5)q] \\ \bar{p}_3 &= \hat{x} [(+4.3)q] + \hat{y} [(-2.5)q].\end{aligned}$$

The net polarization is given by applying Equation (2.2), and is:

$$\bar{P} = \hat{x} [(0.0)q] + \hat{y} [(0.0)q] = 0.0.$$

Now if an applied stress causes the angles between the upper positive charge and the other two positive charges to change

to 115° , and the third angle to change to 130° . the electric dipole moments become:

$$\bar{p}_1 = \hat{x} [(0.0)q] + \hat{y} [(+5.0)q]$$

$$\bar{p}_2 = \hat{x} [(-4.5)q] + \hat{y} [(-2.1)q]$$

$$\bar{p}_3 = \hat{x} [(+4.5)q] + \hat{y} [(-2.1)q].$$

Similarly, Equation (2.2) yields a net polarization:

$$\bar{P} = \hat{x} [(0.0)q] + \hat{y} [(+0.8)q].$$

Thus, the stress causes a net polarization in the positive y direction. In real crystals, the physical deformation and resulting angle change is very small. It is apparent that an increase in stress causes an increase in polarization.

Macroscopic Origin. Piezoelectricity in materials is typically described at the macroscopic level. In 1884, Voigt developed a system to describe the different relations that exist in materials (Cady, 1964:5-8). His system, which neglects atomic theory, describes the piezoelectric properties of a crystal in terms of three different types of directionally-sensitive quantities. These quantities are the electrical (field and polarization), the elastic (stress and strain), and the piezoelectric coefficients. In mathematical terms, the electrical coefficients are vectors (first order tensors), the elastic coefficients are second order tensors, and the piezoelectric coefficients are third order tensors.

The direct piezoelectric effect involves mechanical energy being proportionally converted to electrical energy, and the converse piezoelectric effect involves the inverse conversion process (Cady, 1964:4). Stresses, strains, and piezoelectric constants determine how the energy is converted.

Electrical, mechanical, and electromechanical properties of piezoelectric materials are directionally dependent for different mechanical and electrical excitations (KYNAR Piezo Film Department, 1983:30). Voight's system relates electric field and polarization vectors to stress and strain tensors. His system uses a rectangular coordinate system, but x , y , and z are changed to 1, 2, and 3, respectively. This coordinate system is shown in Figure 2.5.

Quantities are subscripted to indicate directions. Elastic compliances, stiffness coefficients, dielectric susceptibilities, and piezoelectric constants are identified with double numerical subscripts (KYNAR Piezo Film Department, 1983:30-32). With this notation, the first subscript identifies the polarization or electric field axis, and the second subscript identifies the mechanical stress or strain axis. Stresses, strains, electric fields, and polarizations are identified with a single numerical subscript which identifies the applicable axis.

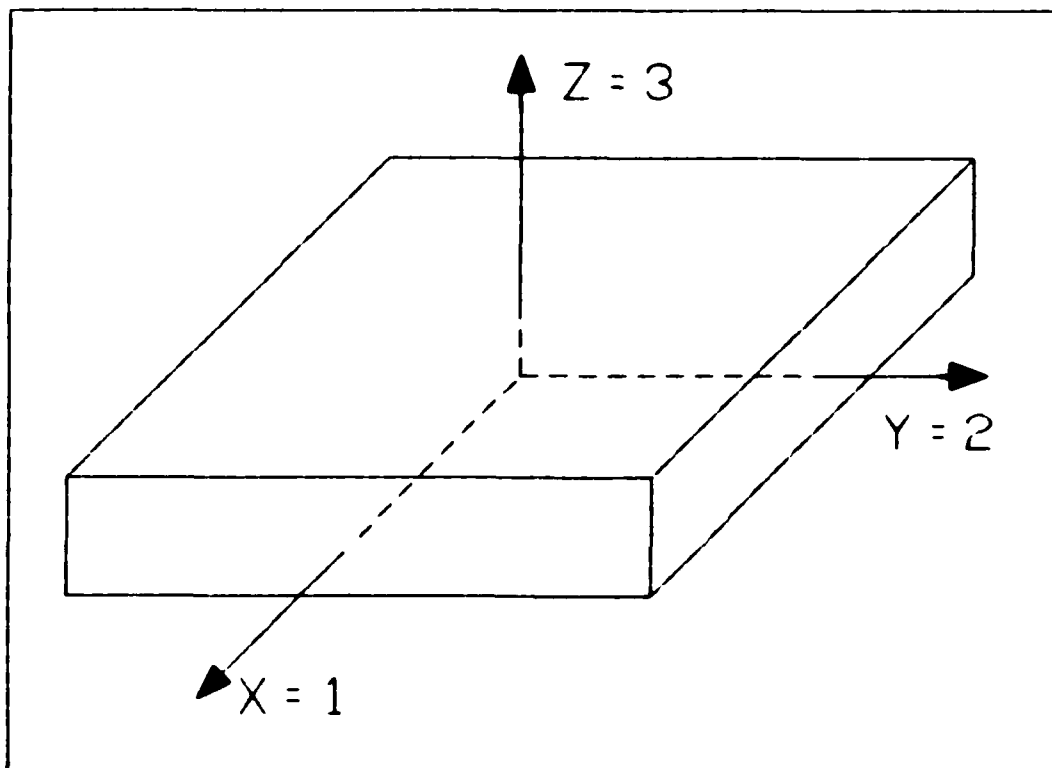


Figure 2.5. Rectangular Coordinate System Used in Crystallography (KYNAR Piezo Film Department, 1983:30)

The mode in which a piezoelectric element operates depends on the boundary conditions that exist (KYNAR Piezo Film Department, 1983:31-32). Table 2.2 describes several constants and their relationship to modes and boundary conditions (Seippel, 1983:124).

Stress (force per unit area), in the most general form, can be resolved into six components, three compressional stresses and three shearing stresses (Cady, 1964:45-47). The compressional stresses are denoted X_x , Y_y , and Z_z and the shearing stress are denoted Y_z , Z_x , and X_y . In each case, the upper-case letters in the notation denotes the

Table 2.2

Material Property Symbols and Definitions

(Seippel, 1983:128-129)

d_{33} Indicates that the piezoelectricity induced strain, or applied stress is in the 3-direction.

Indicates that electrodes are perpendicular to the 3-axis.

$$\frac{\text{strain}}{\text{applied field}} = \frac{\text{short circuit charge/electrode area}}{\text{applied stress}}$$

d_h Indicates that stress is applied equally in the 1-, 2-, and 3-directions (hydrostatic stress); and that electrodes are perpendicular to the 3-axis.

$$\frac{\text{short circuit charge/electrode area}}{\text{applied stress}}$$

ϵ_{15} Indicates that applied stress, or piezoelectrically induced strain is in the shear form around the 2-axis.

Indicates that electrodes are perpendicular to the 1-axis.

$$\frac{\text{field}}{\text{applied stress}} = \frac{\text{strain}}{\text{applied charge/electrode area}}$$

direction of the force, and the lower-case subscript indicates the direction of the normal to the surface on which the force acts. For convenience, the symbols X_x , Y_y , Z_z , Y_z , Z_x , and X_y are usually changed to X_1 , X_2 , X_3 , X_4 , X_5 , and X_6 , respectively. Positive stresses are extensional, and negative stresses are compressional. Figure 2.6 illustrates several of the different stresses.

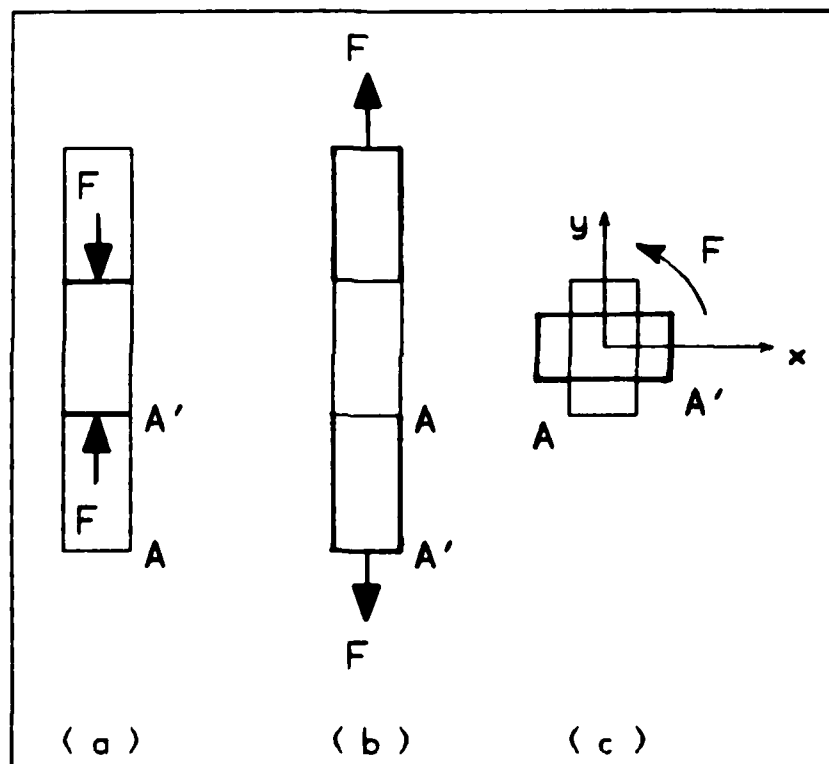


Figure 2.6. Three Common Stresses Found in Stressed Materials: (a) Compressional, (b) Extensional, and (c) Shear.

Strains (relative deformations) can also be resolved into six components, three compressional (x_x , y_y , z_z) and

three shearing strains (y_z , z_x , and x_y) (Cady, 1964:47-50; van der Ziel, 1968:511). They are denoted as S_1 , S_2 , S_3 , S_4 , S_5 , and S_6 , respectively. Positive strains are extensional and negative strains are compressional. Strains are related to displacements as follows: if the undisturbed coordinates of a point are x , y , and z , and u , v , and w describe the displacement of the point, then as the result of a strain, the new coordinates of the point are $(x + u)$, $(y + v)$, and $(z + w)$. Consequently,

$$S_1 = x_x = \frac{\partial u}{\partial x} \quad (\text{unitless}) \quad (2.6)$$

$$S_2 = y_y = \frac{\partial v}{\partial y} \quad (\text{unitless}) \quad (2.7)$$

$$S_3 = z_z = \frac{\partial w}{\partial z} \quad (\text{unitless}) \quad (2.8)$$

$$S_4 = x_y = \frac{\partial v}{\partial x} + \frac{\partial u}{\partial y} \quad (\text{unitless}) \quad (2.9)$$

$$S_5 = y_z = \frac{\partial w}{\partial y} + \frac{\partial v}{\partial z} \quad (\text{unitless}) \quad (2.10)$$

$$S_6 = z_x = \frac{\partial u}{\partial z} + \frac{\partial w}{\partial x} \quad (\text{unitless}) \quad (2.11)$$

Figure 2.7 shows the effect of positive strains occurring in the x , y , and z directions.

Nonpiezoelectric Materials. Hooke's law, assumed in elastic theory, is valid for all materials considered in the elastic limit (Kino, 1987:4; van der Ziel, 1968:511).

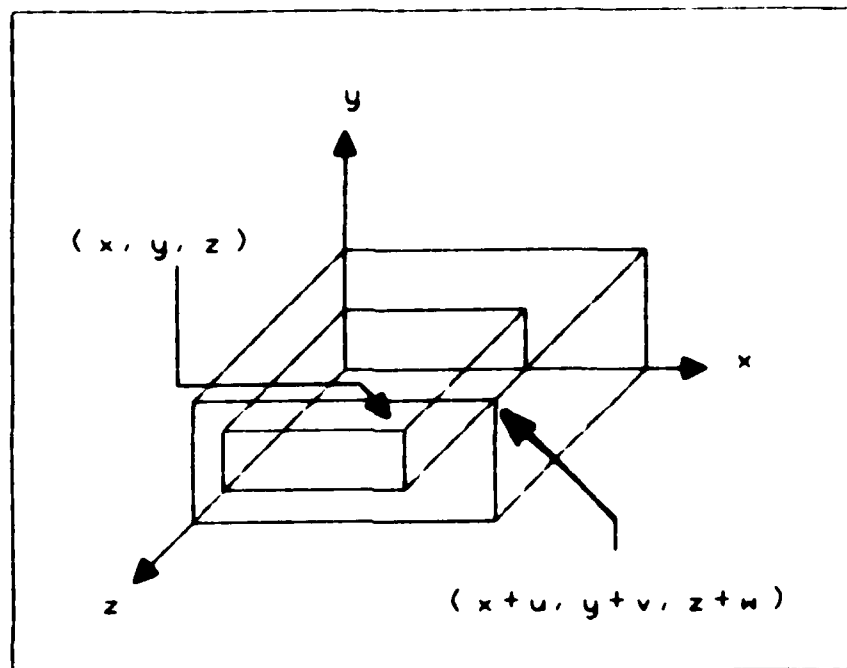


Figure 2.7. Strains in the x, y, and z Directions.

It describes a proportionality relationship that exists between strains and stresses, and can be written as (van der Ziel, 1968:511):

$$S_i = \sum_{k=1}^6 \sum_{j=1}^6 s_{ijk} X_k \quad (\text{unitless}) \quad (2.12)$$

and

$$X_i = \sum_{k=1}^6 \sum_{j=1}^6 c_{ijk} S_k \quad (\text{N/m}^2) \quad (2.13)$$

where

S_i = strain (unitless),

X_i = stress (N/m^2),

s_{ik} = elastic compliance coefficients (also called elastic susceptibility) (m^2/N), and
 c_{ik} = stiffness coefficient (also called elastic coefficient) (N/m^2).

It is obvious from Equations (2.12) and (2.13) that there are 36 elastic compliance coefficients and 36 stiffness coefficients. However, according to elastic theory, $s_{ik} = s_{ki}$ and $c_{ik} = c_{ki}$, so the maximum number of unique elastic compliance coefficients and stiffness coefficients is 21. Each stiffness coefficient can be related to the corresponding elastic compliance coefficient using the equation (van der Ziel, 1968:511):

$$c_{ik} = C_{ik} / D \quad (2.14)$$

where D is the determinant of the elastic compliance coefficients (Equation (2.12) matrix), and C_{ik} is the cofactor of the same determinant with respect to s_{ik} (van der Ziel, 1968:511).

The lowest order symmetrical crystals possess all 21 elastic coefficients that differ from zero (van der Ziel, 1968:511). As symmetry considerations increase, the number of coefficients equaling zero increases.

A linear relationship exists between the vector electric field and the resulting vector electric polarization (van der Ziel, 1968:511):

$$P_m = \sum_{m=1}^3 \sum_{i=1}^6 \epsilon_{im} E_m \quad (C/m^2) \quad (2.15)$$

where the ϵ_{im} 's are the dielectric constants. The subscripts for the polarization and electric field refer to the vector directions that apply.

Piezoelectric Materials. Two new effects occur in piezoelectric materials. The first effect is that an electric field creates an additional stress, and the second effect is that strain produces an additional polarization (van der Ziel, 1968:512). These relationships can be expressed as:

$$X_1 = \sum_{k=1}^6 c_{1k}^E S_k - \sum_{m=1}^3 e_{m1} E_m \quad (N/m^2) \quad (2.16)$$

$$P_m = \sum_{i=1}^6 e_{mi} S_i + \sum_{i=1}^3 \epsilon_{im}^S E_i \quad (C/m^2) \quad (2.17)$$

where the c_{1k}^E 's are the stiffness coefficients, and the ϵ_{im}^S 's are the dielectric constants (Cady, 1964:183; van der Ziel, 1968:512; KYNAR Piezo Film Department, 1983:33). The superscript E indicates a constant electric field, and $E=0$ means the electrode surfaces of a metallized piezoelectric element are connected together (short circuited). The superscript S indicates a constant strain, and $S=0$ means the material is completely restrained to prevent any mechanical deformation when an electric field is applied (clamped).

This parameter is measured only under very special conditions. The 18 e_{mi} 's are called the piezoelectric stress coefficients, or simply, the piezoelectric coefficients. As before, when symmetry increases, the number of coefficients equaling zero increases (van der Ziel, 1968:512).

The strains and polarizations can also be expressed in terms of the stresses and fields (van der Ziel, 1968:512) as:

$$S_i = \sum_{k=1}^6 s_{ik}^E X_k + \sum_{m=1}^3 d_{mi} E_m \quad (\text{unitless}) \quad (2.18)$$

$$P_m = \sum_{i=1}^6 d_{mi} X_i + \sum_{l=1}^3 \epsilon_{im}^X E_l \quad (\text{C/m}^2) \quad (2.19)$$

where the s_{ik}^E 's are the elastic compliance coefficients, and the ϵ_{im}^X 's are the dielectric constants. The superscript X indicates a constant stress and X=0 means no mechanical restraint exists (KYNAR Piezo Film Department, 1983:41; Fukada, 1982:128). The d_{mi} 's are the piezoelectric strain coefficients (van der Ziel, 1968:512).

Additional equations can be arrived at in a similar way (Fukada, 1982:128; KYNAR Piezo Film Department, 1983:41-42). These are:

$$E_m = - \sum_{i=1}^6 g_{mi} X_i + \sum_{n=1}^3 P_n / \epsilon_{mi}^X \quad (\text{V/m}) \quad (2.20)$$

$$E_m = - \sum_{k=1}^6 h_{mi} S_i + \sum_{m=1}^3 P_m / \epsilon_{mi}^S \quad (\text{V/m}) \quad (2.21)$$

$$S_i = \sum_{k=1}^6 s_{ik}^P X_k + \sum_{m=1}^3 g_{mi} P_m \quad (\text{unitless}) \quad (2.22)$$

$$X_i = \sum_{k=1}^6 c_{ik}^P S_k - \sum_{m=1}^3 h_{mi} P_m \quad (\text{N/m}^2) \quad (2.23)$$

where the g_{mi} 's are the piezoelectric strain (or voltage) constants, and the h_{mi} 's are the piezoelectric stress (or voltage) constants (KYNAR Piezo Film Department, 1983:43-44). The superscript P indicates a constant polarization, and P=0 means the electrode surfaces of a metallized element are not connected together (open circuited).

The piezoelectric constants are defined as (Fukada, 1982:128-129; KYNAR Piezo Film Department, 1983:43-44):

$$d = \frac{\partial P}{\partial X_E} = \frac{\text{electrical charge density developed}}{\text{applied mechanical stress}} \quad (2.24)$$

$$d = \frac{\partial S}{\partial E_X} = \frac{\text{strain developed}}{\text{applied electric field}} \quad (2.25)$$

$$g = \frac{\partial E}{\partial X_P} = \frac{\text{electrical field developed}}{\text{applied mechanical stress}} \quad (2.26)$$

$$g = \frac{\partial S}{\partial P_X} = \frac{\text{strain developed}}{\text{applied charge density}} \quad (2.27)$$

$$e = \frac{\partial X}{\partial E_S} = \frac{\text{mechanical stress developed}}{\text{applied electric field}} \quad (2.28)$$

$$e = \frac{\partial P}{\partial S_E} = \frac{\text{electric charge density developed}}{\text{applied strain}} \quad (2.29)$$

$$h = \frac{\partial E}{\partial S_P} = \frac{\text{electrical field developed}}{\text{applied strain}} \quad (2.30)$$

$$h = \frac{\partial X}{\partial P_S} = \frac{\text{mechanical stress developed}}{\text{applied charge density}} \quad (2.31)$$

Equations (2.24), (2.26), (2.28), and (2.30) disclose an electrical response due to a mechanical excitation (the direct piezoelectric effect). Equations (2.25), (2.27), (2.29), and (2.31) reveal a mechanical response to an applied electrical excitation (the converse piezoelectric effect) (Fukada, 1982:128-129).

The dielectric constants (ϵ^S and ϵ^X) and the elastic constants ($c^E = 1/s^E$ and $c^P = 1/s^P$) are correlated using the electromechanical coupling coefficient, k (Fukada, 1982:129). The correlation is:

$$\epsilon^S / \epsilon^X = c^E / c^P = 1 - k^2 \quad (2.32)$$

where $k^2 = gdc^E$ (KYNAR Piezo Film Department, 1983:44). The differences between the dielectric constants (ϵ^S and ϵ^X) and elastic constants (c^E and c^P) can be neglected for piezoelectric polymers where k^2 is less than 0.1 (Fukada, 1982:129). Because this difference can be neglected, the four piezoelectric constants are related to the dielectric and elastic constants as follows:

$$e/d = h/g = c \quad (2.33)$$

$$d/g = e/h = \epsilon. \quad (2.34)$$

The electromechanical coupling coefficient (k) is a parameter which indicates the ability of a material to convert electrical energy to mechanical energy, or to convert mechanical energy to electrical energy (Jaffe and others, 1971:10). The specific relationship is formulated in terms of k^2 . It can be represented for the direct piezoelectric effect as:

$$k^2 = \frac{\text{mechanical energy converted to electrical energy}}{\text{input mechanical energy}} \quad (2.35)$$

For the converse piezoelectric effect, it can be represented as:

$$k^2 = \frac{\text{electrical energy converted to mechanical energy}}{\text{input electrical energy}} \quad (2.36)$$

Jaffe and others have reported the conversion of mechanical to electrical energy is less than unity because the conversion is incomplete (Jaffe and others, 1971:10). Table 2.3 shows some typical values of electromechanical coupling coefficients for some piezoelectric crystals.

Polyvinylidene Fluoride

Of all the polymeric materials investigated, polyvinylidene fluoride (PVDF) exhibits the largest piezoelectric and pyroelectric coefficients when appropriately

Table 2.3

The Electromechanical Coupling Coefficients
for a Select Group of Piezoelectric Crystals
(Jaffe and others, 1971:10)

Crystal	Coupling Coefficient
Quartz	0.1
Barium Titanate Ceramic	0.4
Pb(TiZr)O ₃ Ceramic	0.5 - 0.7
Rochelle Salt	0.9

polarized (Marcus, 1982:29). The significant piezoelectric activity in PVDF is the result of mechanically stretching the polymer film, poling it in a static electric field at temperatures from 80 to 150°C, and then quenching it while the field is still applied (Marcus, 1985a:725). The PVDF polymer in film form is lightweight, durable, flexible, and available in a variety of thicknesses and surface areas. The desirable properties of PVDF has made it useful in numerous piezoelectric applications. Pennwalt describes six application areas for piezoelectric PVDF film. These application areas (KYNAR Piezo Film Department, 1983:64-65) include:

1. Hydrophones (acoustically transparent microphones or hydrophones),

2. Pressure transducers (keyboards, key pads, touch panel, coin sensors, load cells),

3. Audio transducers (microphones, headset speakers, high frequency speakers, phonograph cartridges),

4. Electromechanical devices (optical displays, fans, deformable mirrors, antifouling devices, gauges, motion detectors),

5. Pyroelectric detectors (intrusion detection), and

6. Ultrasonics (medical imaging, pulse-echo).

Advantages and Disadvantages. Chatigny and Robb (Chatigny and Robb, 1986:53) noted there were obvious operating advantages and disadvantages that PVDF film possessed compared to the well-known piezoelectric active materials (such as quartz and piezoceramics). The advantages they noted (Chatigny and Robb, 1986:53) for PVDF film were:

1. The film can operate over an extremely wide frequency range (DC to 10 MHz).

2. It has a wide dynamic range (>286 decibel range).

3. It has a low acoustic impedance. (This feature makes it a good impedance match for medical ultrasound and hydrophone applications.)

4. The film has a higher dielectric strength than piezoceramic material (30 V/micron versus 1.5 V/micron) and, therefore, can be exposed to higher electric fields.

5. The film has a relatively high electrical impedance. (This advantage allows the film to provide a complimentary match to high-impedance devices (for example, CMOS) and circuits.)

6. Since the film is thin and flexible, it can be laminated to a vibrating structure without significantly distorting the motion of the structure.

7. Because the film is a high molecular weight fluoropolymer, it is mechanically strong and resistant to extreme environmental conditions (most solvents, acids, oxidants, and intense ultraviolet radiation).

8. The film can be cut and formed into complex shapes or prepared as a large transducer area.

9. The material and fabrication costs of the film are generally lower than those of other piezoelectric materials.

The disadvantages of PVDF film Chatigny and Robb mentioned (Chatigny and Robb, 1986:53) were:

1. A low electromechanical coupling coefficient compared to piezoelectric ceramics.

2. The piezoelectric activity in the film decreases when subjected to elevated temperatures above a 100°C. (Its applications are limited to operating below a 100°C.)

3. The film is sensitive to electromagnetic interference (EMI) over a wide frequency range. (For certain applications, the active area of the film is shielded from EMI radiation.)

4. Thick films (> 1 millimeter) are difficult to produce due to the enormous electric field required to pole them.

Physical Properties of PVDF. At a molecular level, PVDF is a ferroelectric, semi-crystalline, high-molecular weight polymer whose molecular repeat formula (monomer) is $(\text{CH}_2-\text{CF}_2)_n$ (KYNAR Piezo Film Department, 1983:26-28; Lovinger, 1983:1115). The monomer's (elementary repeating unit of the macromolecular chain) dipole moment is approximately 7.56×10^{-30} C-m (2.27 Debye) (Marcus, 1982:29).

The polymer crystallizes in at least three distinct crystalline forms: alpha (or phase II), beta (or phase I), and gamma (or phase III) (Marcus, 1985a:724-725; Shuford and others, 1976:25-26). The alpha and beta crystalline forms are shown in Figure 2.8. The alpha-form is the most common form, and it is produced by cooling the polymer from the melt (Lovinger, 1983:1116-1117). As shown in Figure 2.8a, the chain conformation of the alpha-form of PVDF is slightly distorted and belongs to an orthorhombic unit cell with lattice parameters: $a = 4.96$ angstroms, $b = 9.65$ angstroms, and c (chain axis) $= 4.62$ angstroms (Bachman and Lando, 1981:40). The antiparallel packing of the chains make the

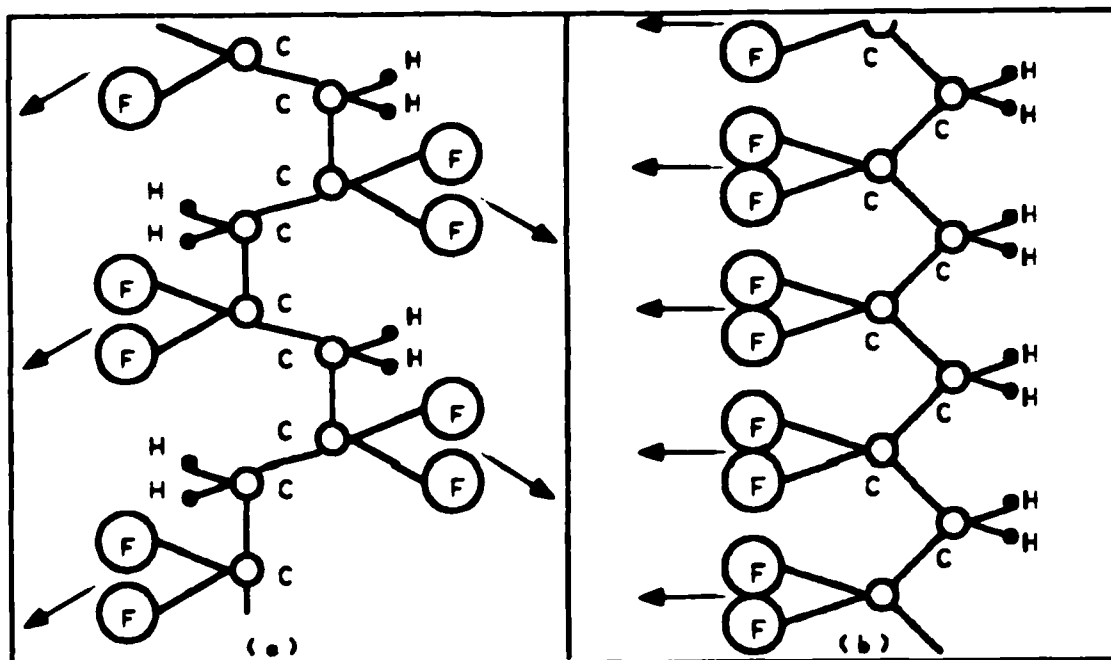


Figure 2.8. Schematic Depiction of the Two Most Common Crystalline Chain Conformations of PVDF: (a) Alpha-Form PVDF and (b) Beta-Form PVDF. (The arrows indicate the projections of the $-CF_2$ dipole directions on the carbon backbone planes. The alpha-form has components of the dipole moment both parallel and perpendicular to the chain axis, while the beta-form has all dipoles essentially normal to the molecular axis.) (Lovinger, 1983:1116).

alpha-form crystallite non-piezoelectric. Mechanically stretching the alpha-form of PVDF at temperatures below 80°C yields the beta-form that is illustrated in Figure 2.8b (Hasegawa and others, 1972:600). The result is a polar crystal with a dipole moment of 6.9×10^{-30} C-m (2.1 Debye) normal to the chain axis, because adjacent chains pack the unit cell with parallel dipoles (Marcus, 1982:29). The most significant piezoelectric response is associated with the

polar beta-form (KYNAR Piezo Film Department, 1983:27). The gamma-form PVDF is produced by crystallization in specific solvent systems (Kobayshi and others, 1975:158) or by high-temperature annealing of the alpha-form (Prest, 1975:4136). This crystalline form is an intermediate between the alpha- and beta-forms (Marcus, 1982:29-30).

Poling causes crystalline phase transitions in PVDF to occur (Davis and others, 1978:4998; Marcus, 1985a:724-725). Poling fields spanning 0.6 to 1.5 MV/cm convert the alpha-form PVDF into a polar alpha-form (also called the delta-form) PVDF (Marcus, 1985a:725; Scheinbeim and others, 1979:6101). The dipole moments are inverted normal to the 'c' direction on alternating chains. Stronger poling fields convert the polar alpha-form PVDF to beta-form PVDF.

Piezoelectric Activity. In 1981, Wada and Hayakawa developed the theory of piezo- and pyroelectricity for PVDF (Wada and Hayakawa, 1981:115). Their theory was based on a model in which spheres with a vector spontaneous polarization (\vec{P}_{sc}) are embedded (or dispersed) in an isotropic matrix (Wada and Hayakawa, 1976:2042-2054; Wada and Hayakawa, 1981:115). They calculated the piezoelectric constants e_{31} and e_{33} (using the model) and discovered their calculations were in good agreement with measured values (Wada and Hayakawa, 1981:115-118). Their theory (Wada and Hayakawa, 1981:115-117) was formulated as follows:

1. The theory started with a composite model (Wada and Hayakawa, 1976:2042-2054) in which spherical particles with a vector spontaneous polarization (\bar{P}_{sc}) are dispersed in an isotropic matrix as illustrated in Figure 2.9. The vector

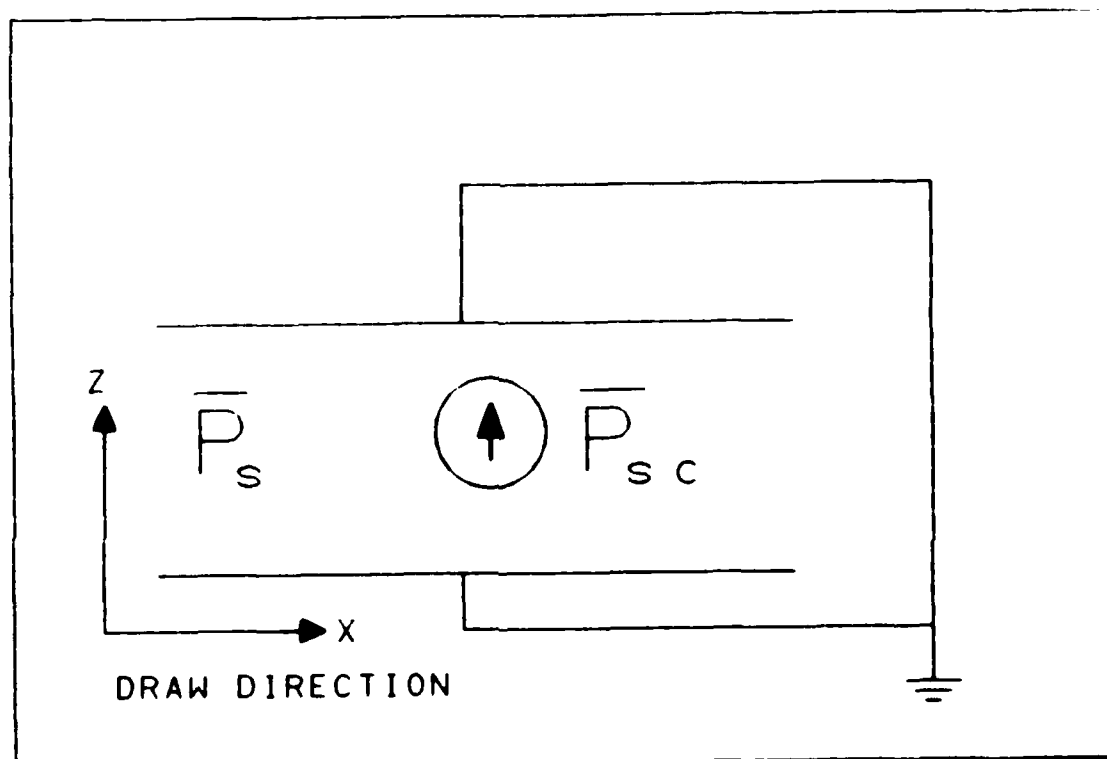


Figure 2.9. A Sphere with Spontaneous Polarization Dispersed in an Isotropic Matrix (Wada and Hayakawa, 1981:115).

spontaneous polarization of the whole film, P_s , is given by (Wada and Hayakawa, 1981:115):

$$\begin{aligned}\bar{P}_s &= (N/A \cdot l) [3\epsilon / (2\epsilon + \epsilon_c)] \nu \bar{P}_{sc} \\ &= \gamma [3\epsilon / (2\epsilon + \epsilon_c)] \bar{P}_{sc}.\end{aligned}\tag{2.37}$$

where

\bar{P}_{sc} = vector spontaneous polarization of the particles
in the isotropic matrix (C/m^2),

N = number of spheres in the film,

v = volume variable of the film (m^3),

A = electrode area (m^2),

l = thickness variable of the film (m),

γ = volume fraction of spheres,

ϵ_c = dielectric constant for a sphere (F/m),

ϵ = dielectric constant for the whole film (includes
the effects of the spheres distributed in the
matrix) (F/m).

2. The measurement of the piezoelectric constant 'e' of
polymer films requires depositing electrodes on both
surfaces of the film. The piezoelectric constant 'e' is
defined as (Wada and Hayakawa, 1981:115):

$$e = \frac{1}{A} \frac{\partial AP}{\partial S_E} \quad (2.38)$$

and not as Equation (2.29):

$$e = \frac{\partial P}{\partial S_E} \quad (2.39)$$

where P is polarization, A is electrode area, E is electric
field, and S is strain. Applying Equation (2.38) to

Equation (2.37), the piezoelectric constant (e) can be
expressed as:

$$e = P_s \left[\left(\frac{\epsilon_c}{2\epsilon + \epsilon_c} \right) \left(\frac{\kappa}{\epsilon} - \frac{\kappa_c}{\epsilon_c} g \right) - \frac{\partial \ln(l)}{\partial s} \right] + \gamma \left(\frac{3\epsilon}{2 + \epsilon_c} \right) e_c g \quad (2.40)$$

where

$\kappa = \frac{\partial \epsilon}{\partial s}$ is the electrostriction constant.

g = ratio of strain (S_c) in the sphere to that in the whole film, and

e_c = piezoelectric constant of the sphere.

The terms ' g ' and ' e_c ' are further defined as:

$$g = [5G / (3G + 2G_c)] \quad (2.41)$$

and

$$e_c = \frac{1}{\nu} \frac{\partial (\nu P_{sc})}{\partial S_c} = P_{sc} \left(\frac{\partial \ln(\nu)}{\partial S_c} + \frac{\partial \ln(P_{sc})}{\partial S_c} \right) \quad (2.42)$$

where

G = elastic modulus of the whole film and

G_c = elastic modulus of the sphere.

3. The origins of piezoelectricity were summarized as:

a. Strain dependence of dielectric constant (ϵ).

b. Strain dependence of the film thickness (l).

(This origin is considered the dimensional effect.)

- c. Strain dependence of the volume (ν).
- d. Strain dependence of particle (or sphere) spontaneous polarization (\bar{P}_{sc}).

Wada and Hayakawa compared their calculations of the piezoelectric constant 'e' to experimental measurements (Wada and Hayakawa, 1981:117-118). Tables 2.4 and 2.5 summarize their results. They noted the dimensional effect

Table 2.4

Theory Compared to Experiment
for the Piezoelectric Constant 'e'
(Wada and Hayakawa, 1981:118)

Piezoelectric Constant (10^{-2} C/m ² at room temperature)		
	Calculated	Observed*
e_{31}	5.5	5.5
$-e_{33}$	>7.3	8.7

* Kepler and Anderson, 1978:4491.

was the major origin of piezoelectricity for PVDF (Wada and Hayakawa, 1981:117-118).

From symmetry and experiments which involve applying stresses to a polarized specimen, it was discovered that the

Table 2.5

Calculated Fractional Contributions (percent)

for the Piezoelectric Constant 'e'

(Wada and Hayakawa, 1981:118)

	Strain Dependence of Dielectric Constant	Dimensional Effect	Crystal*
e_{31}	22	78	~ 0
$-e_{33}$	~ 0	70	30

* Includes oriented amorphous phase and space charges.

piezoelectric strain constant 'd' matrix (Bur and Roth, 1985:713; Fukada, 1982:127-128) for PVDF is:

$$\begin{bmatrix} 0 & 0 & 0 & 0 & d_{15} & 0 \\ 0 & 0 & 0 & d_{24} & 0 & 0 \\ d_{31} & d_{32} & d_{33} & 0 & 0 & 0 \end{bmatrix} \quad (2.43)$$

The effects the constants d_{31} , d_{32} , and d_{33} manifest are usually observed. The effects the constants d_{15} and d_{24} display are normally ignored for thin films (6-800 microns). The reason these constants are ignored is because it is very

difficult to collect charges from the 1- and 2-planes of thin films.

Measuring the thickness-mode piezoelectric activity in PVDF film pressure transducers requires generating a useful figure of merit (Assente, 1985:795-796; Pedotti and others, 1984:166). The most common figure of merit is d_{33}^* , and it is defined as (Pedotti and others, 1984:166):

$$d_{33}^* = d_{33} - (1/2) (d_{31} + d_{32}). \quad (2.44)$$

The motivation for specifying this figure of merit is that, during a measurement, the material is not completely free to move in the plane of the film (Pedotti and others, 1984:166). This situation implies that the effects of the constants d_{31} and d_{32} must be taken into account. These two constants have an opposite sign to d_{33} and result in the subtraction of charges from the total number of electrical charges developed under the thickness-mode of operation.

Orientation Dependence. The piezoelectric activity in PVDF is strongly dependent on the film's orientation (Marcus, 1982:30). Uniaxially oriented film is stretched in only the machine direction (in the 123 coordinate system, this is the 1-direction), and biaxially oriented film is stretched in both the machine and transverse directions (1- and 2-directions). Uniaxially oriented films have a high d_{33} and a low d_{32} , whereas biaxially oriented films have a d_{31} and d_{32} that are approximately equal. Table 2.6 shows a

comparison of some properties of 'well-poled' uniaxially oriented and biaxially oriented films of PVDF.

Table 2.6

Comparison of Parameters of Poled Uniaxially Oriented and Biaxially Oriented PVDF Films (Marcus, 1982:30)

Parameter	Uniaxially Oriented Kureha* Piezo Film 9 microns thick (pC/N)	Biaxially Oriented Kureha* Capacitor Film 25 microns thick (pC/N)
d_{31}	24.0	12.4
d_{32}	2.0	12.3
d_{33}	-39.0	-44.4
d_h	-13.5	-19.7

* The Kureha Chemical Company is a manufacturer of PVDF film.

A number of researchers (Scheinbeim and Chung, 1981:5985-5986; Shuford and others, 1976:25-35) found experimentally that the amount of piezoelectric activity occurring in stretched PVDF film was strongly related to the draw ratios. They discovered the piezoelectric activity for PVDF increased the greatest amount when the draw ratio spanned 3:1 to 5:1. Table 2.7 summarizes the results of the researchers', Shuford, Wilde, Ricca and Thomas.

Table 2.7

Draw Ratio Versus Piezoelectric Constant ' d_{33} ' (Shuford and others, 1976:27) (Poling: 500 KV/cm, 80-85°C, 45 minutes)

	Draw Ratio						
	1:1	2:1	3:1	4:1	5:1	6:1	7:1
d_{33} (pC/N)	2.2	6.2	5.1	8.5	14.5	13.5	13.0

Temperature Dependence. Kolbeck (Kolbeck, 1982:1987-2000) showed in a study that the long-term isothermal aging of piezoelectric PVDF at temperatures between 27 and 160°C could be partitioned into three temperature regimes. The first regime, for temperatures below 60°C, demonstrated there was no measurable decrease in room-temperature piezoelectric constants for samples aged 1.1 years (the length of his study). In the second regime, for temperatures spanning 60 to 100°C, PVDF films showed finite decay rates as a function of aging time. He noted little decrease in piezoelectric constants for periods under a minute. The third regime, for temperatures above a 100°C, showed both finite decay rates and substantial decreases in piezoelectric constants for short-time aging (time periods on the order of a minute).

Piezoelectric PVDF Film Manufacturers. At present, there are three commercial manufacturers of piezoelectric PVDF

film. These manufacturers are the Pennwalt Corporation (900 First Avenue, P.O. Box C, King of Prussia, PA 19406-0018), the Solvay & Cie Company (310, rue de Ransbeek - 1120 Brussels, Belgium), and the Kureha Chemical Industry Co. Ltd. (Iwaki-shi, Fukushima-ken, 974, Japan). Pennwalt calls their piezo film KYNAR. KYNAR is uniaxially oriented and is available in eight thicknesses (in microns): 6, 9, 16, 28, 52, 110, 500, and 750 (KYNAR Piezo Film Depart., 1983:61). Table 2.8 summarizes the published properties of KYNAR. Solvay calls their piezo film Solef. Solef is biaxially oriented and comes in five thicknesses (in microns): 9, 25, 40, 500, and 1000. The published properties of Solef are shown in Table 2.9. Kureha's film is identified as KF. Their film is available in either the uniaxially or biaxially orientation with thicknesses (in microns): 9, 16, 25 and 30.

Inducing the Piezoelectric Effect In Polyvinylidene Fluoride

This section describes the techniques used to induce the piezoelectric effect in polyvinylidene fluoride (PVDF) film. Mechanically stretching and subsequent poling of PVDF film makes it piezoelectric (Lovinger, 1983:1118). Mechanical stretching orientates the PVDF crystalline structure, and thus, imparts limited piezoelectric activity in PVDF (Gerliczy and Betz, 1984:3-4). Poling refers to the momentary application of a strong electric field to the PVDF

Table 2.8

Typical Properties for KYNAR

(KYNAR Piezo Film Department, 1987:14-15)

(Uniaxially Oriented and Corona Poled)

Piezoelectric Strain or Charge Constants

$$d_{31} = 23 \times 10^{-12} \text{ (m/m)/(V/m) or (C/m)/(N/m)}$$

$$d_{32} = 3 \times 10^{-12} \text{ (m/m)/(V/m) or (C/m)/(N/m)}$$

$$d_{33} = -33 \times 10^{-12} \text{ (m/m)/(V/m) or (C/m)/(N/m)}$$

$$d_h = -7 \times 10^{-12} \text{ (m/m)/(V/m) or (C/m)/(N/m)}$$

$$d_t = 22 \times 10^{-12} \text{ (m/m)/(V/m) or (C/m)/(N/m)}$$

Electromechanical Coupling Constants

$$k_{31} = 12\% (\text{at } 1 \text{ KHz})$$

$$k_{33} = 29\% (\text{at } 1 \text{ KHz})$$

ϵ	Permittivity	$106-113 \times 10^{-12} \text{ F/m}$
ϵ_r	Relative Permittivity	12-13
C	Capacitance	379 pF/cm^2 (28 micron thick film, @ 10 KHz)
Y	Youngs modulus	$2 \times 10^9 \text{ N/m}^2$
Z_a	Acoustic Impedance	$2.7 \times 10^6 \text{ Kg/m}^2\text{-s}$ (transverse)
Z_e	Electrical Impedance	1350 ohms (100 cm^2 , thickness = 9 μm , 1 KHz)
c	Elastic Modulus	$3 \times 10^9 \text{ N/m}^2$

Table 2.8 (continued)

ρ	Mass Density	$1.78 \times 10^3 \text{ Kg/m}^3$
ρ_v	Volume Resistivity	$1.5 \times 10^{13} \text{ ohm-meter}$
ρ_s	Surface Metallization Resistivity	1 ohm per square for Al 23 ohm per square for Ni
E_o	Maximum Operating Field	10 V/micron (● DC) 30 V/micron (● AC)
	Compressive Strength	$55-70 \times 10^6 \text{ N/m}^2$
	Melting Point	$165-180^\circ\text{C}$

film. The poling process enhances and stabilizes the piezoelectric properties to such a degree that they are of practical significance.

PVDF is composed of many crystallites in random orientation (KYNAR Piezo Film Department, 1983:7, 29). Each unit cell within these crystallites contains a dipole. Poling causes these dipoles to align with the field, thus making PVDF piezoelectric. The unit cells of PVDF do not have a center of symmetry, and therefore, allows PVDF to become piezoelectric after poling. The electric field does not align all of the dipoles, but enough of them do align to achieve piezoelectric activity (Seippel, 1983:123-124). PVDF, once polarized, exhibits specific electrical and physical properties.

Orientation Techniques. A number of film orientation techniques exist for producing uniaxially and biaxially

Table 2.9

Principal Properties for the Solef Material (Solvay, 1984:1)
(Biaxially Oriented and Corona Poled)

Piezoelectric Strain or Charge Constants

$$d_{31} = 8 \times 10^{-12} \text{ (m/m)/(V/m) or (C/m)/(N/m)}$$

$$d_{32} = 8 \times 10^{-12} \text{ (m/m)/(V/m) or (C/m)/(N/m)}$$

$$d_{33}^* = 16 \times 10^{-12} \text{ (m/m)/(V/m) or (C/m)/(N/m)}$$

Piezoelectric Strain or Charge Constants (after 100 hours of exposure at 70°C)

$$d_{31} = 7 \times 10^{-12} \text{ (m/m)/(V/m) or (C/m)/(N/m)}$$

$$d_{32} = 7 \times 10^{-12} \text{ (m/m)/(V/m) or (C/m)/(N/m)}$$

$$d_{33}^* = 15 \times 10^{-12} \text{ (m/m)/(V/m) or (C/m)/(N/m)}$$

Relative Dielectric Constant 11.0

Shrinkage (after 100 hours of exposure to 80°C) 2 %

Tensile Strength $180 \times 10^6 \text{ N/m}^2$

Elongation 50 %

Elastic Modulus $2000 \times 10^6 \text{ N/m}^2$

oriented PVDF films (Marcus, 1985b:894). These techniques include hot-roll relaxing, drafting, oven stretching, tentering, and compression rolling (Marcus, 1985b:894). Uniaxially stretched film is stretched in the longitudinal (machine) direction whereas biaxially stretched film is stretched in the longitudinal direction, as well as the

transverse direction. The piezoelectric constant d_{31} increases as the degree of orientation increases in a film. Specific processing descriptions follow (Marcus, 1985b:894-897):

1. Hot-roll relaxing. This technique uses overdriving takeup rollers with respect to takeoff rollers to uniaxially stretch the film. The takeoff rollers are normally heated, and infrared heater banks are placed between the rollers to improve film adhesion to the stretching rollers.

2. Drafting. Drafting usually consists of grasping the side edges of the film and pulling it in the machine direction while the film is heated. This technique results in a uniaxially stretched film.

3. Oven stretching. In this technique, the film is gripped at its ends in an oven and elongated so the film becomes uniaxially stretched.

4. Tenting. The film is stretched in the width (transverse) direction in this technique. The film's edges are simply gripped and pulled. This technique is used to make uniaxially oriented film biaxially oriented.

5. Compression rolling. In compression rolling, the film is passed through heated rotating rollers under extremely high pressures. The film becomes uniaxially oriented with minimal change to its width.

Table 2.10 summarizes the dielectric data which results from the different orientation techniques.

Table 2.10

Dielectric Data for Different Orientation Techniques
(Marcus, 1985b:898)

Technique	Dielectric Constant		Draw Ratio	Breakdown Field (MV/cm)
	1 KHz	10 KHz		
Cast	11.8	11.5		1.8
Hot Rolled Relaxed	13.2	12.9	3.5	2.3
Oven Stretched	15.1	14.7	4.0	2.2
Compression Rolled	14.6	14.2	3.5	2.1

Poling Techniques. Electric field, corona, and plasma poling are the three distinct poling techniques that have been used to make PVDF film piezoelectric. Electric field poling uses a static potential difference applied across electrodes that are positioned on opposite surfaces of the film (Groner and Hirsh, 1985:912). Corona poling uses a corona discharge to deposit charges on one surface of the film while the other surface is held at a polarity opposite that of the corona. The deposited charges flow through the

film and create an electric field across the PVDF film. McKinney, Davis, and Broadhurst developed the most recent technique, called plasma poling (McKinney and others, 1979:1676-1681). To implement this technique, the PVDF film is clamped in an electrode assembly with one surface of the film grounded to an electrode, and the other surface exposed to a plasma of opposite polarity. This situation results in the creation of an electric field across the thickness of the PVDF film. In all three techniques, the piezoelectric activity increases with increases:

1. In the applied field and temperature for field poling (Shuford and others, 1976:29-32);
2. In the applied charge for corona poling (Groner and Hirsh, 1985:912; Das-Gupta and Doughty, 1978:4602-4603); and
3. In the impressed electric field for plasma poling (McKinney and others, 1980:1676-1681).

Field poling occurs in different forms. Figure 2.10 shows that one form of field poling uses an applied field between 0.60 to 1.5 MV/cm at 80 to 120°C for up to an hour, with a subsequent cooling under the influence of the applied field (Gerliczy and Betz, 1984:3-4; Marcus, 1982:30). This form of field poling is called thermal poling. In 1983, Wang and von Seggern demonstrated field poling could be accomplished using the setup in Figure 2.11 (Wang and von Seggern, 1983:4602-4604). This version of field poling was

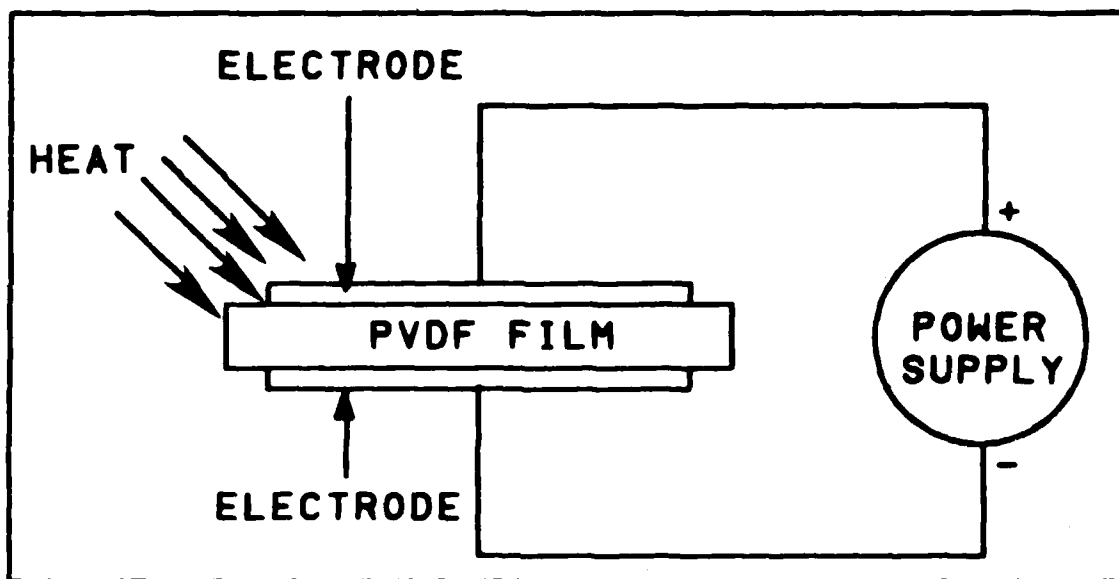


Figure 2.10. High Field Poling (Gerliczy and Betz, 1984:20).

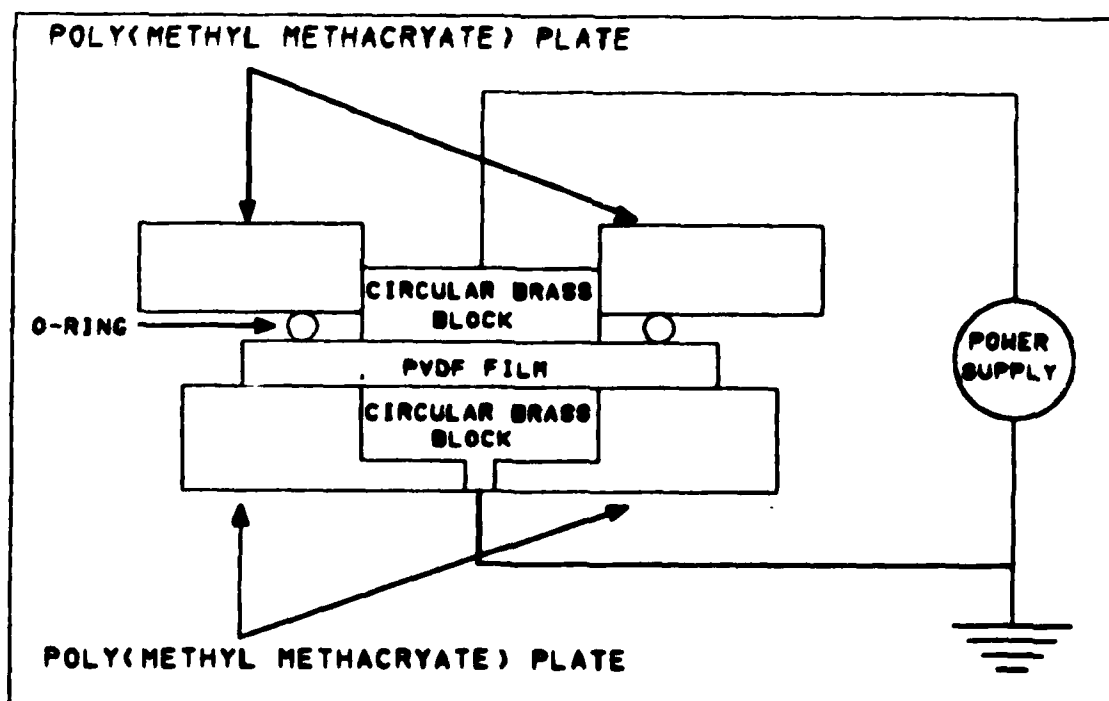


Figure 2.11. Schematic Drawing of Wang and von Seggern's Poling Arrangement (Wang and von Seggern, 1983:4602).

accomplished at room temperature, and the electric field was greater than 6 MV/cm (Wang and von Seggern, 1983:4602-4604). The duration of poling was short, 5 to 10 seconds (Wang and von Seggern, 1983:4602-4604). One year later, with West and Keith, Wang and von Seggern reported (Wang and others, 1984:249-256) the development of a different version of their high electric field poling technique. This version utilizes an electric field strength spanning 0.2 to 1.2 MV/cm at room temperature that is applied for 25 seconds using a current limiting circuit. This technique used essentially the same configuration seen in Figure 2.11, but as shown in Figure 2.12, a large-valued resistor (between 5×10^7 to 10^{11} ohms) was added in series with the power supply. The resistor was used to control the voltage

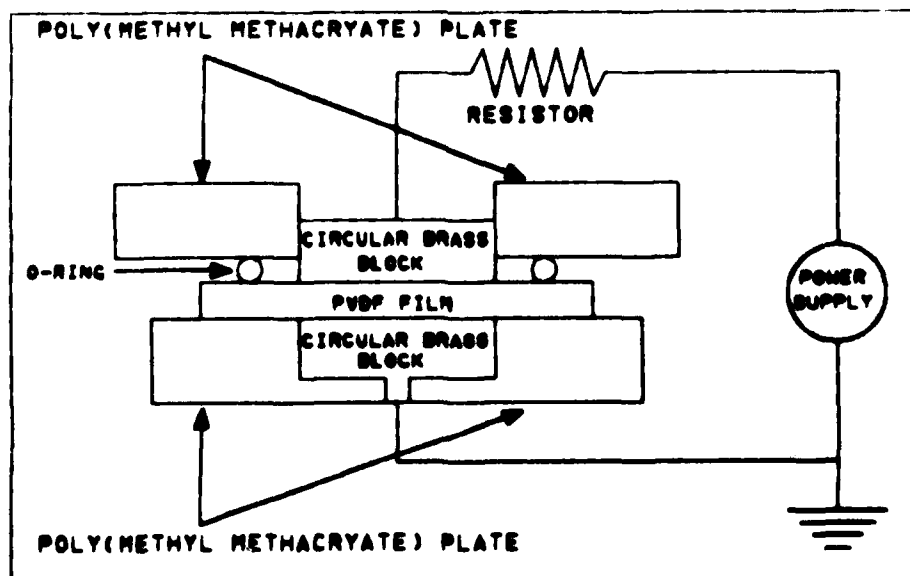


Figure 2.12. Schematic Drawing of the Current Limiting Poling Arrangement (Wang and others, 1984:250).

buildup across the PVDF film and to limit the current flow through the film to minimize breakdown.

Figure 2.13 illustrates a corona poling arrangement. An aluminum electrode is evaporated on the surface of the film, and it is used to make contact with the ground plate.

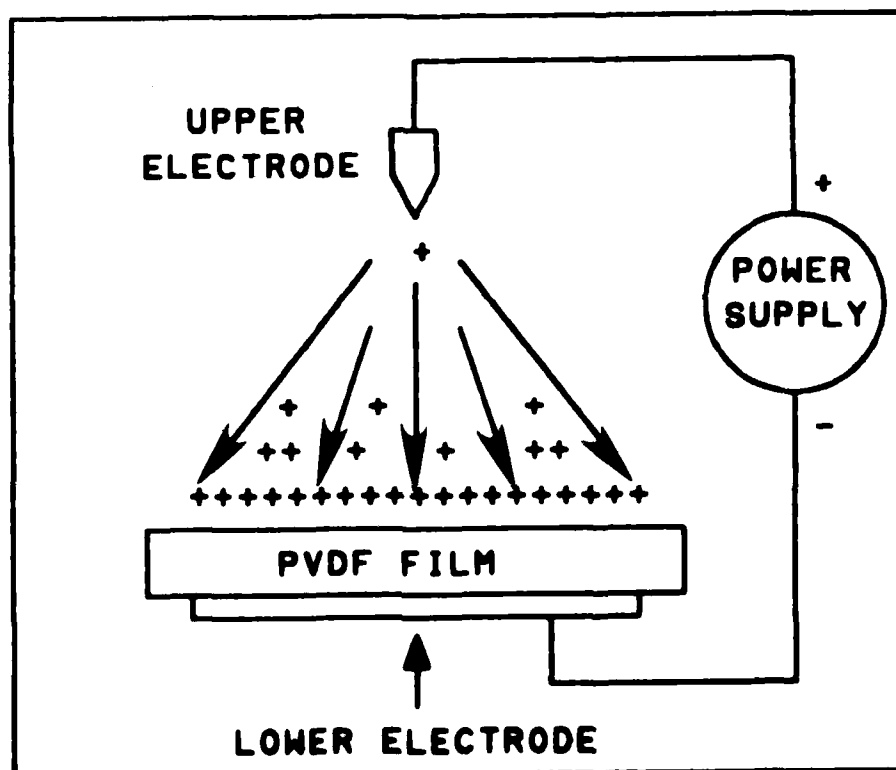


Figure 2.13. Corona Poling (Gerliczy and Betz, 1984:22).

The film is then clamped with the non-metallized surface exposed to the corona. Corona poling subjects the PVDF film with an effective field across the film of 5 to 10 MV/cm (Das-Gupta and Doughty, 1978:4601) for 40 to 60 seconds (Gerliczy and Betz, 1984:4).

The piezoelectric PVDF film manufacturer, Solvay & Cie, uses corona poling because it is a faster process and substantially more economical than field poling for processing large, continuous quantities of film (Gerliczy and Betz, 1984:4-5).

Tactile Sensors

'Tactile sensing' is defined (Harmon, 1982:1; McAlpine, 1986:7) as 'the continuous-variable sensing of forces in an array and is meant to relate skin-like properties where areas of force sensitive surfaces are capable of reporting graded signals and parallel patterns of touching.' This section describes what the human tactile sense perceives, what tactile characteristics are desirable for a robotic tactile sensor, and several robotic tactile sensor designs.

Sensors have been built to measure contact force (Dario and DeRossi, 1985:46). A robot, using a computer, interprets data from these sensors and adjusts its grip to the correct level of force needed to hold an object securely.

Currently, four major types of tactile sensors exist for measuring contact forces (Dario and DeRossi, 1985:46):

1. Optical sensors. The contact force moves a membrane attached to a pin that blocks a portion of a light beam transmitted onto a detector.

2. Conductive elastomer (elastic polymer) sensors. The electrical resistance changes with contact force.

3. Silicon strain gauges. Miniature load cells measure the contact force normal to the surface of the load cells.

4. Ferroelectric polymer sensors. These sensors measure a contact force using either an ultrasonic technique, or the fact that the polymers produce a piezoelectric voltage that varies proportionately with force.

Human Tactile Sensing. Humans, with their tactile sense, can perform a wide range of manipulative, identification, and qualitative measurement tasks with great facility (KYNAR Piezo Film Department, 1984:79). Humans can perform these tasks because they use information from arrays of touch receptors in the epidermis. It is logical to develop tactile sensors for robotics that are required to do human-like tasks by considering the characteristics of human tactile sensing. Robots, with tactile sensors that model these touch receptors, could achieve human-like task capabilities.

The human tactile sense uses information from different touch receptors in the skin (KYNAR Piezo Film Department, 1984:79; Dario and others, 1984:2). These receptors are located at varying depths in the skin and relate to the skin's spatial resolution and response to slow and fast stimuli (Dario and others, 1984:2). The touch receptors relate tactile information through a variety of tactile sensory modalities (KYNAR Piezo Film Department, 1984:79-80).

A modality is defined as the fact, state, or quality of being a mode characteristic. If these sensor modalities could be duplicated, they would be useful for designing robotic tactile sensors which are required to perform human-like tasks. These modalities (Harmon, 1980:11-17; KYNAR Piezo Film Department, 1984:79-80) include:

1. Simple touch. The equivalent is a simple limit switch. Simple touch effectively detects a contact force above a set threshold level.

2. Normal and shear force sensing. This provides information about the contact force vector at a point. A special case of force sensing is simple touch.

3. Contact force distribution. Provides the pattern of contact between an object and sensor. Force distribution information is useful for surface discontinuity and texture sensing. Arrays of simple touch or force sensitive sensors could accomplish the contact force distribution mode in a robotic tactile sensor.

4. Slip. This measures the object's position change with respect to time due to the object's lateral motion. Slip indication can be used to assist in moving an object and determining a materials texture. 'Slip is related to shear and normal forces, and the coefficient of static and sliding friction between the sensor and an object' (KYNAR Piezo Film Department, 1984:80). Analyzing contact

distribution change over time might be a method of detecting slip.

5. Heat flow. The heat flow between a sensor and a contacted object can give important temperature data of the object. A sensor that possesses pyroelectric properties could be used to sense different heat flow rates.

Not all robots require their tactile sensor systems to possess all the modalities mentioned. A tactile sensor system would incorporate the necessary modality combinations for a specific task. To emulate a modality, a complementary set of discrete sensors of different technologies could be integrated to realize the desired capability.

Robotic Tactile Sensing. Harmon surveyed researchers and manufacturers of industrial manipulators (Harmon, 1980:1-36). The survey focused on present and future tactile-sensing requirements and potentials (Harmon, 1982:3). Harmon (Harmon, 1982:9) asked in his survey, "What performance specifications would seem to be required or useful?" He summarized (Harmon, 1982:12) the results to the question as follows:

1. A touch-sensing transducer array should consist of at least a 10 x 10 array of force-sensing elements arranged on a 1 inch² flexible surface.

2. "Each element should have a response time of 1-10 milliseconds, preferably 1 millisecond."

3. Each element should have a threshold sensitivity of 1 gram, and an upper limit sensitivity of 1,000 grams.

4. The sensor element's response does not have to be linear, but they must have a low hysteresis.

5. The skin-like sensing material should be robust and able to tolerate harsh industrial environments.

Some issues a design engineer might consider are (KYNAR Piezo Film Department, 1984:81):

1. Transducer linearity. A robot's processor (using calibration look-up tables) could eliminate most non-linearity in a tactile transducer.

2. Transducer hysteresis. The transducer's hysteresis should be low. If the hysteresis is not low, the proper processing could track the transducers state or the combination with another transducer of a different type could indicate the transducer's state.

3. Sensor compliance. A compliant tactile sensor can conform to the surface of an object and provide additional information.

4. Sensory data processing. The tactile sensor array should operate as a stand-alone system and not pass low-level tactile information on to the main processor of a robot.

5. Physical size. The size of the sensor system should be appropriate to the task. Systems the size of a fingertip are desirable.

6. Transducer and sensor speed. Brief periods of high transducer activity and relatively long periods of inactivity often characterize tactile events. Activity only occurs during changes in tactile contact. Transducers and sensors must be able to respond to peak demands and transfer control feedback in a timely manner.

Tactile Sensor Designs. PVDF's well-known physical and piezoelectric properties, as well as its resistance to environmental conditions (for example, recommended for components, such as pipes or pumps, in contact with corrosive fluids), has made it the subject of many papers concerned with using it as tactile sensors (Dario and others, 1984:2). Sensors designed from this polymer have been as simple as the one shown in Figure 2.14, or as complex as the one shown in Figure 2.15.

The simple sensor design depicted in Figure 2.14 is composed of two polymer sheets, each carrying suitable electrode patterns, with an interposed layer of a compliant material and a rigid back support (Bardelli and others, 1983:48-49). The compliant material isolates (from light, PVDF is also pyroelectric) the lower polymer layer and increases the upper layer's sensitivity to stresses (because

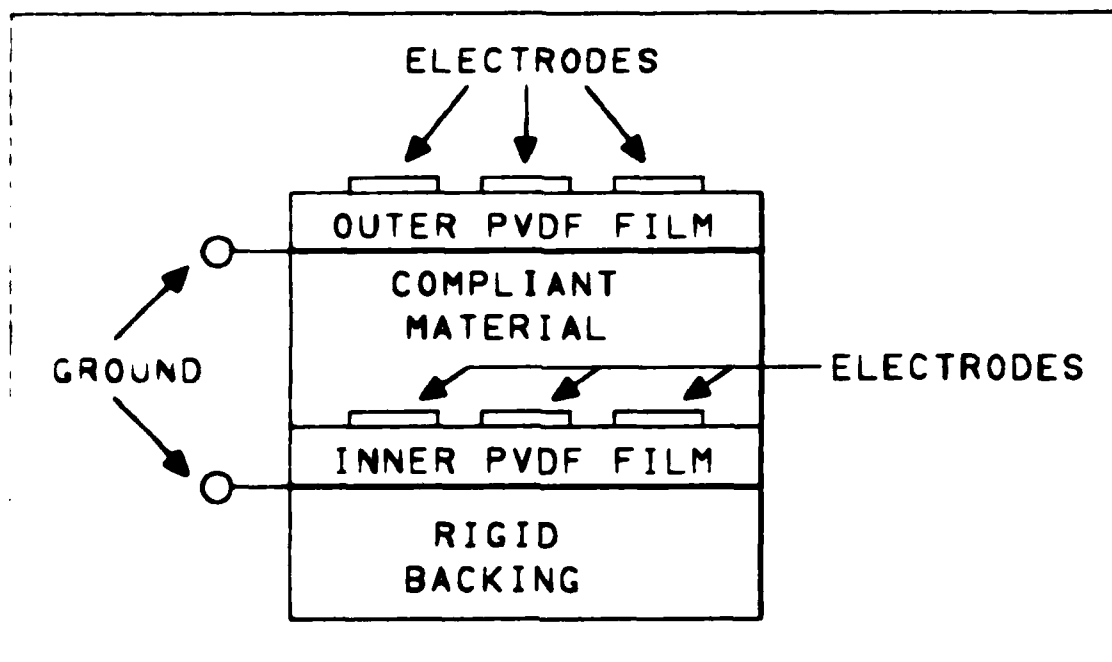


Figure 2-14. Simple Tactile Sensor (Bardelli and others, 1983:49).

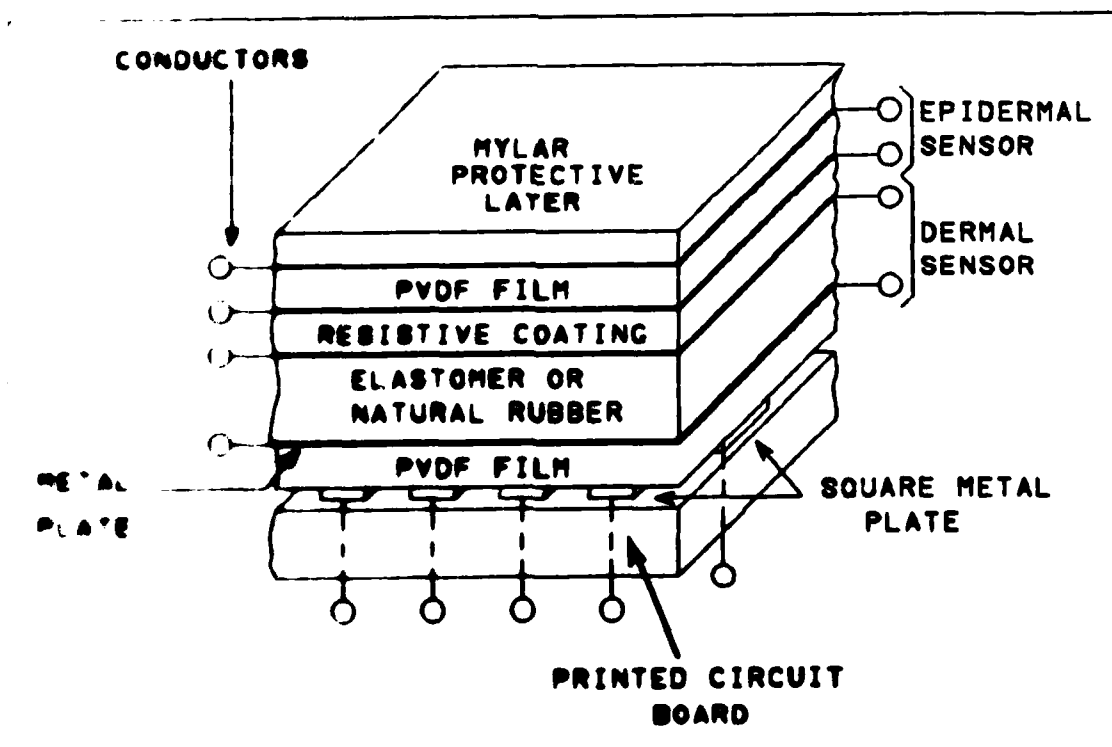


Figure 2-19. Complex Tactile Sensor (Dario and DeRossi, 1989:92).

the layer will stretch more, and thus, a greater response will result).

Dario and DeRossi proposed the complex tactile sensor design in Figure 2.15 (Dario and DeRossi, 1985:52). This tactile sensor had additional layers of construction to account for a wider range of tactile sensing capabilities. Their explanation of the construction of the tactile sensor was:

This developmetal tactile sensor for a robot gripper has PVDF film at its base, simulating the human dermis, or inner layer of skin. A PVDF film represents the epidermis, or outer layer. An elastomer layer between the two provides a compliant backing for the epidermal layer. Metal plated on its upper surface, the dermal PVDF is bonded with nonconductive glue to a supporting printed circuit board. Electric charges are generated by mechanical deformation of the surfaces of the dermal PVDF film, and these charges are capacitively coupled to square metal electrodes on the circuit board. Electrodes on the top and bottom of the epidermal PVDF film layer similarly collect the charges generated there, transferring them to conductors (Dario and DeRossi, 1985:52).

Summary

This chapter presented the background necessary for understanding piezoelectric pressure sensors for robotics. The discussion was devoted to the piezoelectric effect, the polymer, polyvinylidene fluoride, the inducement of the piezoelectric effect (in polyvinylidene fluoride), and tactile sensors. In the Piezoelectric Effect Section, the historical perspective and theory behind this effect were

described. The properties and characteristics of PVDF were discussed in the Polyvinylidene Fluoride Section. The stretching and poling techniques used for inducing the piezoelectric effect in PVDF were explained in the Inducing the Piezoelectric Effect in Polyvinylidene Fluoride Section. Tactile sensor designs were discussed in the Tactile Sensors Section.

III. Experimental Designs, Fabrication Procedures, and Evaluation Procedures

The experimental designs, sensor fabrication procedures, and evaluation procedures are described in this chapter. The reasons for, and the construction of the 16 different Piezoelectric-Polymer, Tactile-Sensor Arrays (PPTSAs) are explained in the first section. The second section, Sensor Fabrication Procedures, describes the fabrication of the different PPTSAs. The thermal poling arrangement and operational procedures are discussed in the third section. The instrument interfaces, equipment, and procedures used to evaluate the PPTSAs are discussed in the final section.

Sensor Designs

This section presents the sensor configurations contemplated and the final designs that were fabricated. The configuration process involved designing a PPTSA which would be capable of differentiating pressures and discerning an object's shape. The actual sensors were constructed of piezoelectric polyvinylidene fluoride (PVDF) film, aluminum electrodes, printed circuit board, plus several miscellaneous materials to obtain the pressure sensitivity and object shape discerning capabilities.

The desirable performance characteristics of the experimental sensor designs were formulated considering the

ultimate application of having a robot refuel an aircraft. A robot's sensing system is comprised of an interpreting and controlling computer, interfaces, and sensors. The capability of a sensing system to discern objects and the applied forces (pressures) is ultimately dependent on the sensor elements and their arrangement. The sensor design formulation involved designing the sensors so they could differentiate pressures (forces) and be arranged in a fashion for discerning an object's shape. The pressure sensing capability was incorporated in the sensor's designs by using PVDF film. PVDF film is highly pressure sensitive. A planar 5 x 5 array of identical, but discrete sensors (composed of PVDF film and electrodes) was envisioned for realizing the object's shape recognition capability. Since the PVDF film might lose its piezoelectric properties under certain environmental conditions (for example, prolonged operation above a 100°C), the design formulation had to include a method for regenerating these properties.

The design formulation process was an evolutionary process. The process began with two basic PPTSA configurations and concluded with 16 unique PPTSA configurations. One of the basic PPTSA configurations was called the square-pad design, and the other configuration was called the stripe design. Figures 3.1 and 3.2 depict the electrode structures of the two basic configurations. The 16

different PPTSA configurations were variations of these two basic PPTSA configurations.

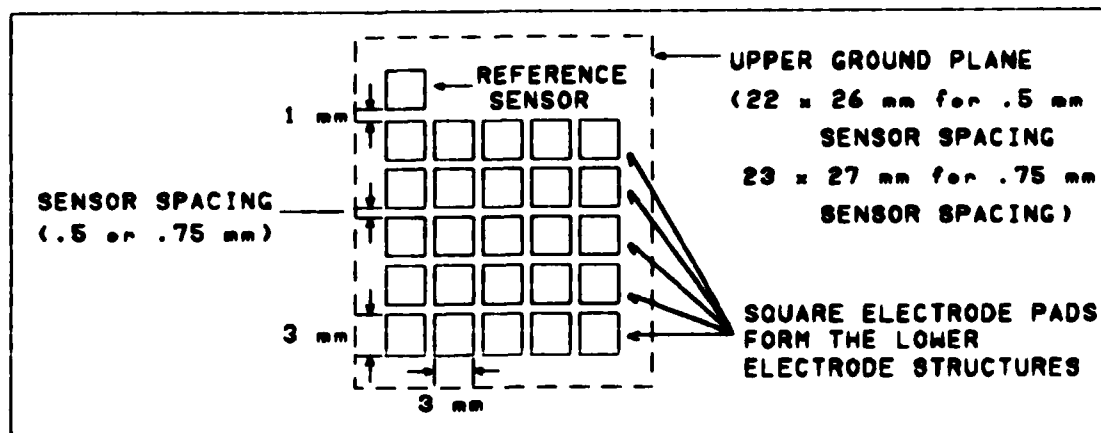


Figure 3.1. Electrode Structure of the Square-Pad Configuration.

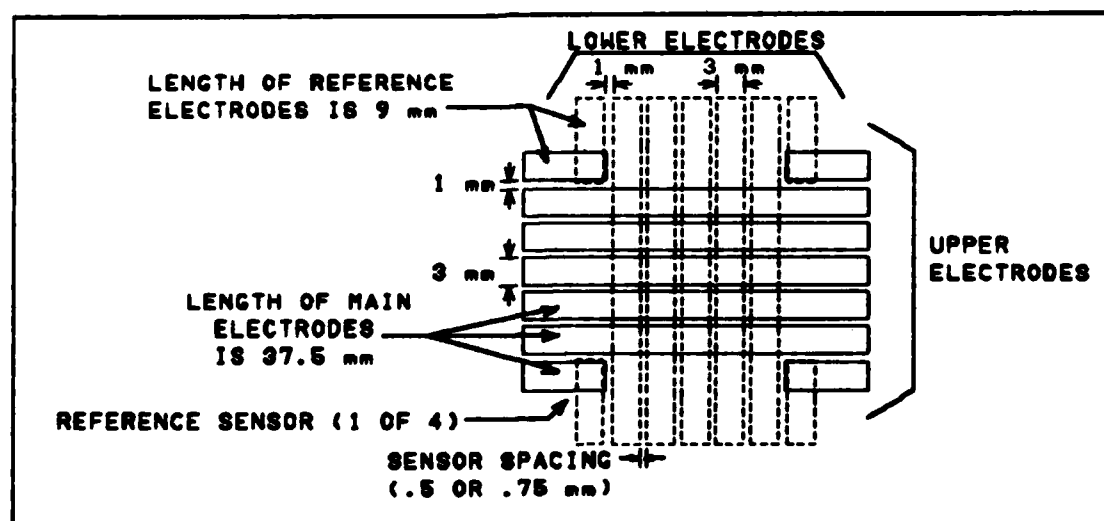


Figure 3.2. Electrode Structure of the Stripe Configuration.

Three performance based questions were addressed during the formulation process to realize the 16 PPTSAs. These questions were:

1. Will one electrode-structure fabrication process have more adverse effects than another fabrication process? Adverse effects are classified as those that degrade the piezoelectric activity of the PVDF film or produce nonuniform electrode structures. A nonuniform electrode is a structure that has a distorted surface area or thickness dimension.

2. Will a thicker PVDF film perform better than a thinner film? The piezoelectric response of a PVDF film sample is proportional to the thickness of the film.

3. Would increasing the spacing between sensors significantly reduce sensor crosstalk? Sensor crosstalk (mechanical coupling) occurs when a force applied to one sensor is detected by an adjacent sensor.

It was anticipated that varying the electrode-structure fabrication process, the PVDF film thickness, and the sensor spacing would answer these questions and produce a PPTSA with optimum performance characteristics. One of the selected electrode-structure fabrication processes involved thermally evaporating aluminum on the PVDF film. Evaporation masks were used to obtain the desired electrode structures. The other selected fabrication process used a photolithography process to form the electrode structure from the aluminum film that was on the surfaces of the metallized PVDF film. The two PVDF film thicknesses chosen were 25 and 40 microns. The capacity of the 3 KV power

supply in the thermal poling arrangement and the requirement to pole the PVDF film at 750 KV/cm limited selecting a PVDF film thickness greater than 40 microns. The maximum PVDF film thickness was calculated from the relationship:

$$t = V/E \quad (m) \quad (3.1)$$

where

t = the thickness of the PVDF film (m).

V = the maximum potential of the poling arrangement's power supply (V).

E = the maximum electric field required for thermal poling (V/m).

The two sensor spacings selected were 500 and 750 microns. The 500 micron sensor spacing was selected because it was the smallest spacing possible using the thermal evaporation electrode-structure fabrication process. Any smaller than 500 microns, the evaporation masks (in the process) would be too fragile. The 750 micron sensor spacing was selected because it was 50 percent larger than the 500 micron sensor spacing. Table 3.1 summarizes the 16 PPTSAs that were formulated.

The thickness of the electrode structures on the PVDF film's surface was limited to 400 angstroms. The purpose of maintaining this thickness was to minimize its influence on the sensor's response. It was envisioned that varying the

Table 3.1

The 16 Sensor Configurations Formulated

PPTSA Identifi- cation Designator	Electrode- Structure Fabrication Process	PPTSA Design Category	PVDF Film Thickness (microns)	Element Spacing (microns)
1	Evaporation	Stripe	25	500
2	Evaporation	Stripe	25	750
3	Evaporation	Stripe	40	500
4	Evaporation	Stripe	40	750
5	Evaporation	Square-Pad	25	500
6	Evaporation	Square-Pad	25	750
7	Evaporation	Square-Pad	40	500
8	Evaporation	Square-Pad	40	750
9	Photolithography	Stripe	25	750
10	Photolithography	Stripe	25	750
11	Photolithography	Stripe	40	500
12	Photolithography	Stripe	40	750
13	Photolithography	Square-Pad	25	500
14	Photolithography	Square-Pad	25	750
15	Photolithography	Square-Pad	40	500
16	Photolithography	Square-Pad	40	750

electrode's thickness would distort the distribution of the stresses applied to the PVDF film's surface.

The rigid backing of all the PPTSAs was realized with printed circuit (PC) board. PC board was selected for the substrate because it was easily machinable, rigid, sturdy, flat, and uniform. Glass was eliminated because it was neither easily machinable nor as sturdy as PC board. The PC board also offered the advantage of having a film of copper on one side. For the square-pad design PPTSAs, this copper

film was patterned to reflect the desired conductor configurations.

The surface area of the discrete sensors was held constant for all the PPTSAs (3 mm x 3 mm). The 3 mm x 3 mm size was selected because it made the 5 x 5 sensor matrix approximately the size of a human's fingerprint.

The basic PPTSA configurations (or designs) shared common and different characteristics. The common characteristics were that they shared the same 5 x 5 sensor matrix size, discrete sensor surface area dimensions (3 mm x 3mm), and electrode thickness (400 angstroms) of the electrode structures. The differences between the two configurations were notably with respect to their electrode structure configurations and method of fabrication.

The Square-Pad Design. Figure 3.3 shows the different construction levels of the square-pad design. Working from

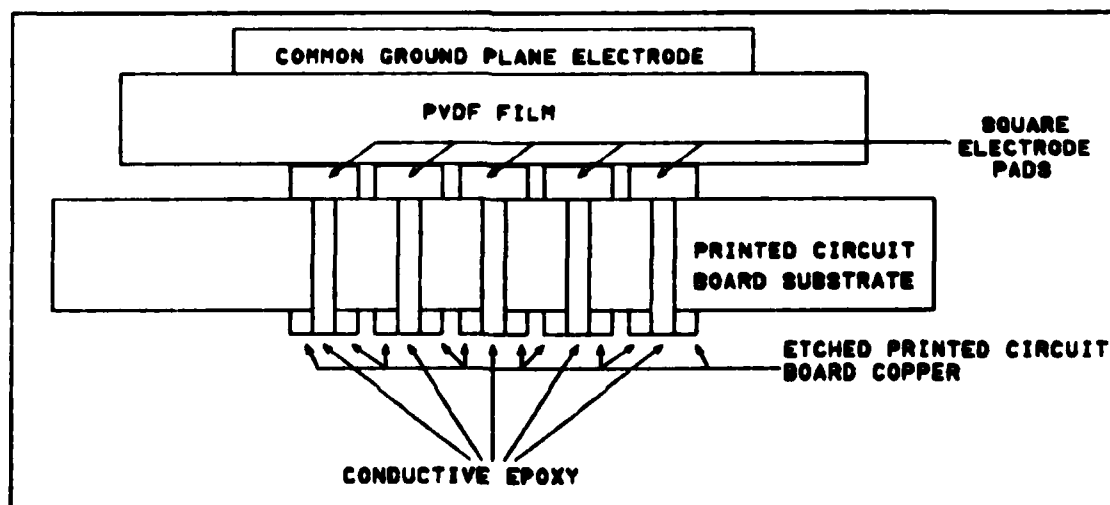


Figure 3.3. A Cross-Sectional Diagram of the Square-Pad Design.

the upper most level to the lower most level of the square pad design. the descriptions and functions of each level are:

1. The upper most level served as a common ground plane electrode for the square electrode pads two levels below. The aluminum ground plane was approximately 400 angstroms thick. Depending on whether the 500 or 750 micron discrete sensor spacing was used, the ground plane was either 26 mm x 22 mm or 27 mm x 23 mm, respectively. An evaporation mask and thermal evaporation deposition system was used to deposit the ground plane on the unmetallized PVDF film. A photolithographic system using dry film and a chemical etchant (one half-percent hydrofluoric acid) were used to pattern the ground plane. Figure 3.4 illustrates the ground plane electrode of the square-pad design PPTSA.

2. The second level was the piezoelectric PVDF film. The PVDF film was biaxially oriented Solef from Solvay & Cie and was either 25 microns or 40 microns thick.

3. The fourth level consisted of 26 identical, discrete square-electrode pads. Figure 3.4 shows 25 of the square pads that defined the 5 x 5 sensor array. The aluminum pads (400 angstroms thick) were 3 mm x 3 mm. The remaining square pad in the figure was the reference sensor. The fabrication procedures used to fabricate the sensors were the same used for patterning the ground plane.

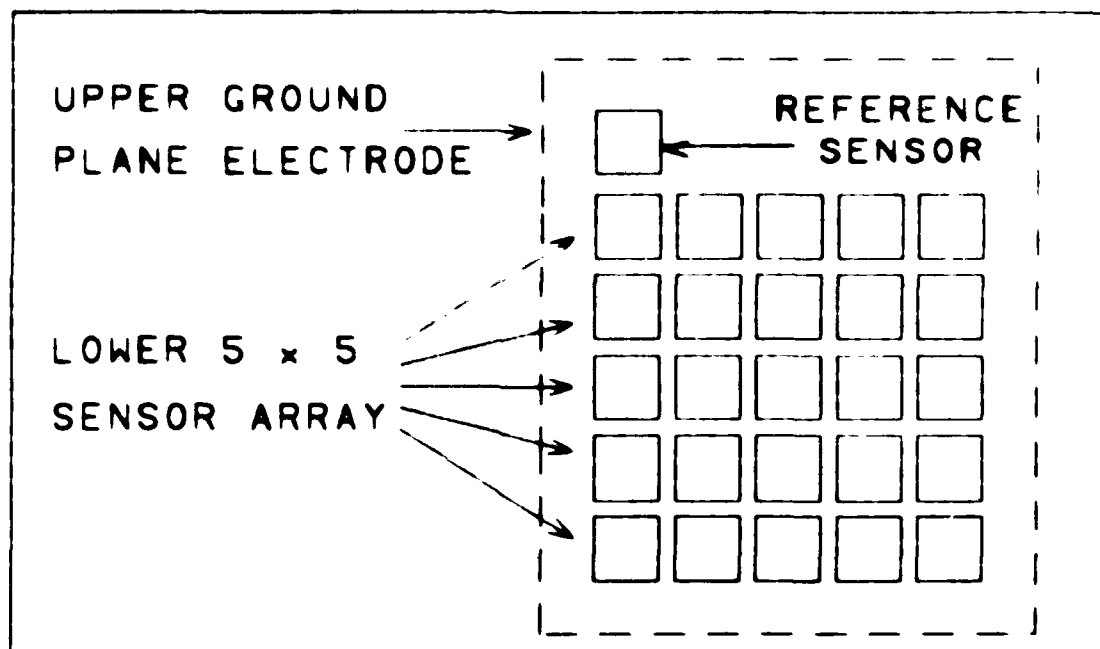


Figure 3.4. The Square-Pad Design Electrode Pattern.

4. The printed circuit (PC) board substrate comprised the fourth level. It provided physical support and a method to electrically access the discrete square electrode pads. The PC board substrate (20 mils thick) was an epoxy, single-sided copper board. The access holes in the board were 40 mils in diameter. The copper was etched to provide a conductor pattern.

5. The fifth level consisted of a copper conductor pattern. A bottom view of the conductor pattern is shown in Figure 3.5. The discrete square electrode pads in the fourth level were accessed to the conductor pattern using conductive epoxy. The conductor pattern provided a platform to connect leads to the PPTSA. The pattern was formed using

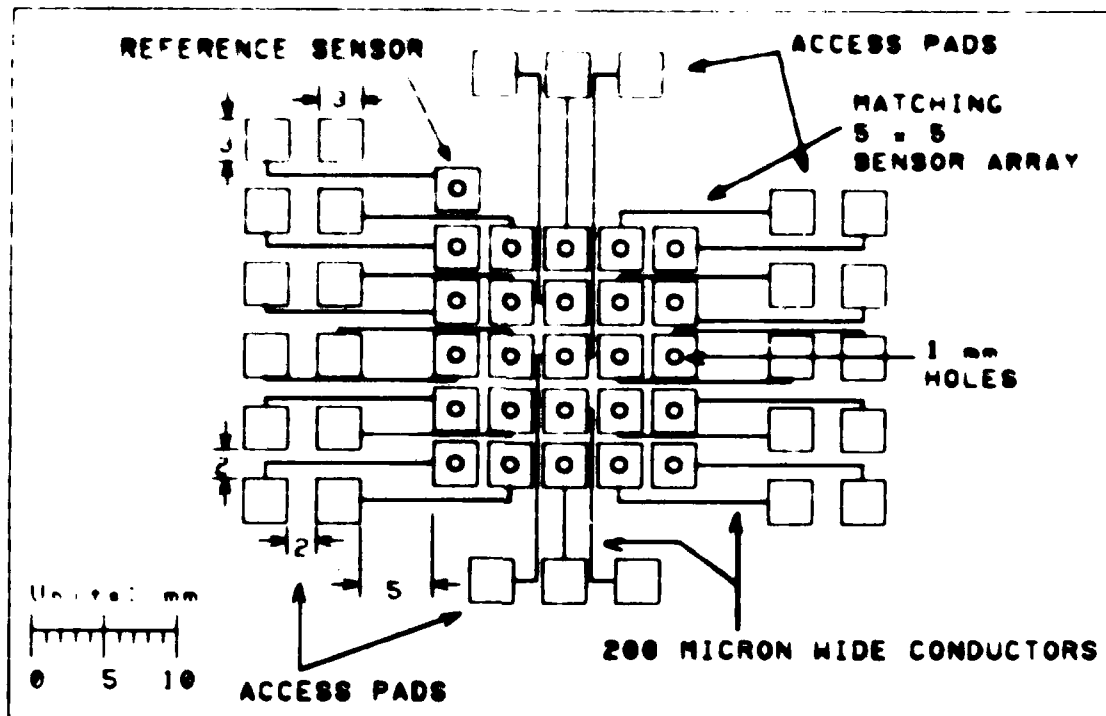


Figure 3.5. The Conductor Pattern for the Square-Pad Design.

a dry film photolithographic system; ferric chloride served as the copper etchant.

6. Conductive epoxy (the sixth level) was used to connect the square electrode pads to the conductor pattern. A syringe was used to inject the epoxy into the holes.

The Stripe Design. The construction levels of the stripe design are schematically shown in Figure 3.6. The descriptions and functions of each level are:

1. The upper most level consisted of an electrode structure. This aluminum electrode structure (400 angstroms thick) consisted of nine electrode stripes. Figure 3.7 shows this upper electrode structure.

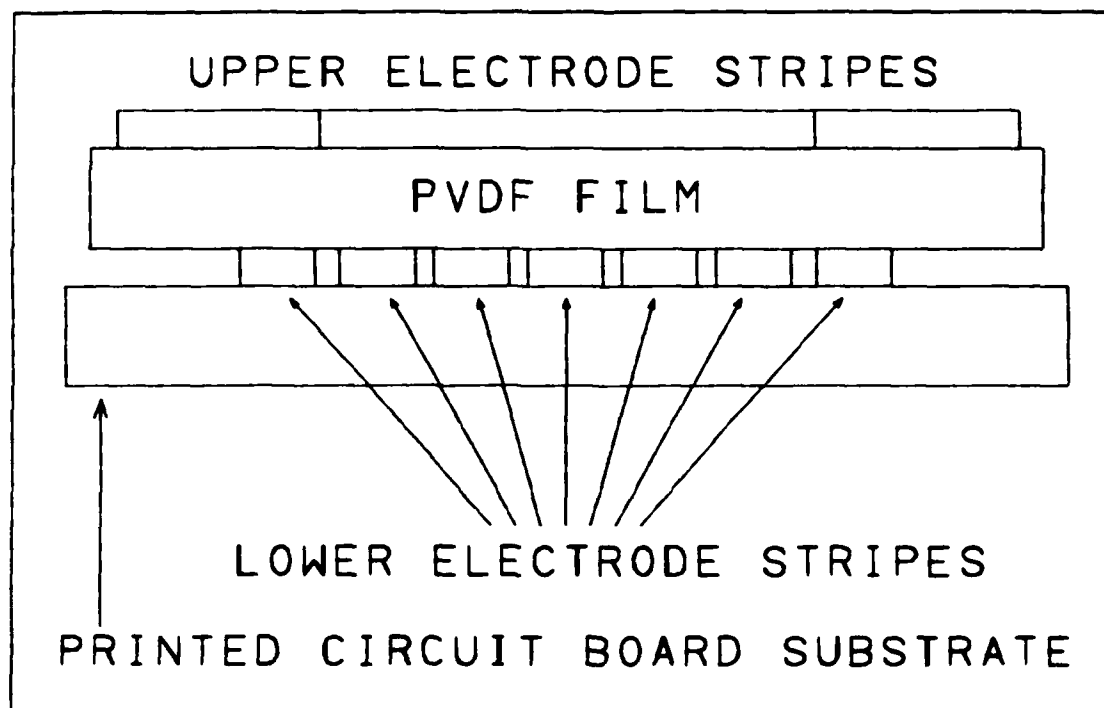


Figure 3.6. A Cross-Sectional Diagram of the Stripe Design.

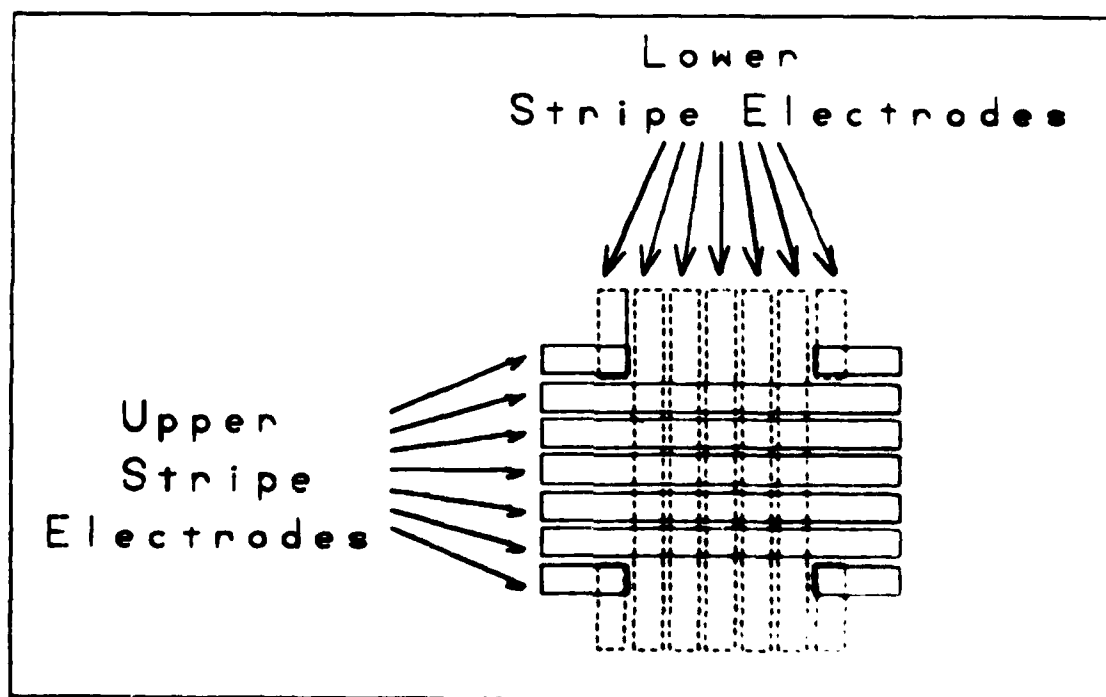


Figure 3.7. The Stripe Electrode Design

AD-A188 852

PIEZOELECTRIC POLYMER TACTILE SENSOR ARRAYS FOR
ROBOTICS(U) AIR FORCE INST OF TECH WRIGHT-PATTERSON AFB
OH SCHOOL OF ENGINEERING D G PIROLO DEC 87

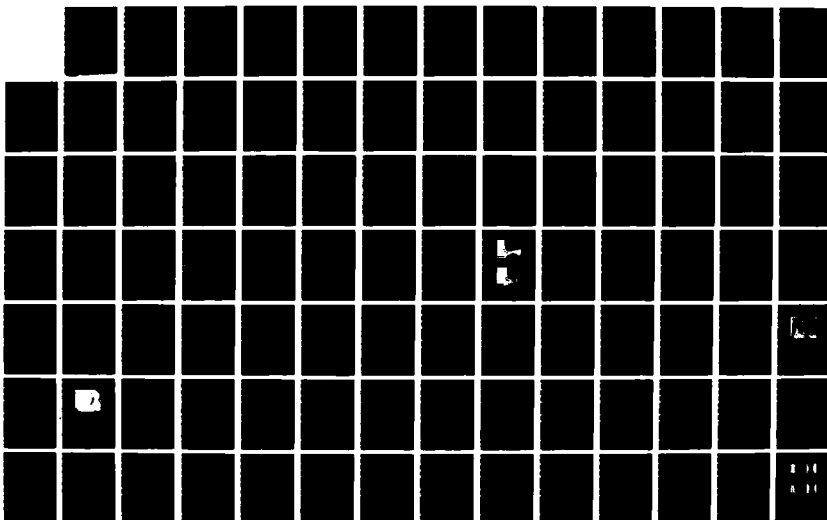
2/3

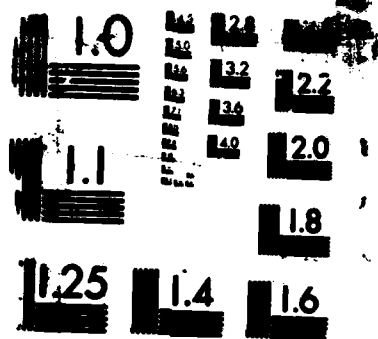
UNCLASSIFIED

AFIT/GE/ENG/87D-52

F/G 17/11

NL





MICROCOPY RESOLUTION TEST CHART

2. The piezoelectric PVDF film formed the second level. This film was identical to the film used in the square-pad design.

3. The third level consisted of an electrode structure that was identical to the electrode structure in the first level. Figure 3.7 shows this electrode structure. These structures were orthogonal to each other. The five center stripes on one surface, when overlapped with the five center stripes on the opposite surface, formed the 5 x 5 sensor matrix as shown in Figure 3.7. The remaining stripes formed four reference sensors. The sensors in the 5 x 5 matrix were accessed using a row (an upper electrode stripe) and column (lower electrode stripe) method.

4. The fourth level was a layer of pressure sensitive adhesive. This adhesive provided a temporary mount during testing.

5. The epoxy PC board substrate which formed the fifth level provided physical support during testing.

Sensor Fabrication Procedures

This section describes how to fabricate the 16 different PPTSAs. The PPTSA designs have been further defined in this section. Stripe PPTSA designs that have 500 or 750 micron discrete sensor spacings were identified as the 500-stripe design and 750-stripe design, respectively. Square-pad PPTSAs were identified the same way. They were referred to as the 500-square-pad design and 750-square-pad design.

The fabrication of the 16 different PPTSAs were divided equally into four phases. Many of the fabrication steps were exactly the same.

The four Phase I PPTSAs were the stripe design and fabricated from the unmetallized PVDF film. A thermal evaporation method was used to realize the aluminum electrode patterns. The PPTSA identification designators and geometrical specifications were:

1. 25 micron thick film, 500 micron electrode spacing,
2. 25 micron thick film, 750 micron electrode spacing,
3. 40 micron thick film, 500 micron electrode spacing,
4. 40 micron thick film, 750 micron electrode spacing.

The four Phase II PPTSAs consisted of the square-pad design and were fabricated from unmetallized PVDF film. This phase also used thermal evaporation to obtain the electrode patterns. The PPTSA identification designators and geometrical specifications were:

5. 25 micron thick film, 500 micron electrode spacing,
6. 25 micron thick film, 750 micron electrode spacing,
7. 40 micron thick film, 500 micron electrode spacing,
8. 40 micron thick film, 750 micron electrode spacing.

With the exception of being fabricated from commercial aluminum metallized PVDF film, and using the dry film method, the PPTSAs in Phases III and IV were constructed identical to those in Phase I and II, respectively. The PPTSA designs, identification designators, and geometrical specifications were:

Phase III: Stripe Design

9. 25 micron thick film, 500 micron electrode spacing.
10. 25 micron thick film, 750 micron electrode spacing.
11. 40 micron thick film, 500 micron electrode spacing.
12. 40 micron thick film, 750 micron electrode spacing.

Phase IV: Square-Pad Design

13. 25 micron thick film, 500 micron electrode spacing.
14. 25 micron thick film, 750 micron electrode spacing.
15. 40 micron thick film, 500 micron electrode spacing.
16. 40 micron thick film, 750 micron electrode spacing.

Six separate fabrication procedures were developed for fabricating the different PPTSAs. Each of these procedures are discussed in Appendices A through H. A procedure for making the high resolution plate (HRP) masks was the first procedure developed and is discussed in Appendix A. This procedure describes how to make a HRP mask from a rubylith pattern. Eight HRP masks were made using this procedure. Each of the stripe designs required one HRP mask, and each of the square-pad designs needed three HRP masks (ground plane, square pads, and conductor pattern). Appendix A also describes a method for producing negatives from all of the HRP masks. A procedure for fabricating evaporation masks is discussed in Appendix B. One evaporation mask was fabricated for each of the stripe designs, and two evaporation masks were fabricated for each of the square-pad designs. Appendix C describes a procedure for fabricating electrode structures on the surfaces of unmetallized PVDF film using thermal evaporation. Appendix D

describes the other procedure implemented for fabricating electrode structures. This procedure used a photolithography process to form the electrode structures from the aluminum film which covered the surfaces of metallized PVDF film. The photolithography process used dry film resist as the light sensitive material. The final assembly of the PPTSAs distinguished the two remaining procedures (Appendices E and F). Appendix E concerns the stripe design and Appendix F concerns the square-pad design, respectively. Appendix G illustrates photocopies of the HRP and evaporation masks fabricated in this thesis. The fabrication procedures are summarized as:

- Appendix A: HRP masks,
- Appendix B: Evaporation masks,
- Appendix C: Evaporation fabrication method,
- Appendix D: Dry film fabrication method,
- Appendix E: Final assembly for the stripe design, and
- Appendix F: Final assembly for the square-pad design.

The following procedures were used for fabricating the different phases of the PPTSAs:

- Phase I : Appendices A, B, and E,
- Phase II : Appendices A, B, and F,
- Phase III: Appendices A, C, and E, and
- Phase IV : Appendices A, C, and F.

Thermal Poling

A thermal poling process was used to regenerate or enhance the piezoelectric activity of the PVDF film in the PPTSAs. The process involved first raising the temperature

of the PVDF film to 120°C . When the PVDF film reached 120°C , a 1 MV/cm electric field was applied across the thickness of the PVDF film for a 60 minute duration. After the 60 minutes, the temperature of the film was reduced to 50°C . The electric field was removed after the temperature of the PVDF film fell below 50°C to complete the process.

The Thermal Poling Arrangement. Figure 3.8 shows a schematic of the thermal poling arrangement. The arrange-

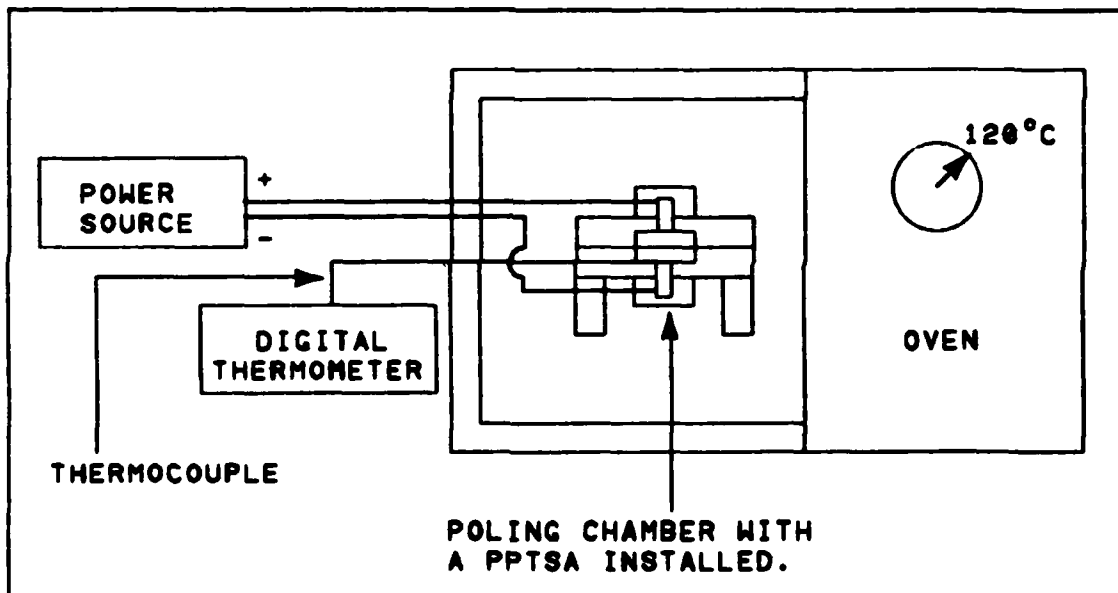


Figure 3.8. Schematic of the Thermal Poling Arrangement.

ment consisted of a power source, an oven, a digital thermometer, and a poling chamber. The power source (Power Designs Model 3K10B photomultiplier high voltage calibrated power source, Power Designs Inc., 1700 Shames Drive, Westbury, NY 11590) was used for applying an electric field

across the thickness of the PVDF film. The oven (Tenney Jr. bench model high-low temperature test chamber, Tenney Engineering, Inc., 1090 Springfield Road, Union, NJ 07083) was used for elevating the temperature of the PVDF film. The digital thermometer (Omega Model 175-KCL, Omega Engineering, Inc., One Omega Drive, Box 4047, Stanford, CT 06907) was used for monitoring the temperature of the PVDF film. The poling chamber was designed by the experimenter and fabricated by the AFIT Model Shop. The chamber was designed to handle a high voltage (3 KV) and a high temperature (120°C). Appendix H discusses the poling chamber design in detail. The poling chamber provided an apparatus for holding the PPTSA during thermal poling. When the power supply was operating, the chamber's two electrodes supplied an electric field across the thickness of the PVDF film of a PPTSA.

The Thermal Poling Procedure. The thermal poling process subjected the PVDF film of a PPTSA to heat and an electric field for a duration. The critical steps for poling a PPTSA were:

1. The PPTSA was installed in the poling chamber. Preventing arcing (or edge flashover) during the thermal poling process was a major concern. Arcing was prevented by using a 125 micron thick BeCu spacer and positioning an additional PVDF film ring around the PPTSA. After the PPTSA was installed in the chamber, the chamber was placed in the

oven. Figures 3.9 and 3.10 depict the installation of the stripe and square pad designs.

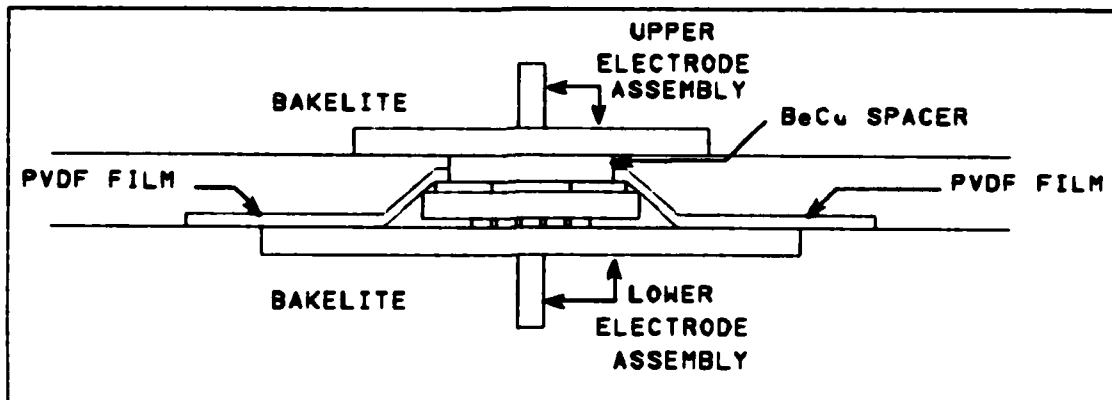


Figure 3.9. Drawing of an Installed Stripe Design PPTSA in the Poling Chamber. (BeCu is an abbreviation for beryllium copper.)

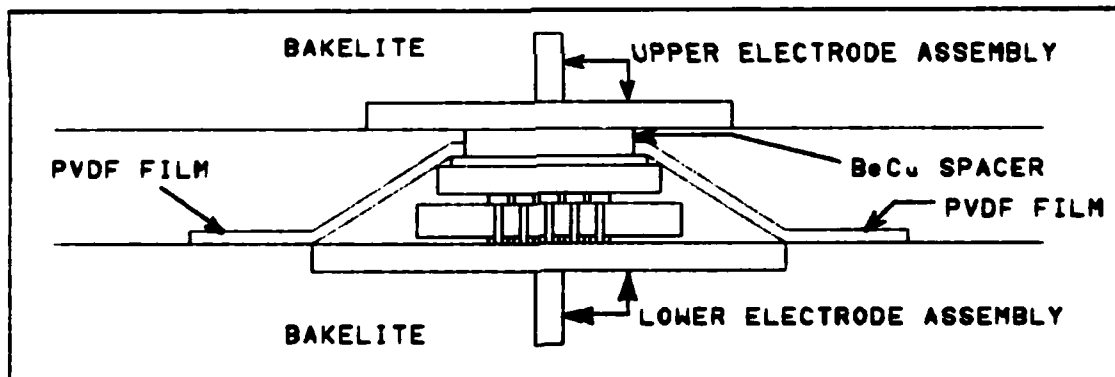


Figure 3.10. Drawing of an Installed Square-Pad Design PPTSA in the Poling Chamber. (BeCu is an abbreviation for beryllium copper.)

2. The system was tested for arcing before the temperature of the PPTSA was elevated. The power supply was connected to the poling chamber and the oven's door was open during this test. The test involved turning the power

source on, a visual (sparks) and audio (crackling) check for arcing in the oven, and a check of the power source's fuse. The power source's fuse would fail if a short circuit occurred in the poling chamber. The test was a success if neither arcing or the fuse remained in tact. The PPTSA was ready for poling after this test.

3. The temperature of the PVDF film in the PPTSA was raised to 120°C . This was accomplished by securing the oven door, setting the oven temperature, and turning the oven on. The digital thermometer was used for monitoring the poling chamber's temperature, and thus, the temperature of the PVDF film.

4. After the PPTSA reached the poling condition's temperature, the electric field was applied by turning on the power supply. It usually took about five hours for the PVDF film to reach and stabilize at the 120°C temperature. The power source was set to 1,875 volts for the 25 micron-thick PVDF film. The 1,875 voltage setting provided an effective 1 MV/cm electric field across the thickness of the PVDF film.

5. The oven was turned off and the oven door was opened after the 60 minute poling duration. The system was cooled to a temperature below 50°C . A fan was used to accelerate cooling. Cooling the system to room temperature required approximately four hours. The electric field was removed after the temperature fell below 50°C . The PPTSA was

removed from the poling chamber shortly after the electric field was removed. This fifth step concluded the thermal poling process.

Evaluation Procedures

The procedures used for evaluating the PPTSA configurations are discussed in this section. This section presents two evaluations that are also discussed in Chapters IV, V, and VI. Each of these chapters address a different portion of the evaluations. Chapter IV contains the data portion and Chapter V consists of the discussion and analysis portion. Finally, Chapter VI presents the conclusions portion. The first evaluation was that of the electrode-structure fabrication processes, and it was composed of two parts. The first part involved a dimensional error analysis of the electrode structures that were formed using the two electrode-structure fabrication processes. The performance of the stripe electrodes was determine in the second part of the evaluation. The second evaluation was that of the piezoelectric activity and consisted of an interrogation of the piezoelectric activity data. The purpose and description of each of the evaluations are presented in an introductory paragraph at the beginning of each of the respective subsections.

Electrode-Structure Fabrication Process Evaluation Procedure. This procedure was used for evaluating the evaporation and the photolithographic electrode-structure

fabrication processes. This process involved forming aluminum electrode structures on the surfaces of the PVDF film. The thermal evaporation process (Appendix C) was used with evaporation masks to realize the aluminum electrode structures on the unmetallized PVDF film. Alternatively, the photolithographic process (Appendix D) used a photoresist and a chemical etchant to form the aluminum electrode structures from the continuous aluminum film that was already on the surfaces of the metallized PVDF film. This evaluation had two purposes. The first purpose was to determine how precise the fabricated electrode structures compared to the design specifications. The second purpose was to determine the relative performance of the stripe electrodes.

Electrode-Structure Dimension Evaluation

Procedure. The purpose of this procedure was to provide data for a dimensional error analysis of the fabricated electrode structures. The dimensional error analysis was used to determine how precise the fabricated electrode structures compared to design specifications. Table 3.2 lists the eight different fabricated electrode structures that were measured. The spacings between the electrodes and the thicknesses of the electrodes were the dimensions measured. The average dimensions of an electrode structures were derived from the spacing measurements. The spacings were measured with an optical microscope (Model M20 Optical

Table 3.2

The Eight Electrode Structures Measured

Electrode Structure Fabrication Process	PPTSA Design	Element Spacing (microns)
Evaporation	Stripe	500
Evaporation	Stripe	750
Evaporation	Square Pad	500
Evaporation	Square Pad	750
Photolithographic	Stripe	500
Photolithographic	Stripe	750
Photolithographic	Square Pad	500
Photolithographic	Square Pad	750

Microscope, Wild Heerburg Limited, CH-9435 Heerburg, Switzerland) that was equipped with an optical micrometer. At the 4X magnification used, the optical micrometer could measure dimensions up to 1,040 microns with a 0.8 micron accuracy. Figures 3.11 and 3.12 show the electrode structure numbering system that was used to accomplish this evaluation.

The spacings between the five main stripe electrodes (number 2 to 6 in Figure 3.11) were measured at three different places, the two ends (lower and upper) and the middle. Figure 3.13 shows where these measurements were taken.

Since the surface of the PVDF film had thickness variations greater than 1,000 angstroms, the thin electrode

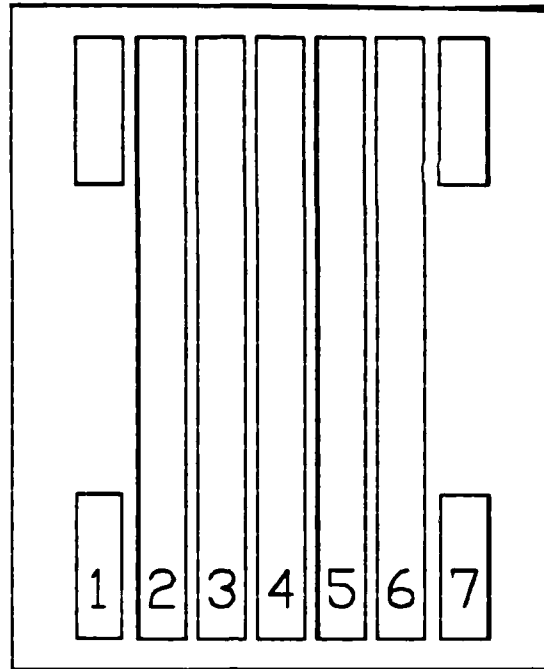


Figure 3.11. Electrode Structure Numbering System for the Stripe Design Configurations.

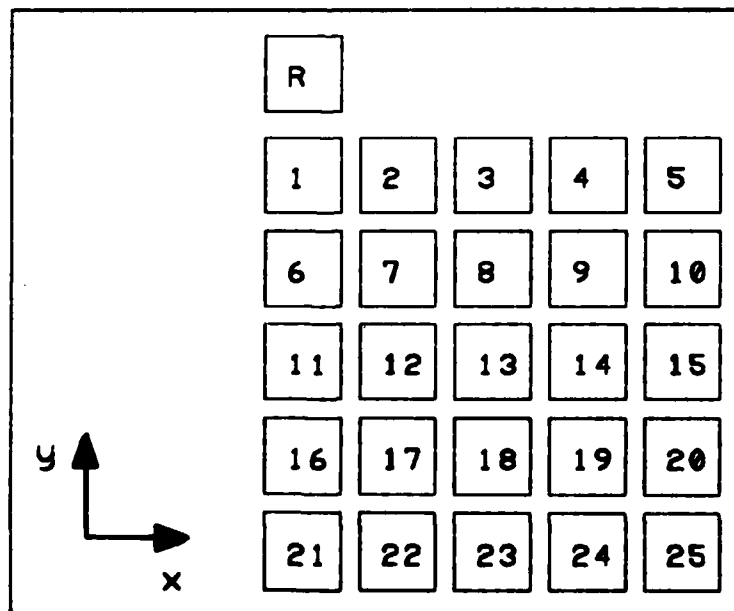


Figure 3.12. Electrode Structure Numbering System for the Square Pad Design Configurations.

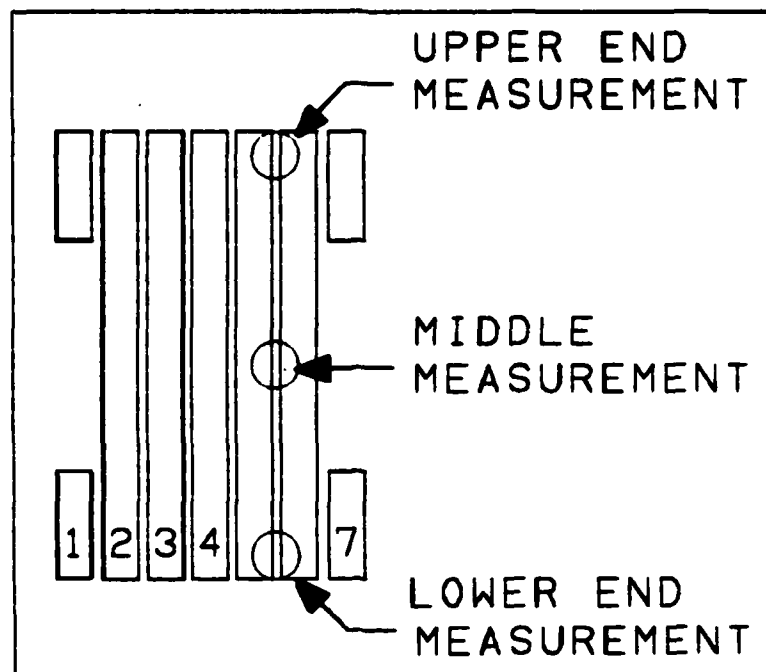


Figure 3.13. Showing where the Measurements were Taken Between the Main Stripe Electrodes.

structures (400 - 1,000 angstroms) could not be measured with any confident degree of accuracy. Solvay reported the thickness of the aluminum film on the metallized PVDF was approximately 400 angstroms (Solvay & Cie, 1983:1). The approximate thickness of an electrode structure formed by the thermal evaporation method was measured indirectly. An electrode structure thickness was determined using the glass slide that was positioned in the evaporation chamber (coplanar with the substrate) while the electrodes were deposited.

Stripe Electrode Impedance Evaluation Procedure. The impedance of the PPTSAs stripe electrodes were also

measured. The purpose of this measurement was to determine the relative electrical performance of the stripe electrodes. A low impedance was considered desirable, and an open circuit was considered undesirable. Only the five main stripe electrodes that formed the 5 x 5 sensor array matrix were measured. Figure 3.14 illustrates these electrodes, and they were identified as X2 through X6 for the vertical electrodes, and as Y2 through Y6 for the horizontal electrodes.

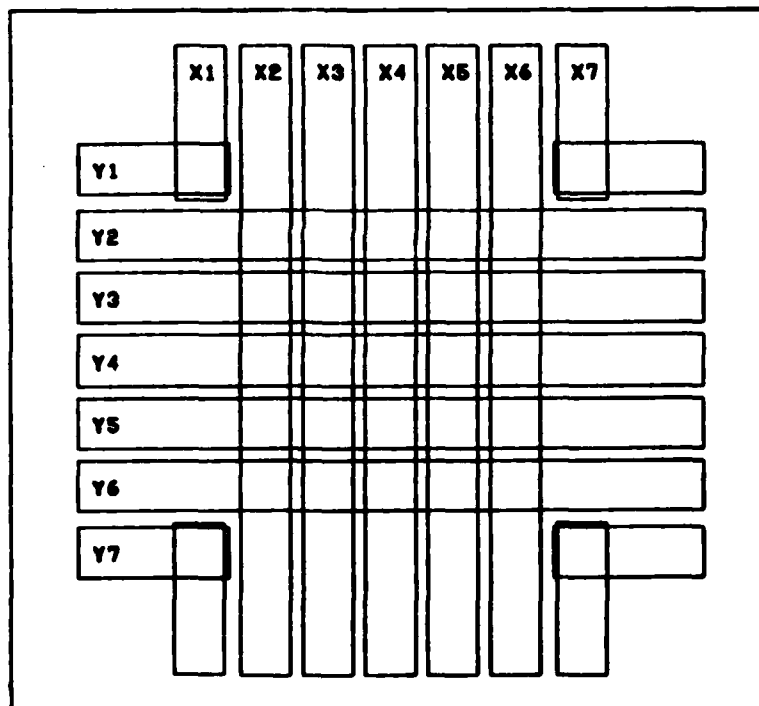


Figure 3.14. Identification of the Stripe Electrodes for the Impedance Measurements.

The procedure for measuring the impedance of the electrodes involved cleaning them, and then measuring the

electrodes with a Micronta digital multimeter (Catalog Number 22-185, Radio Shack, Fort Worth, TX 76102). The electrodes were cleaned with Freon TF Solvent (Miller-Stephenson Chemical Co., Inc., George Washington Highway, Danbury, CT 06810). Special multimeter test leads were fabricated. The probe points on the test leads were replaced with micro-alligator clips (Catalog Number 270-373, Radio Shack, Fort Worth, TX 76102). These clips were modified for these measurements. The lower jaws were insulated with heat-shrink tubing and the upper jaws were polished smooth with 600-grit emery paper. Polishing the upper jaws improved the physical and electrical contact with the sensor's electrodes.

Piezoelectric Activity Evaluation Procedure. The relative piezoelectric activity of the PVDF film in six of the PPTSA configurations was measured. It was decided these six configurations could answer key questions concerning the configuration designs. The questions were:

1. Are the square pad design configurations better than (or worse than) the stripe design? And if so, why?
2. Is a thicker PVDF film better than a thinner film? Better in this question refers to the piezoelectric activity of the PVDF film.
3. Does one electrode-structure fabrication process adversely effect the PVDF film more than the other process?

4. How does the thermal poling process affect the PVDF film? Is the piezoelectric activity of the PVDF film improved or degraded? What are the limitations of this process?

Figure 3.15 and Table 3.3 illustrate the six configurations. The stripe design PPTSA configuration fabricated using the

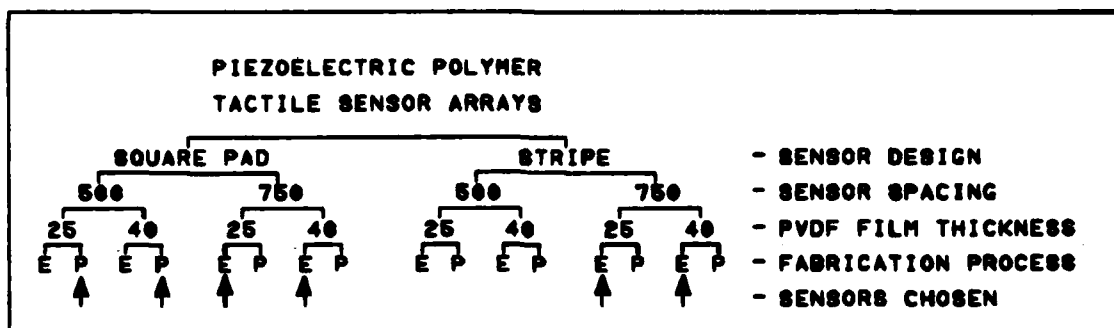


Figure 3.15. Diagram Showing the Six Configurations that were Measured.

Table 3.3

The Six Configurations Measured

PPTSA Number	Electrode Structure Process	PPTSA Design	PVDF Film Thickness (microns)	Element Spacing (microns)
2	Evaporation	Stripe	25	750
4	Evaporation	Stripe	40	750
6	Evaporation	Square Pad	25	750
8	Evaporation	Square Pad	40	750
13	Photolithographic	Square Pad	25	500
15	Photolithographic	Square Pad	40	500

photolithographic process were excluded from the measurement program for two reasons. One reason is that during the development of the measuring procedure it was discovered that the electrode structures were very fragile and fractured easily under a load. The other reason that was discovered, was that many of the stripe electrode structures were open circuited between ends, and therefore, functionally useless.

One striped design PPTSA (PPTSA #2) and one square-pad design PPTSA (PPTSA #13) were chosen from the six PPTSAs for thermal poling. The stripe design PPTSA #2 was selected because one of the center electrodes of the other PPTSA (PPTSA #4) was broken during piezoelectric-activity measurements. The square-pad design PPTSA #13 was chosen because it contained PVDF film of the same thickness, and it used the other electrode-structure fabrication process.

The piezoelectric activity procedure was to determine the relative magnitude of the piezoelectric activity in the PVDF film of the different PPTSA configurations. These measurement were considered relative because actual piezoelectric activity measurements require the piezoelectric material (PVDF film) to be unrestricted. The PVDF film in this study was restricted. The piezoelectric PVDF film produced a voltage response proportional to an applied pressure. In this study, pressures were produced by applying a load (force) over an area. A center and a corner

discrete sensor for each of the PPTSAs tested were measured with six different loads (grams): 100, 200, 500, 700, 1000 and 1500. Referring to Figures 3.12 and 3.14, these sensors were numbered 13 (center) and 21 (corner) for the square pad configurations and X4Y4 (center) and X2Y6 for the stripe configurations. Five to nine measurements were taken for each of the loads for a discrete sensor.

Piezoelectric Activity Measurement Arrangement. A schematic of the arrangement that was used for measuring the piezoelectric activity of PPTSA configuration is shown Figure 3.16. The loading machine was a modified Model LR

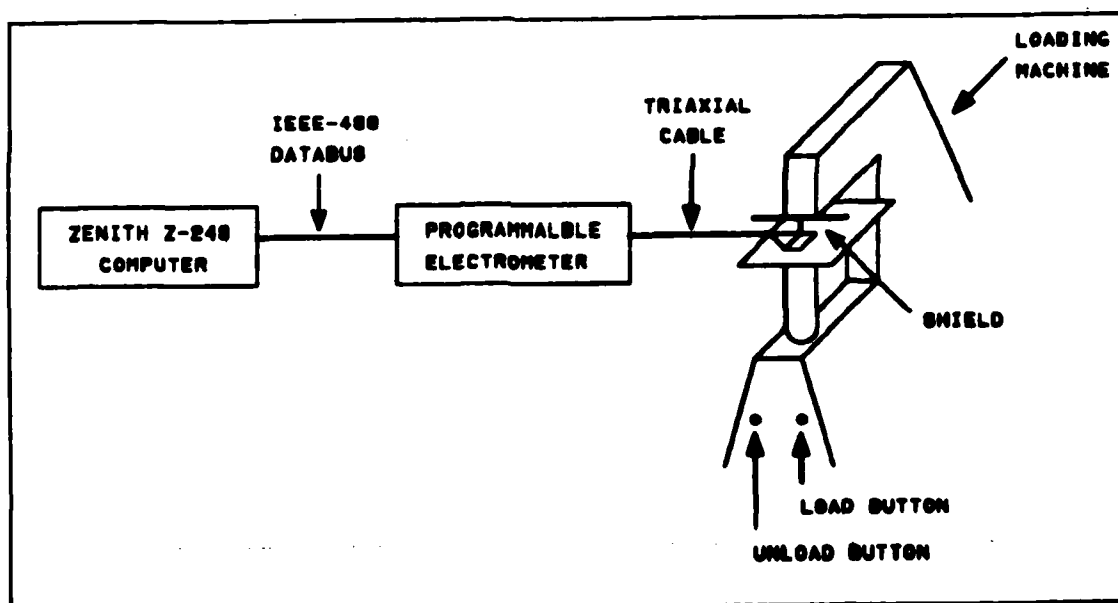


Figure 3.16. Schematic of the Piezoelectric Activity Measurement Arrangement.

Tukon Hardness Tester (Wilson Mechanical Instrument Co., Inc., 383 Concord Avenue, New York, NY). The indenter on the hardness tester was replaced with a blunt point that was

fabricated by the AFIT Model Shop. Figure 3.17 shows a drawing of how a load was applied to a discrete sensor. The

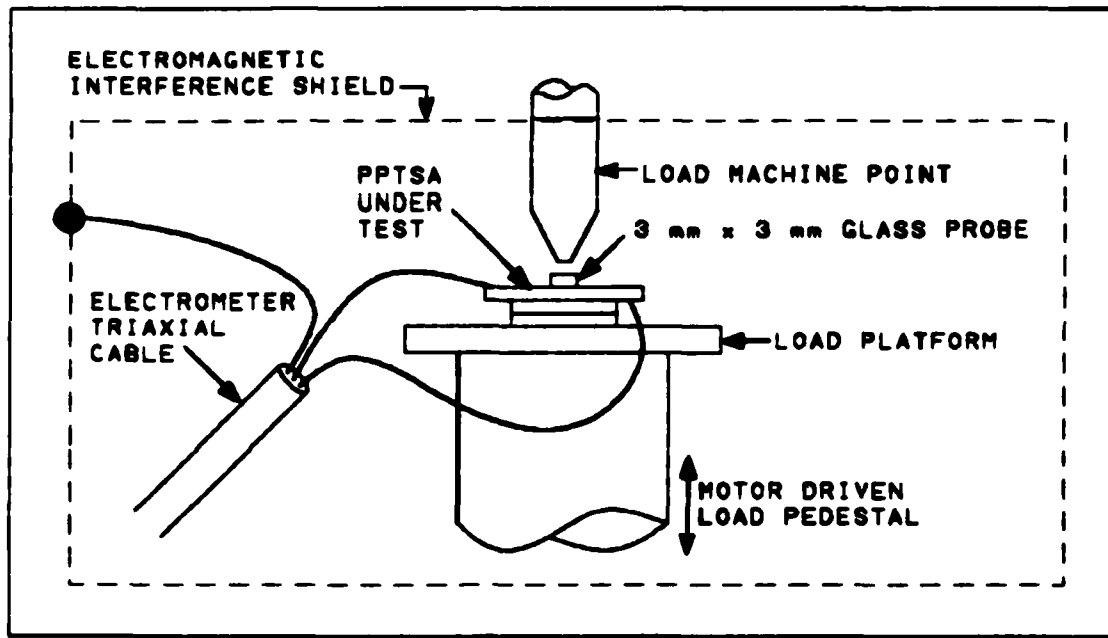


Figure 3.17. A Drawing Illustrating the Technique Used to Apply a Load to a Discrete Sensor. (To apply a load, the load button was pressed and the motor driven pedestal machine would move the load up. The pedestal would stop when the full weight of the given load was applied. To remove a load, the reverse operation would occur. The glass probe was used to apply the load over the surface of a discrete sensor under test. The glass probe provided electrical isolation from the load machine.)

voltage response was measured using a Keithley Model 617 Programmable Electrometer (Keithley Instruments, Inc., 28775 Aurora Road, Cleveland, Ohio 44139). The voltage response data was transferred to a Zenith Model Z-248 computer through an IEEE-488 interface, and then with the aid of a computer program, recorded on a 5.25" floppy diskette. The

electrometer was operated at its fastest reading (conversion) rate. This measurement rate was a data point collected every 360 milliseconds (Keithley Instruments, 1984a:2-28). The computer program used for collecting the data is listed in Appendix I. This program (written in BASIC and IEEE-488 interface code) provided the experimenter with real time information on the computer screen. At the end of each measurement, the program computed and listed the maximum and minimum response values in the measurement cycle.

Piezoelectric Activity Measurement Procedure. The piezoelectric activity measurement process was semi-automatic. Applying the load, removing the load, and recording the data were performed automatically with the press of a button (or computer key). Mounting and positioning a PPTSA for a measurement, selecting loads, and following a sequence of events to take a measurement were all manual tasks.

Figure 3.18 illustrates the sequence of events that to performed during a single measurement. The first part of the sequence involved executing the electrometer's zero correct and zero check commands. These commands worked together to eliminate any internal offsets (or system drifts) that might influence the accuracy of the data (Keithley Instruments, 1984a:3-26). To accomplish a measurement, the zero check operation was disabled and the

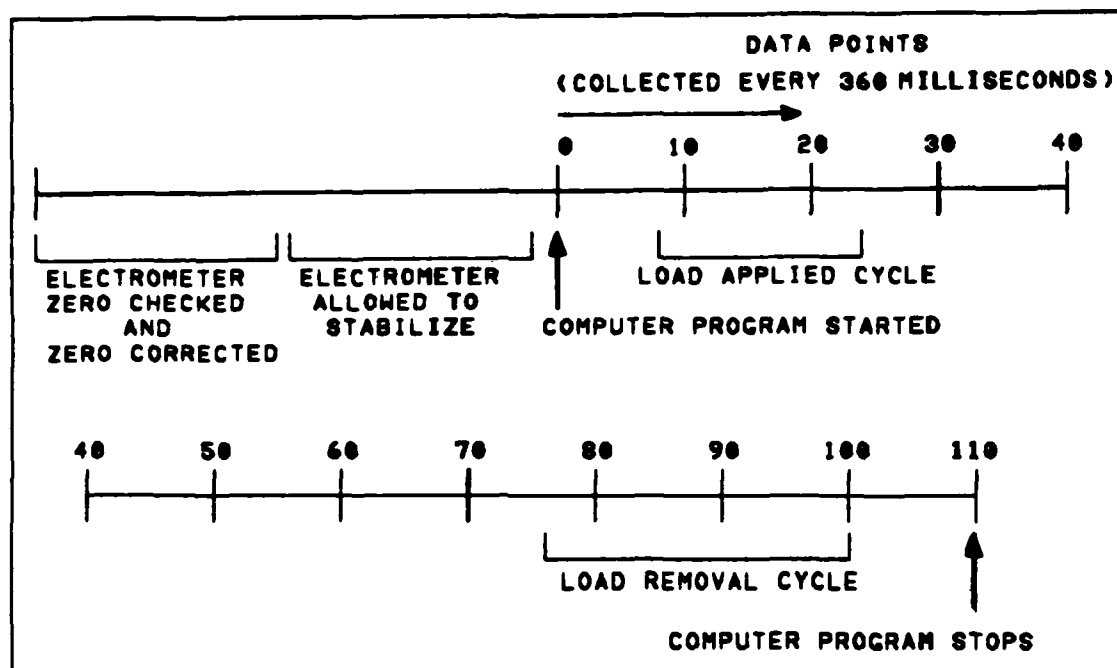


Figure 3.18. Sequence of Events Accomplished to Perform a Measurement Cycle.

electrometer was allowed to stabilize. Data collection started with the data execution of the collection computer program. This computer program (DATA.BAS) is listed in Appendix I. The load button on the loading machine was pressed when eight to ten data points had been collected. It took the loading machine about 5.7 seconds (or 15 to 16 data intervals) to complete the load cycle. The load removal cycle started 23.7 seconds after the load button had been pressed. When the load removal cycle routine was inoperative (a common but random occurrence), the unload button was pressed between the 85th to 90th data point. The load removal cycle took about 6 seconds to complete. The

measurement was finish after the 110th data point was collected.

Reducing the Piezoelectric Activity Measurement Data. This part of the piezoelectric activity measurement procedure involved reducing the collected measurement data. The data was first printed and then plotted. The data was examined for uniformity and any irregularities that might have biased the data. The data that showed a consistent uniform pattern was reduced to voltage response data. An example of a consistent uniform pattern is shown in Figure 3.19. Data that showed gross irregularities were

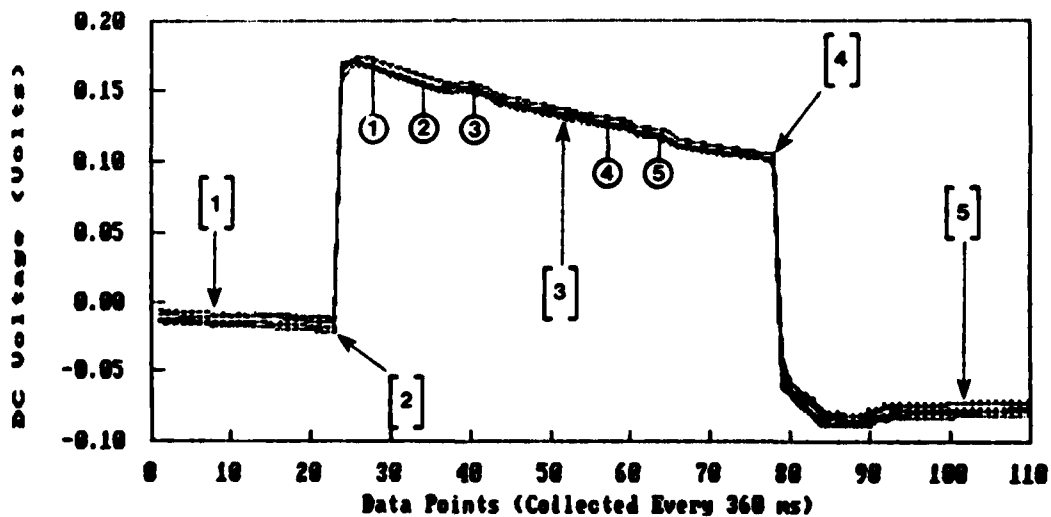


Figure 3.19. An Example of Five Measurements Having a Consistent Uniform Pattern. (The vertical axis represents the sensor's DC response voltage. Key to measurement states: [1] Pre-load, [2] Load application, [3] Steady-state response, [4] Load removal, and [5] Post-load.)

excluded from the data reduction process. Figure 3.20 shows an example of a data set that has gross irregularities.

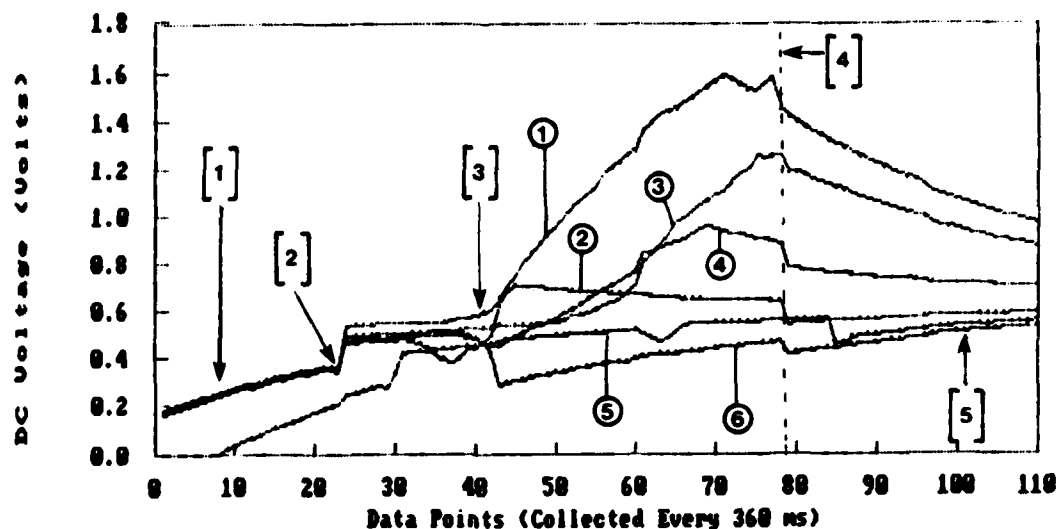


Figure 3.20. An Example of a Data Set of Six Measurements that has Gross Irregularities. (The vertical axis represents the sensor's DC response voltage. Key to measurement states: [1] Pre-load, [2] Load application, [3] Steady-state response, [4] Load removal (occurs about the 78 data point), and [5] Post-load.)

A computer program (DELTA.BAS) was used to accomplish the data reduction process. With an acceptable input, this program computed the load response for a measurement. The program required a file name and the location of six data points in a measurement. Figure 3.21 illustrates a graph with the input and computed data points that are associated with this program. The six input data points were selected manually (from the printouts and graphs) and were reported in three pairs: A-B, C-D, and E-F. The points that formed a pair were separated by at least 10 data points. Points that formed a transient response curve, like those shown in Figure 3.22, were omitted from the data point selection

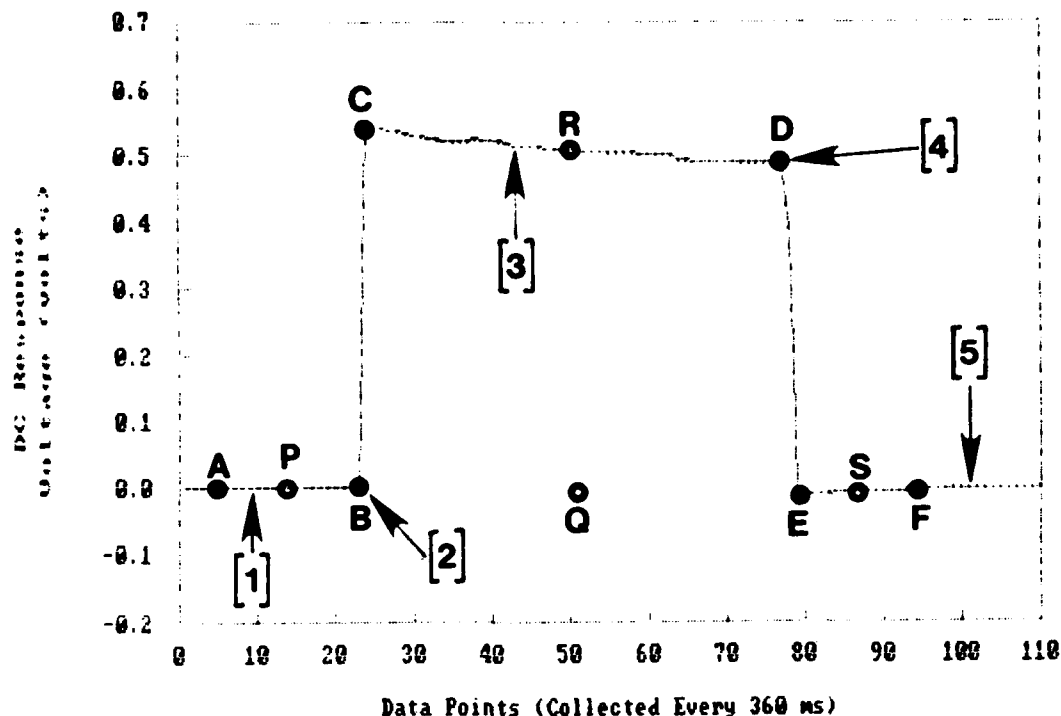


Figure 3.21. An Example of a Graph with the Input and Computed Data Points that are Associated with the DELTA.BAS Computer Program. (Key to measurement states: [1] Pre-load, [2] Load application, [3] Steady-state response, [4] Load removal, and [5] Post-load.)

process. The program computed (using a linear least squares curve fit routine) a midpoint for each of the pairs. The linear least square curves computed for the pairs A-B and E-F (Figure 3.21) were considered initial and final reference levels, respectively. The average of the midpoints P and S (corresponding to the pairs A-B and E-F) were used to establish a common baseline reference level point Q. The linear least square curve computed for the C-D pair was considered the voltage response curve. The voltage response

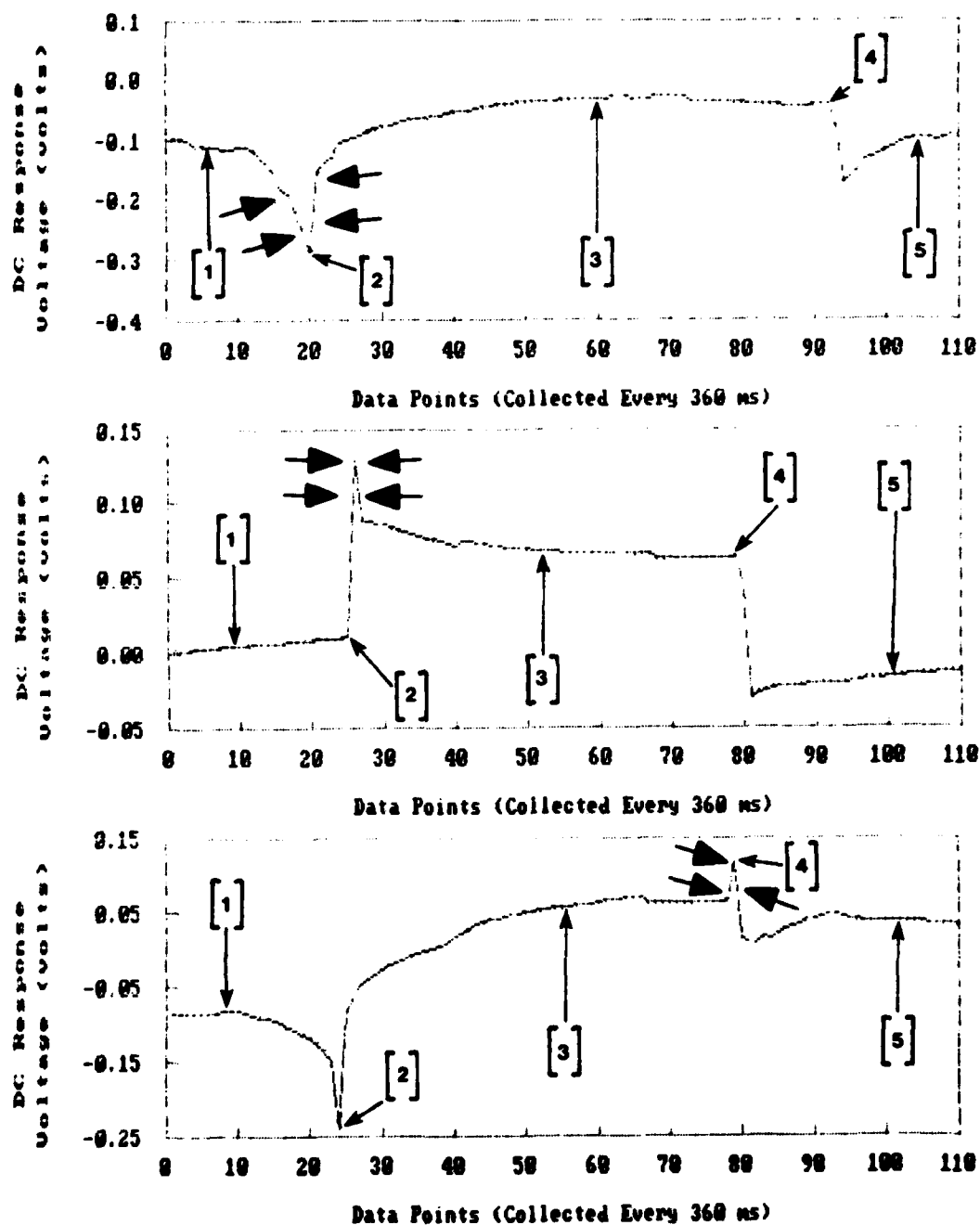


Figure 2.22. Points that Formed a Transient Response Curve, Like Those Shown (Between the Arrows), were Omitted From the Input Point Selection Process. (Key to measurement states: [1] Pre-load, [2] Load application, [3] Steady-state response, [4] Load removal, and [5] Post-load.)

was computed as the difference between the baseline reference level point Q and the midpoint (R) of the voltage response curve. An average and standard deviation was computed for each set of load measurements. The averages and standard deviations from these computations were recorded in Chapter IV.

Summary

The experimental sensor designs, the sensor fabrication procedures, the thermal poling process, and the evaluation procedures were described in this chapter. The reasons for, and construction of the two basic PPTSA designs (stripe and square-pad), and their variations, were discussed in the experimental sensor design section. This section also described the procedures that were used to fabricate the different PPTSA configurations. The thermal poling process was discussed in the third section. The arrangements and procedures used to evaluate the PPTSA configurations were described in the final section.

IV. Experimental Data

This chapter contains the data collected from the evaluation procedures described in Chapter III. The data was categorized in two sections. The first section contained the data from the electrode-structure fabrication process evaluation. The piezoelectric activity data was organized in the second section.

Electrode-Structure Fabrication Process Evaluation Data

The fabrication process evaluation was categorized into two parts. The first part was concerned with performing a dimensional error analysis of the electrode structures that were formed using the two fabrication procedures. The fabrication processes in this section were identified as 'Evap' for Evaporation and 'Phot' for Photolithographic. The second part of the evaluation pertained to the relative performance of the stripe electrodes.

The dimensional error analysis associated with electrode structures consisted of measuring the spacing between discrete electrodes. Tables 4.1 and 4.2 summarize the spacing data for the stripe and square pad design configurations, respectively. The spacing between any two electrodes was reported as A/B, where A and B are adjacent electrodes. The approximate thickness of the electrode structures formed using the evaporation fabrication process are posted in Table 4.3. The stripe electrode impedance data is tabulated

Table 4.1

Sensor Spacing Measurement Data
for the Stripe Design Configurations

Sensor Spacing (microns)	Electrode- Structure Fabrication Process	Spacing Between Electrodes	Measured Spacing (microns)		
			Lower	Middle	Upper
500	Evap	2/3	497.6	614.8	450.8
		3/4	492.8	744.4	496.0
		4/5	486.0	656.0	478.4
		5/6	476.4	644.4	470.8
500	Phot	2/3	668.0	692.8	678.4
		3/4	668.0	683.2	674.4
		4/5	652.8	684.0	678.0
		5/6	661.6	682.8	673.6
750	Evap	2/3	704.0	830.8	742.4
		3/4	708.8	902.8	748.8
		4/5	678.8	879.6	749.6
		5/6	696.0	895.6	739.6
750	Phot	2/3	939.2	928.8	944.0
		3/4	933.6	933.6	924.0
		4/5	935.2	944.8	920.0
		5/6	938.4	968.0	947.2

in Table 4.4. Table 4.4 shows the results of the PPTSA configurations that were used, and also a few configurations from experimenting.

Table 4.2

Sensor Spacing Measurement Data
for the Square-Pad Design Configurations

Spacing Between Electrodes	Measured Spacing (microns)	Spacing Between Electrodes	Measured Spacing (microns)
----------------------------------	----------------------------------	----------------------------------	----------------------------------

500 micron Sensor Spacing, Evaporation Fabrication:

1/2	535.2	2/3	543.2
3/4	543.2	4/5	512.8
6/7	567.6	7/8	580.0
8/9	535.2	9/10	550.4
11/12	576.0	12/13	583.6
13/14	559.2	14/15	545.2
16/17	565.6	17/18	589.6
18/19	480.0	19/20	555.6
21/22	536.0	22/23	547.2
23/24	484.0	24/25	532.0

1/6	520.0	2/7	563.2
3/8	550.4	4/9	512.8
5/10	560.0	6/11	545.6
7/12	568.8	8/13	596.0
9/14	536.8	10/15	534.0
11/16	548.8	12/17	590.4
13/18	603.6	14/19	573.2
15/20	510.0	16/21	553.2
17/22	593.6	18/23	589.2
19/24	555.6	20/25	524.0

500 micron Sensor Spacing, Photolithographic Fabrication:

1/2	584.8	2/3	562.4
3/4	573.6	4/5	583.2
6/7	560.8	7/8	569.6
8/9	549.2	9/10	565.6
11/12	570.4	12/13	571.2
13/14	550.4	14/15	561.2
16/17	547.2	17/18	552.0
18/19	559.2	19/20	562.4
21/22	548.0	22/23	558.4
23/24	444.8	24/25	551.2

Table 4.2 (continued)

Spacing Between Electrodes	Measured Spacing (microns)	Spacing Between Electrodes	Measured Spacing (microns)
1/6	550.4	2/7	564.0
3/8	566.8	4/9	566.0
5/10	568.8	6/11	576.0
7/12	567.2	8/13	575.2
9/14	580.8	10/15	584.0
11/16	576.0	12/17	569.2
13/18	572.8	14/19	586.0
15/20	560.8	16/21	571.2
17/22	576.8	18/23	580.0
19/24	572.0	20/25	576.0

750 micron Sensor Spacing, Evaporation Fabrication:

1/2	806.8	2/3	797.6
3/4	811.2	4/5	786.8
6/7	861.6	7/8	876.8
8/9	864.8	9/10	828.0
11/12	882.8	12/13	903.6
13/14	876.8	14/15	847.2
16/17	884.4	17/18	898.0
18/19	872.4	19/20	852.8
21/22	869.6	22/23	872.8
23/24	862.4	24/25	844.0
1/6	818.4	2/7	843.2
3/8	836.0	4/9	821.6
5/10	794.0	6/11	845.6
7/12	866.0	8/13	893.6
9/14	848.0	10/15	819.6
11/16	860.8	12/17	898.4
13/18	881.6	14/19	863.2
15/20	822.0	16/21	856.0
17/22	891.6	18/23	881.6
19/24	865.2	20/25	814.4

Table 4.2 (continued)

Spacing Between Electrodes	Measured Spacing (microns)	Spacing Between Electrodes	Measured Spacing (microns)
750 micron Sensor Spacing, Photolithographic Fabrication:			
1/2	912.0	2/3	926.4
3/4	924.0	4/5	915.2
6/7	912.8	7/8	894.4
8/9	903.2	9/10	895.2
11/12	898.4	12/13	896.4
13/14	892.8	14/15	892.0
16/17	896.4	17/18	896.8
18/19	888.0	19/20	883.2
21/22	896.0	22/23	900.8
23/24	892.0	24/25	896.0
1/6	922.4	2/7	912.0
3/8	904.8	4/9	920.0
5/10	885.6	6/11	922.4
7/12	906.4	8/13	925.6
9/14	910.4	10/15	902.0
11/16	909.6	12/17	896.8
13/18	906.4	14/19	900.0
15/20	895.2	16/21	911.2
17/22	912.8	18/23	916.0
19/24	919.2	20/25	912.8

Table 4.3

Thickness of the Aluminum Electrode Structures
for the Configurations Fabricated
Using the Evaporation Process

PPTSA Identification Designater	Electrode Metallization Thickness* (Angstroms)	
	Surface 1	Surface 2
1a	1,040	650
2a	1,040	650
1b	1,100	1,080
2b	1,100	1,080
3	725	860
4	725	860
5	1,040	650
6	1,040	650
7	725	860
8	725	860

* The two surfaces of the PVDF film are represented as surface 1 and surface 2.

Table 4.4

Stripe Electrode Impedance Data

PPTSA Number	Stripe Electrode	Impedance (ohms)	Stripe Electrode	Impedance (ohms)
1a	X2	8.3	Y2	17.9
	X3	9.2	Y3	17.6
	X4	7.6	Y4	18.3
	X5	7.4	Y5	18.5
	X6	6.9	Y6	21.5
1b	X2	5.4	Y2	10.4
	X3	5.4	Y3	10.2
	X4	5.5	Y4	10.3
	X5	5.7	Y5	10.7
	X6	5.7	Y6	10.6
2a	X2	10.7	Y2	12.2
	X3	12.1	Y3	12.2
	X4	11.2	Y4	12.1
	X5	11.4	Y5	12.6
	X6	11.4	Y6	12.2
2b	X2	4.5	Y2	10.4
	X3	4.4	Y3	10.2
	X4	4.4	Y4	10.3
	X5	4.4	Y5	10.6
	X6	4.5	Y6	10.4
3	X2	19.9	Y2	11.3
	X3	16.9	Y3	10.7
	X4	OC	Y4	11.0
	X5	15.0	Y5	12.1
	X6	17.8	Y6	12.5
4	X2	13.5	Y2	10.9
	X3	12.8	Y3	11.4
	X4	13.9	Y4	11.4
	X5	14.6	Y5	11.0
	X6	14.7	Y6	10.9

Table 4.4 (continued)

PPTSA Number	Stripe Electrode	Impedance (ohms)	Stripe Electrode	Impedance (ohms)
9a	X2	OC	Y2	29.1
	X3	239.9	Y3	26.8
	X4	55.5	Y4	25.7
	X5	OC	Y5	37.4
	X6	64.7	Y6	291.1
9b	X2	13.4	Y2	13.6
	X3	13.2	Y3	12.4
	X4	13.9	Y4	13.9
	X5	14.8	Y5	15.9
	X6	OC	Y6	14.9
10a	X2	OC	Y2	OC
	X3	OC	Y3	OC
	X4	OC	Y4	OC
	X5	21.6	Y5	OC
	X6	16.5	Y6	OC
10b	X2	27.2	Y2	OC
	X3	21.4	Y3	12.5
	X4	13.0	Y4	12.3
	X5	12.3	Y5	12.1
	X6	12.0	Y6	14.8
11a	X2	21.4	Y2	20.9
	X3	23.1	Y3	16.5
	X4	OC	Y4	22.2
	X5	27.0	Y5	21.1
	X6	OC	Y6	29.2
11b	X2	20.4	Y2	28.6
	X3	OC	Y3	39.0
	X4	17.1	Y4	37.3
	X5	13.7	Y5	18.2
	X6	24.0	Y6	19.4
12a	X2	23.2	Y2	OC
	X3	22.7	Y3	OC
	X4	21.4	Y4	OC
	X5	19.8	Y5	OC
	X6	23.0	Y6	OC

Table 4.4 (continued)

PPTSA Number	Stripe Electrode	Impedance (ohms)	Stripe Electrode	Impedance (ohms)
12b	X2	20.4	Y2	17.9
	X3	21.7	Y3	22.6
	X4	25.2	Y4	24.7
	X5	51.6	Y5	30.7
	X6	20.1	Y6	31.0
12c	X2	OC	Y2	13.6
	X3	14.9	Y3	12.4
	X4	13.8	Y4	13.9
	X5	12.2	Y5	15.9
	X6	12.4	Y6	14.9

* OC This stripe electrode is open circuited between its ends.

Piezoelectric Activity Measurement Data

This section contains the piezoelectricity activity data for the six PPTSA configurations (PPTSAs #2b, #4, #6, #8, #13, and #15). A center and a corner discrete sensor from each configuration was measured for piezoelectric activity. The stripe configuration sensors were numbered X4Y4 (center) and X2Y6 (corner). The square pad configuration sensors were numbered 13 (center) and 21 (corner). Table 4.5 summarizes the data that was collected. Two of the configurations (PPTSAs #2b and #13) were measured twice. They were measured before and after supplemental poling in the laboratory. Graphs of the before and after piezoelectric activity data for these two configurations were plotted. The best (Figures 4.1 through 4.6) of these plots are in this chapter, and the remaining plots are Appendix J. Figures 4.1 through 4.6 represent the piezoelectric activity measurements for the corner sensor of the PPTSA #13 configuration.

Table 4.5

Piezoelectric Activity Measurement Data

PPTSA /Sensor	Load (grams)	DC Voltage Response (volts)	Standard Deviation (volts)	Number of Measurements
2b/X4Y4	100	Unresolvable		
	200	Unresolvable		
	500	0.16837	0.00235	5
	700	0.28869	0.00574	6
	1000	0.41185	0.00709	4
	1500	0.67512	0.01000	6
2b/X2Y6	100	Unresolvable		
	200	0.05264	0.00558	5
	500	0.23666	0.00666	5
	700	0.42165	0.01077	5
	1000	0.56647	0.00740	4
	1500	0.80568	0.01816	5
2b/X4Y4 Poled	100	0.02586	0.00305	4
	200	0.05901	0.00414	5
	500	0.13034	0.00094	5
	700	0.19799	0.00207	5
	1000	0.28218	0.00339	4
	1500	0.38972	0.01102	5
2b/X2Y6 Poled	100	0.06168	0.00045	5
	200	0.09354	0.00109	5
	500	0.18090	0.00108	5
	700	0.24907	0.00274	5
	1000	0.36597	0.00123	6
	1500	0.45846	0.00590	5
4/X4Y4	100	Unresolvable		
	200	0.05076	0.00728	6
	500	0.31644	0.00643	7
	700	0.39604	0.01207	6
	1000	Broken Electrode		
	1500	Broken Electrode		

Table 4.5 (continued)

PPTSA /Sensor	Load (grams)	DC Voltage Response (volts)	Standard Deviation (volts)	Number of Measurements
4/X2Y6	100	Unresolvable		
	200	0.05039	0.00742	6
	500	0.30738	0.02800	4
	700	0.39028	0.01319	5
	1000	0.57080	0.02222	3
	1500	0.81148	0.01044	5
6/13	100	0.04817	0.00415	6
	200	0.10372	0.00049	5
	500	0.28439	0.00650	5
	700	0.37775	0.00253	5
	1000	0.51633	0.00493	6
	1500	0.77702	0.00284	5
6/21	100	0.08210	0.00511	5
	200	0.12491	0.00584	5
	500	0.18041	0.00947	5
	700	0.20631	0.00507	7
	1000	0.24624	0.00540	5
	1500	0.39988	0.00268	5
8/13	100	1.04430	0.05514	7
	200	0.89197	0.01553	6
	500	1.09652	0.02033	5
	700	1.16691	0.01007	5
	1000	1.36159	0.01356	6
	1500	1.60194	0.00597	6
8/21	100	0.40602	0.00829	6
	200	0.43137	0.00801	5
	500	0.62894	0.01875	5
	700	0.73775	0.00516	5
	1000	0.89054	0.00329	5
	1500	1.17041	0.00436	6

Table 4.5 (continued)

PPTSA /Sensor	Load (grams)	DC Voltage Response (volts)	Standard Deviation (volts)	Number of Measurements
13/13	100	0.24492	0.01030	5
	200	0.30722	0.00131	5
	500	0.47732	0.00155	6
	700	0.57270	0.00353	5
	1000	0.75331	0.00230	5
	1500	1.04538	0.00653	5
13/21	100	0.33835	0.00451	5
	200	0.33246	0.00166	5
	500	0.43416	0.00964	5
	700	0.48410	0.00713	6
	1000	0.57077	0.00344	5
	1500	0.83318	0.00729	5
13/13 Poled	100	0.11250	0.00633	5
	200	Unresolvable		
	500	0.23596	0.01149	4
	700	0.28909	0.00469	6
	1000	0.32447	0.00875	4
	1500	0.46634	0.00549	5
13/21 Poled	100	0.02836	0.00200	5
	200	0.05770	0.00248	5
	500	0.13326	0.00344	6
	700	0.17962	0.00152	7
	1000	0.25897	0.00030	5
	1500	0.40819	0.00327	5
15/13	100	0.30890	0.01539	5
	200	0.37476	0.01796	5
	500	0.44093	0.01837	5
	700	0.58624	0.02319	5
	1000	0.64627	0.02416	5
	1500	0.87747	0.02671	5
15/21	100	0.12639	0.00566	6
	200	0.17131	0.00895	5
	500	0.33796	0.00389	5
	700	0.44839	0.00730	5
	1000	0.62881	0.02022	4
	1500	0.90248	0.02322	5

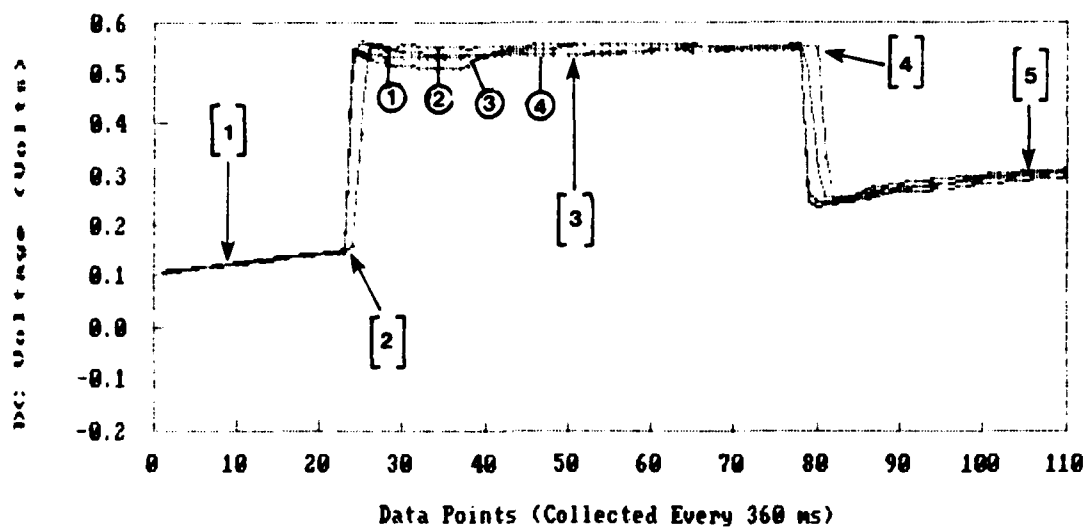


Figure 4.1. Response of Four Measurements for the PPTSA #13 Configuration. These Measurements were for the Corner Sensor and 100 Gram Load. (The vertical axis represents the sensor's DC response voltage. Key to measurement states: [1] Pre-load, [2] Load application, [3] Steady state response, [4] Load removal, and [5] Post-load.)

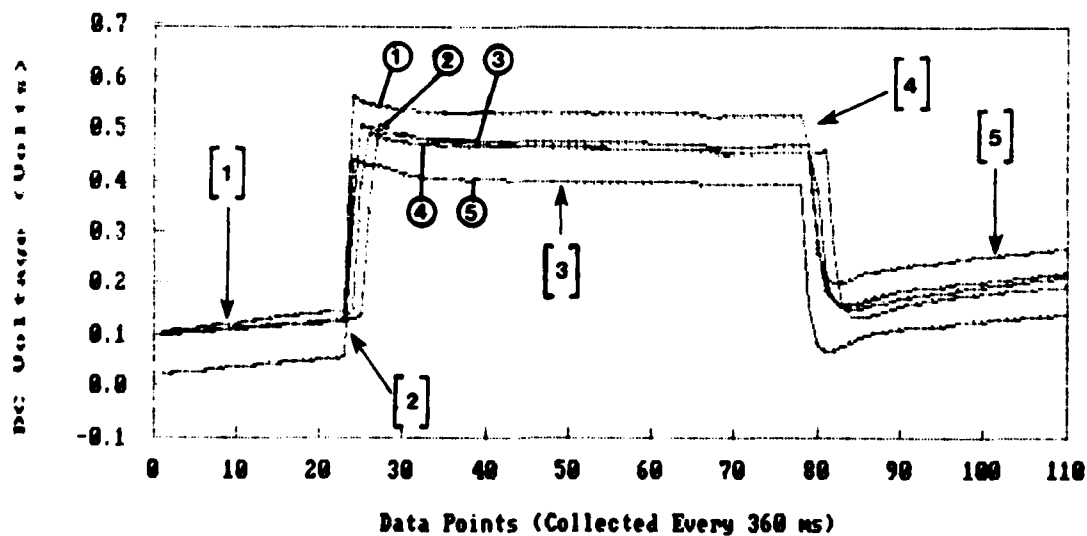


Figure 4.2. Response of Five Measurements for the PPTSA #13 Configuration. These Measurements were for the Corner Sensor and 200 Gram Load. (The vertical axis represents the sensor's DC response voltage. Key to measurement states: [1] Pre-load, [2] Load application, [3] Steady state response, [4] Load removal, and [5] Post-load.)

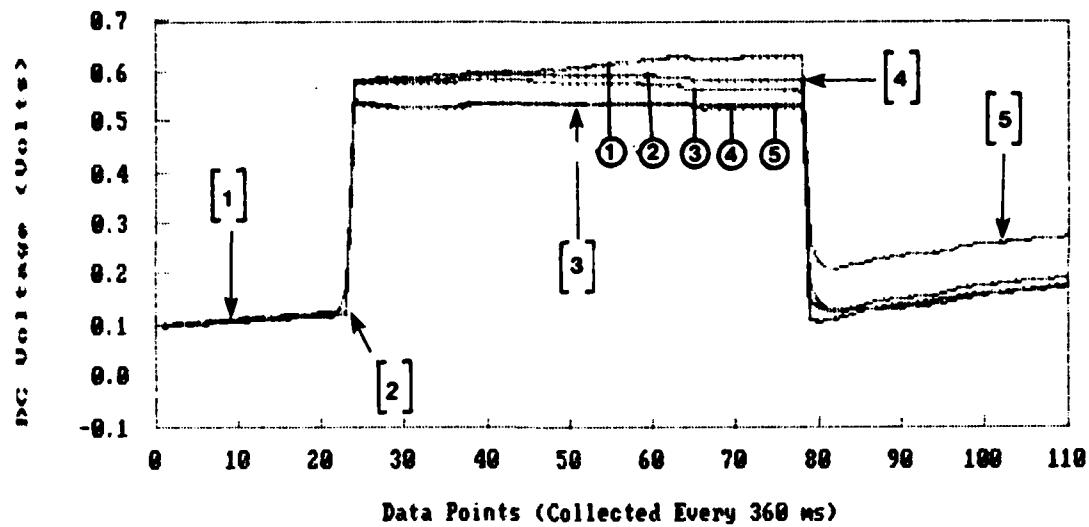


Figure 4.3. Response of Five Measurements for the PPTSA #13 Configuration. These Measurements were for the Corner Sensor and 500 Gram Load. (The vertical axis represents the sensor's DC response voltage. Key to measurement states: [1] Pre-load, [2] Load application, [3] Steady state response, [4] Load removal, and [5] Post-load.)

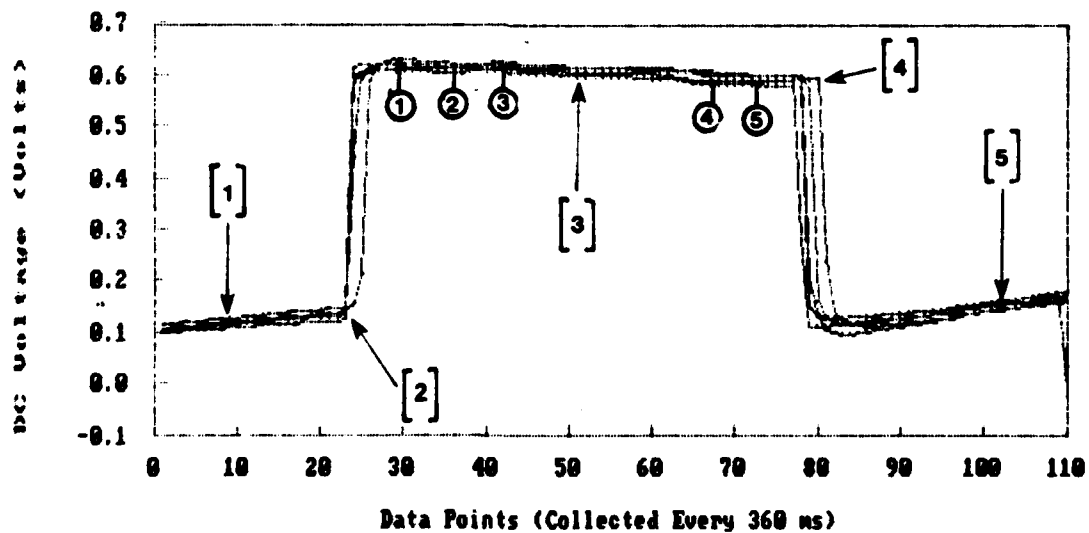


Figure 4.4. Response of Five Measurements for the PPTSA #13 Configuration. These Measurements were for the Corner Sensor and 700 Gram Load. (The vertical axis represents the sensor's DC response voltage. Key to measurement states: [1] Pre-load, [2] Load application, [3] Steady state response, [4] Load removal, and [5] Post-load.)

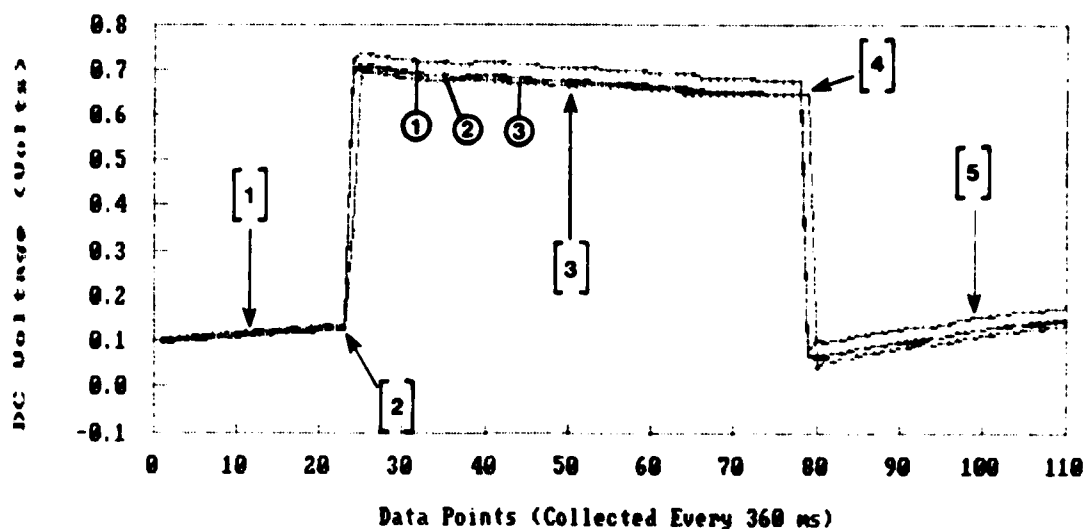


Figure 4.5. Response of Six Measurements for the PPTSA #13 Configuration. These Measurements were for the Corner Sensor and 1,000 Gram Load. (The vertical axis represents the sensor's DC response voltage. Key to measurement states: [1] Pre-load, [2] Load application, [3] Steady state response, [4] Load removal, and [5] Post-load.)

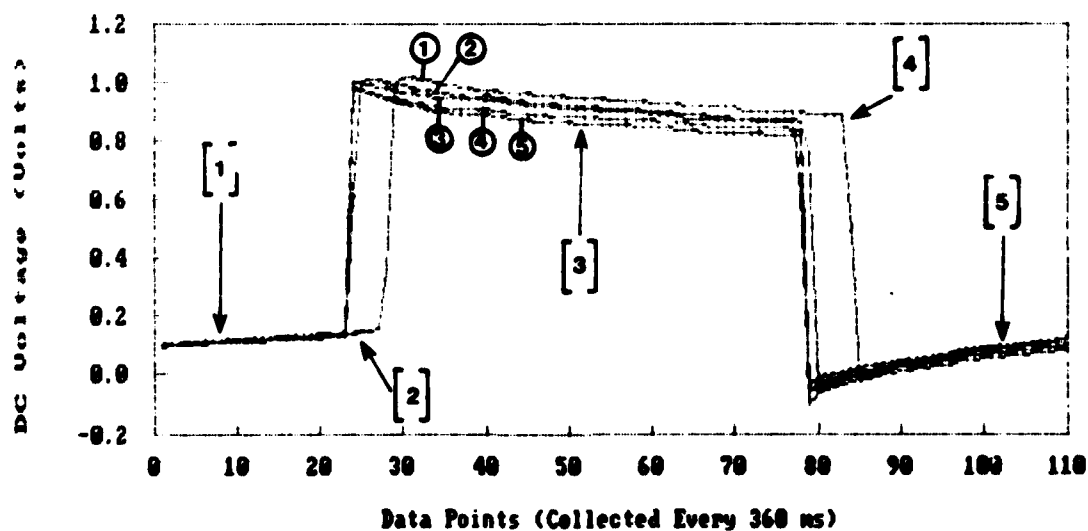


Figure 4.6. Response of Five Measurements for the PPTSA #13 Configuration. These Measurements were for the Corner Sensor and 1,500 Gram Load. (The vertical axis represents the sensor's DC response voltage. Key to measurement states: [1] Pre-load, [2] Load application, [3] Steady state response, [4] Load removal, and [5] Post-load.)

Summary

This chapter contained the data for the electrode-structure fabrication process and piezoelectric activity evaluations. The data was categorized in two sections. The first section contained dimensional and impedance data associated with the electrode-structure fabrication process. The piezoelectric activity data was organized in the second section.

V. Discussion and Analysis

This chapter contains the electrode-structure fabrication process and the piezoelectric activity evaluations. The electrode-structure fabrication process evaluation involved determining how precise the fabricated electrode structures compared to the design specifications, and determining the relative performance of the stripe electrodes. The piezoelectric activity data were examined, analyzed, and interpreted in the piezoelectric activity evaluation. A discussion on the effects of the thermal poling process was included in the piezoelectric activity evaluation.

Electrode-Structure Fabrication Process Evaluation

The electrode-structure fabrication process evaluation was separated into two parts. The first part of this evaluation involved determining how precise the fabricated electrode structures compared to the design specifications. The relative performance of the stripe electrode structures were evaluated in the second part of this evaluation. To determine how precise the electrode structures compared to the design specifications, a dimensional error analysis was performed. This analysis was based on the sensor spacing data that was collected for the eight different electrode structure types. From the sensor spacing data, average sensor spacings (with standard deviations) and average

electrode dimensions were computed. The average electrode dimension (AED) was computed using the equation

$$\text{AED} = \text{DSS} - \text{AMSS} + 3,000 \quad (\text{microns}) \quad (5.1)$$

where DSS was the design sensor spacing, AMSS was the average measured sensor spacing, and the constant (3,000 microns) represents the designed electrode dimension. The computed average electrode dimensions were considered approximations because they were not measured directly. Two error parameters were computed. The first error parameter was based on the averaged measured sensor spacing and the designed sensor spacing (500 or 750 microns). The second error parameter was based on the computed average electrode dimension compared to the designed electrode dimension (3,000 microns).

The different types of stripe design structures were analyzed first. The measured sensor spacing data for the four types of stripe design structures were posted in Table 4.1. Table 5.1 lists the error data for the stripe design structures.

Two trends were evident from the sensor spacing data (Table 4.1) and associated error analysis (Table 5.1) for the stripe design structures. The evaporation electrode-structure process produced structures closer to the design specifications compared to the photolithographic electrode-structure process. By comparing the measurements associated

Table 5.1

Electrode Structure Dimension Error Data
for the Stripe Design Configurations

Sample Designator and Measured Location	Average Spacing and Standard Deviation (microns)*	Spacing Error (percent)	Average Electrode Width (microns)	Electrode Width Error (percent)
---	---	-------------------------	-----------------------------------	---------------------------------

500 micron sensor spacing.

Thermal Evaporation Electrode-Structure Fabrication Process

Upper	488.2 & 4.0	2.36	3,011.8	0.39
Middle	664.9 & 24.1	32.98	2,835.1	5.50
Lower	474.0 & 8.1	5.20	3,026.0	0.87

500 micron Sensor Spacing.

Photolithographic Electrode-Structure Fabrication Process

Upper	662.6 & 3.1	30.52	2,837.4	5.42
Middle	685.7 & 2.1	37.14	2,814.3	6.19
Lower	676.1 & 1.1	35.22	2,823.9	5.87

750 micron sensor spacing.

Thermal Evaporation Electrode-Structure Fabrication Process

Upper	696.9 & 5.7	3.08	3,053.1	1.77
Middle	877.2 & 14.0	16.96	2,872.8	4.24
Lower	745.1 & 2.1	0.65	3,004.9	0.16

750 micron sensor spacing.

Photolithographic Electrode-Structure Fabrication Process

Upper	936.6 & 1.1	24.88	2,813.4	6.22
Middle	943.8 & 7.6	25.84	2,806.2	6.46
Lower	933.8 & 6.0	24.51	2,816.2	6.13

* Both the average spacing and the standard deviation are in microns.

with the middle sections to those of the end sections, it is observed that the photolithographic process formed more uniform electrodes.

The errors for the square-pad design structures were based on the average of the sensor spacings collected along the x- and y-axes. From these average sensor spacings, average electrode dimensions for the different types of square-pad structures were computed (Equation 5.1). The error data associated with these computations is summarized in Table 5.2.

The thermally evaporated electrode-structure fabrication process for the different types of square-pad structures produced electrodes closer to specifications compared to the photolithographic process. Table 5.2 revealed that this difference was marginal. The most noticeable difference between the structures formed by the two processes was the definition (sharpness) associated with the electrode corners. Figures 5.1 and 5.2 illustrate this difference. The corners of the thermally evaporated electrodes were rounder than the corners of the photolithographic-formed electrodes. The radii of the corners were measured with an optical microscope that was equipped with an optical micrometer. The radii of evaporation-formed corners spanned 8 to 16 microns, whereas, the radii of photolithographic-formed corners spanned 1 to 3 microns.

Table 5.2

Electrode Structure Dimension Error Data
for the Square-Pad Design Configurations

Sample Designator and Measured Location	Average Spacing and Standard Deviation (microns)*	Spacing Error (percent)	Average Electrode Width (microns)	Electrode Width Error (percent)
500 micron sensor spacing, Thermal Evaporation Electrode-Structure Fabrication Process				
X-Axis	546.1 & 12.4	9.22	2,953.9	1.54
Y-Axis	556.5 & 13.8	11.29	2,943.5	1.88
500 micron Sensor Spacing, Photolithographic Electrode-Structure Fabrication Process				
X-Axis	561.3 & 14.1	12.26	2,938.7	2.04
Y-Axis	572.0 & 14.2	14.40	2,928.0	2.40
750 micron sensor spacing, Thermal Evaporation Electrode-Structure Fabrication Process				
X-Axis	855.0 & 7.2	14.00	2,845.0	3.50
Y-Axis	851.0 & 9.7	13.47	2,849.0	3.37
750 micron sensor spacing, Photolithographic Electrode-Structure Fabrication Process				
X-Axis	900.6 & 10.4	20.08	2,849.4	5.02
Y-Axis	909.6 & 10.6	21.28	2,840.4	5.32

In addition to determining how close the electrode structure dimensions compared to specifications, the relative performance of the stripe electrode structures was examined. This examination involved measuring the impedance

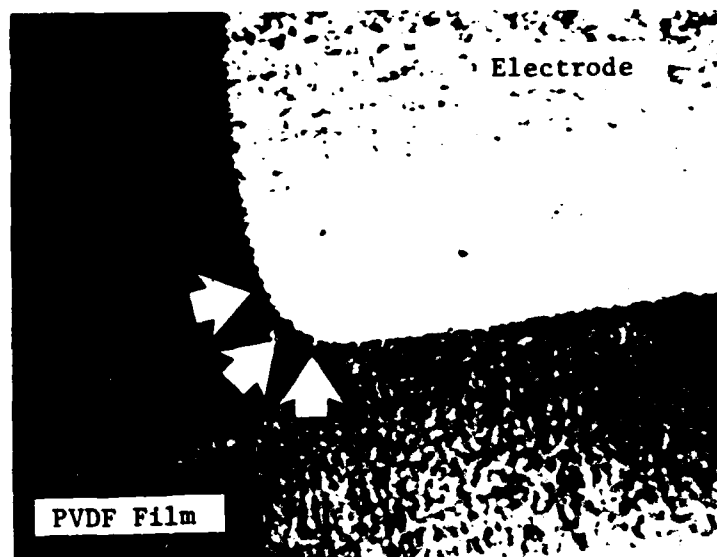


Figure 5.1. The Radii of Evaporation-Formed Corners Spanned 8 to 16 Microns.

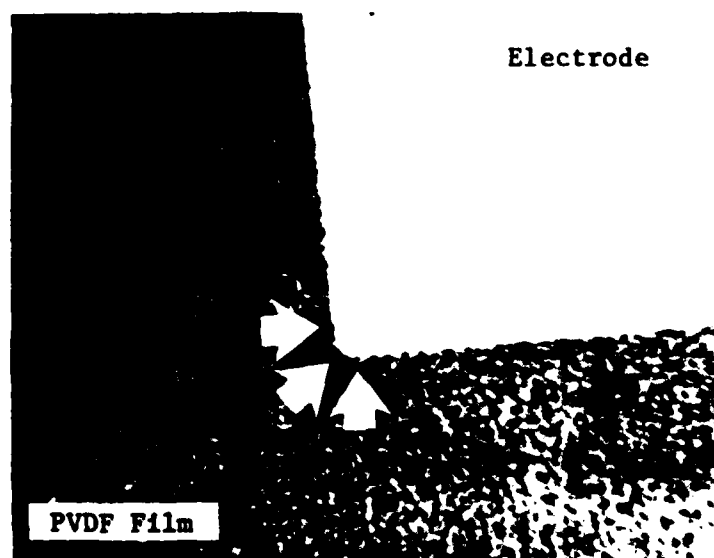


Figure 5.2. The Radii of Photolithographic-Formed Corners Spanned 1 to 3 Microns.

between the ends of the stripe electrodes. By measuring impedances, the relative effect of conductor resistance on the sensor's performance could be discerned. A small electrode resistance (4-20 ohms) had little or no effect on the sensor's performance. More importantly, electrodes displaying an open circuit were considered useless.

Table 4.4 summarized the impedance data that were collected for the different stripe design configurations. Configurations with a PPTSA number 8 or less were fabricated using the evaporation process and those with a PPTSA number 9 or greater were fabricated using the photolithographic process. Examination of this data revealed that photolithographic formed configurations had higher impedances than those formed using the other process, and were frequently plagued with open circuits. In addition to these problems, it was discovered (during the development of the piezoelectric activity measurement procedure) that these configurations had difficulty withstanding repeated loads. This reliability problem was attributed to the 400 angstrom thickness of the electrode structures. The thicknesses of the thermally evaporated configurations spanned 650 to 1,100 angstroms (Table 4.3). Another related cause is the non-uniformity of the aluminum film thickness covering the surface of the metallized PVDF film. The manufacturer used RF sputtering to form this film. A close examination revealed holes and scratches in the aluminum film. These

defects were attributed to the vendor's manufacturing and handling process. A scratch across an electrode frequently resulted in an open-circuit it. The impedance data revealed that usually one surface had a more significant problem with open circuits (caused by scratches) compared to the other surface (Table 4.4). These problems might not have been noticed had the electrode widths been larger.

Piezoelectric Activity Evaluation

This section contains an evaluation of the piezoelectric activity data that were collected for six PPTSA configurations (PPTSAs #2b, #4, #6, #8, #13, and #15). This evaluation was not restricted to the piezoelectric activity data. Observed side effects and the sensor designs were also included in the evaluation. Three distinct sections composed the evaluation. The first section pertained to examining the collected piezoelectric activity data. An analysis of the data was accomplished in the second section. The analyzed data was interpreted in the third section, and the four key questions that were posed in Chapter III were answered. These questions were:

1. Are the square-pad design configurations better than (or worse than) the stripe design configurations?
2. Is a thicker PVDF film better than a thinner film? (Better in this question refers to the piezoelectric activity and character of the PVDF film.)

3. Does one electrode-structure fabrication process adversely effect the PVDF film more than the other process?

4. How does thermal poling affect the PVDF film? Is the piezoelectric activity improved or degraded? Are there any side effects?

Examining the Collected Data. An examination of the collected piezoelectric activity data indicated the existence of transients in some of the data. The data interpretation process described in Chapter III was used to eliminate the effect of these transients. The situations encountered were organized into three categories:

1. System drift. System drift occurred when the system would drift from the steady state condition. The steady state condition was considered to have been achieved for periods during the measurement cycle when no planned activity (like a load being applied or removed) was occurring and the sensor response was essentially invariant. The absolute magnitude of the system's drift varied from measurement to measurement. Figure 5.3 shows measurements where system drift was (a) very detectable and (b) almost undetectable.

It was speculated that the high electrical impedances of the electrometer (2×10^{14} ohms) and the discrete sensor under test were the primary contributors of the system drift. The impedance of an unloaded sensor could not be measured on the electrometer. The electrometer had an upper resistance-measurement limit of 2×10^{11} ohms (Keithley

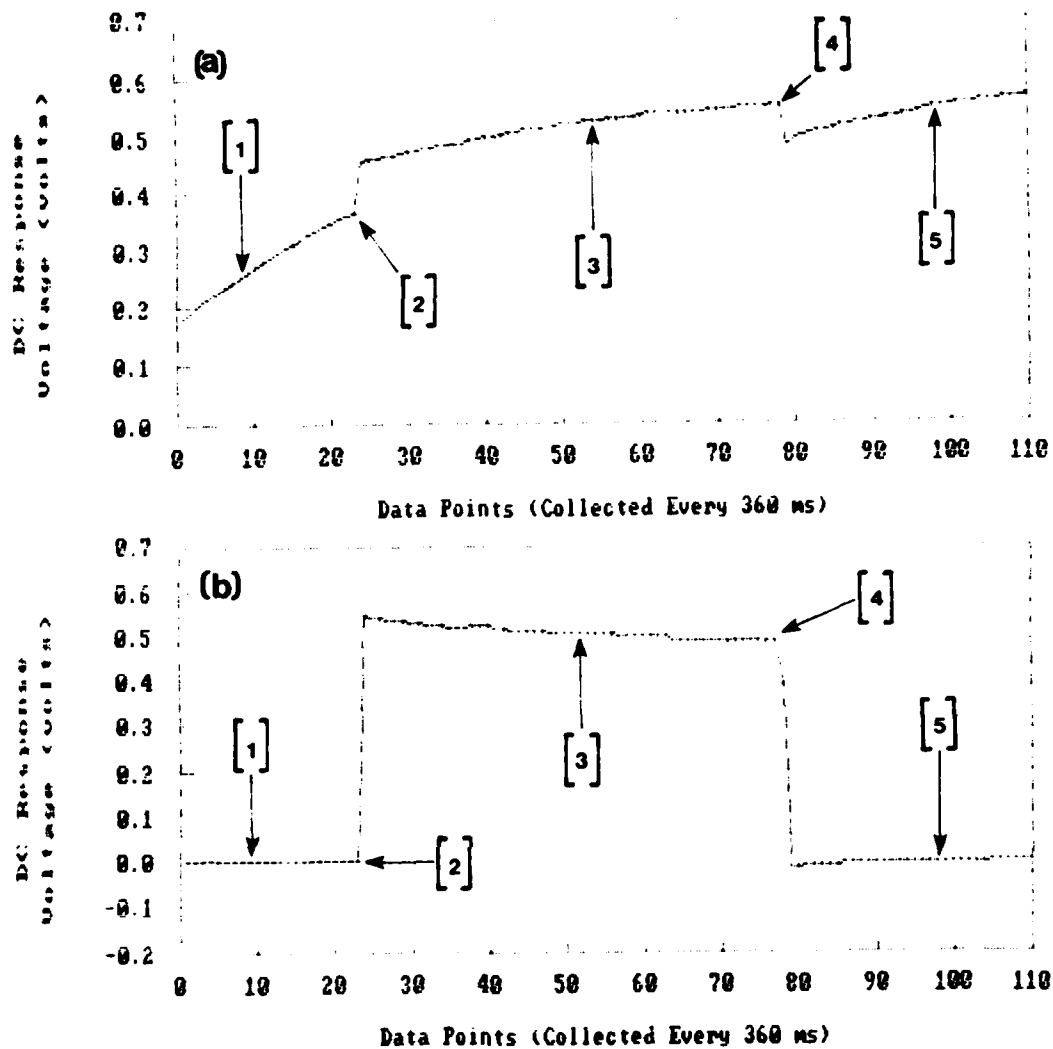


Figure 5.3. Examples of (a) Detectable and (b) Undetectable System Drift. (The vertical axis represents the sensor's DC response voltage. Key to measurement states: [1] Pre-load, [2] Load application, [3] Steady-state response, [4] Load removal, and [5] Post-load.)

Instruments, 1984b:65-66). It was concluded the impedance of the sensor was greater than the electrometer's upper limit. An unloaded sensor essentially looks like an open circuit to the electrometer. Because of this open-circuit

effect, the electrometer's input capacitance was charged because of random processes (for example, thermal noise). A charging capacitance would likely contribute to the drift. Keithley Instruments (the electrometer manufacturer) anticipated the influence of drift and installed a zero check and correct circuit (function) to minimize its effect. This function was exercised at the beginning of every measurement to reduce the amount of drift introduced into the data. Additional drift (not eliminated by the electrometer's zero functions) was removed in the data interpreting process. By taking the average of the data before and after an applied load and comparing this to a load response value, most of the drift was eliminated. It is conceded that this technique (described in Chapter III) only worked well when the drift was nearly constant during the span of a measurement cycle.

2. Charging and discharging parasitic capacitances. The charging and discharging of parasitic capacitances were evident in many of the measurements. These capacitances were associated with the leads, contacts, and coupling effects. Usually the effects of these capacitances were relatively small (0-0.1 volts) and caused an offset in the collected data. The only notable effect a parasitic capacitance (coupling) had in the measurements was detected in the data for the center sensor of the PPTSA #8 configuration. Figure 5.4 shows a graph of one of the

measurements for this configuration. The offset caused by this capacitor was on the order of 0.9 volts. It appears

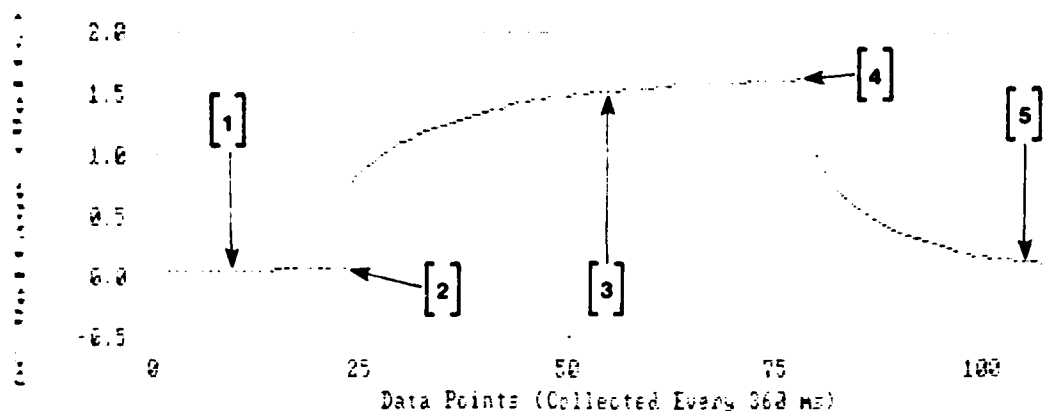


Figure 5.4. Example of the Adverse Effect a Parasitic Capacitance had on a Measurement. (PPTSA #8 configuration, center sensor. The vertical axis represents the sensor's DC response voltage. Key to measurement states: [1] Pre-load, [2] Load application, [3] Steady-state response, [4] Load removal, and [5] Post-load.)

that the silver epoxy and silver paint mixture used to connect the square electrode pad (on the surface of the PVDF film) to the copper conductor pattern did not function well. Figure 5.5 shows a schematic of the arrangement. The mixture was suppose to form a low impedance connection on the order of 1 ohm or less. From the graph in Figure 5.4, it appears the connection had a rather high impedance because of the high RC time constant (on the order of 5 seconds) that was observed. The parasitic capacitor depicted in Figure 5.5b was believed to be the result of the square electrode pads and the 20 mil-thick epoxy circuit board. The approximate capacitance formed (dielectric constant of the epoxy is assumed equal to 3) would be on the

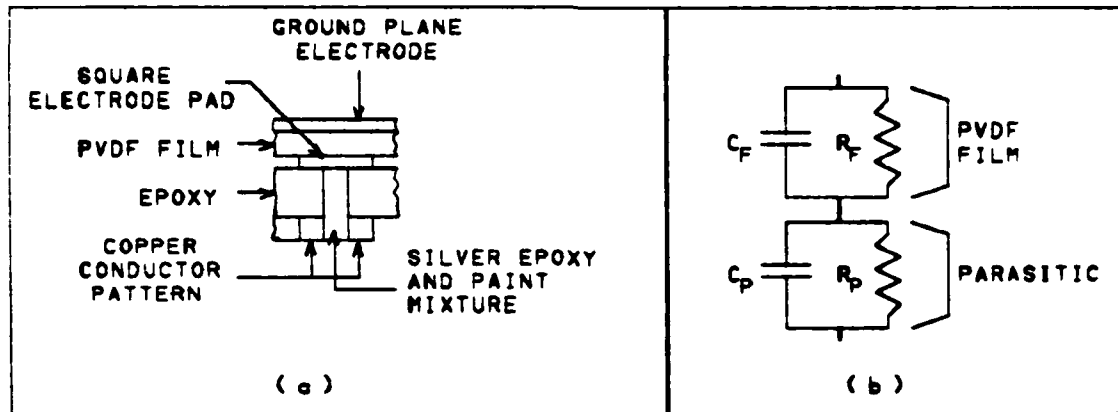


Figure 5.5. Schematic of the Center Sensor of the PPTSA #8 Configuration. (A (a) cross-sectional drawing and (b) circuit diagram of the center sensor.)

order of 0.5 picofarads ($C = \epsilon A/d$). If the capacitance was on the order of 0.5 picofarads and the time constant was estimated to be 5 seconds, then the impedance of the connection would be on the order of 10^{13} ohms.

3. Transients caused by the load machine. The load machine occasionally caused a dip, a spike, or a slight inflection in the piezoelectric activity data. If a dip occurred in a measurement, it usually spanned the data points from 10 to 30. Figures 5.6 illustrates an example of measurement cycle with a dip. Dips were evident in the center and corner sensor data for the unpoled PPTSA #2b and #4 configurations. Dips were also evident in the corner sensor data for the PPTSA #15 configuration. The voltage response for the lighter loads (100 and 200 grams) were often unresolvable due to the magnitude (0.1 to 0.3 volts) of these dips. The load machine's motor was attributed to

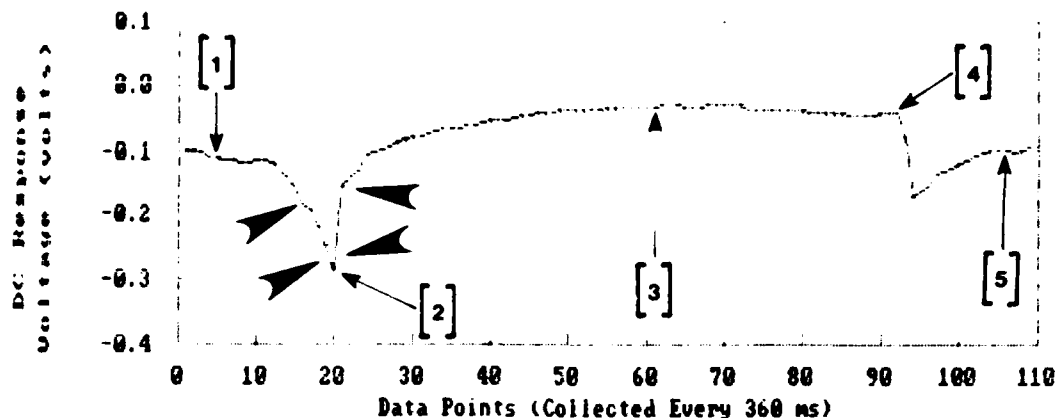


Figure 5.6. Example of a Measurement with a Dip. (The vertical axis represents the sensor's DC response voltage. Key to measurement states: [1] Pre-load, [2] Load application, [3] Steady-state response, [4] Load removal, and [5] Post-load.)

be the cause of these dips because it operated during the entire dip. Spikes occasionally occurred in the data and at a point when the load was either being applied or removed. Figure 5.7 shows the occurrence of spikes in two different measurements. The only configuration that escaped an occasional spike in its piezoelectric activity data was the PPTSA #8 configuration. Spikes were caused by the load pedestal being jerked upward abruptly, adding an additional force to the sensor. Both the dips and spikes were eliminated from the data that were used to determine a voltage response. A description of how these transients were eliminated can be found in Chapter III. A load machine relay changing states (twice) would occasionally cause two slight transients. The first change of state would increase the voltage and the second change of state would decrease the

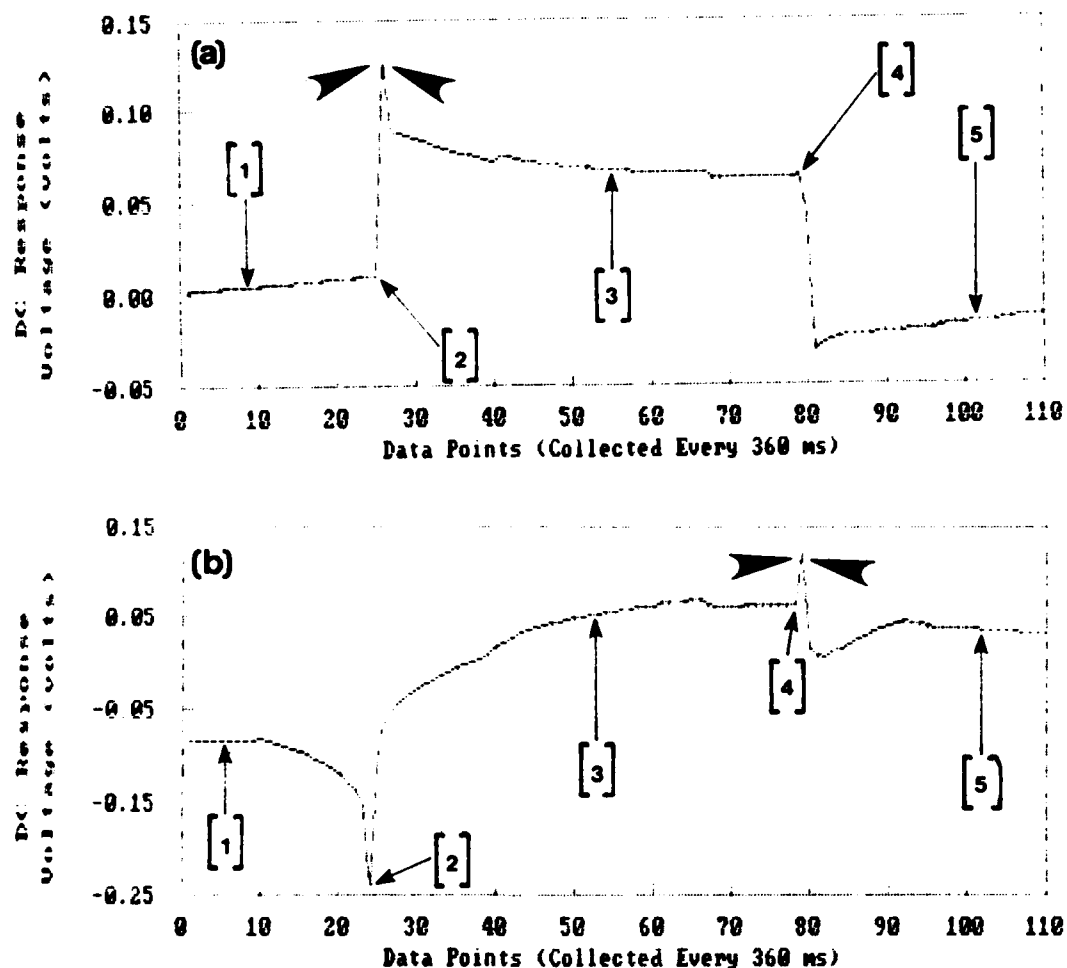


Figure 5.7. Examples of Spikes Occurring at (a) the Application of a Load and at (b) the Removal of a Load. (The vertical axis represents the sensor's DC response voltage. Key to measurement states: [1] Pre-load, [2] Load application, [3] Steady-state response, [4] Load removal, and [5] Post-load.)

voltage. These increases and decreases were less than 5 millivolts. These transients occurred while a load was applied to a sensor. Figure 5.8 shows the effects of these transients. Since these transients were small (less than 5 millivolts), they were ignored.

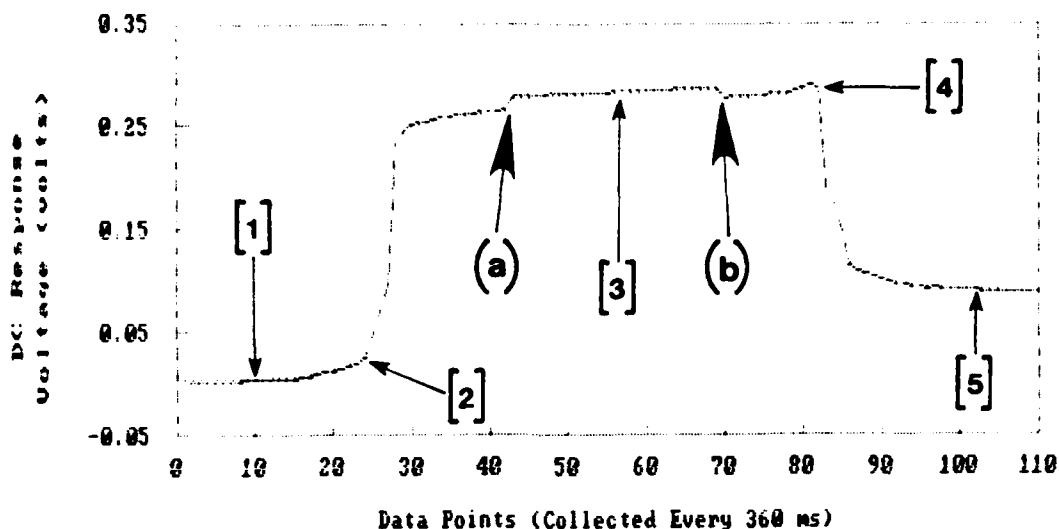


Figure 5.8. A Load Machine Relay changing States (Twice) Would Occasionally Cause Two Slight Transients. (a) The First Change of State Would Increase the Voltage and (b) the Second Change of State Would Decrease the Voltage. (The vertical axis represents the sensor's DC response voltage. Key to measurement states: [1] Pre-load, [2] Load application, [3] Steady-state response, [4] Load removal, and [5] Post-load.)

Data Analysis. The relative magnitude of the piezoelectric activity of the PVDF film within the six PPTSA configurations was measured. Table 3.2 listed these configurations. Two (PPTSA #2 and #13) of these six were measured twice. The purpose of repeating measurements with these two configurations was that these configurations were subsequently poled after being measured once.

The average and standard deviation for a set of discrete measurements of a load was computed and recorded in Tables 4.4 and 4.5. A center and corner discrete sensor for each of the six configurations were measured with six loads

(100, 200, 500, 700, 1000, and 1500 grams). A linear least squares curve fit was applied to the averages for each discrete sensor. A straight line can be represented by the equation

$$y = Mx + B \quad (5.2)$$

where M is the slope of the line and B is the y-axis intercept ($x = 0$). For these curves, the voltage responses were plotted on the y-axis and the various loads were plotted on the x-axis. In theory, piezoelectric activity is linear (van der Ziel, 1968:511). Thus, the slope (M) would be considered a proportionality constant between an applied pressure and an observed voltage response. It would also follow that the y-axis intercept (B) is a system offset. This system offset should equal zero because an applied pressure of zero should not produce a voltage response. The computed linear least squares curve fit coefficients for the various configurations were listed in Table 5.3. Figures 5.9 through 5.14 show the curves and averages for the different configurations graphed.

Interpreting the Data. An interpretation of the analyzed data provides several answers to the four questions that were posed in Chapter III, and again, at the beginning of this section. The first three of the questions pertained to comparing the design configurations (stripe and square pad), the PVDF film thicknesses, and the electrode-structure

Table 5.3

Linear Least Squares Curve Fit Coefficients
for the Measured Piezoelectric Activity Data

PPTSA Designator	Discrete Sensor Location	Slope (M) (mV/gram)	y-Axis Intercept (B) (mV)
2b	X4Y4	0.4979	-74.56
	X2Y6	0.5812	-36.68
2b/Poled	X4Y4	0.2632	5.36
	X2Y6	0.2939	39.02
4	X4Y4	0.7060	-75.03
	X2Y6	0.5702	-18.67
6	13	0.5164	69.96
	21	0.2092	67.17
8	13	0.4638	884.68
	21	0.5538	34.16
13	13	0.5677	18.83
	21	0.3506	26.51
13/Poled	13	0.2376	103.53
	21	0.2674	-0.59
15	13	0.3952	27.56
	21	0.5597	62.72

processes. The fourth question addressed the effects the thermal poling process had on the poled configurations.

Comparing the Design Configurations. The stripe and square-pad design configuration each possessed factors that made them desirable and undesirable. The stripe design

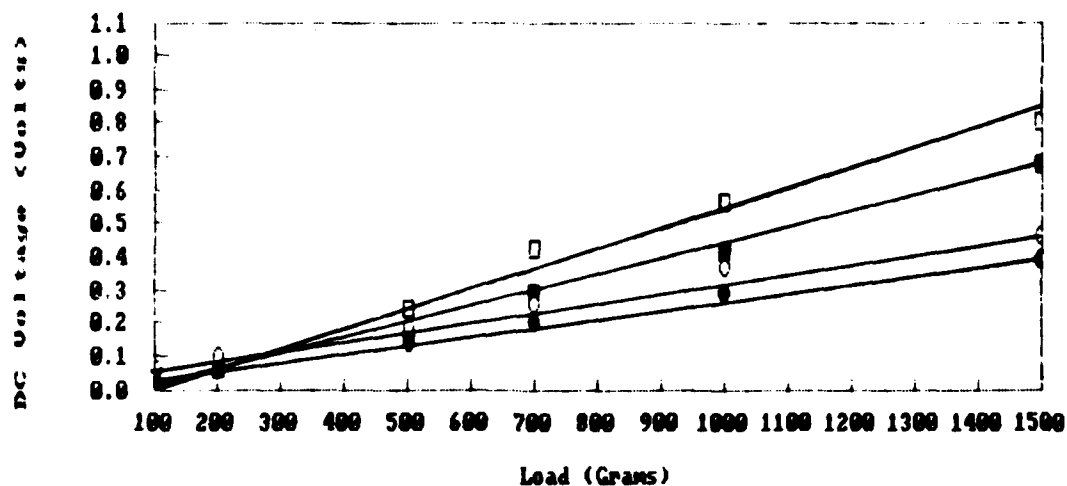


Figure 5.9. Linear Least Squares Curve Fit for the PPTSA #2 Configuration. (Unpoled: center - solid squares, corner - open squares; poled: center - solid ovals, corner - open ovals. The vertical axis represents the sensor's average DC response voltage.)

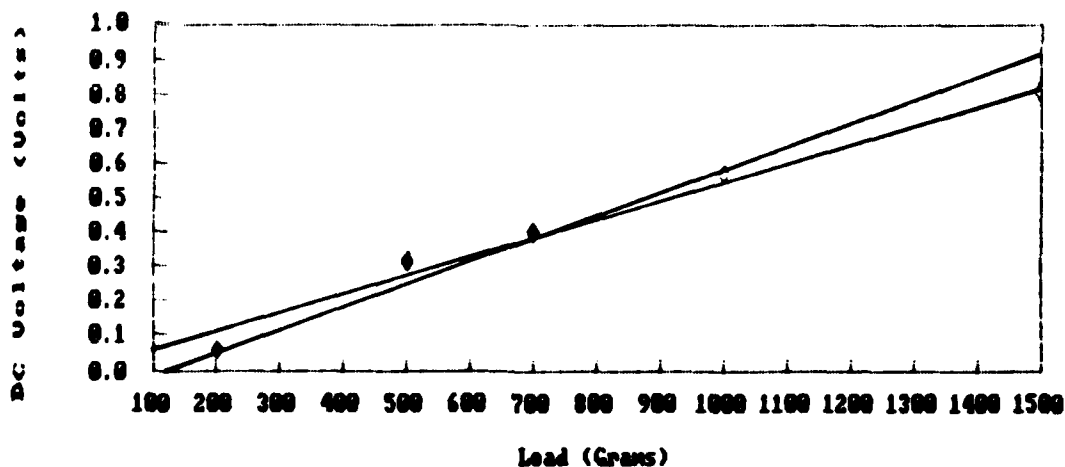


Figure 5.10. Linear Least Squares Curve Fit for the PPTSA #4 Configuration. (Center - solid diamonds, corner - open diamonds. The vertical axis represents the sensor's average DC response voltage.)

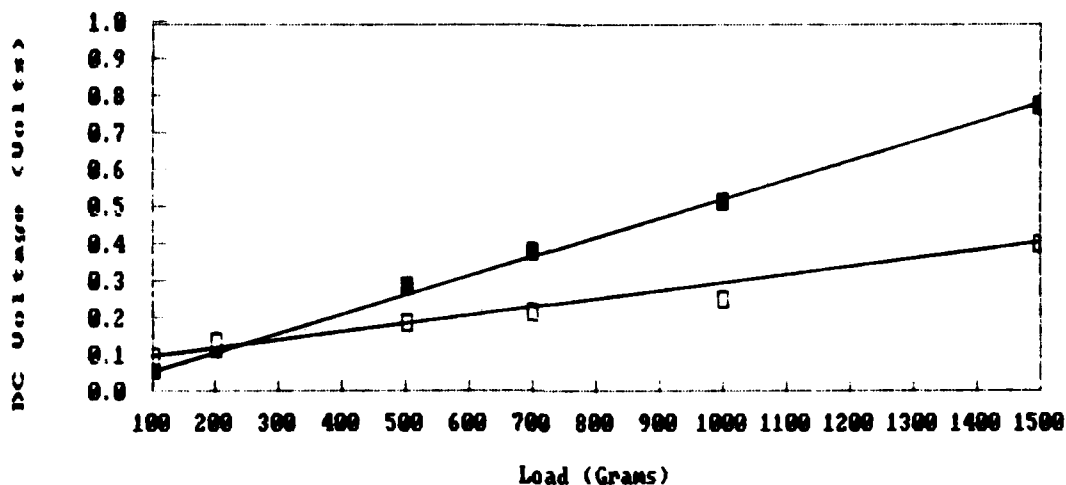


Figure 5.11. Linear Least Squares Curve Fit for the PPTSA #6 Configuration. (Center - solid squares, corner - open squares. The vertical axis represents the sensor's average DC response voltage.)

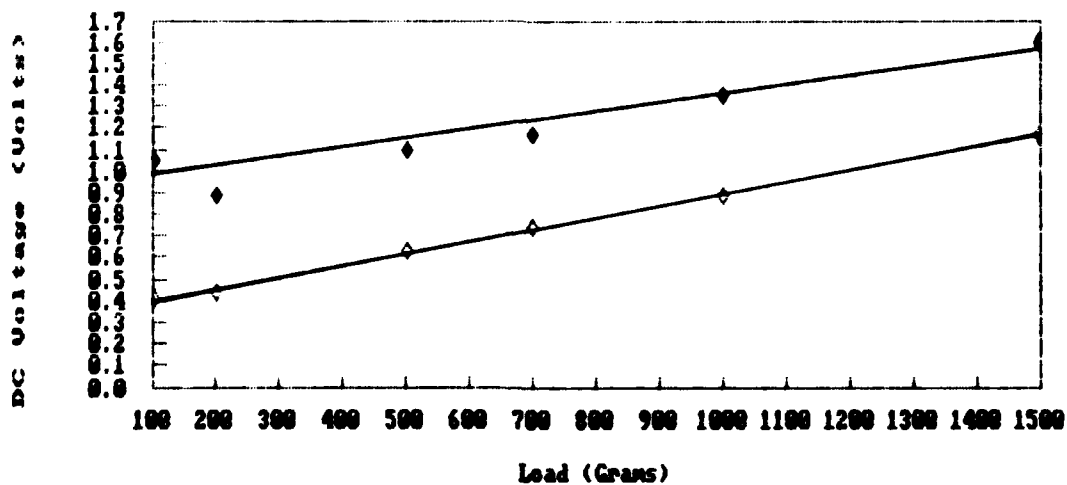


Figure 5.12. Linear Least Squares Curve Fit for the PPTSA #8 Configuration. (Center - solid diamonds, corner - open diamonds. The vertical axis represents the sensor's average DC response voltage.)

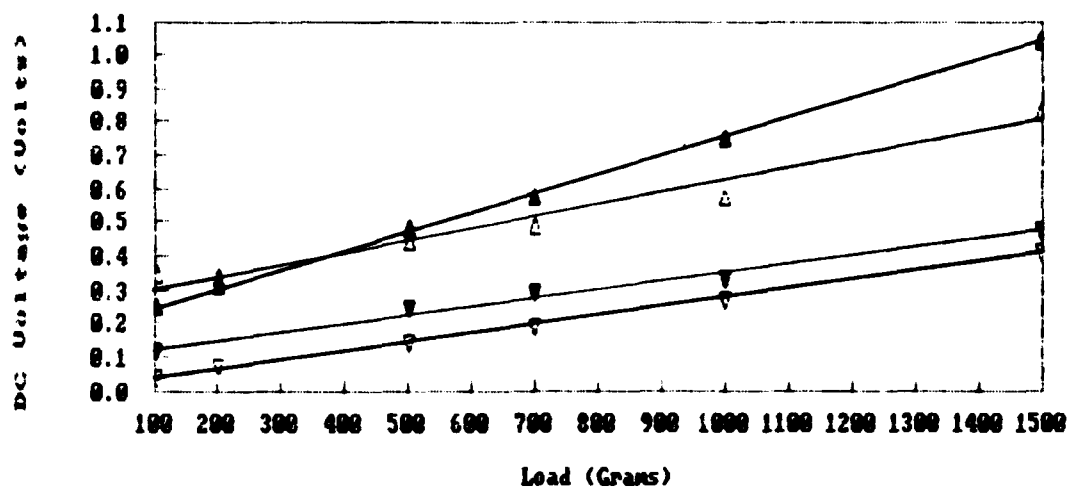


Figure 5.13. Linear Least Squares Curve Fit for the PPTSA #13 Configuration. (Unpoled: center - solid triangles, corner - open triangles; poled: center - solid inverted triangles, corner - open inverted triangles. The vertical axis represents the sensor's average DC response voltage.)

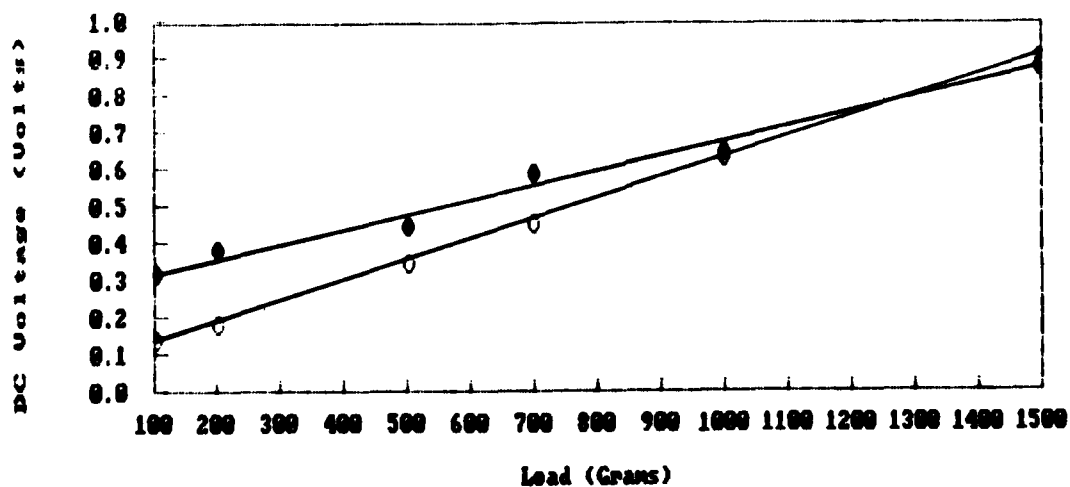


Figure 5.14. Linear Least Squares Curve Fit for the PPTSA #15 Configuration. (center - solid ovals, corner - open ovals. The vertical axis represents the sensor's average DC response voltage.)

configurations were easier to fabricate, but were also very susceptible to failure. A broken stripe electrode eliminated five sensors or 20 percent of the active sensors in a configuration. The interface that would be required to access the 5 x 5 matrix of 25 discrete sensors would be more complicated than that for the square-pad design. Locating the discrete sensors on a square-pad design configuration was slightly more work and had a fair margin of uncertainty. A permanent marker was used to draw the locations of the discrete sensors on the upper ground electrode. This drawing was not precise.

Comparing the PVDF Film Thicknesses. A comparison between the two PVDF film thicknesses (25 and 40 microns) revealed that the 40 micron film was better than the 25 micron film for two reasons. The first reason came as result of interpreting the linear least-squares curve fit coefficients in Table 5.3. By averaging the slopes for the 25 micron film (PPTSAs #2b, #6, and #13) and the 40 micron film (PPTSAs #4, 8, and 15), it was discovered that the 40 micron film produced a larger piezoelectric activity response for a given load. This result was expected, because in theory, a thicker film should produce a larger response. The second reason is subjective and based on observation of the films. It was observed that nearly 50 percent of the unmetallized 25 micron film was wrinkled, and thus, could not be used in any sensor processing. The

metallized 25 micron film had several wrinkled regions, but they were avoided. The 40 micron film did not have any wrinkles.

Comparing the Electrode-Structure Fabrication Processes. The two electrode-structure fabrication processes each had desirable characteristics. Neither of these processes appeared to adversely effect the piezoelectric activity of the PVDF film. The evaporation electrode-structure fabrication process produced electrodes closer to design specifications (lower errors in Tables 5.1 and 5.2). The photolithographic process produced more uniform stripe electrodes (Table 5.1) and sharper corners. Sturdier stripe electrodes were formed by the evaporation process. This was evident from the data in Table 4.4. The stripe electrodes formed using the photolithographic process were fragile and would fracture with repeated flexure. The only occurrence when an evaporated electrode broke (and became intermittently open circuited) was during the measurement of the PPTSA #4 configuration. The X4 stripe electrode broke while measuring the voltage responses for the 1000 grams load. Figure 5.15 shows the voltage response data as the electrode was failing. The electrode broke at the point where the micro-alligator clip was attached. Figure 5.16 shows a scanning electron microscope picture of the fracture.

Effects of Thermal Poling. From the linear least squares curve fit data in Table 5.3, it is obvious the

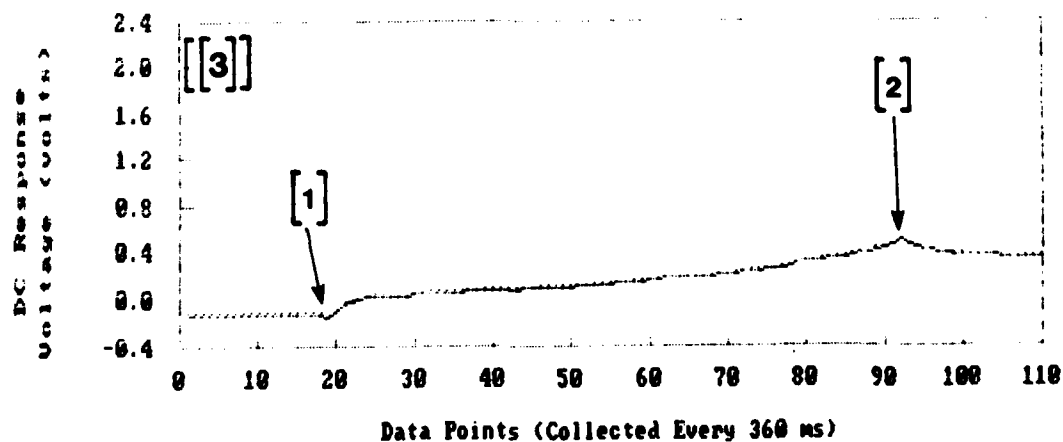
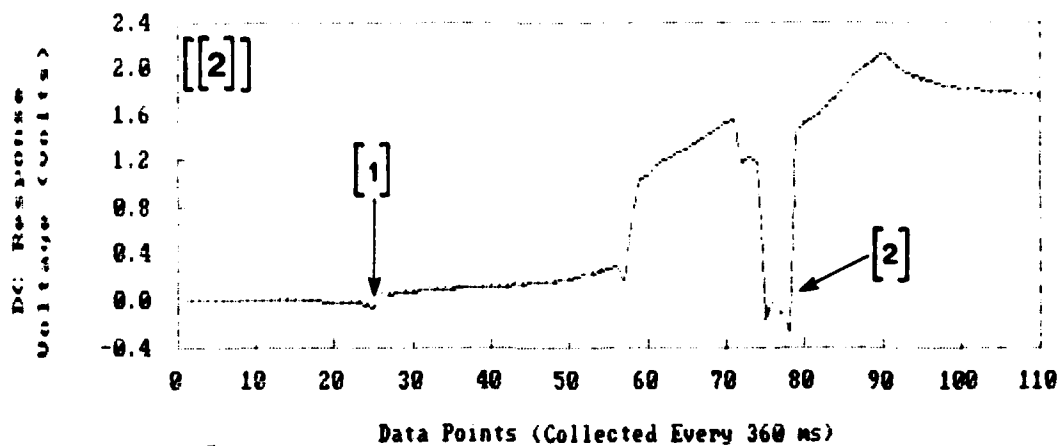
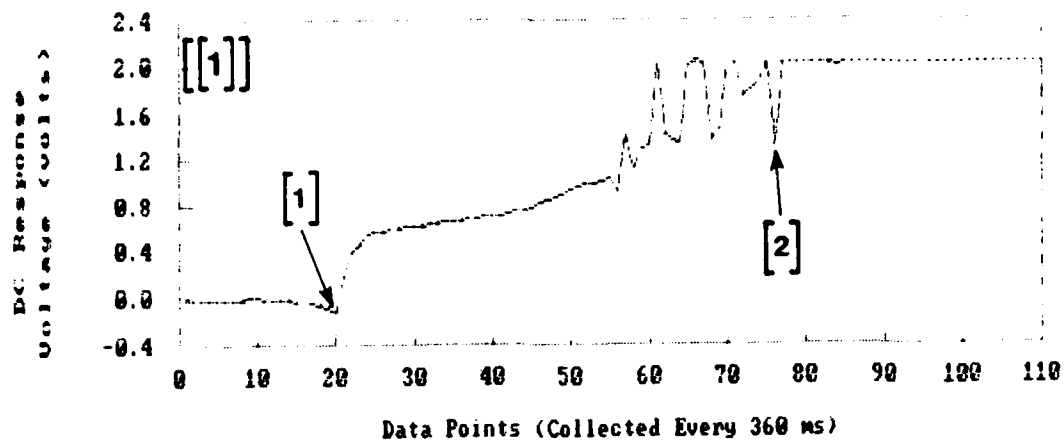


Figure 5.15. The Sequence of Three Measurements for the PPTSA #4 Configuration as the X4 Stripe Electrode was Fracturing. (The vertical axis represents the sensor's DC response voltage. Key to measurement states: [1] Load application and [2] Load removal.)

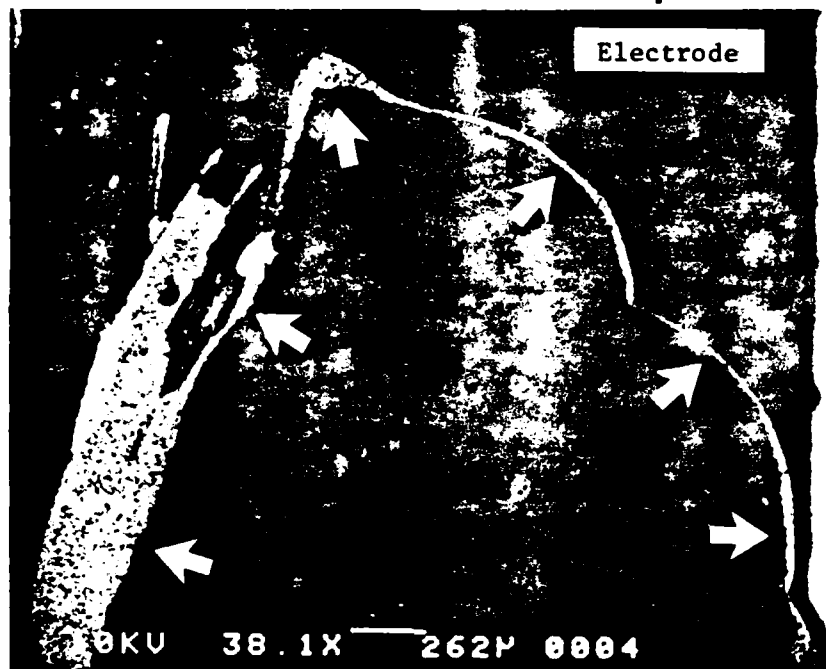


Figure 5.16. A Scanning Electron Microscope Picture of the Break in the X4 Stripe Electrode of the PPTSA #4 Configuration. (The charged region indicates the fracture.)

thermal poling process did not improve the piezoelectric activity for the PPTSA #2b and PPTSA #13 configurations. In fact, the piezoelectric activity for the configurations was degraded (on an average) by over 45 percent.

The thermal poling process exhibited several undesirable effects on the configurations. For both configurations, the poling process caused the unrestricted PVDF film to wrinkle. The unrestricted portion of the film

consisted of those regions not restricted by the BeCu spacer and the weight of the upper portion of the poling chamber. The film wrinkled because the 120°C thermal poling temperature relieved the stresses that were induced in the film during the vendor's mechanical stretching process. This process was described in Chapter II. Consequently, the piezoelectric activity of the restricted portion of the film could be degraded if the stresses within it were also partially relieved. In addition, the PVDF film turned a yellow color during this process. The yellow color was an indicator that the film had been heated. The most undesirable effect happened to the square-pad configuration (PPTSA #13). The electric field (1 MV/cm) burned a hole (approximately 1 millimeter in diameter) through the center of the number 11 discrete sensor. Figure 5.17 shows a scanning electron microscope picture of this hole. The hole was caused because the film was poled at the breakdown field (a statistical parameter) or because there was a flaw present in the PVDF film. Not only were the electrodes destroyed, but the silver epoxy and paint mixture was also destroyed.

Summary

The electrode-structure fabrication processes and the piezoelectric activity measurement data were evaluated in this chapter. The electrode fabrication process evaluation involved determining how precisely the fabricated electrode

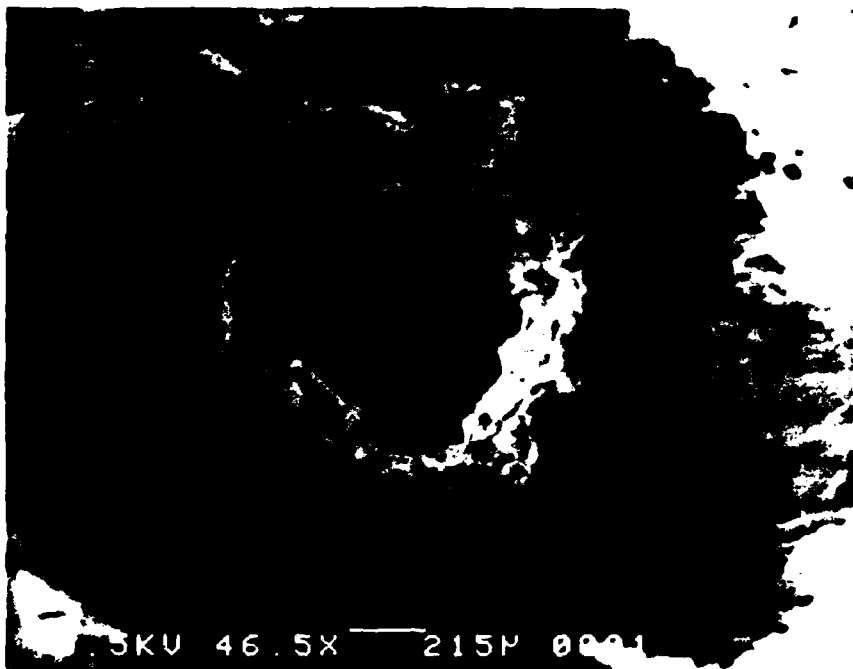


Figure 5.17. A Picture of the Burned Hole in the Number 11 Discrete Sensor of the #13 Configuration. (This hole was caused by the thermal poling process.)

structures compared to the design specifications, and determining the relative performance of the stripe electrodes. In addition, the piezoelectric activity data were examined, analyzed, and interpreted. Finally, the effects of the thermal poling process were discussed.

VI. Conclusions and Recommendations

Conclusions

This research effort resulted in the successful design and fabrication of 16 different piezoelectric polymer tactile sensor arrays (PPTSAs) for robotics. The study's evaluations did not unequivocally reveal that one configuration was better than the other. The evaluation did indicate that the square-pad design configurations were slightly better than the stripe design configurations because they did not have the problem of electrode fractures. It was also envisioned that interfacing the stripe design configurations would be a more complicated (and difficult) process. The stripe design configurations did have one significant advantage over the square-pad design; they are easier to fabricate.

The 40 micron thick PVDF film was determined to be the best of the PVDF film thicknesses. It was shown to possess a higher piezoelectric activity and more desirable characteristics than the 25 micron thick PVDF film. The higher piezoelectric activity was expected. The unmetallized 25 micron thick PVDF film had the undesirable characteristic of wrinkling. Fifty percent of this film was wrinkled and was not usable in the fabrication process.

The two electrode-structure fabrication processes (evaporation and photolithographic) were shown to have no adverse effects on the piezoelectric activity of the PVDF

film. The fragile stripe electrodes produced by the photolithographic process were the only notable deficiency. This deficiency was not attributed to the process. It was discovered that the aluminum film on the surfaces of the metallized PVDF film had too many processing flaws in it. These flaws made the stripe electrodes fragile.

From the linear least squares curve fit plots in Figures 5.9 to 5.13, it was apparent the DC response voltages for the different PPTSAs were very linear. This response linearity provides a pressure differentiating capability.

The load machine was attributed as the main cause of the unwanted transients (dips and spikes) that occurred in the piezoelectric activity measurement data. Although the effects of these transients were minimized, this load machine should be replaced in follow-on efforts.

It is concluded, that an alternative poling procedure be used in future studies because of the undesirable effects that were observed. It was obvious from the piezoelectric activity data (Tables 4.5 and 5.3) that the thermal poling process degraded the piezoelectric activity of the PVDF film in the two poled configurations (PPTSAs #2b and 13). The PVDF film turned yellow, and in some areas, it wrinkled. In the square-pad configuration that was poled, a hole was burned through a sensor.

In conclusion, this study did produce a set of four PPTSA configurations which performed significantly better than the others. These four configurations were of the square-pad design and used the 40 micron thick PVDF film. Both sensor element spacings (500 and 750 microns) and electrode fabrication processes (evaporation and photolithographic) were represented equally in the fabrication of this set.

Recommendations

It is recommended that follow-on studies continue this effort. The future efforts should remain focused on the goal of developing a PPTSA that will have the necessary resolution and pressure sensitivity capabilities for robotic tactile sensing. The following are specific recommendations for the future studies:

1. Redesign the piezoelectric activity evaluation procedure. A new measurement system should be designed to collect the data at intervals of 10 milliseconds or less. This would make the system more dynamic. All sources of electromagnetic interference should be eliminated. The load machine in the present study introduced too many errors and transients.

2. Using the photolithographic electrode-structure process, redesign a ground plane electrode structure for the

square-pad design that will allow easy location of the discrete sensors.

3. Perform a sensor crosstalk (mechanical coupling) evaluation. Sensor crosstalk occurs when a force applied to one sensor is detected by an adjacent unloaded sensor.

4. Design and construct a 26 channel data collection system for the square-pad design configurations.

5. Build a PPTSA pattern recognition system that would be capable of discerning simple shapes (squares, circles, and triangles).

6. Develop a PPTSA based on a large array of identical MOSFETs. This PPTSA design insitu couple would use the voltage responses from the PVDF film and result in the activation of the gates of the MOSFETs.

7. Either use an alternative poling process or redesign the thermal poling process that was used. Alternative poling processes (corona, plasma, current limiting, and high field) were discussed in Chapter II. The existing thermal poling process can be redesigned such that the temperature of the PVDF film can be changed quickly.

Appendix A

Procedure for Fabricating the High Resolution Plate Masks

The following procedure was used to fabricate the positive and negative High Resolution Plate (HRP) masks. The rubylith patterns used were cut at the Air Force Avionics Laboratory (Building 620). The photolithographic equipment used in this procedure was located in the AFIT Electronic and Materials Cooperative Laboratory (Building 125). The steps involved in this procedure were:

1. A rubylith pattern was made for each of the different electrode, conductor, and evaporation mask patterns. The rubylith pattern dimensions were 10 times (10x) larger than the final HRP mask dimensions. Each of the patterns (electrode, conductor, and evaporation mask) were first drawn on graph paper. From the graph paper, the pattern dimensions and features were transferred to a computer system that was used for cutting the rubylith patterns. The computerized transfer process was accomplished by Dave Via of the Air Force Avionics Laboratory (Building 620). After the rubylith patterns were cut, they were transported to the AFIT Electronic and Materials Cooperative Laboratory (Building 125).

2. To obtain the necessary 10x reduction, the mask generation camera (in the AFIT Electronic and Materials

Cooperative Laboratory, Building 125) was configured to the following specifications:

Equipment: 9-1/2" Goertz Lens
2" x 2" HRP holder
2-1/2" x 2-1/2" HRP holder (used only
for the conductor patterns)

Settings: Lens - f-11 stop
front camera box - 75.800"
rear camera box - 55.592"
HRP exposure - 150 seconds

3. A rubylith pattern was mounted on the copy board. The corners of the rubylith were taped with masking tape to ensure it was perfectly flat.

4. An unexposed HRP was loaded in the reduction camera plate holder. To accomplish this task, a red photolithographic light source was turned on, and all other light sources in the room were turned off before the HRP was loaded. A 2" x 2" Kodak HRP (Eastman Kodak Company, Rochester, New York 14650) was used for the electrode and evaporation masks; a 2-1/2" x 2-1/2" Kodak HRP was used for the conductor masks. The emulsion surface of the HRP was positioned in the plate holder so that it would face the rubylith pattern that was positioned on the copy board. The plate holder was then loaded into the reduction camera.

5. The HRP was exposed for 150 seconds. This step required first turning on the copy board's green light source and turning off all the unwanted light sources. The HRP was then exposed.

6. The exposed HRP was developed in the darkroom. The HRP was transferred to the dark room in the plate holder. The dark room's red photolithographic light source was turned on, and the remaining lights in the darkroom were turned off. The HRP was then removed from the plate holder and placed in a holder designed for developing HRP's. The following process was used to develop the HRP:

a. The HRP was placed in a Kodak D-8 Developer solution (mixed in a 1:4 ratio with deionized water) for 5 minutes. Regulating the developer's temperature at 70°C produced the best results.

b. The HRP was placed in a Kodak SB-5 Stop Bath (room temperature) for 30 seconds.

c. The HRP was dipped in a KODAK F-5 fixing bath (room temperature) for one minute.

d. The HRP was rinsed in deionized water for 5 minutes.

e. The HRP was immersed in a mixture of methanol and deionized water (a 1:1 ratio) for 30 seconds.

f. The HRP was dried with compressed nitrogen gas.

7. The HRP was inspected for defects under a light microscope. The exposed pattern was checked for opaqueness, distinct edges, and pin holes. If defects became apparent in the inspection, the HRP was discarded and the process was repeated, starting with Step 4. The HRP was used for an HRP mask if it was free of defects.

A procedure was developed for fabricating negative (or reverse image) HRP masks from the previous procedure's HRP masks. An HRP copying machine (located in Building 125) replaced the previous procedures' reduction camera arrangement. The previous procedure's HRP masks are referred to in this procedure as HRP masters. The procedure's steps were:

1. The negative HRP's were exposed in the HRP copying machine. The process started with turning on the copy machine and positioning the HRP master to be copied in the master position. The emulsion surface of the HRP master faced outward. The master vacuum button was pressed to secure the master. The machine was set for an exposure time of 4 seconds. A red photolithographic light source was turned on and the other light sources in the room were turned off. The HRP master was copied using an unexposed HRP. To make a copy, the emulsion surfaces of the unexposed HRP and the HRP master were placed in contact with each other. The unexposed HRP was positioned in the holder on the door of the HRP copy machine. The HRP was centered before the copy vacuum button was pressed to secure the HRP. The emulsion surfaces of the HRP's came into contact when the copy machine's door was closed and latched. The vacuum levels on all of the gauges (master, copy, and system) came up to 25 psi. The expose cycle button was pressed. The door's latch was released at the end of the cycle. The exposed HRP was transported to the darkroom in an HRP box.

2. With one exception, the exposed HRP was developed and inspected using the same steps (Steps 6 and 7) in the previous procedure. The one exception was the time the HRP was left in the developer. This time was changed to 30 seconds. The negative HRP mask was finished after developing and inspecting.

Appendix B

Procedure for Fabricating Evaporation Masks

This procedure was used for fabricating the evaporation masks that were used in the thermal evaporation process. The masks were made from 5 mil (127 micron) thick beryllium copper (BeCu) stock. The procedure is basically a photolithographic and etching process. The photolithography component used dry film equipment that was located in the Electronic Section (Building 5) of the 4950th Test Wing's R&D Aircraft Fabrication - Modification Center. The BeCu was etched with ferric chloride in the AFIT Electronic and Materials Cooperative Laboratory (Building 125). The steps for fabricating the evaporation masks were:

1. The BeCu stock was cut into 2-1/4" x 2-1/4" pieces. NGK Metals Corporation (21412 Protecta Drive, Elkhart IN 46516) manufactures the BeCu, and their trade name for it is Berylco. They identified the Berylco as a 25 alloy and a XHM temper.

2. The pieces of BeCu were polished and cleaned before they were laminated with a dry film resist. Both surfaces of the BeCu pieces were polished on a slurry table (Building 125). The BeCu pieces were cleaned in a 1:10 mixture of sodium hydroxide and deionized water for one minute and then rinsed in deionized water for a several minutes. Compressed nitrogen gas was used to dry the BeCu. After cleaning the

pieces, they were placed in a clean container and taken to the Electronic Section of the 4950th Test Wing's R&D Aircraft Fabrication - Modification Center (Building 5). It was in Building 5 where the BeCu stock was laminated with the dry film resist.

3. Both surfaces of the clean BeCu pieces were laminated with dry film resist. Mr. William Kingery, a test wing technician, supervised the lamination process. The dry film resist used was DuPont Electronics Division's Riston 218R Photopolymer film resist (Photosystems and Electronic Products Department, Riston Products Division, Wilmington, DE 19898). The rollers of the HRL-24 Laminator (DuPont Electronics Division) were set to a laminating temperature of 100°C and to a laminating speed of 4 fpm. Both surfaces of the BeCu pieces were laminated simultaneously with the dry film resist.

4. The different PPTSA electrode designs were patterned in the dry film resist using a Colight ultraviolet light table (Model DMVL-1030, 820 Decature Avenue North, Minneapolis, MN 55427) and a spray developer. The laminated BeCu pieces were placed on the lower tray of the light table. A High Resolution Plate (HRP) electrode mask was centered on top of each of the BeCu pieces. The emulsion surface of the HRP mask was put in contact with the dry film resist. Both surfaces of the laminated dry film resist were exposed simultaneously to an ultraviolet light source. The

dry film on the unmasked surface became hard (the dry film resist was a negative resist) and provided a protective coating for the chemical etching process. The dry film was developed in the spray developer. The developer sprayed Riston Developer 2000 (DuPont) for 1-1/2 minutes. After the dry film was developed, it was rinsed with deionized water and dried with compressed air.

5. The dry-film pattern was checked under an optical microscope. It was inspected for opaqueness, distinct edges, and pin-hole type defects. If the pattern had defects, the dry film was removed with Stripper S-1100X (DuPont) and the process was started again at Step 2.

6. The unwanted BeCu was chemically etched in ferric chloride. The etching process took approximately 170 minutes to complete.

7. The dry film was removed with either Riston stripper (DuPont) or a heated (100°C) 1:10 mixture of sodium hydroxide and deionized water.

8. The etched BeCu patterns were inspected for defects under an optical microscope. The inspection involved looking for straight edges and pin-hole type defects in the BeCu. The BeCu was discarded if it had defects that were unrepairable. Pin holes were filled with epoxy. The fabrication process was repeated for the BeCu pieces that had repairable defects. The evaporation masks were finished at the end of this step.

Appendix C

Procedure for Evaporating Aluminum Electrode Structures on the Unmetallized PVDF Film

This procedure was used for evaporating the aluminum electrode structures on the unmetallized polyvinylidene fluoride (PVDF) film. One thousand angstrom thick aluminum electrode patterns were evaporated on the PVDF film using a vacuum deposition system and evaporation masks. The evaporation masks used in this procedure were fabricated using the procedure discussed in Appendix C. The vacuum deposition system was located in AFIT Electronic and Materials Cooperative Laboratory (Building 125). The steps for fabricating the electrode structures on the unmetallized PVDF film were:

1. The unmetallized PVDF film was cut into 45 mm x 45 mm pieces and then cleaned. The film was cleaned in a 1:20 mixture of sulfuric acid and deionized water for 2 minutes and then rinsed in deionized water for another 2 minutes.
2. The PVDF film was sandwiched between the evaporation mask and a 50 mm x 50 mm piece of a 1.2 mm thick glass plate with small office binder clips. Figure C.1 shows a schematic of this arrangement. The evaporation mask was centered on the PVDF.
3. The vacuum deposition system was prepared with an eight-turn-coil, tungsten wire filament. The filament was

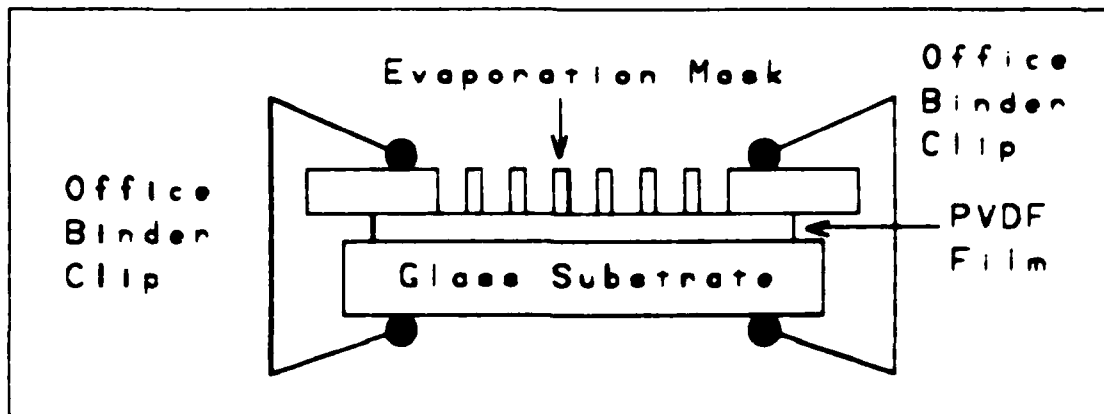


Figure C.1. Schematic of the Evaporation Mask, PVDF Film, and Glass Plate Sandwich.

loaded with aluminum wire that was to be deposited. The coil filaments were selected because they produce the least amount of heat in a deposition cycle.

4. One thousand angstroms of aluminum was evaporated on the PVDF film using a vacuum deposition system. The sandwich (consisting of the evaporation mask, PVDF film and glass plate) was positioned in the vacuum deposition chamber coplanar with the PVDF film arrangement. A reference glass slide with an evaporation mask was also placed in the chamber. The reference glass slide was used to determine the thickness of the evaporated aluminum. To reduce the potential of heating the PVDF film, the sandwich was positioned as far away from the aluminum source as possible. A 20' separation was obtained with the equipment in Building 125.

5. The evaporated aluminum on the PVDF film was inspected under an optical microscope. Coverage at the edges was checked. If some of the edges were not covered,

the sandwich was reassembled and additional aluminum was evaporated to cover the edges sufficiently. To verify the thickness of the deposited aluminum, the reference glass slide was used in conjunction with the Dektak stylus profilometer to determine the actual evaporated aluminum's thickness.

For Phase I type PPTSAs (stripe design), the following procedure was implemented:

6. The sandwich was disassembled, the PVDF film was flipped over, the evaporation mask was turned 90 degrees, aligned, and sandwiched as before (Step 2).

7 Steps 3, 4 and 5 were repeated. The PVDF film pieces were ready for final stripe PPTSA assembly after this step

For Phase II type PPTSAs (square-pad design), the following procedure was implemented:

6. The sandwich was disassembled and the PVDF film was flipped over. Square pad PPTSAs used a pair of evaporation masks for the two different electrode structures. The pair consisted of an evaporation mask for the common ground plane and one for the square pads. The evaporation mask not used in Step 4 was reassembled in the sandwich (Step 2). This evaporation mask was aligned with the existing evaporated

aluminum electrode pattern on the other surface of the PVDF film.

7. Steps 3, 4 and 5 were repeated. The PVDF film pieces were ready for final square-pad PPTSA assembly.

Appendix D

Procedure for Etching the Electrode Structures from the Commercially Metallized PVDF Film

This procedure was implemented for patterning the electrode structures from the commercially metallized PVDF film. A four hundred angstrom thick film of aluminum was deposited on both surfaces of the PVDF film by the manufacturer. This aluminum film was converted to electrode structures using a photolithographic and etching process. The photolithography process used the same dry film equipment and chemicals discussed in Appendix B. Certain steps in the photolithography process were identical or similar to those in Appendix B. A one half-percent solution of hydrofluoric acid was used in the etching process to etch the aluminum film. The key steps were:

1. The metallized PVDF film was cleaned with freon. The freon used was MS-180 Freon TF Solvent manufactured by the Miller-Stephenson Chemical Company (George Washington Highway, Danbury, Connecticut 06810).

2. Both surfaces of the cleaned PVDF film were laminated with dry film resist. The roller temperatures were set to 100°C and the laminating speed was set to 4 fpm on the HRL-24 Laminator. Since the PVDF film was very thin in comparison to a PC board, only one surface of the PVDF film could be laminated during a given cycle. The PVDF film was

placed on a clean PC board and fed through the laminator. The PC board provided the needed thickness. The laminated PVDF film was removed from the PC board with a razor knife. The other surface was laminated using the same method.

3. The dry film was developed and inspected using Steps 4 and 5 in Appendix B.

4. The unwanted aluminum film was removed with a 1:500 mixture of hydrofluoric acid and deionized water. A 1/4' x 1/4' piece of the dry film was removed from both surfaces of one corner. Removing the dry film pieces helped determine if the etching process was complete. The film at this corner became transparent when the etching process was finished. The etching process took 3-1/2 to 4 minutes. The PVDF film was rinsed with deionized water.

5. The dry film resist was removed from the PVDF film with Riston S-1100X stripper. Afterwards, the PVDF film was rinsed in deionized water for one minute. Compressed nitrogen was used to dry the PVDF film.

6. The electrode structures on the PVDF film were inspected under an optical microscope. The inspection involved checking for distinct edges, pin holes, and other defects that would render the electrode structures useless. If the electrode structure had these defects in the critical areas (active sensor regions), the above process was repeated with a fresh piece of PVDF film. Specimens passing

this inspection had one surface of the PVDF film with a functional electrode structure.

7. The aluminum film on the other surface of the PVDF film was patterned by repeating the above steps. Extra care was taken in Step 4 because the second pattern needed to be aligned with the first. Since it was difficult to see through 1,000 angstroms of aluminum and two layers of dry film, the second surface was first laminated with dry film and then patterned using the light table. The ground plane for the square pad design was configured larger than the square pad array to accommodate alignment errors. Pin holes were intentionally incorporated in the alignment marks in the stripe pattern pieces. The pin holes facilitated aligning the second stripe pattern. It was important to remember when aligning the second stripe pattern to make sure it was rotated 90 degrees with respect to the other pattern. The PVDF film pieces were ready for final PPTSA assembly after this step.

Appendix E

Procedure for Final Assembly of a Stripe Design Piezoelectric Polymer Tactile Sensor Array

The following procedure was used to realize the stripe design piezoelectric polymer tactile sensor arrays (PPTSAs). The final assembly of the stripe PPTSAs involved attaching leads to the ends of the electrode stripes and temporarily mounting the patterned PVDF film on a copper-free printed circuit (PC) board substrate. This procedure was accomplished in the AFIT Electronic and Materials Cooperative Laboratory (Building 125). The critical steps were:

1. A single lead was attached to each end of the electrode stripes (a total of 28 leads were attached). To facilitate this process, 1/4" copper foil tape was cut into 28, 1' x 1/16" strips. It was experimentally determined that 3M's #1181 copper foil tape (3M Center, St. Paul, MN 55144) with conductive acrylic pressure-sensitive adhesive was useful for accomplishing this step. As shown in Figure E.1, each of these strips were centered and positioned 1/4" in from the end of an electrode.

2. The patterned PVDF film was temporarily mounted on a 1' x 1' x 20 mil thick, copper-free printed circuit board substrate with spray adhesive (Catalog number 648, M. Grumbacher, Inc., 460 West 34th., New York, NY 10001). This mounting procedure prevented the PVDF film from moving

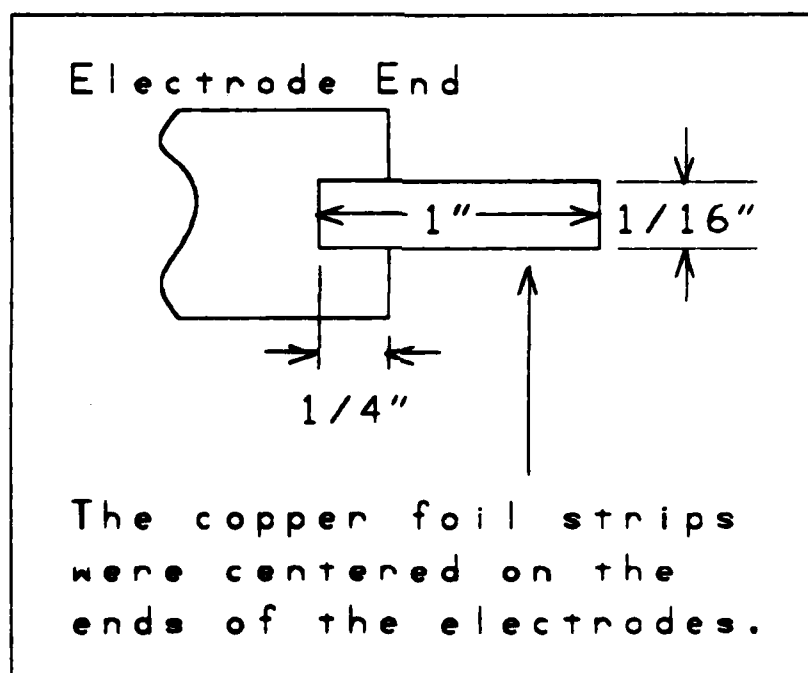


Figure E.1. Mounting the Copper Foil Tape to the Electrode Stripes.

during testing. A temporary mount was used because the patterned PVDF film needed to be removable for a subsequent poling process. Only the mounting surface of the PC board substrate was coated with spray adhesive. The spray adhesive was allowed to dry for 5 minutes before the bond was made. This completed the fabrication of a stripe design PPTSA.

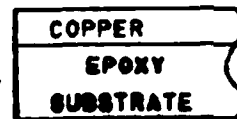
Appendix F

Procedure for Final Assembly of a Square-Pad Design Piezoelectric Polymer Tactile Sensor Array

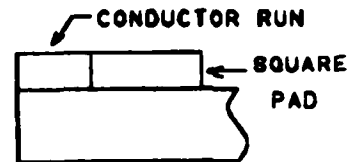
The following procedure was used to assemble the square-pad design PPTSAs. In this procedure, the electrode patterned PVDF film was mounted on a printed circuit (PC) board which contained a copper conductor pattern for accessing the square pads on the PVDF film. The copper conductor pattern was etched on the opposite side of the PC board so that the square pads could be accessed through 0.04" holes that were filled with conductive epoxy. This procedure was accomplished with the same equipment and facilities discussed in Appendix C. Figure F.1 depicts the process used to accomplish this procedure.

1. A photolithographic process was used to produce the conductor patterns on 2-1/2" x 2-1/2", single-sided copper, 20 mil thick PC boards. This process was similar to those discussed in Appendix B and D. The PC boards were cleaned before they were laminated with dry film. The cleaning process involved buffing the copper with a wetted-sheet of 600-grit emery paper. After buffing, the PC boards were rinsed with deionized water and dried with compressed air. The dry film resist was processed using the procedures described in Appendix B. The copper was etched with ferric chloride. The etcher in Building 5 was able to etch the

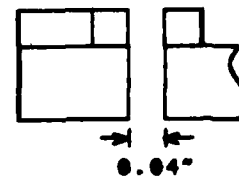
START WITH A SINGLE-SIDED
COPPER PRINTED CIRCUIT BOARD.



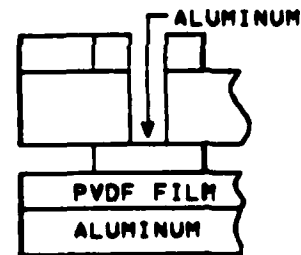
PATTERN THE COPPER LAYER
WITH A CONDUCTOR PATTERN.



DRILL A 0.04" HOLE FOR
EACH SQUARE PAD.



CLAMP THE PATTERNED PVDF
FILM TO THE BOTTOM OF
THE PRINTED CIRCUIT BOARD.



FILL THE HOLE WITH
CONDUCTIVE EPOXY.

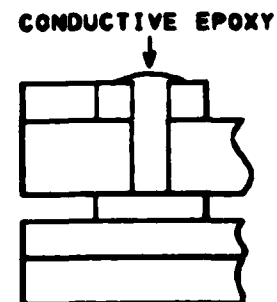


Figure F.1. A Process for Final Assembly of a Square-Pad
Design Piezoelectric Polymer Tactile Sensor
Array.

copper in 3.5 minutes. The conductor pattern was inspected under an optical microscope for line definition and pin-holes. If the conductor pattern was determined unuseable, the PC board was discarded and the process was started over again.

2. Each of the square electrode pads (in the conductor pattern) had a 0.040" hole drilled through the center. The holes were drilled from the bare epoxy side.

3. The electrode patterned PVDF film was sandwiched between a PC board and a 2-1/2" x 2-1/2" piece of glass with office binder clips.

4. The holes (facing upward) were filled with conductive epoxy. A 3-cc syringe and needle were used to inject the epoxy into the holes. The syringe (#5585) and needle (#5176) were from the Luer Lok series manufactured by Becton Dickinson & Company (Rutherford, NJ 07070). The conductive epoxy used was E-Solder 3021 from Acme (Div. of Allied Products Corporation; New Haven, CT 06505).

5. The edges of the PVDF film were glued to the PC board with non-conductive epoxy.

The square pad design PPTSA was finished at the end of this procedure.

Appendix G

Photocopies of the High Resolution Plate and Evaporation Masks

This appendix illustrates photocopies of the High Resolution Plate (HRP) and evaporation masks that were fabricated in this study. The photocopies of the HRP and the evaporation masks for the stripe design PPTSAs are shown in Figures G.1 and G.2. The square-pad design PPTSAs' HRP and evaporation masks are shown in Figures G.3 through G.6.

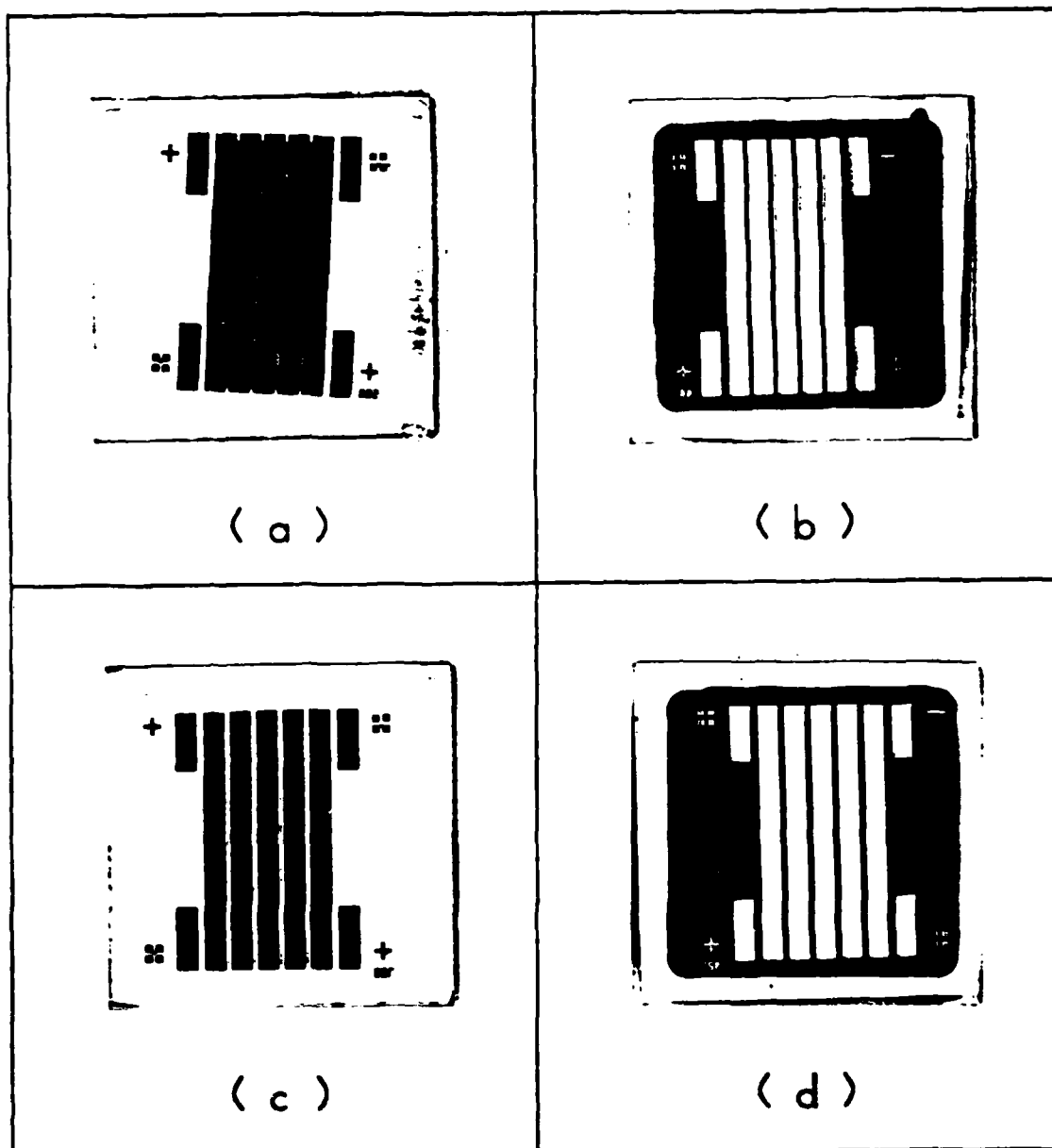


Figure G.1. Photocopies of the Stripe Design PPTSA High Resolution Plate Masks. (The positive and negative HRP masks for the stripe design PPTSAs that have an inner electrode spacing of 500 microns are shown in (a) and (b), respectively. The positive and negative HRP masks for the stripe design PPTSAs that have an inner electrode spacing of 750 microns are shown in (c) and (d), respectively.)

NO-A188 852

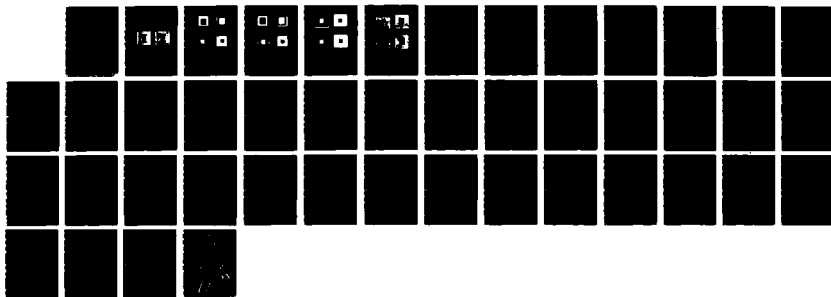
PIEZOELECTRIC POLYMER TACTILE SENSOR ARRAYS FOR
ROBOTICS(U) AIR FORCE INST OF TECH WRIGHT-PATTERSON AFB
OH SCHOOL OF ENGINEERING D G PIROLO DEC 87

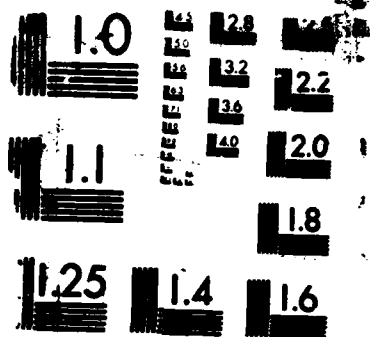
1/3

UNCLASSIFIED

F/G 17/11

ML





MICROCOPY RESOLUTION TEST CHART

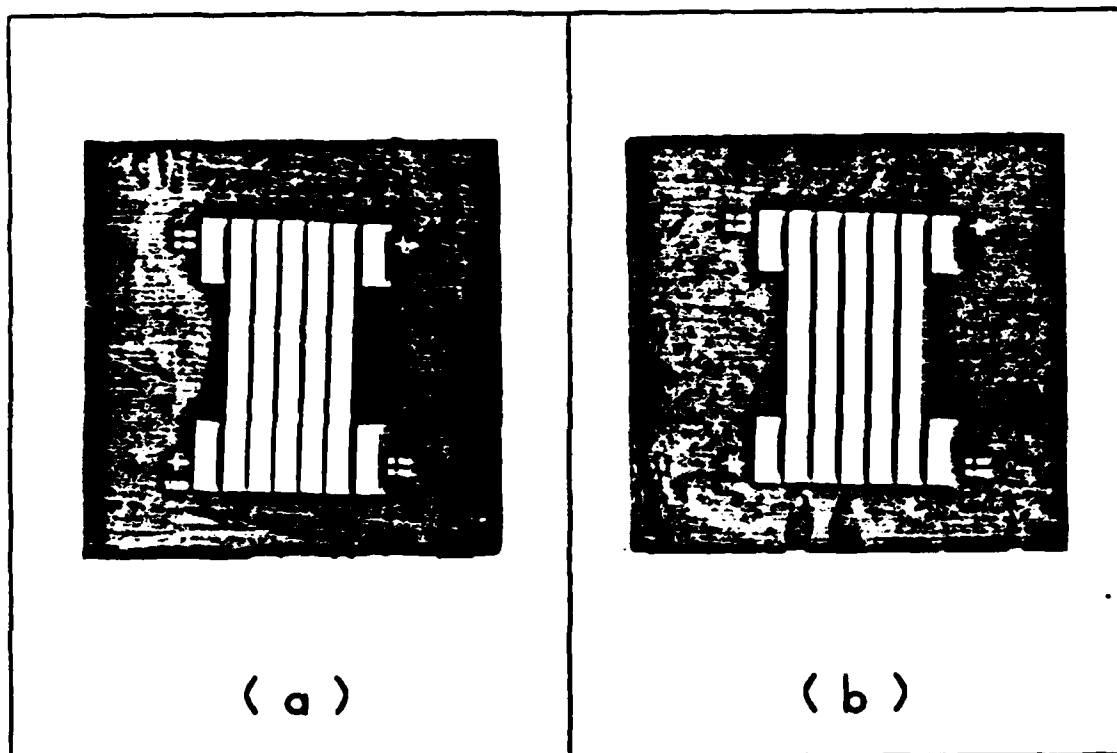


Figure G.2. Photocopies of the Evaporation Masks for (a) the Stripe Design PPTSAs that have an Inner Electrode Spacing of 500 Microns and (b) the Stripe Design PPTSAs that have an Inner Electrode Spacing of 750 Microns.

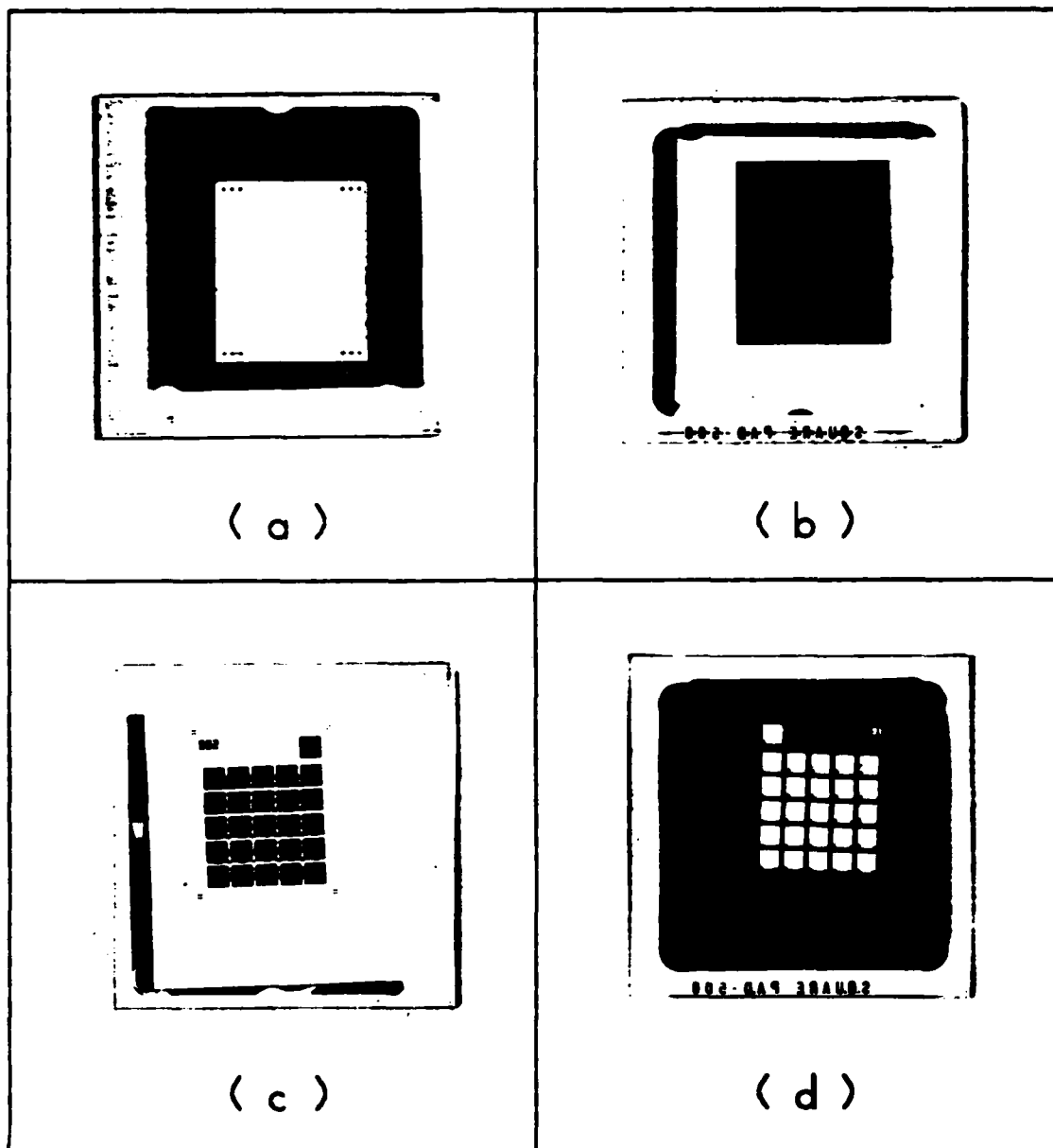


Figure G.3. Photocopies of the High Resolution Plate Masks for the Square-Pad Design PPTSAs that have an Inner Electrode Spacing of 500 Microns. (The positive and negative HRP masks for the ground plane electrode are shown in (a) and (b), respectively. The positive and negative HRP masks for the square electrode pads are shown in (c) and (d), respectively.)

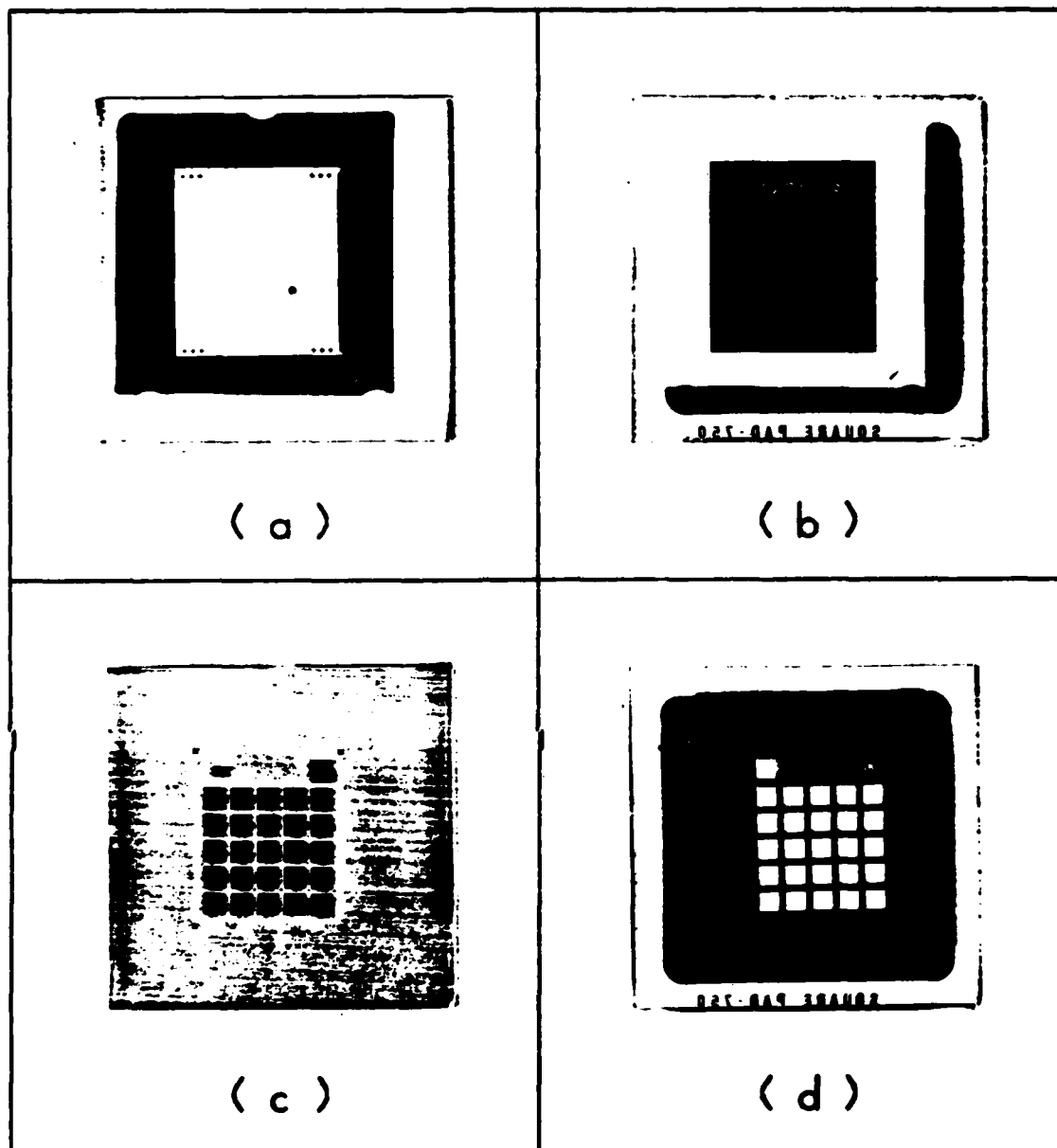


Figure G.4. Photocopies of the High Resolution Plate Masks for the Square-Pad Design PPTSAs that have an Inner Electrode Spacing of 750 Microns. (The positive and negative HRP masks for the ground plane electrode are shown in (a) and (b), respectively. The positive and negative HRP masks for the square electrode pads are shown in (c) and (d), respectively.)

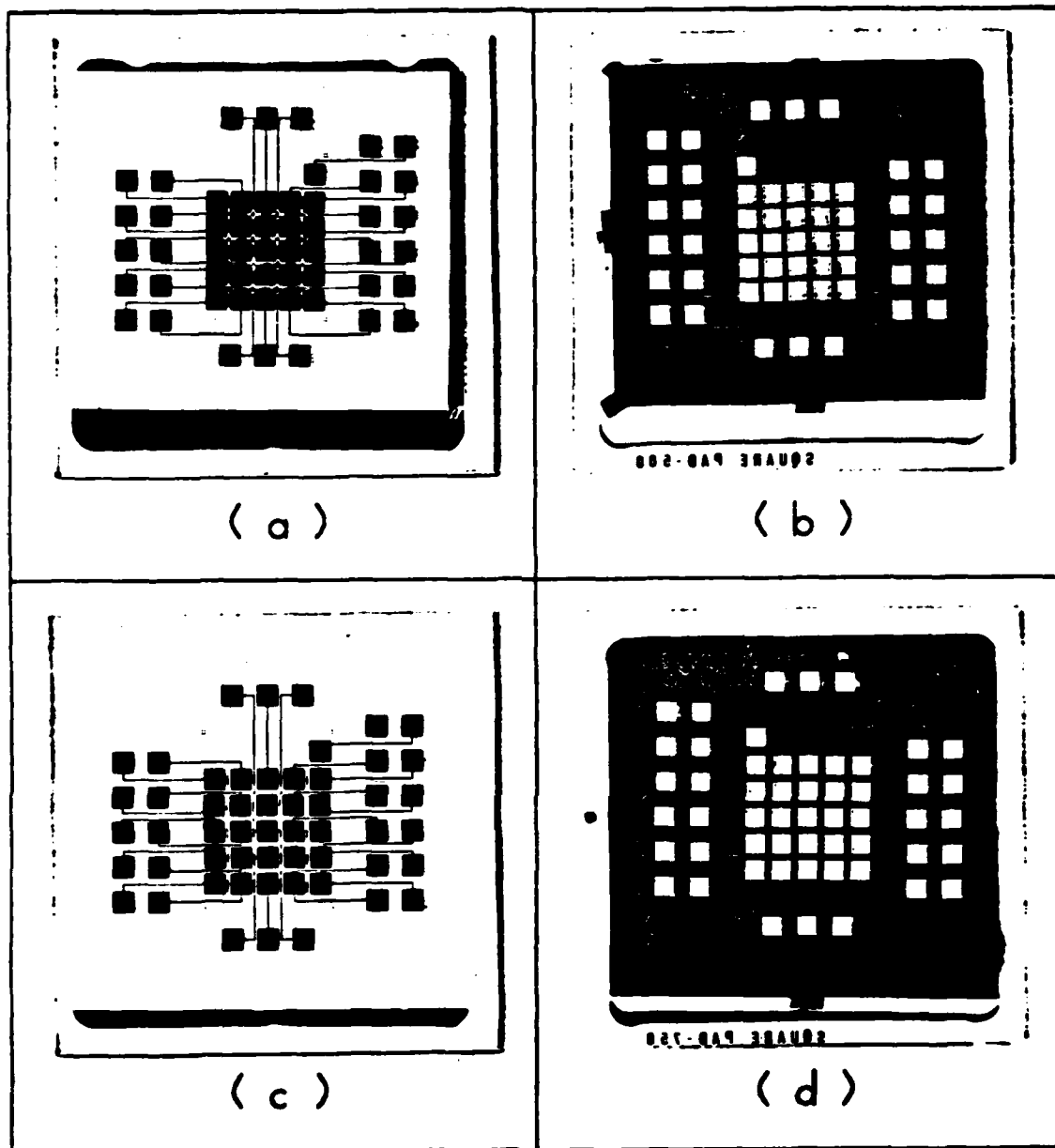


Figure G.5. Photocopies of the High Resolution Plate Masks for the Square-Pad Design PPTSA Conductor Patterns. (The positive and negative HRP masks for PPTSAs that have an inner electrode spacing of 500 microns are shown in (a) and (b), respectively. The positive and negative HRP masks for PPTSAs that have an inner electrode spacing of 750 microns are shown in (c) and (d), respectively.)

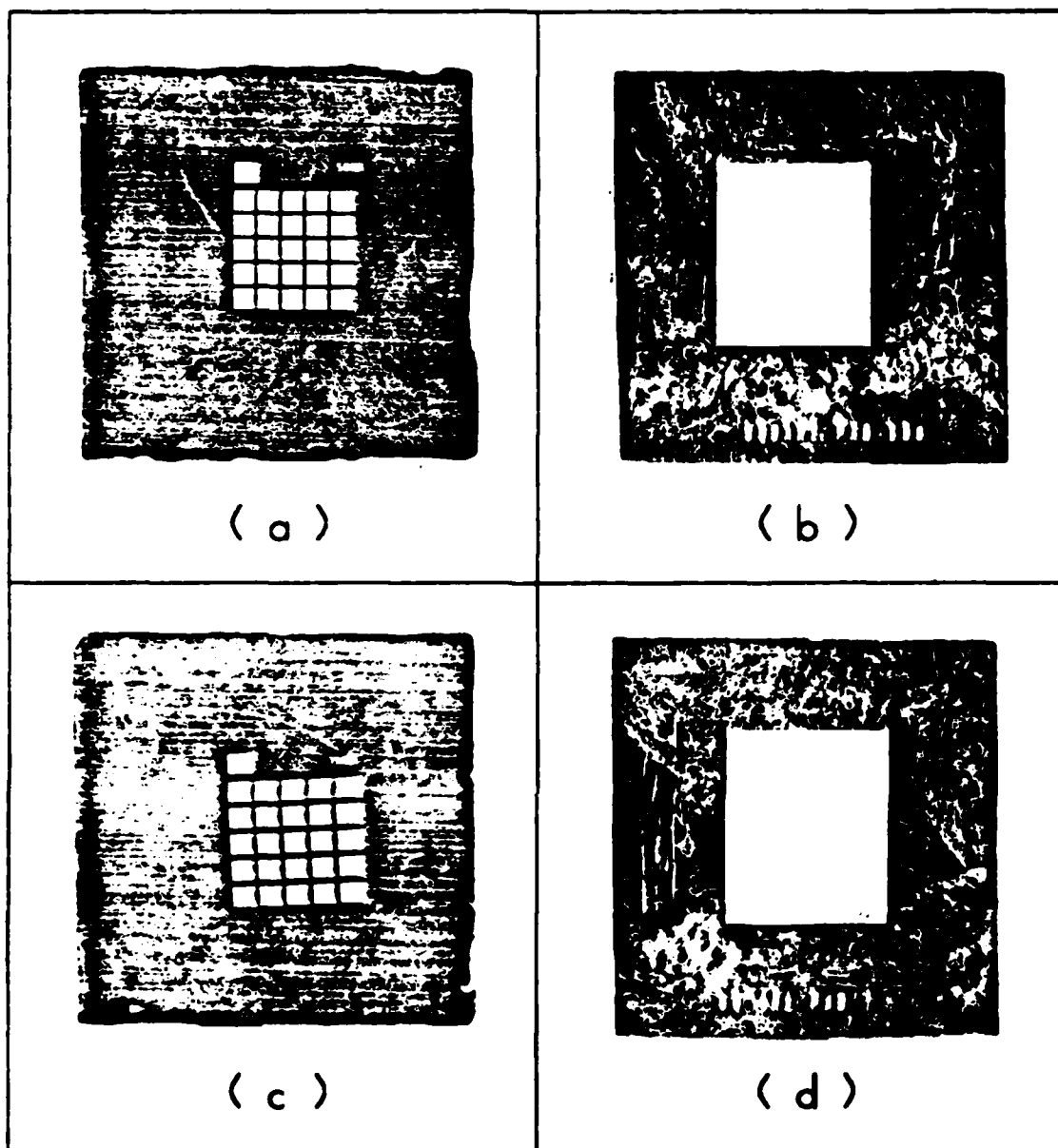


Figure G.6. Photocopies of the Evaporation Masks for the Square-Pad Design PPTSA Electrode Structures. (The evaporation masks for the ground plane and square electrode pads of PPTSAs that have an inner electrode spacing of 500 microns are shown in (a) and (b), respectively. The evaporation masks for the ground plane and square electrode pads of PPTSAs that have an inner electrode spacing of 750 microns are shown in (c) and (d), respectively.)

Appendix H

Thermal Poling Chamber

The thermal poling chamber provided an apparatus for holding a PPTSA configuration during thermal poling. The AFIT Model Shop fabricated the poling chamber. A drawing of the poling chamber is shown in Figure H.1. The chamber

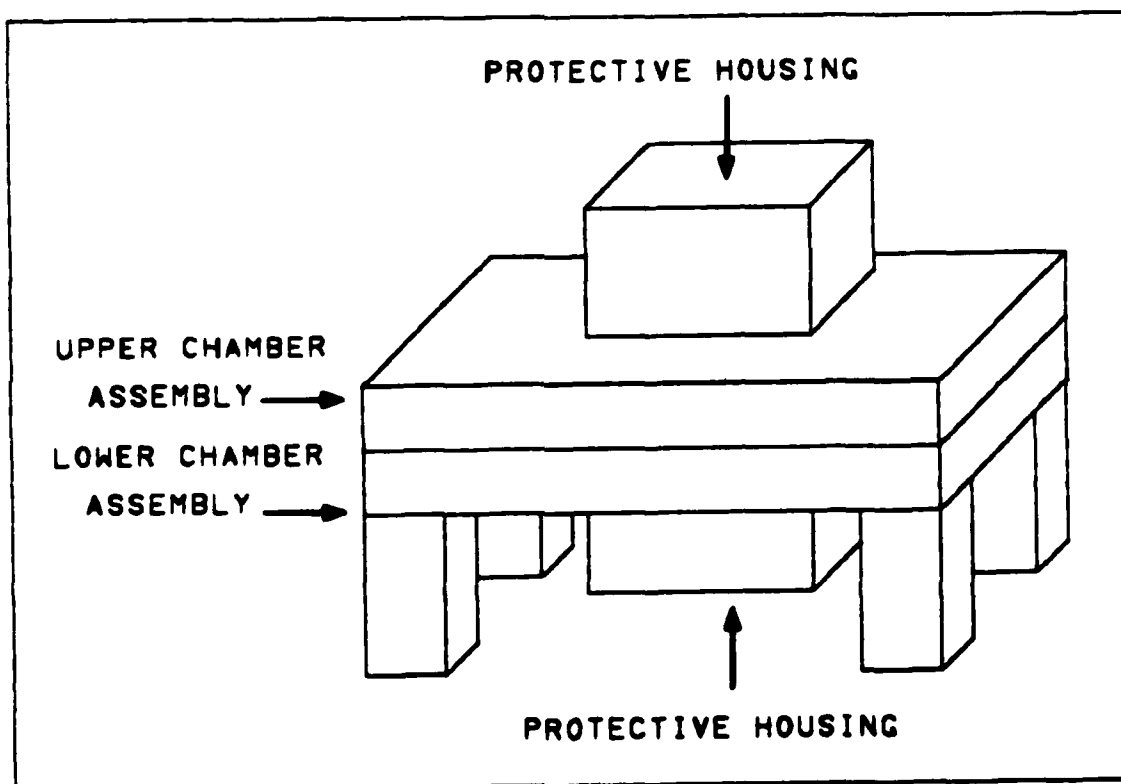


Figure H.1. Drawing of the Thermal Poling Chamber.

consisted of five main parts: an upper chamber assembly, a lower chamber assembly, two protective housings, and an electrode assembly. Figures H.2 through H.5 depict these component parts. The dimensions of these component are in

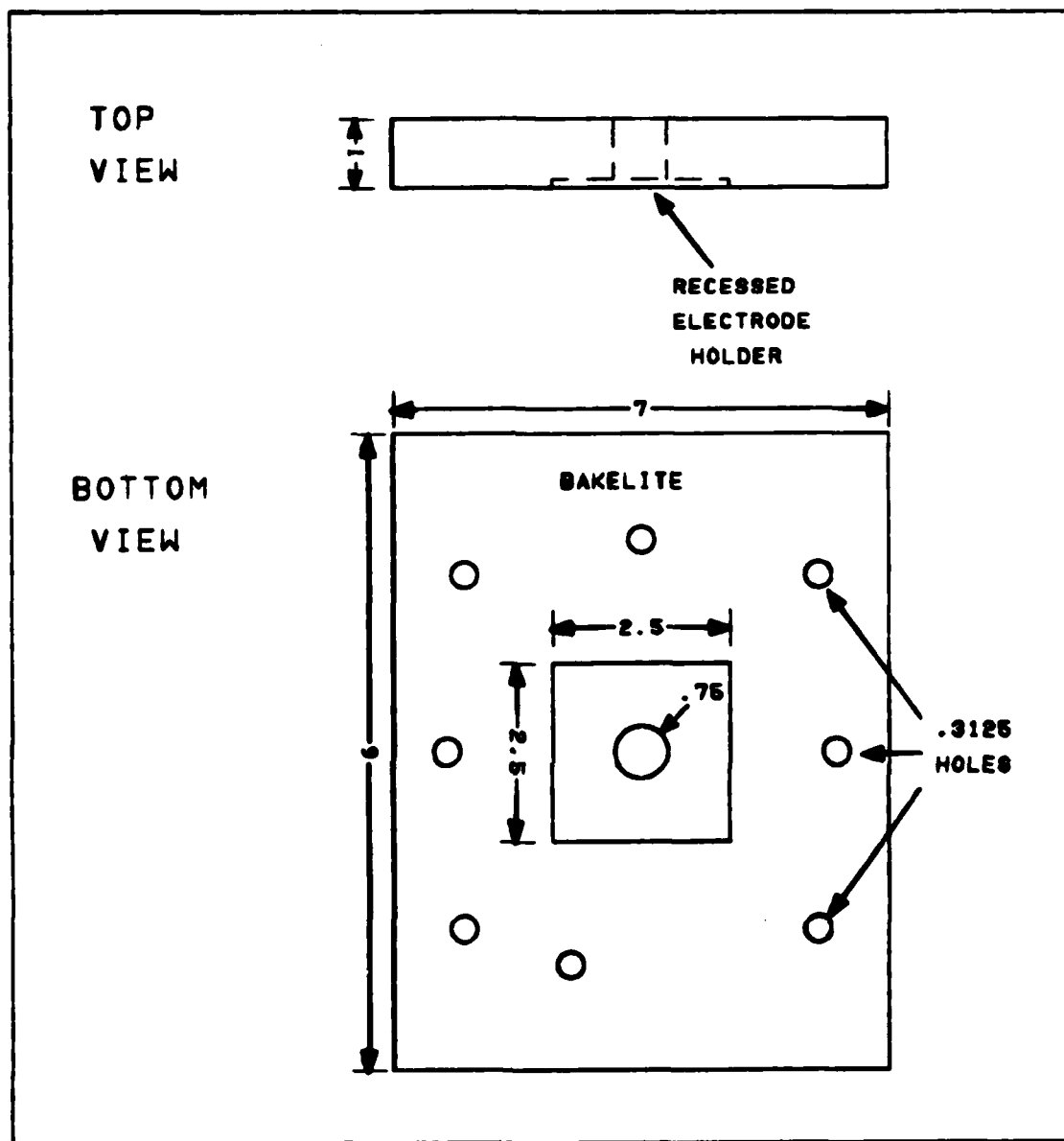


Figure H.2. Drawing of the Upper Chamber Assembly.

inches. The chamber was constructed from phenolic, bakelite, and copper. Phenolic was used for the protective housings and the legs. Bakelite was used for the upper and the lower chamber assemblies. The electrode assembly was

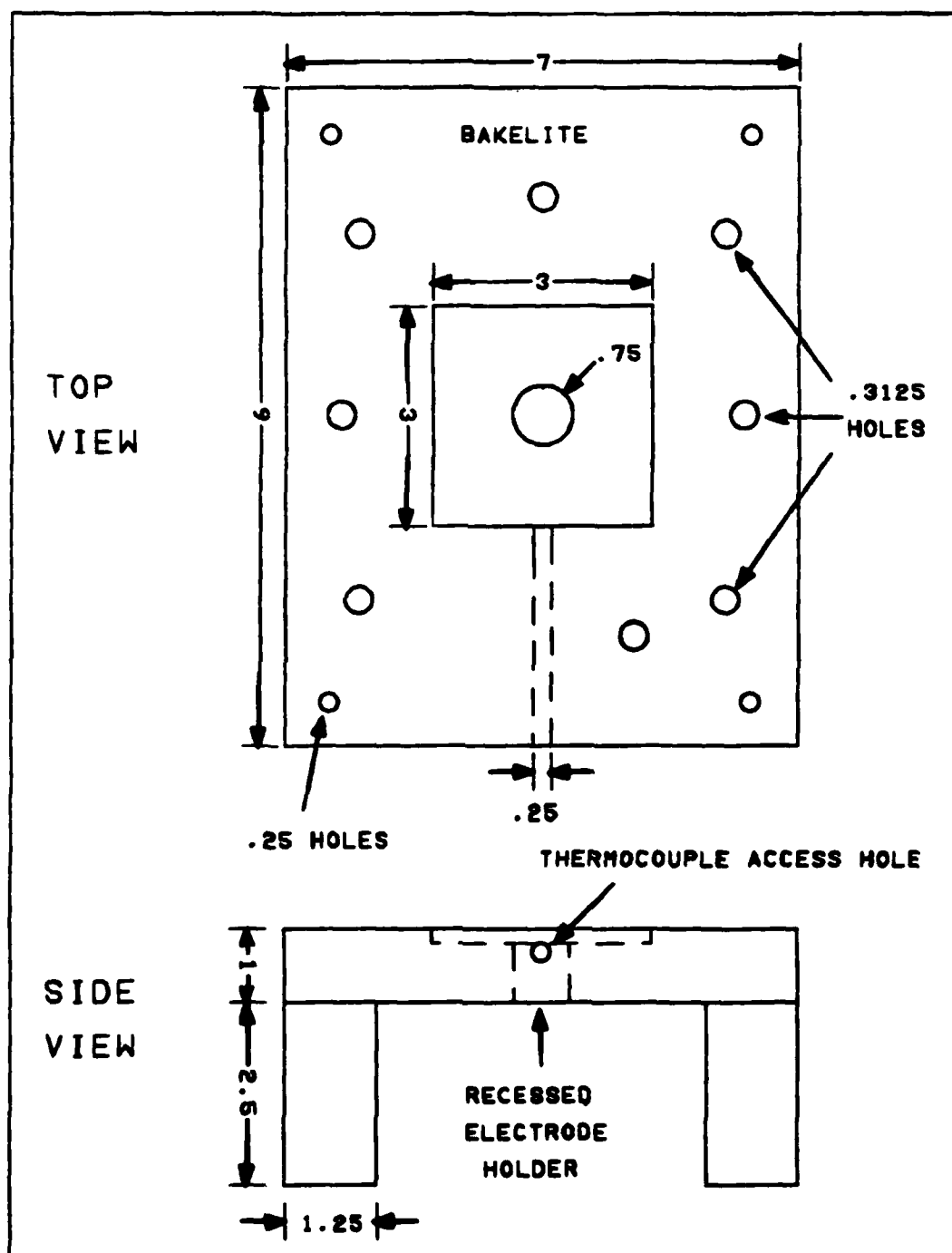


Figure H.3. Drawing of the Lower Chamber Assembly.

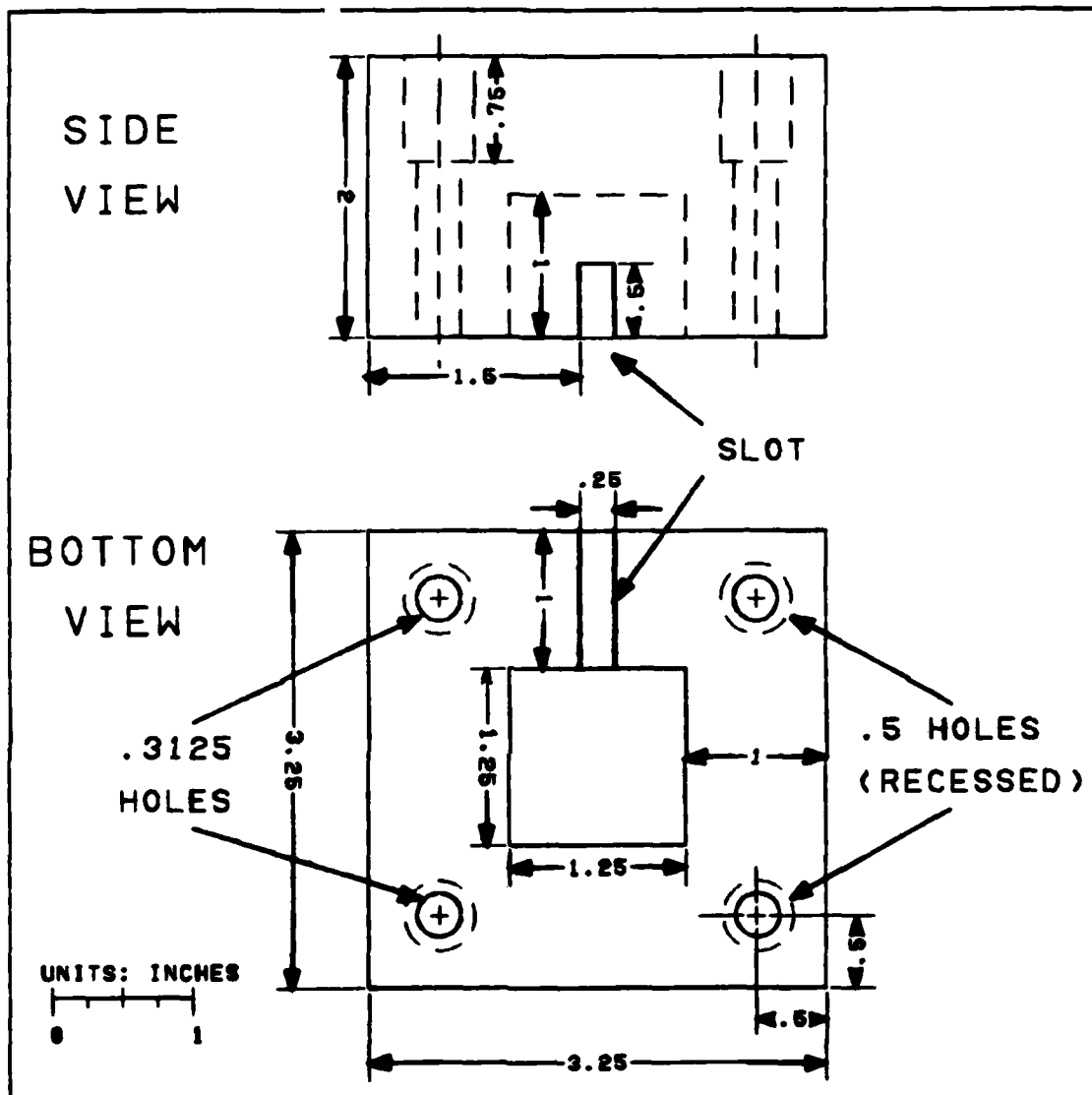


Figure H.4. Drawing of a Protective Housing.

fabricated from copper. The chamber was held together with eight 1/4" x 3" steel bolts, eight 1/4" x 2" nylon screws, and four steel 1/4" x 2" screws. (None of these bolts and screws were shown in the figures.) The steel bolts held the

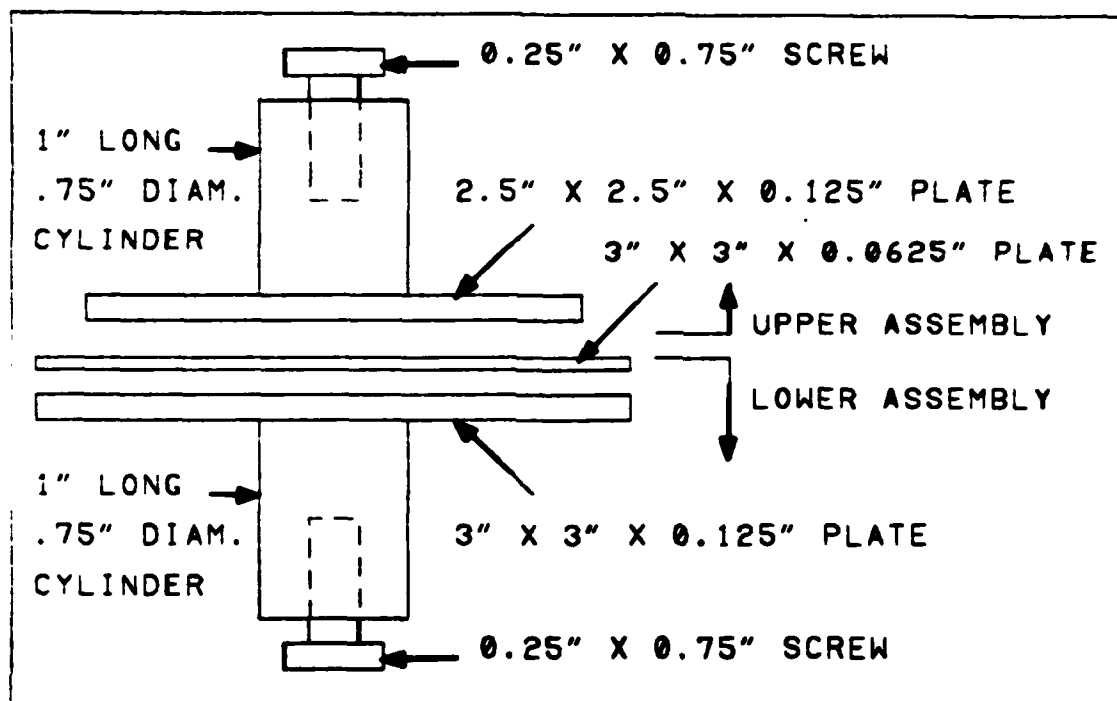


Figure H.5. Drawing of the Electrode Assembly.

upper and the lower chamber assemblies. The nylon screws were used to attach the protective housings to the chamber. The four steel screws were used to attach the legs to the lower chamber assembly.

Appendix I
Computer Programs

```
10 : Program Name: DATA.BAS
20 : *****
30 :
40 :         This program was used for collecting points
50 :         of data data for one discrete sensor. The data
60 :         is put in a datafile that is later accessed.
70 :
80 :         This program is a version of programs
90 :         written by Captain James Godfrey and programmers
100 :        at Keithley and Capital Equipment.
110 :
120 : *****
130 :
140 :        DEF SEG=&HC400
150 :        INITIALIZE=0 : SEND=9 : ENTER=21
160 :        MY.ADDRESS%=21 : LEVEL%=0
170 :        CALL INITIALIZE(MY.ADDRESS%,LEVEL%)
180 :        ADDRESS%=27
190 :
200 :        PRINT : PRINT
210 :        INPUT NAME OF OUTPUT FILE: ; OUTPUT#
220 :        OPEN OUTPUT# FOR OUTPUT AS #1
230 :
240 :        FOR I = 1 TO 110
250 :            S$ = 'MEASURE'
260 :            CALL SEND(ADDRESS%,S$,STATUS%)
270 :            R$ = SPACE$(80) : D$ = SPACE$(80)
280 :            CALL ENTER(R$,LENGTH%,ADDRESS%,STATUS%)
290 :            R$ = LEFT$(R$,LENGTH%)
300 :            D$ = RIGHT$(R$, (LEN(R$)-4))
310 :            PRINT #1,1,D$ : PRINT 1,D$
320 :        NEXT I
330 :            E = 999
340 :            PRINT #1,E,E
350 :            CLOSE
360 :
370 :        OPEN OUTPUT# FOR INPUT AS #2
380 :        INPUT#2, X, Y : MIN = Y : MAX = Y
390 :        INPUT#2, X, Y
400 :        IF X = 999 GOTO 440
410 :        IF Y < THEN MIN = Y : MINX = X
420 :        IF Y > THEN MAX = Y : MAXX = X
430 :        GOTO 390
440 :        PRINT 'THE MINIMUM IS: ', MIN, ' AT ',MINX
450 :        PRINT 'THE MAXIMUM IS: ', MAX, ' AT ',MAXX
460 :        CLOSE 2 : RESET : END
470 : *****
```

```

10 ' Program Name: DELTA.BAS
20 ' *****
30 '
40 '       This program was used for computing the
50 '       DC response voltage for a measurement.
60 '
70 '       The linear least squares fit routines used
80 '       came from the book 'IBM PC, Programs in Science
90 '       and Engineering' by J. H. Gilder and S. P Gilder.
100 '       Hasbrouck Heights, New Jersey: Hayden, 1984.
110 ' *****
120 ' *****
130 '
140       DIM AV(111,2)
150       INPUT 'PPTSA SENSOR NUMBER ' ; PPTSA$
160       INPUT 'WHAT IS THE INPUT FILE NAME ' ; F$
170       OPEN F$ FOR INPUT AS #1
180       INPUT 'LOCATION OF POINT A ' ; A
190       INPUT 'LOCATION OF POINT B ' ; B
200       INPUT 'LOCATION OF POINT C ' ; C
210       INPUT 'LOCATION OF POINT D ' ; D
220       INPUT 'LOCATION OF POINT E ' ; E
230       INPUT 'LOCATION OF POINT F ' ; F
240 '
250       G = F + 1
260       FOR I = 1 TO 110
270         INPUT#1, TIME, VOLT
280         IF TIME = G      GOTO 300
290         IF TIME = 999    GOTO 300
300         AV(I,1) = TIME : AV(I,2) = VOLT
310       NEXT I
320       CLOSE 1
330 '
340       LPRINT 'INPUT FILE NAME: ' ; F$ , ' PPTSA #' ; PPTSA$
350       LPRINT 'A:' ; A ; AV(A,2) ; ' , B:' ; B ; AV(B,2) ;
360       LPRINT 'C:' ; C ; AV(C,2) ; ' , D:' ; D ; AV(D,2) ;
370       LPRINT 'E:' ; E ; AV(E,2) ; ' , F:' ; F ; AV(F,2) ;
380 '
390       X1=0 : Y1=0 : XY=0 : X2=0
400       FOR I = A TO B
410         X1 = X1 + AV(I,1)
420         Y1 = Y1 + AV(I,2)
430         XY = XY + AV(I,1) * AV(I,2)
440         X2 = X2 + AV(I,1) * AV(I,1)
450       NEXT I
460 '

```

```

470      N1=0 : J1=0 : M1=0 : B1=0
480      N1 = B - A + 1
490      J1 = N1 * X2 - X1 * X1
500      M1 = (N1 * XY - X1 * Y1)/J1
510      M1 = INT(100000! * M1 + .5)/100000!
520      B1 = (Y1 * X2 - X1 * XY)/J1
530      B1 = INT(100000! * B1 + .5)/100000!
540
550      MIDAB = A + (B-A)/2
560      LSTAB = MIDAB * M1 + B1
570      LPRINT 'M1: ';M1; ', B1: ';B1
580      LPRINT 'A-B (P): ';MIDAB; ',LSTAB
590
600      X1=0 : Y1=0 : XY=0 : X2=0
610      FOR I = C TO D
620          X1 = X1 + AV(I,1)
630          Y1 = Y1 + AV(I,2)
640          XY = XY + AV(I,1) * AV(I,2)
650          X2 = X2 + AV(I,1) * AV(I,1)
660      NEXT I
670
680      N2=0 : J2=0 : M2=0 : B2=0
690      N2 = D - C + 1
700      J2 = N2 * X2 - X1 * X1
710      M2 = (N1 * XY - X1 * Y1)/J2
720      M2 = INT(100000! * M2 + .5)/100000!
730      B2 = (Y1 * X2 - X1 * XY)/J2
740      B2 = INT(100000! * B2 + .5)/100000!
750
760      MIDCD = C + (D-C)/2
770      LSTCD = MIDCD * M2 + B2
780      LPRINT 'M2: ';M2; ', B2: ';B2
790      LPRINT 'C-D (R): ';MIDCD; ',LSTCD
800
810      X1=0 : Y1=0 : XY=0 : X2=0
820      FOR I = E TO F
830          X1 = X1 + AV(I,1)
840          Y1 = Y1 + AV(I,2)
850          XY = XY + AV(I,1) * AV(I,2)
860          X2 = X2 + AV(I,1) * AV(I,1)
870      NEXT I
880
890      N3=0 : J3=0 : M3=0 : B3=0
900      N3 = F - E + 1
910      J3 = N3 * X2 - X1 * X1
920      M3 = (N3 * XY - X1 * Y1)/J3
930      M3 = INT(100000! * M3 + .5)/100000!
940      B3 = (Y1 * X2 - X1 * XY)/J3
950      B3 = INT(100000! * B3 + .5)/100000!
960

```

```

970      MIDEF = F + (F-E)/2
980      LSTEF = MIDEF * M3 + B3
990      LPRINT 'M3: ';M3; ', B3: ';B3
1000     LPRINT 'E-F (S): ';MIDEF; ',LSTEF
1010'
1020     BASE = (LSTAB + LSTEF)/2
1030     RESPONSE = LSTCD - BASE
1040     LPRINT 'BASE (Q): ';MIDCD; ', ';BASE
1050     LPRINT 'RESPONSE: ';RESPONSE
1060     GOTO 150
1070     END
1080'*****

```

Appendix J

Piezoelectric Activity Data Plots

This appendix contains plots for the piezoelectric activity data for the two PPTSA configurations (PPTSA #2b and #13) which were poled. The best of these plots (PPTSA #13, center sensor) were placed in Chapter IV.

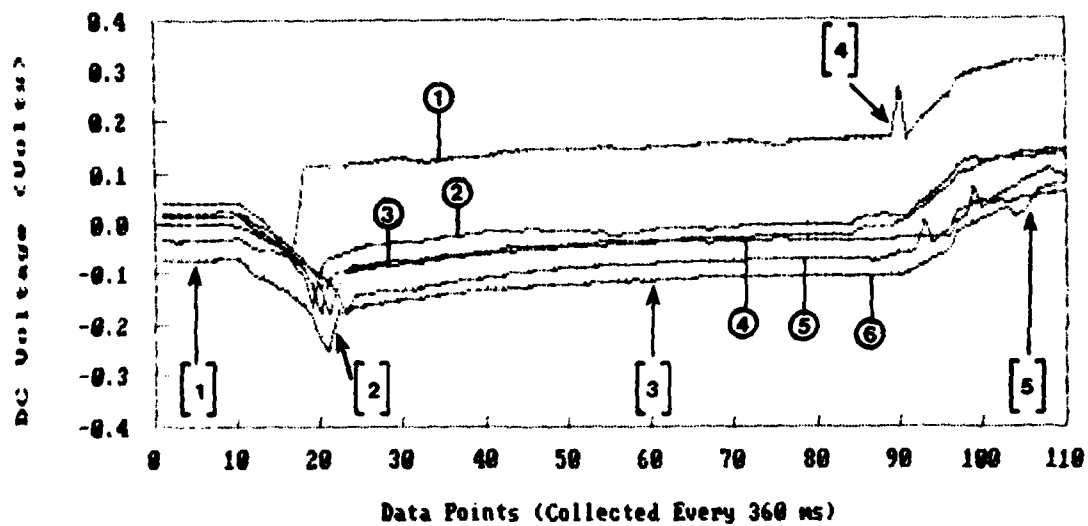


Figure J.1. Response of Six Measurements for the PPTSA #2b Configuration. These Measurements were for the Center Sensor and 100 Gram Load. (The vertical axis represents the sensor's DC response voltage. Key to measurement states: [1] Pre-load, [2] Load application, [3] Steady-state response, [4] Load removal, and [5] Post-load.)

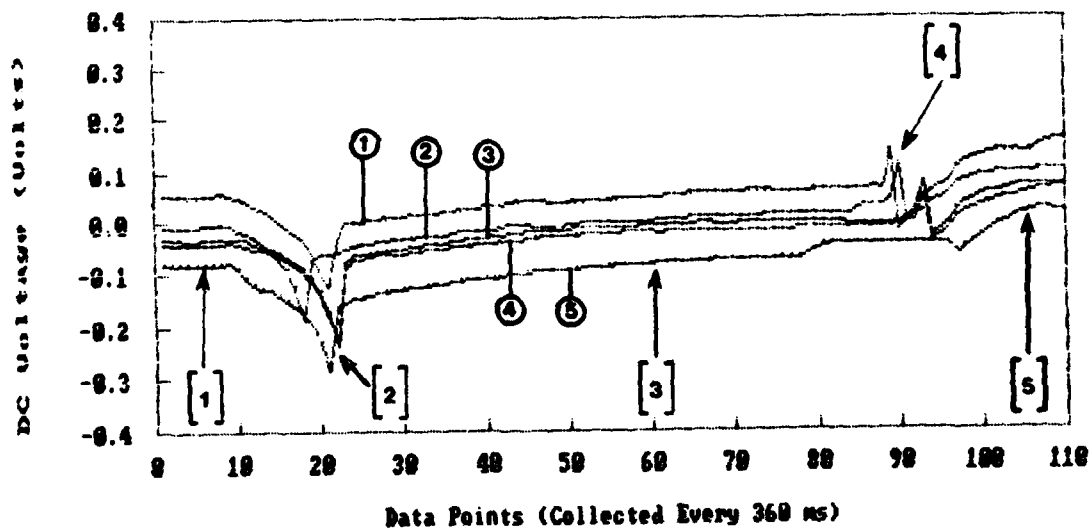


Figure J.2. Response of Five Measurements for the PPTSA #2b Configuration. These Measurements were for the Center Sensor and 200 Gram Load. (The vertical axis represents the sensor's DC response voltage. Key to measurement states: [1] Pre-load, [2] Load application, [3] Steady-state response, [4] Load removal, and [5] Post-load.)

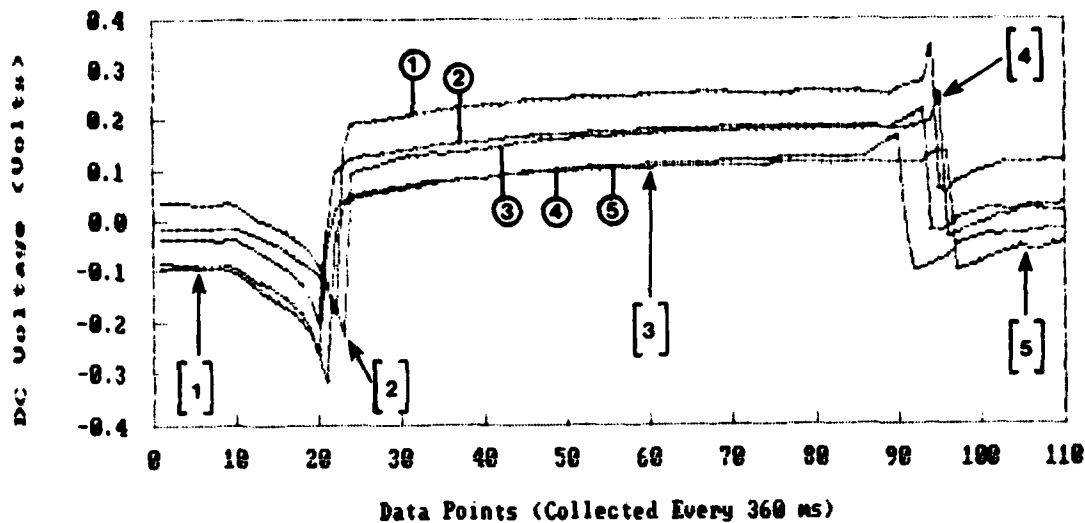


Figure J.3. Response of Five Measurements for the PPTSA #2b Configuration. These Measurements were for the Center Sensor and 500 Gram Load. (The vertical axis represents the sensor's DC response voltage. Key to measurement states: [1] Pre-load, [2] Load application, [3] Steady-state response, [4] Load removal, and [5] Post-load.)

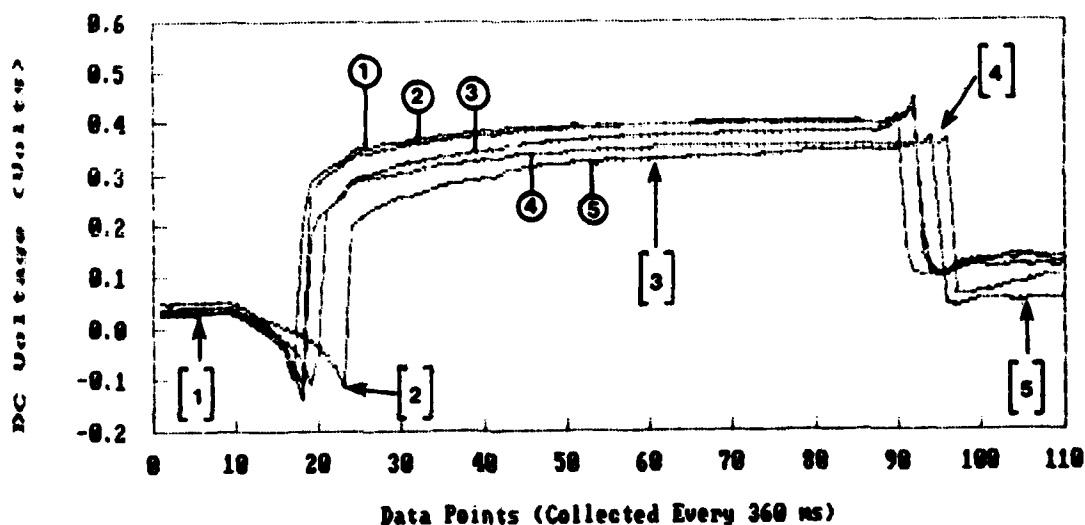


Figure J.4. Response of Five Measurements for the PPTSA #2b Configuration. These Measurements were for the Center Sensor and 700 Gram Load. (The vertical axis represents the sensor's DC response voltage. Key to measurement states: [1] Pre-load, [2] Load application, [3] Steady-state response, [4] Load removal, and [5] Post-load.)

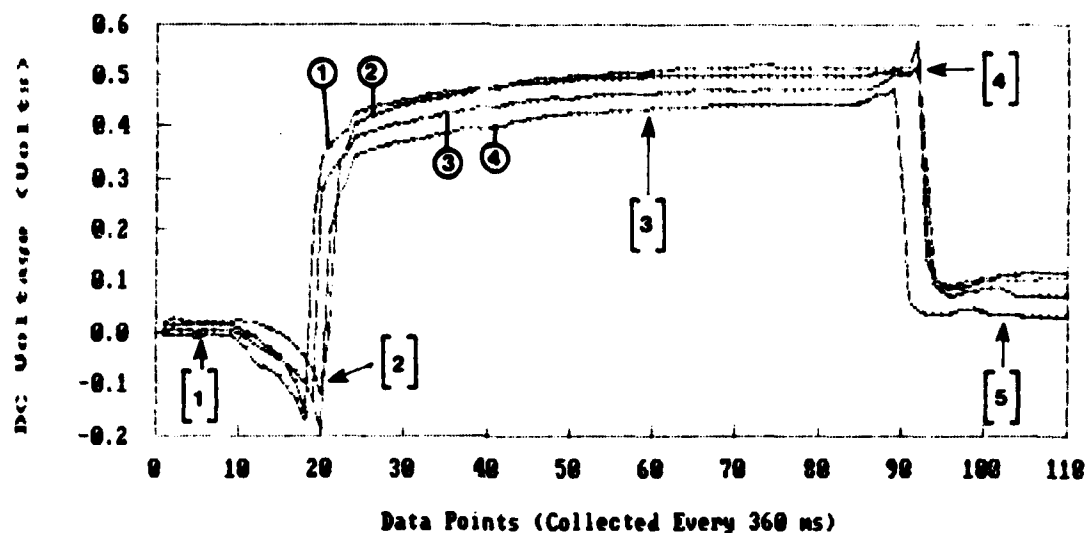


Figure J.5. Response of Four Measurements for the PPTSA #2b Configuration. These Measurements were for the Center Sensor and 1,000 Gram Load. (The vertical axis represents the sensor's DC response voltage. Key to measurement states: [1] Pre-load, [2] Load application, [3] Steady-state response, [4] Load removal, and [5] Post-load.)

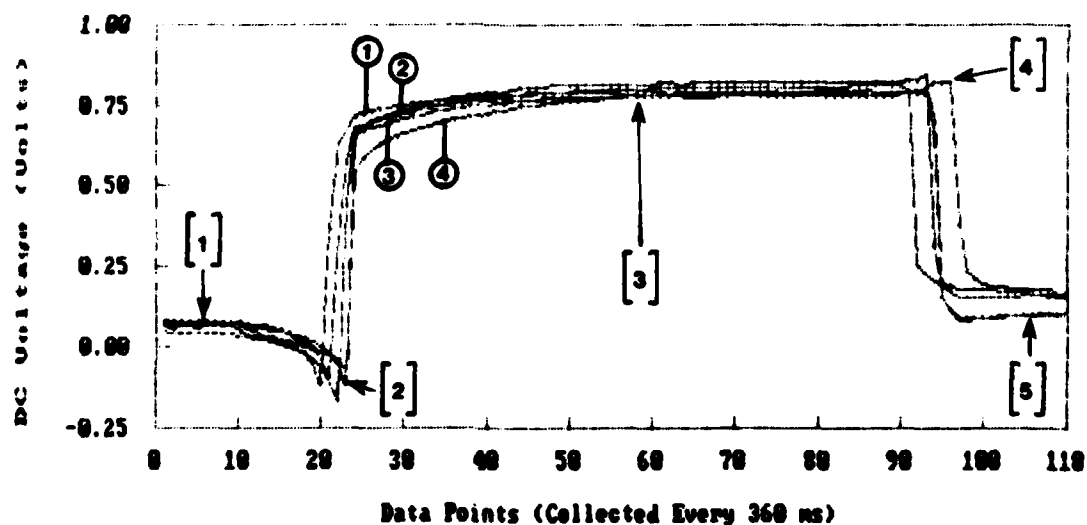


Figure J.6. Response of Four Measurements for the PPTSA #2b Configuration. These Measurements were for the Center Sensor and 1,500 Gram Load. (The vertical axis represents the sensor's DC response voltage. Key to measurement states: [1] Pre-load, [2] Load application, [3] Steady-state response, [4] Load removal, and [5] Post-load.)

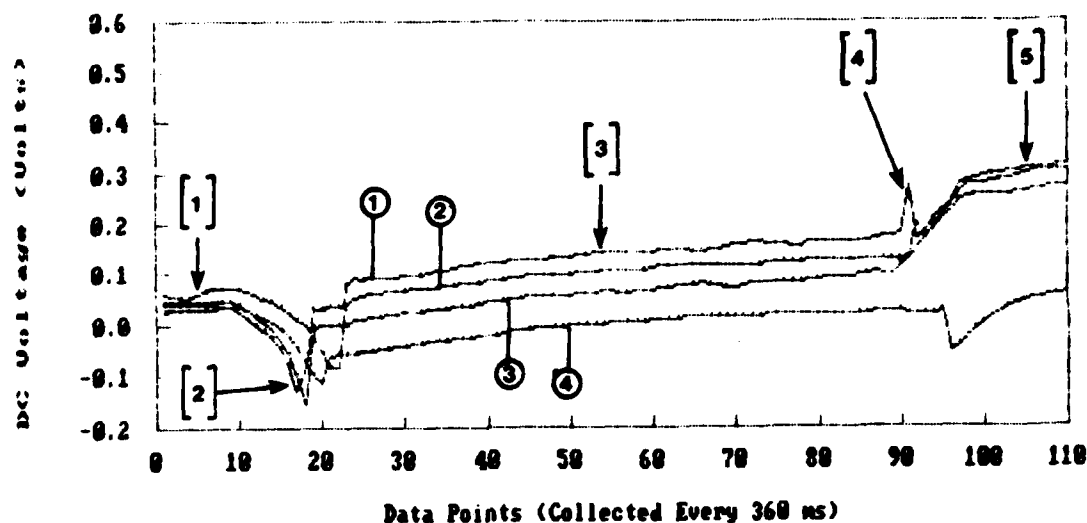


Figure J.7. Response of Four Measurements for the PPTSA #2b Configuration. These Measurements were for the Corner Sensor and 100 Gram Load. (The vertical axis represents the sensor's DC response voltage. Key to measurement states: [1] Pre-load, [2] Load application, [3] Steady-state response, [4] Load removal, and [5] Post-load.)

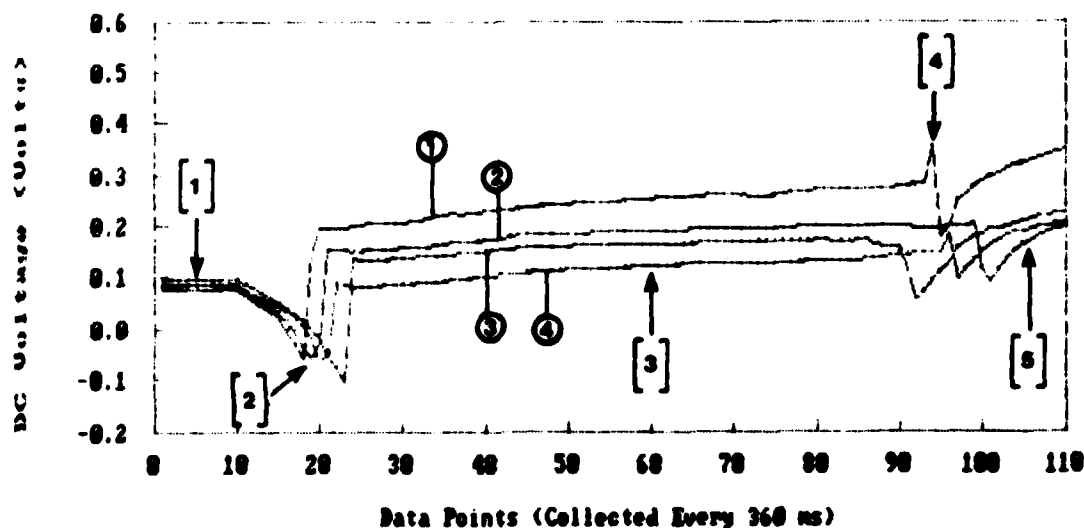


Figure J.8. Response of Four Measurements for the PPTSA #2b Configuration. These Measurements were for the Corner Sensor and 200 Gram Load. (The vertical axis represents the sensor's DC response voltage. Key to measurement states: [1] Pre-load, [2] Load application, [3] Steady-state response, [4] Load removal, and [5] Post-load.)

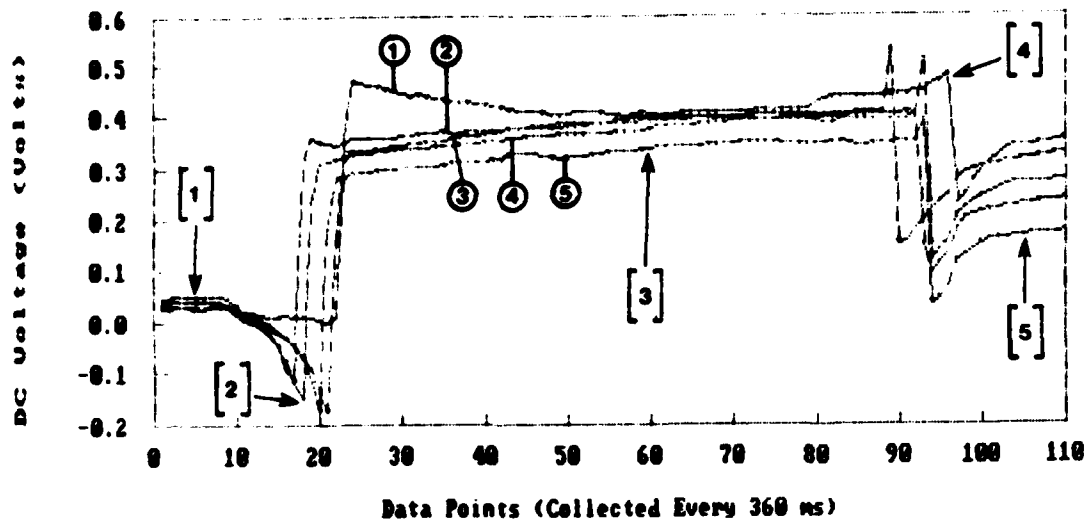


Figure J.9. Response of Five Measurements for the PPTSA #2b Configuration. These Measurements were for the Corner Sensor and 500 Gram Load. (The vertical axis represents the sensor's DC response voltage. Key to measurement states: [1] Pre-load, [2] Load application, [3] Steady-state response, [4] Load removal, and [5] Post-load.)

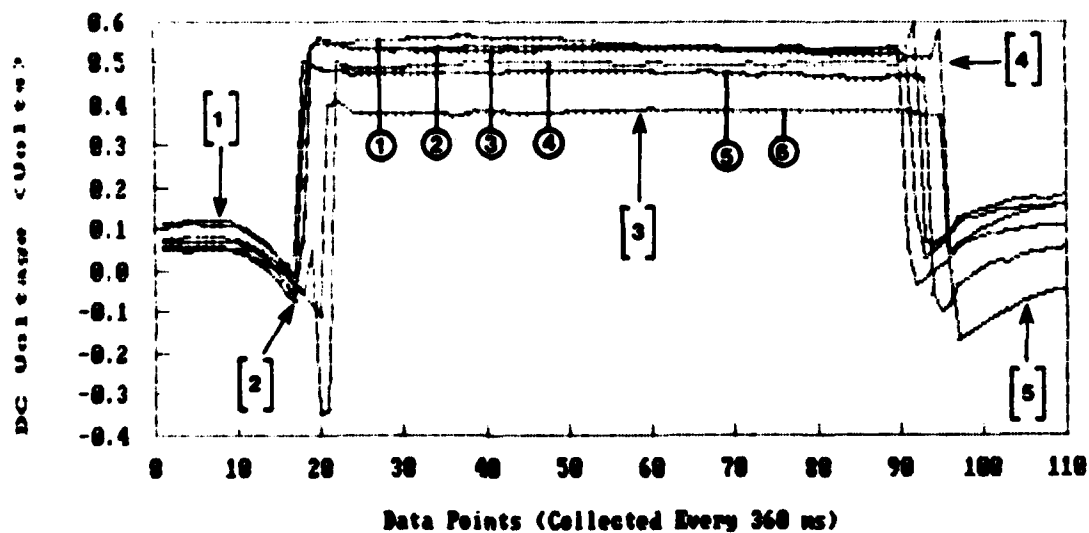


Figure J.10. Response of Six Measurements for the PPTSA #2b Configuration. These Measurements were for the Corner Sensor and 700 Gram Load. (The vertical axis represents the sensor's DC response voltage. Key to measurement states: [1] Pre-load, [2] Load application, [3] Steady-state response, [4] Load removal, and [5] Post-load.)

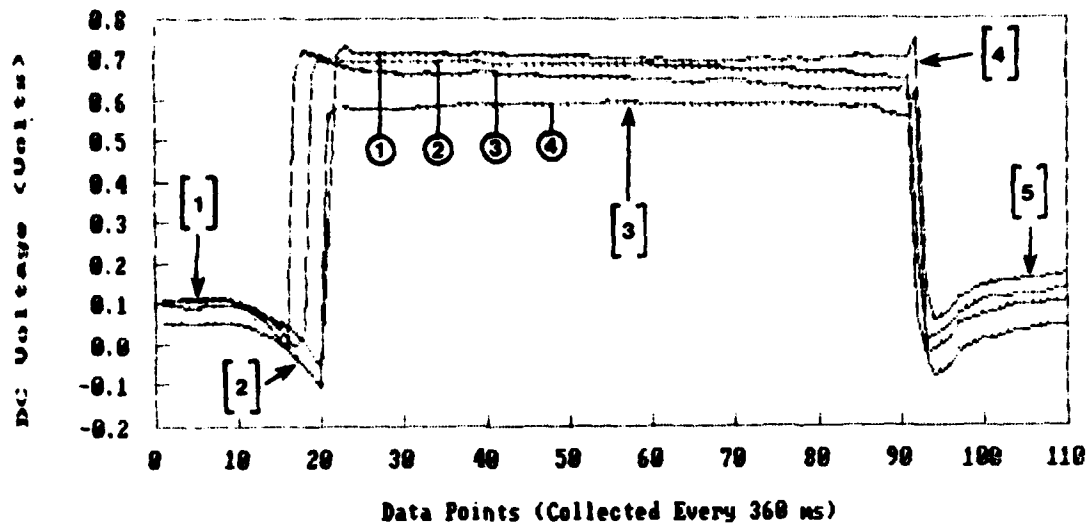


Figure J.11. Response of Four Measurements for the PPTSA #2b Configuration. These Measurements were for the Corner Sensor and 1,000 Gram Load. (The vertical axis represents the sensor's DC response voltage. Key to measurement states: [1] Pre-load, [2] Load application, [3] Steady-state response, [4] Load removal, and [5] Post-load.)

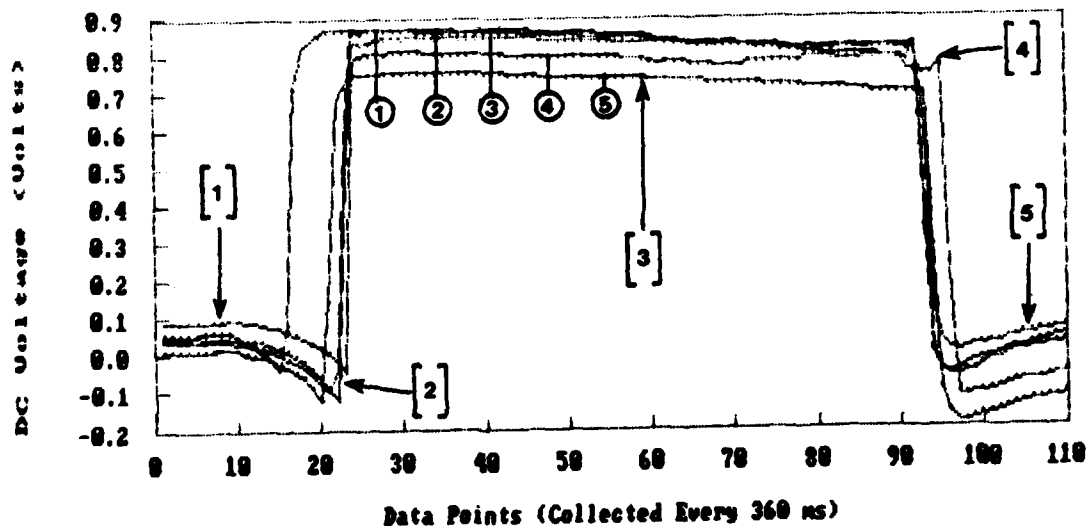


Figure J.12. Response of Five Measurements for the PPTSA #2b Configuration. These Measurements were for the Corner Sensor and 1,500 Gram Load. (The vertical axis represents the sensor's DC response voltage. Key to measurement states: [1] Pre-load, [2] Load application, [3] Steady-state response, [4] Load removal, and [5] Post-load.)

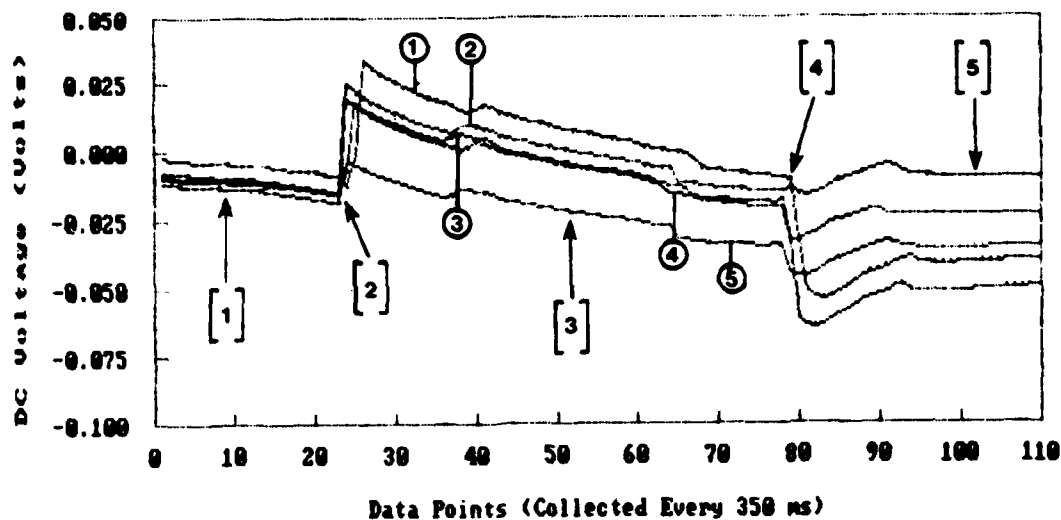


Figure J.13. Response of Five Measurements for the Poled PPTSA #2b Configuration. These Measurements were for the Center Sensor and 100 Gram Load. (The vertical axis represents the sensor's DC response voltage. Key to measurement states: [1] Pre-load, [2] Load application, [3] Steady-state response, [4] Load removal, and [5] Post-load.)

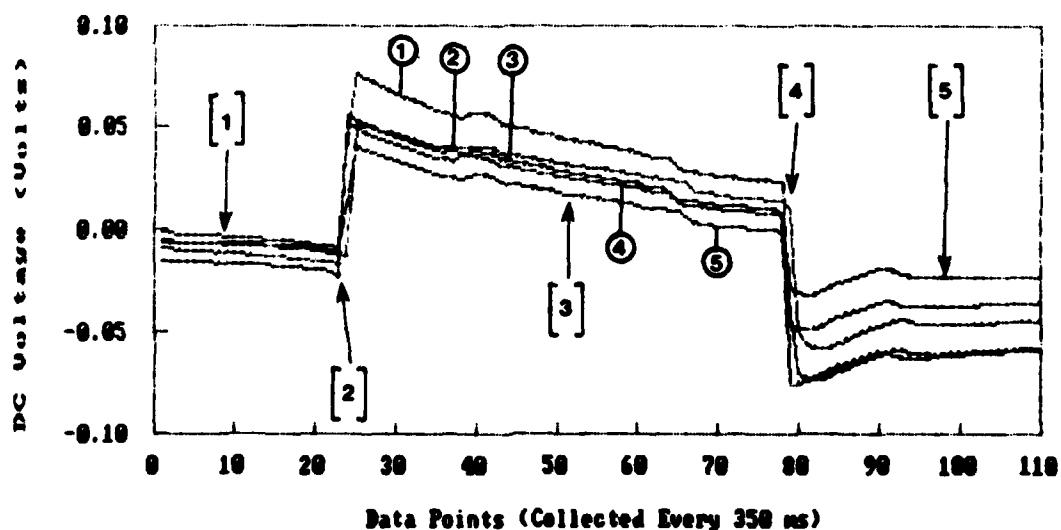


Figure J.14. Response of Five Measurements for the Poled PPTSA #2b Configuration. These Measurements were for the Center Sensor and 200 Gram Load. (The vertical axis represents the sensor's DC response voltage. Key to measurement states: [1] Pre-load, [2] Load application, [3] Steady-state response, [4] Load removal, and [5] Post-load.)

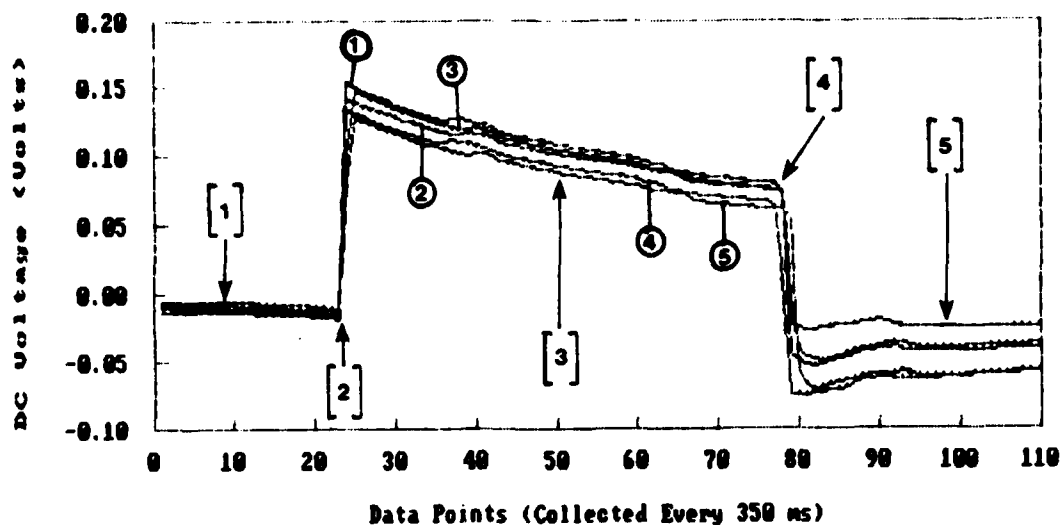


Figure J.15. Response of Five Measurements for the Poled PPTSA #2b Configuration. These Measurements were for the Center Sensor and 500 Gram Load. (The vertical axis represents the sensor's DC response voltage. Key to measurement states: [1] Pre-load, [2] Load application, [3] Steady-state response, [4] Load removal, and [5] Post-load.)

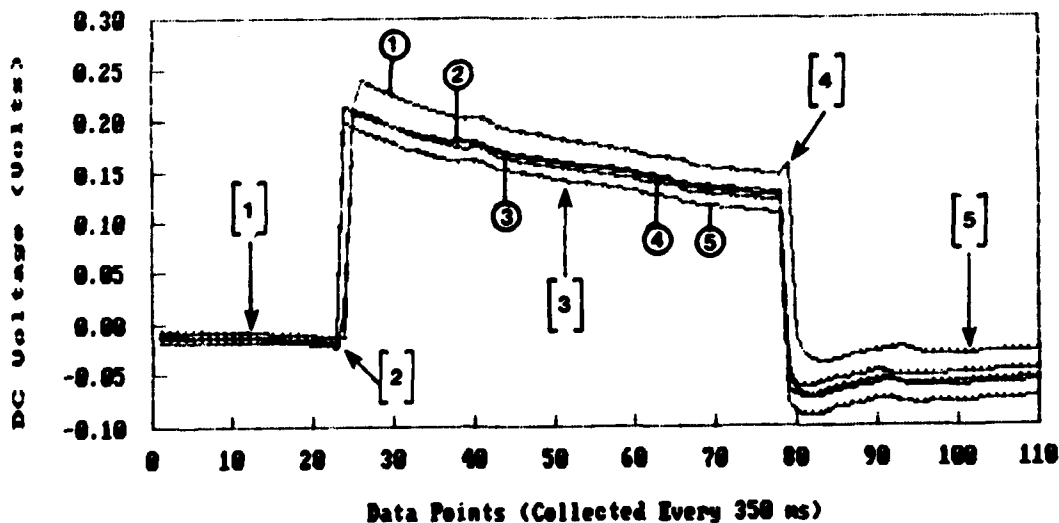


Figure J.16. Response of Five Measurements for the Poled PPTSA #2b Configuration. These Measurements were for the Center Sensor and 700 Gram Load. (The vertical axis represents the sensor's DC response voltage. Key to measurement states: [1] Pre-load, [2] Load application, [3] Steady-state response, [4] Load removal, and [5] Post-load.)

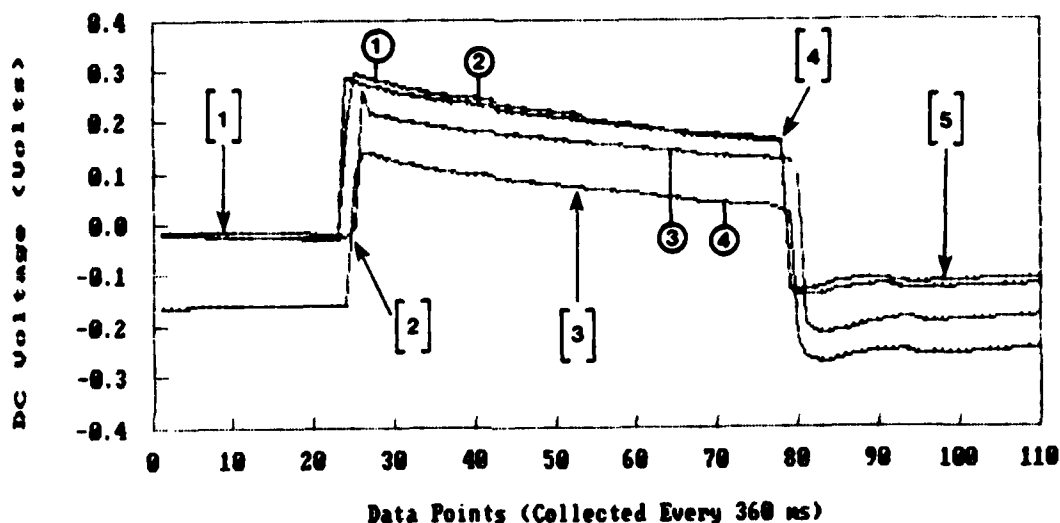


Figure J.17. Response of Four Measurements for the Poled PPTSA #2b Configuration. These Measurements were for the Center Sensor and 1,000 Gram Load. (The vertical axis represents the sensor's DC response voltage. Key to measurement states: [1] Pre-load, [2] Load application, [3] Steady-state response, [4] Load removal, and [5] Post-load.)

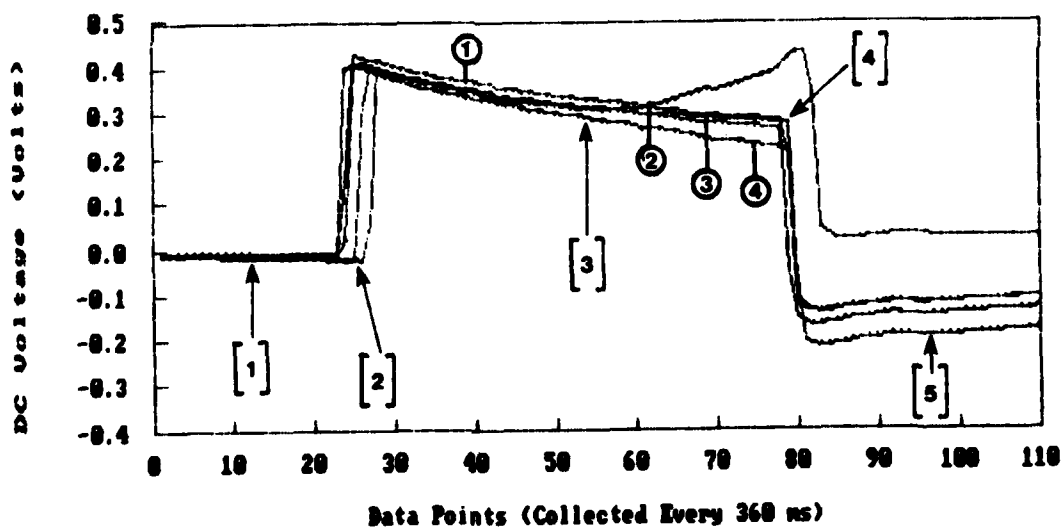


Figure J.18. Response of Four Measurements for the Poled PPTSA #2b Configuration. These Measurements were for the Center Sensor and 1,500 Gram Load. (The vertical axis represents the sensor's DC response voltage. Key to measurement states: [1] Pre-load, [2] Load application, [3] Steady-state response, [4] Load removal, and [5] Post-load.)

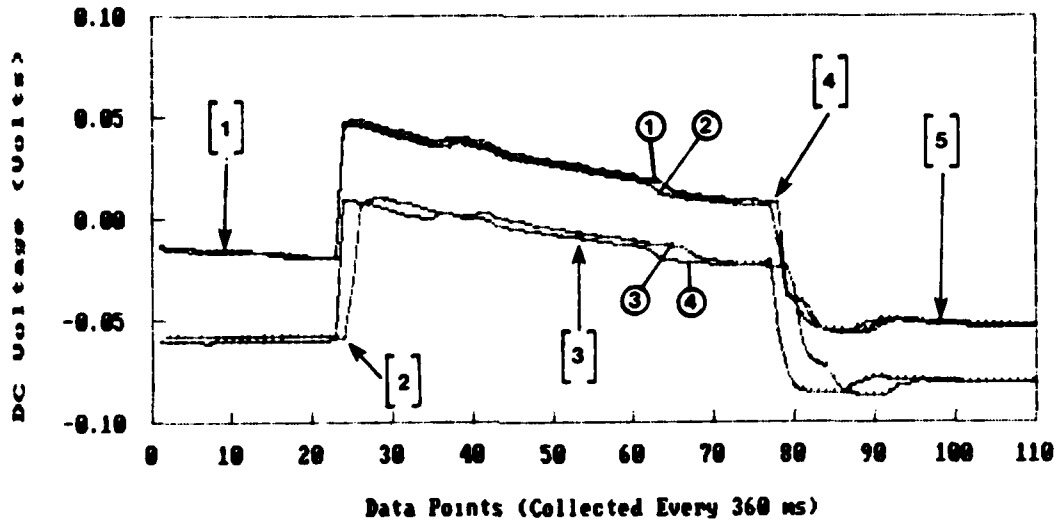


Figure J.19. Response of Four Measurements for the Poled PPTSA #2b Configuration. These Measurements were for the Corner Sensor and 100 Gram Load. (The vertical axis represents the sensor's DC response voltage. Key to measurement states: [1] Pre-load, [2] Load application, [3] Steady-state response, [4] Load removal, and [5] Post-load.)

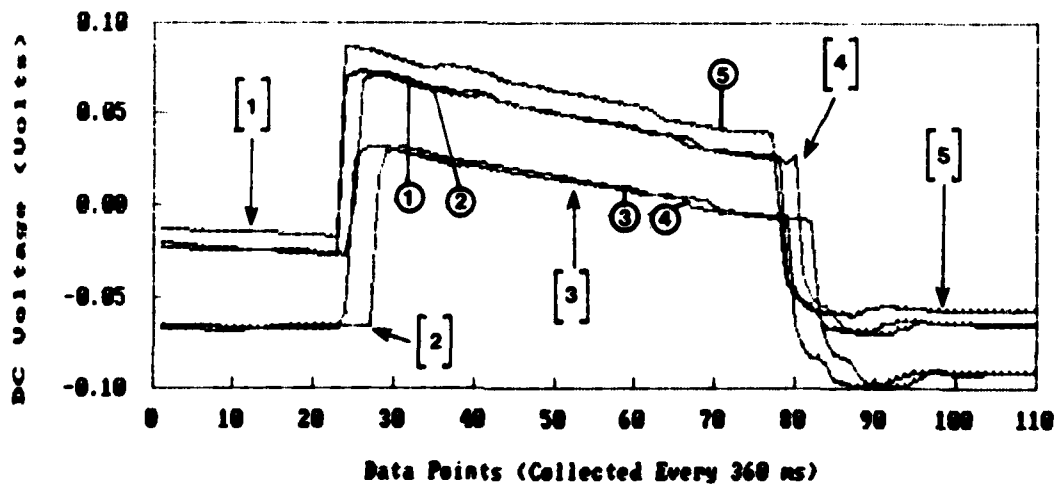


Figure J.20. Response of Five Measurements for the Poled PPTSA #2b Configuration. These Measurements were for the Corner Sensor and 200 Gram Load. (The vertical axis represents the sensor's DC response voltage. Key to measurement states: [1] Pre-load, [2] Load application, [3] Steady-state response, [4] Load removal, and [5] Post-load.)

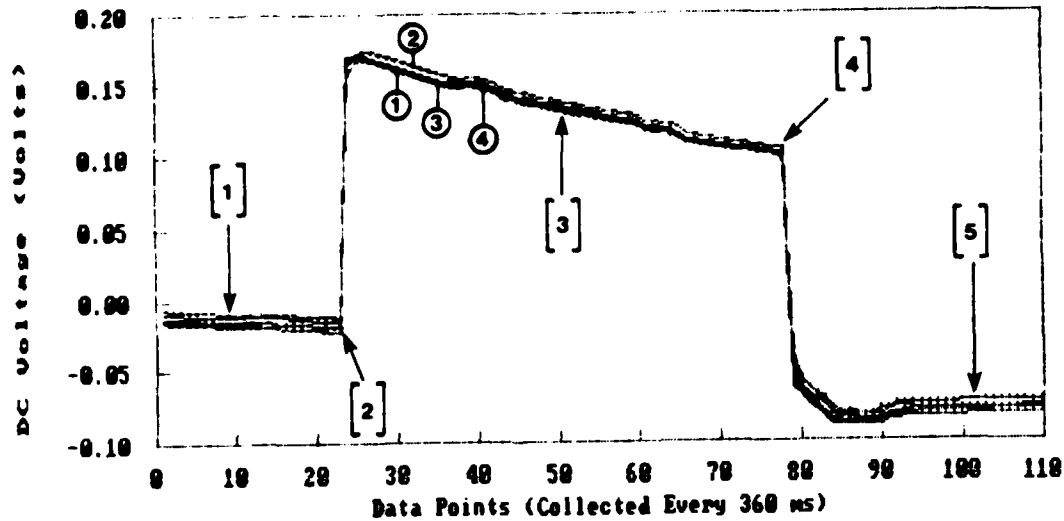


Figure J.21. Response of Four Measurements for the Poled PPTSA #2b Configuration. These Measurements were for the Corner Sensor and 500 Gram Load. (The vertical axis represents the sensor's DC response voltage. Key to measurement states: [1] Pre-load, [2] Load application, [3] Steady-state response, [4] Load removal, and [5] Post-load.)

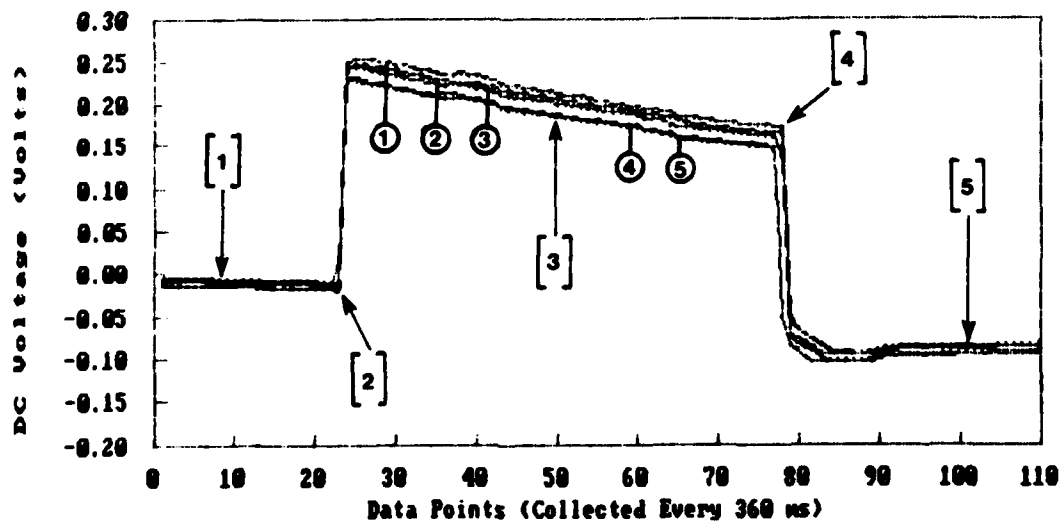


Figure J.22. Response of Five Measurements for the Poled PPTSA #2b Configuration. These Measurements were for the Corner Sensor and 700 Gram Load. (The vertical axis represents the sensor's DC response voltage. Key to measurement states: [1] Pre-load, [2] Load application, [3] Steady-state response, [4] Load removal, and [5] Post-load.)

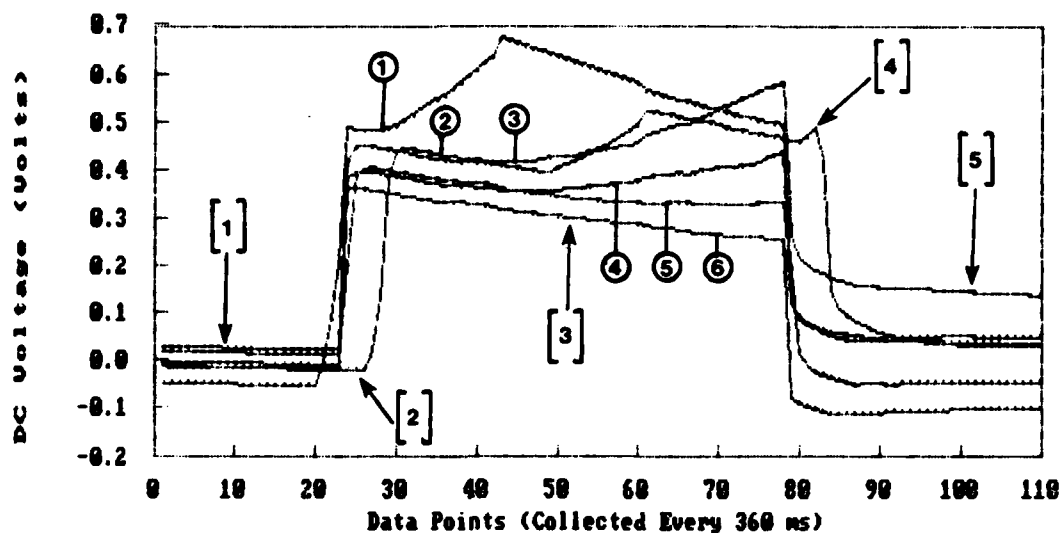


Figure J.23. Response of Six Measurements for the Poled PPTSA #2b Configuration. These Measurements were for the Corner Sensor and 1,000 Gram Load. (The vertical axis represents the sensor's DC response voltage. Key to measurement states: [1] Pre-load, [2] Load application, [3] Steady-state response, [4] Load removal, and [5] Post-load.)

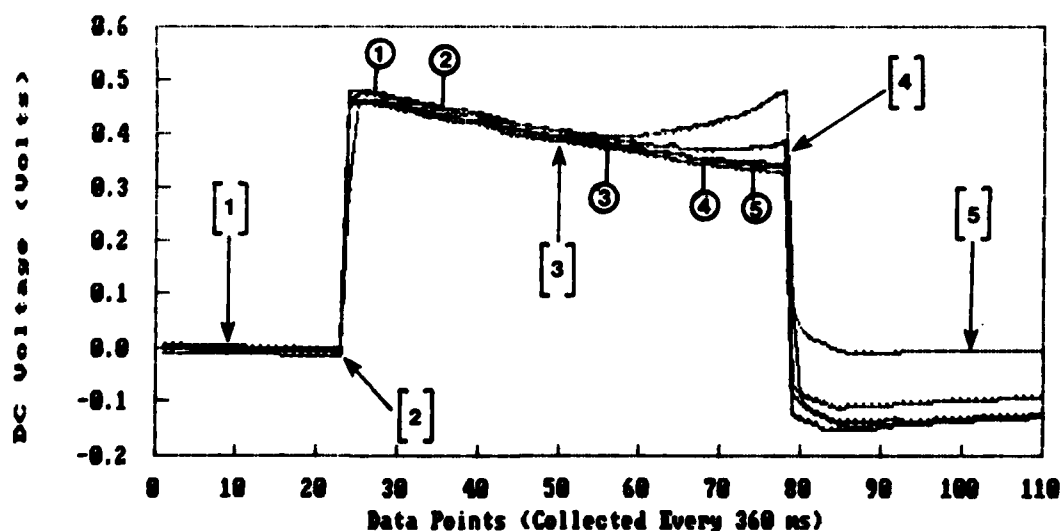


Figure J.24. Response of Five Measurements for the Poled PPTSA #2b Configuration. These Measurements were for the Corner Sensor and 1,500 Gram Load. (The vertical axis represents the sensor's DC response voltage. Key to measurement states: [1] Pre-load, [2] Load application, [3] Steady-state response, [4] Load removal, and [5] Post-load.)

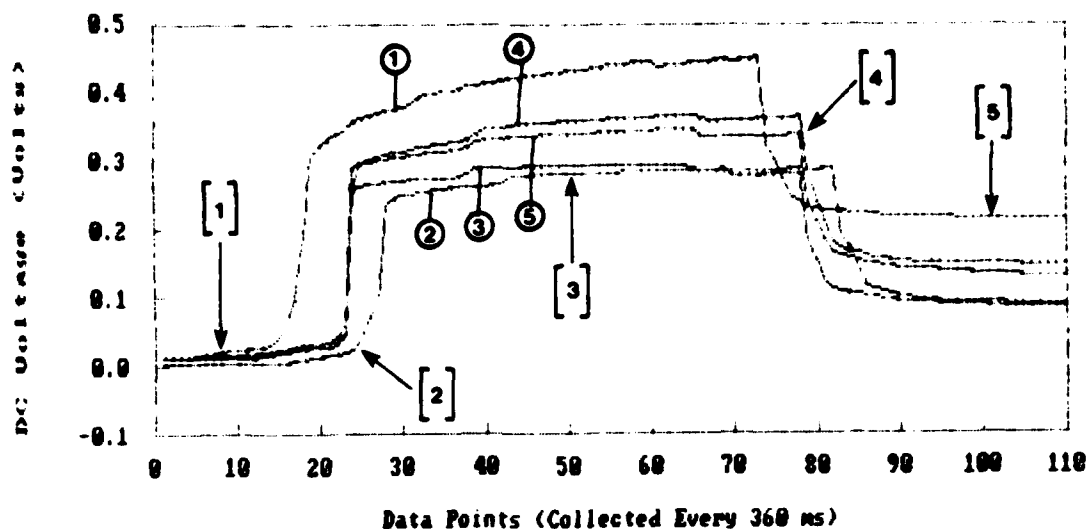


Figure J.25. Response of Five Measurements for the PPTSA #13 Configuration. These Measurements were for the Center Sensor and 100 Gram Load. (The vertical axis represents the sensor's DC response voltage. Key to measurement states: [1] Pre-load, [2] Load application, [3] Steady-state response, [4] Load removal, and [5] Post-load.)

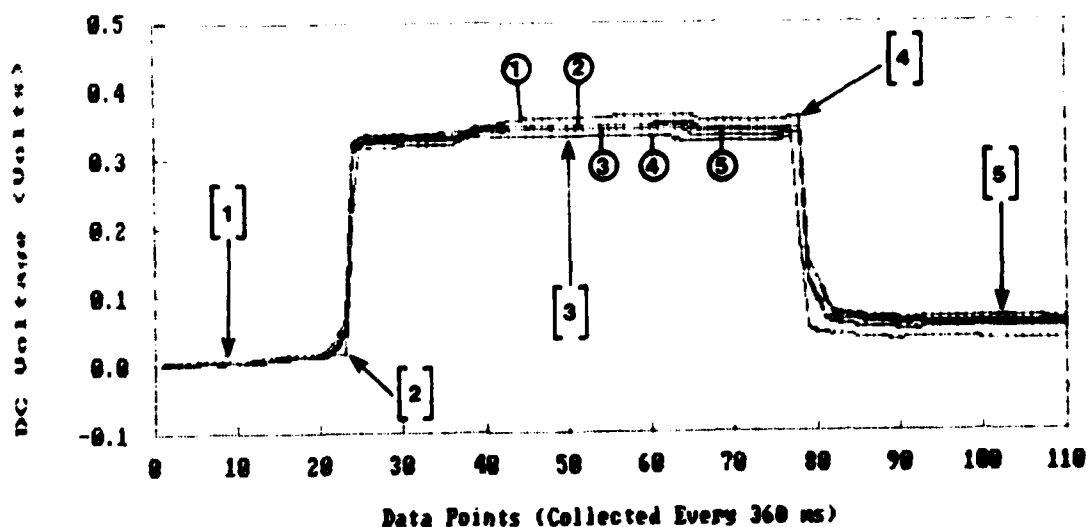


Figure J.26. Response of Five Measurements for the PPTSA #13 Configuration. These Measurements were for the Center Sensor and 200 Gram Load. (The vertical axis represents the sensor's DC response voltage. Key to measurement states: [1] Pre-load, [2] Load application, [3] Steady-state response, [4] Load removal, and [5] Post-load.)

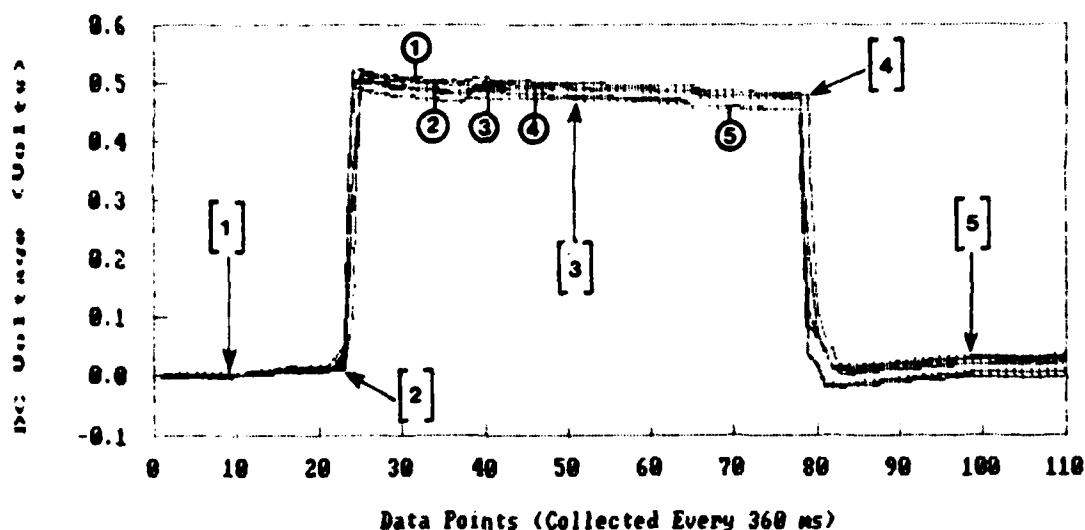


Figure J.27. Response of Five Measurements for the PPTSA #13 Configuration. These Measurements were for the Center Sensor and 500 Gram Load. (The vertical axis represents the sensor's DC response voltage. Key to measurement states: [1] Pre-load, [2] Load application, [3] Steady-state response, [4] Load removal, and [5] Post-load.)

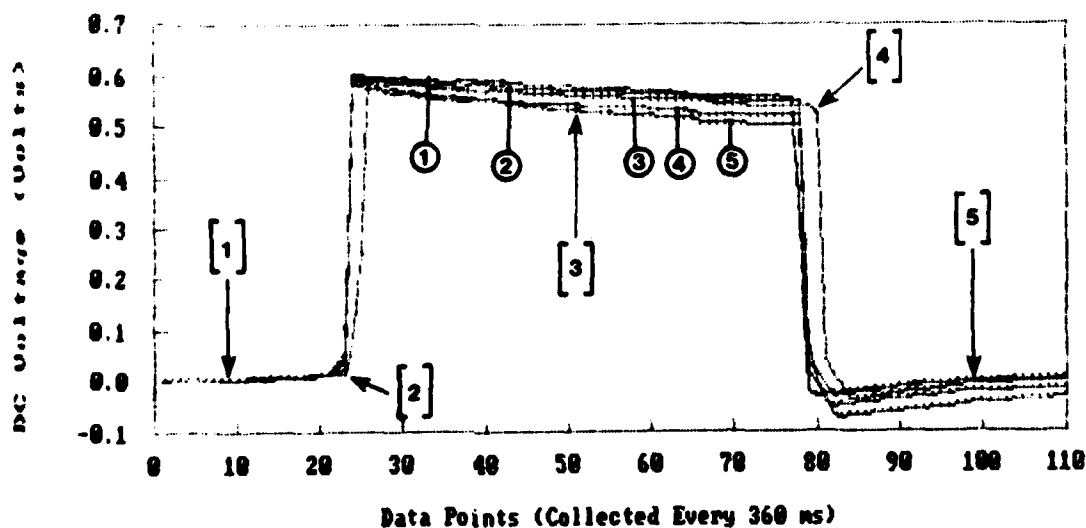


Figure J.28. Response of Five Measurements for the PPTSA #13 Configuration. These Measurements were for the Center Sensor and 700 Gram Load. (The vertical axis represents the sensor's DC response voltage. Key to measurement states: [1] Pre-load, [2] Load application, [3] Steady-state response, [4] Load removal, and [5] Post-load.)

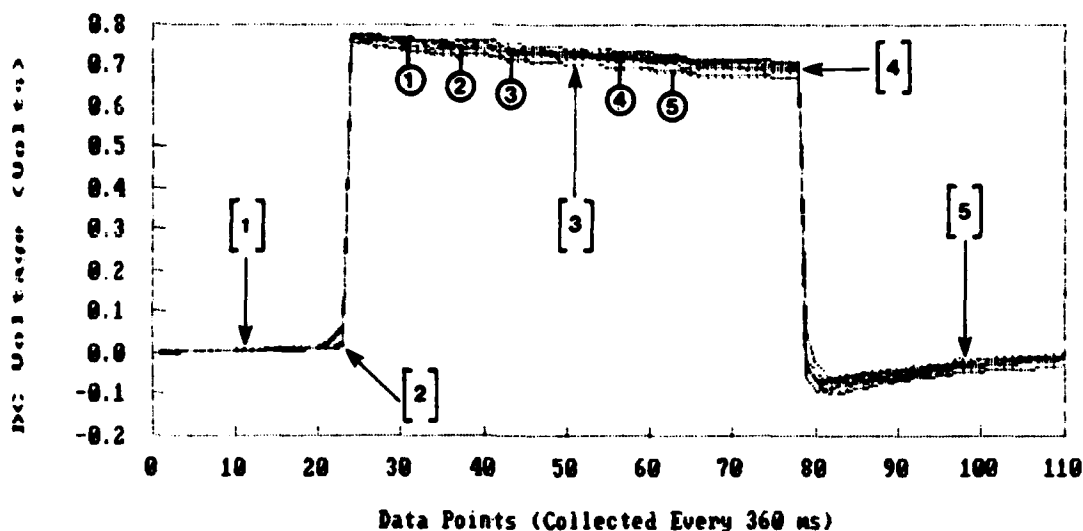


Figure J.29. Response of Five Measurements for the PPTSA #13 Configuration. These Measurements were for the Center Sensor and 1,000 Gram Load. (The vertical axis represents the sensor's DC response voltage. Key to measurement states: [1] Pre-load, [2] Load application, [3] Steady-state response, [4] Load removal, and [5] Post-load.)

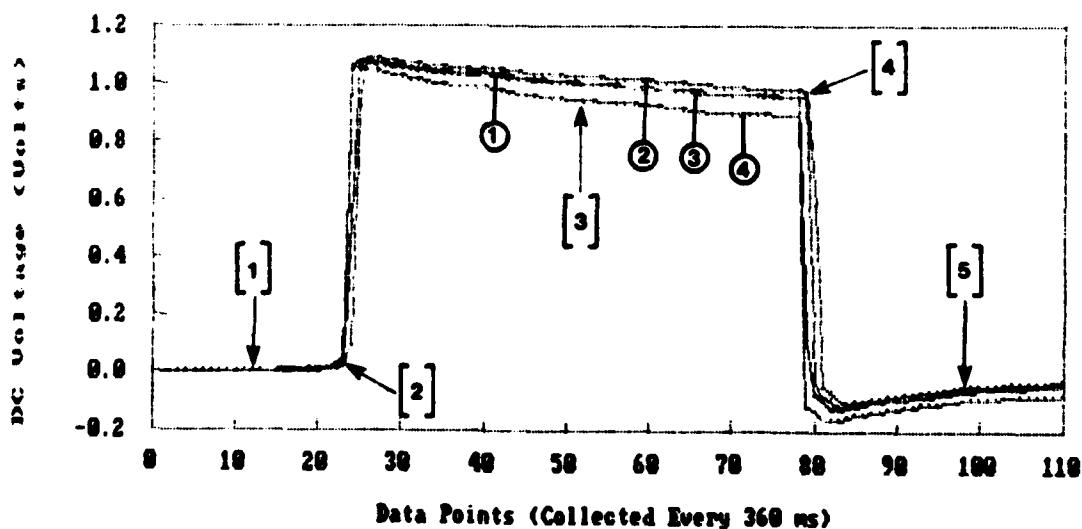


Figure J.30. Response of Four Measurements for the PPTSA #13 Configuration. These Measurements were for the Center Sensor and 1,500 Gram Load. (The vertical axis represents the sensor's DC response voltage. Key to measurement states: [1] Pre-load, [2] Load application, [3] Steady-state response, [4] Load removal, and [5] Post-load.)

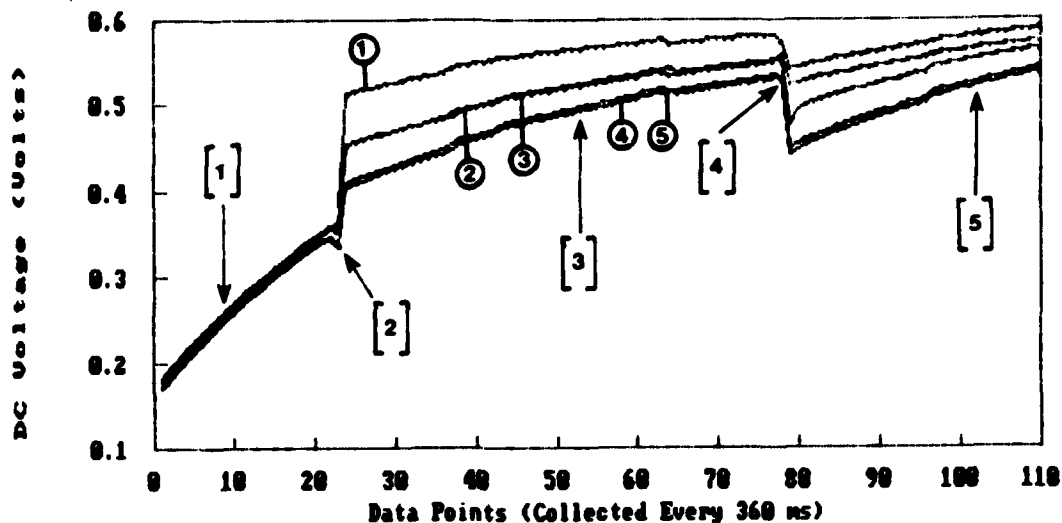


Figure J.31. Response of Five Measurements for the Poled PPTSA #13 Configuration. These Measurements were for the Center Sensor and 100 Gram Load. (The vertical axis represents the sensor's DC response voltage. Key to measurement states: [1] Pre-load, [2] Load application, [3] Steady-state response, [4] Load removal, and [5] Post-load.)

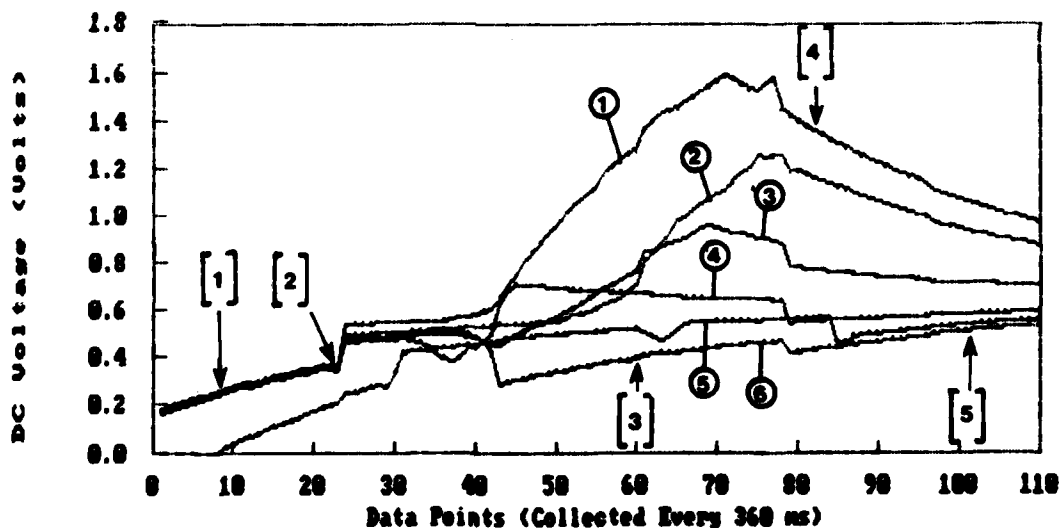


Figure J.32. Response of Six Measurements for the Poled PPTSA #13 Configuration. These Measurements were for the Center Sensor and 200 Gram Load. (The vertical axis represents the sensor's DC response voltage. Key to measurement states: [1] Pre-load, [2] Load application, [3] Steady-state response, [4] Load removal, and [5] Post-load.)

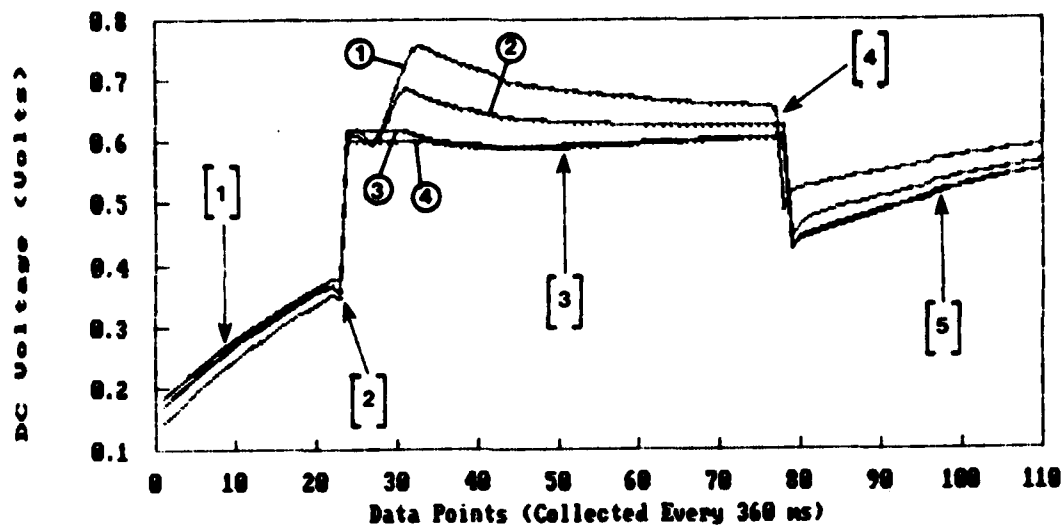


Figure J.33. Response of Four Measurements for the Poled PPTSA #13 Configuration. These Measurements were for the Center Sensor and 500 Gram Load. (The vertical axis represents the sensor's DC response voltage. Key to measurement states: [1] Pre-load, [2] Load application, [3] Steady-state response, [4] Load removal, and [5] Post-load.)

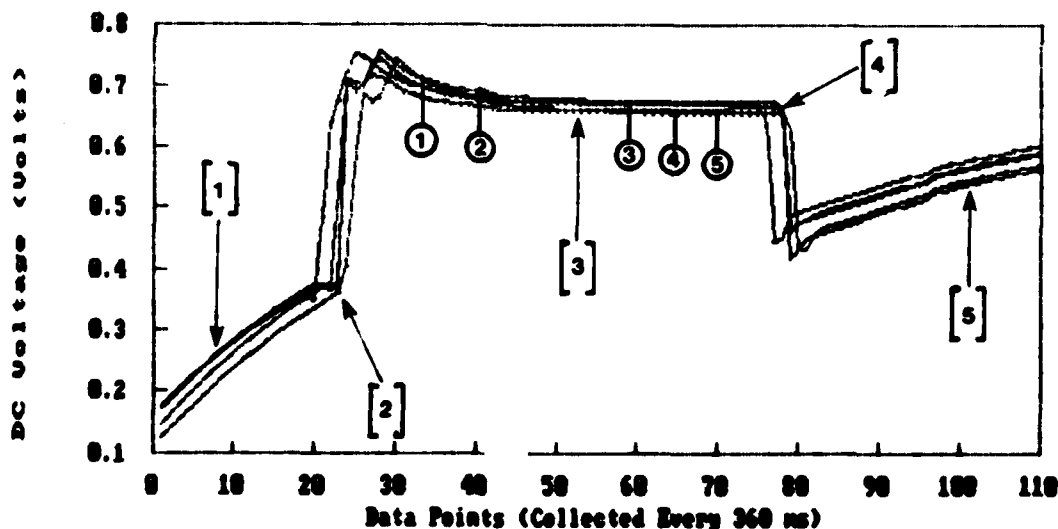


Figure J.34. Response of Five Measurements for the Poled PPTSA #13 Configuration. These Measurements were for the Center Sensor and 700 Gram Load. (The vertical axis represents the sensor's DC response voltage. Key to measurement states: [1] Pre-load, [2] Load application, [3] Steady-state response, [4] Load removal, and [5] Post-load.)

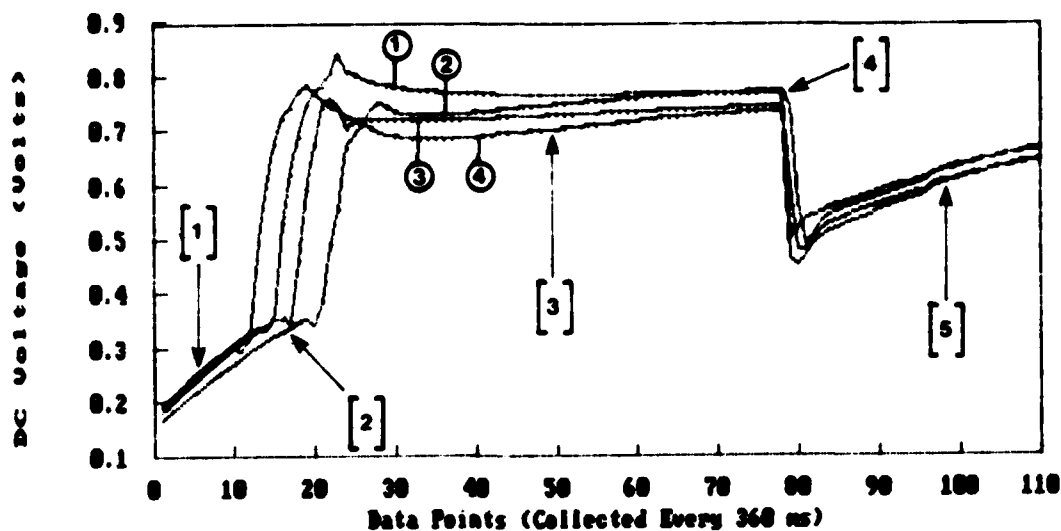


Figure J.35. Response of Four Measurements for the Poled PPTSA #13 Configuration. These Measurements were for the Center Sensor and 1,000 Gram Load. (The vertical axis represents the sensor's DC response voltage. Key to measurement states: [1] Pre-load, [2] Load application, [3] Steady-state response, [4] Load removal, and [5] Post-load.)

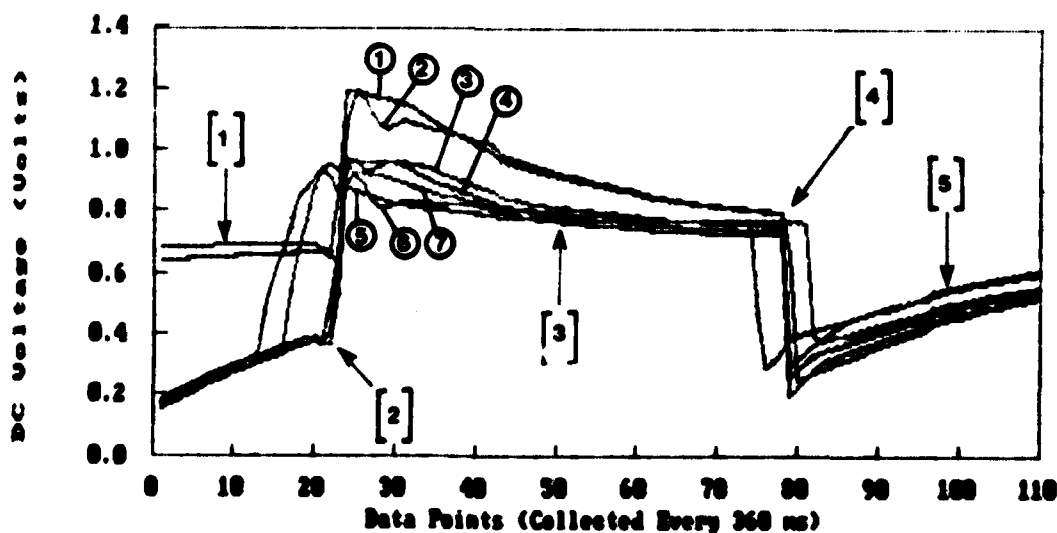


Figure J.36. Response of Seven Measurements for the Poled PPTSA #13 Configuration. These Measurements were for the Center Sensor and 1,500 Gram Load. (The vertical axis represents the sensor's DC response voltage. Key to measurement states: [1] Pre-load, [2] Load application, [3] Steady-state response, [4] Load removal, and [5] Post-load.)

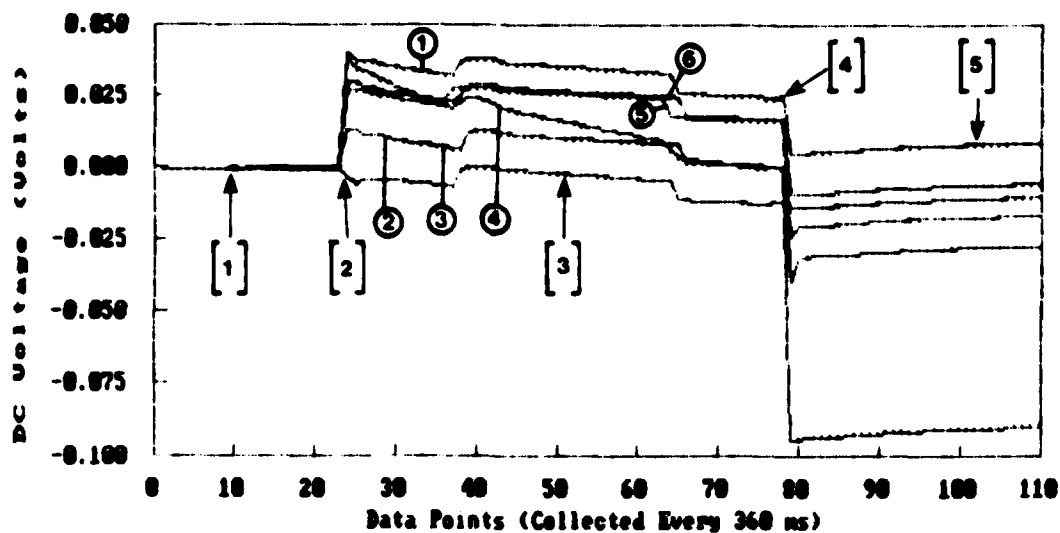


Figure J.37. Response of Six Measurements for the Poled PPTSA #13 Configuration. These Measurements were for the Corner Sensor and 100 Gram Load. (The vertical axis represents the sensor's DC response voltage. Key to measurement states: [1] Pre-load, [2] Load application, [3] Steady-state response, [4] Load removal, and [5] Post-load.)

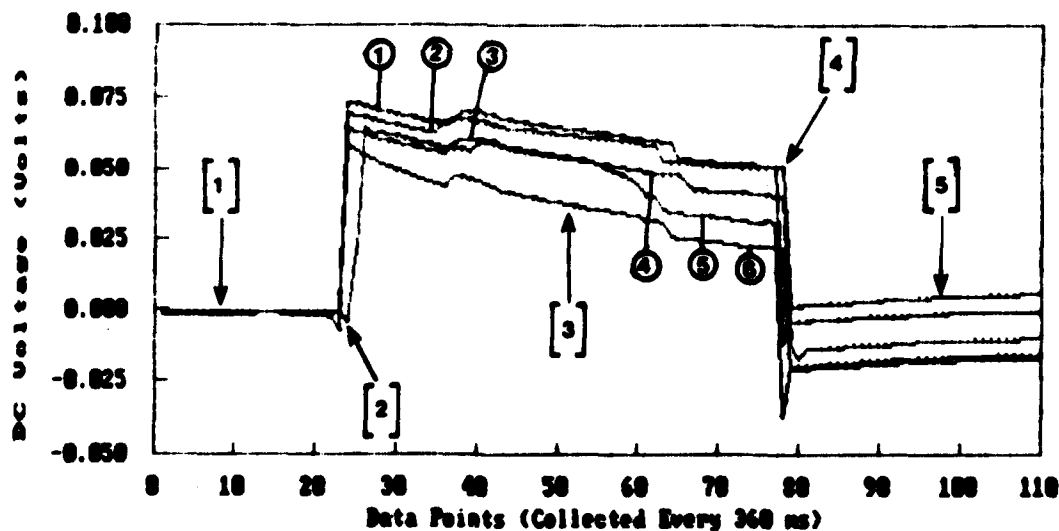


Figure J.38. Response of Six Measurements for the Poled PPTSA #13 Configuration. These Measurements were for the Corner Sensor and 200 Gram Load. (The vertical axis represents the sensor's DC response voltage. Key to measurement states: [1] Pre-load, [2] Load application, [3] Steady-state response, [4] Load removal, and [5] Post-load.)

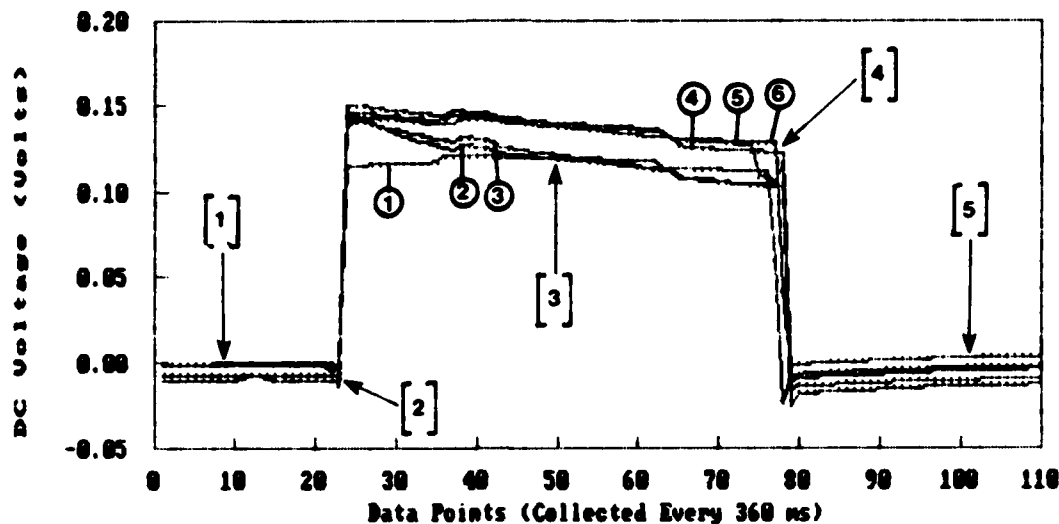


Figure J.39. Response of Six Measurements for the Poled PPTSA #13 Configuration. These Measurements were for the Corner Sensor and 500 Gram Load. (The vertical axis represents the sensor's DC response voltage. Key to measurement states: [1] Pre-load, [2] Load application, [3] Steady-state response, [4] Load removal, and [5] Post-load.)

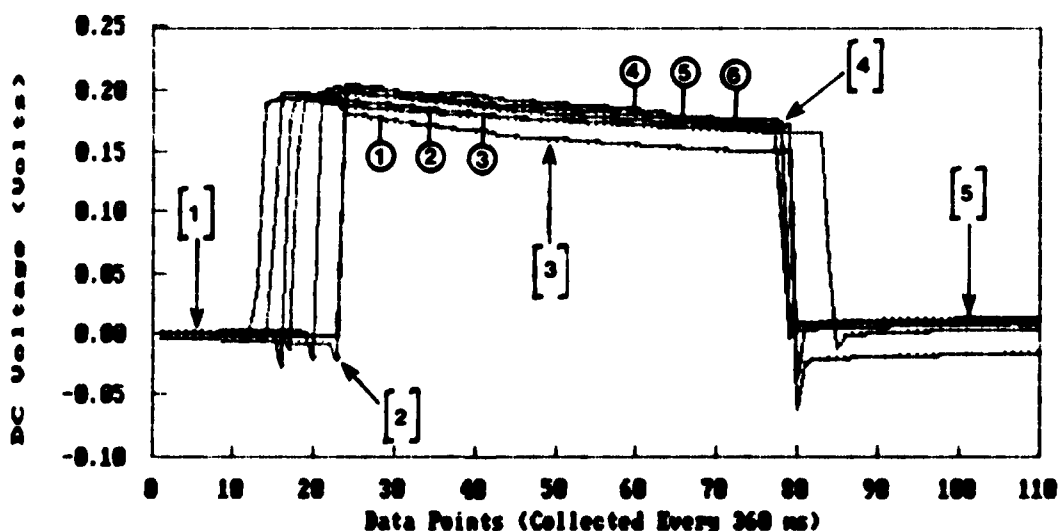


Figure J.40. Response of Six Measurements for the Poled PPTSA #13 Configuration. These Measurements were for the Corner Sensor and 700 Gram Load. (The vertical axis represents the sensor's DC response voltage. Key to measurement states: [1] Pre-load, [2] Load application, [3] Steady-state response, [4] Load removal, and [5] Post-load.)

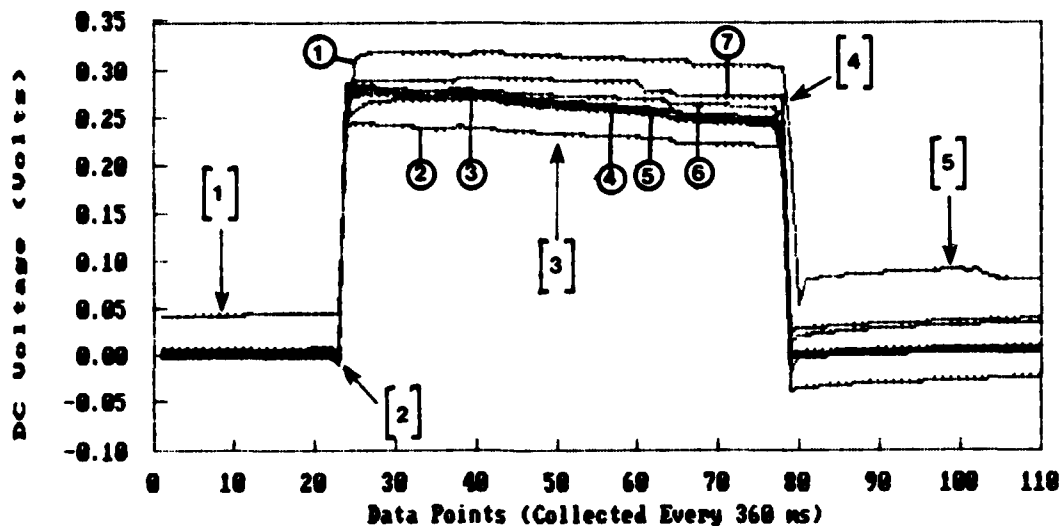


Figure J.41. Response of Seven Measurements for the Poled PPTSA #13 Configuration. These Measurements were for the Corner Sensor and 1,000 Gram Load. (The vertical axis represents the sensor's DC response voltage. Key to measurement states: [1] Pre-load, [2] Load application, [3] Steady-state response, [4] Load removal, and [5] Post-load.)

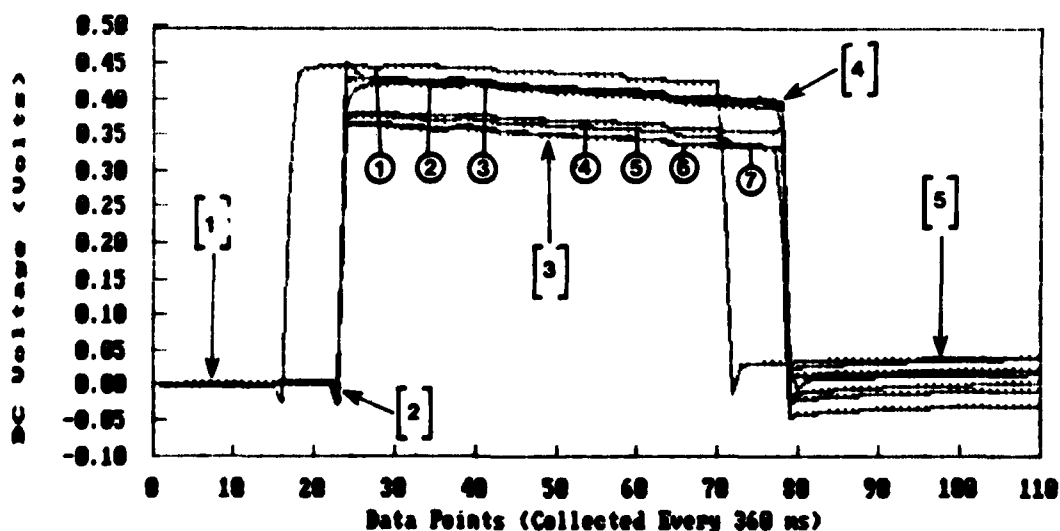


Figure J.42. Response of Seven Measurements for the Poled PPTSA #13 Configuration. These Measurements were for the Corner Sensor and 1,500 Gram Load. (The vertical axis represents the sensor's DC response voltage. Key to measurement states: [1] Pre-load, [2] Load application, [3] Steady-state response, [4] Load removal, and [5] Post-load.)

Bibliography

- Assente, Roberto, Giancarlo Ferrigno and Antonio Pedotti.
"Distributed Multiplexing for PVDF Multitransducer
Platform Scanning: A Theoretical and Practical
Approach," Proceeding 5th International Symposium on
Electrets. 795-800. IEEE Press, New York, 1985.
- Bachmann, M. A., W. L. Gordon, J. L. Koenig and J. B. Lando.
"An Infrared Study of Phase-III Poly(vinylidene
Fluoride)," Journal of Applied Physics, 50: 6106-6112
(October 1979).
- Bardelli, R., P. Dario, D. De Rossi, and P.C. Pinotti.
"Piezo- and Pyroelectric Polymers Skin-Like Tactile
Sensors for Robots and Prostheses," Proceeding of the
13th International Symposium on Industrial Robots,
Chicago: 18-15 to 18-55 (1983).
- Bergman, J. G. "Polyvinylidene Fluoride as an Active Device
Element," Proceedings of Piezoelectric and Pyroelectric
Symposium-Workshop held at Gaithersburg, Maryland:
138-164 (April 1975). DTIC AD A016843.
- Bur, Anthony J. and Steven C. Roth. "Characterization of
Polyvinylidene Fluoride Pressure Transducers,"
Proceedings of the IEEE 5th International Symposium on
Electrets. 713-717. IEEE Press, New York, 1985.
- Cady, Walter G. Piezoelectricity, An Introduction to the
Theory and Applications of Electromechanical Phenomena.
Volumes I. New York: Dover, 1964.
- Carlisle, Ben H. "Piezoelectric Plastics Promise New
Sensor," Machine Design: 6 pages (reprint) (October
1986).
- Chatigny, J. Victor and Lester E. Robb. "Piezo Film
Sensors," Sensors: 50-55 (May 1986).
- Dario, P. and D. De Rossi. "Tactile Sensors and the
Gripping Challenge," IEEE Spectrum: 46-52 (August
1985).
- Dario, P., D. De Rossi, C. Domenici and R. Francesconi.
"Ferroelectric Polymer Tactile Sensors with Features,"
Received from Pennwalt Corporation, King of Prussia, PA
(1984).

- Das-Gupta, D. K., and K. Doughty. "Corona charging and the piezoelectric effect in polyvinylidene fluoride," Journal of Applied Physics, 49: 4601-4603 (August 1978).
- Davis, G. Thomas, J. E. McKinney, M. G. Broadhurst and S. C. Roth. "Electric-Field-Induced Phase Changes in Poly(vinylidene Fluoride)," Journal of Applied Physics, 49: 4998-5002 (October 1978).
- Doll, W. W. and J. B. Lando. Journal of Macromolecule Science, Physics Edition, B2: 219 (1968)
- Fukada, Eiichi. "Chapter 3, Piezoelectricity of Biological Materials," Electronic Conduction and Mechano-electrical Transduction in Biological Materials, Edited by Boguslaw Lipinski. New York: Marcel Dekker, 1982.
- Gerliczy, G. and R. Betz. SOLEF (TM) PVDF Biaxially Oriented Piezo and Pyro-electric Films for Transducers. Solvay Report. Solvay Technologies, Inc., New York (1984).
- Gilder, Jules H. and Scott P. Gilder. IBM PC, Programs in Science and Engineering. Hasbrouck Heights, New Jersey: Hayden, 1984.
- Groner, G. F. and M. N. Hirsh. "Comparison of Poling Techniques for Inducing Piezoelectric Behavior in PVF₂," Proceedings of the IEEE 5th International Symposium on Electrets. 912-917. IEEE Press, New York, 1985.
- Harmon, Leon D. "Automated Tactile Sensing," International Journal on Robotics Research, 1: 3-32. (1982)
- "Touch-sensing Technology: A Review," Society of Manufacturing Engineers Technical Report MSR80-83 (1980).
- Hayakawa, Reinosuke and Yasaku Wada. "Piezoelectricity and Pyroelectricity of Polymer Films Arising from Heterogeneity and Embedded Charges," Reports on Progress in Polymer Physics in Japan, XIX: 321-324 (1976).
- Jaffe, Bernard, William R. Cook, Jr., and Hans Jaffe. Piezoelectric Ceramics. New York: Academic Press, 1971.

Kawai, Heiji. "The Piezoelectricity of Poly (vinylidene Fluoride)," Japan Journal of Applied Physics, 8: 975-976 (May 1969).

Kiethley Instruments, Incorporated. Instruction Manual, Model 617 Programmable Electrometer. Cleveland, Ohio, 1984a.

----- Low Level Measurements. Third Edition. Cleveland, Ohio, 1984b.

Kenney, James M. and Steven C. Roth. "Fabrication of Piezoelectric Polymer Film," NBS J. Research, Washington, D. C. (September 1978). DTIC AD-A070822

Kepler, R. G. and R. A. Anderson. "Piezoelectricity and Pyroelectricity in Polyvinylidene Fluoride," Journal of Applied Physics, 49: 4490-4494 (August 1978).

Kino, Gordon S. Acoustic Waves: Devices, Imaging and Analog Signal Processing. Englewood Cliffs, New Jersey: Prentice-Hall, 1987.

Kobayashi, M., K. Tashiro and H. Tadokoro. "Molecular Vibrations of Three Crystal Forms of Polyvinylidene Fluoride," Macromolecules, 13: 158 (March 1975).

Kolbeck, A. G. "Aging of Piezoelectricity in Poly(vinylidene Fluoride)," Journal of Polymer Science: Polymer Physics Edition, 20: 1987-2001. (1982a)

Kraus, John D. Electromagnetics (Third Edition). New York: McGraw-Hill, 1984.

KYNAR Piezo Film Department. KYNAR Piezo Film Technical Manual. Pennwalt Corporation, King of Prussia PA, 1987.

----- KYNAR Piezo Film Technical Manual. Manual 10-M-11-83-M. Pennwalt Corporation, King of Prussia PA, 1983.

----- Appendix A, Human Tactile Capabilities. Pennwalt Corporation, King of Prussia, PA, 4 pages (1984).

Lovinger, Andrew J.. "Ferroelectric Polymers," Science, 220: 1115-1121 (10 June 1983).

Marcus, Michael A. "Applications of Polyvinylidene Fluoride Films," Proceedings of the IEEE 5th International Symposium on Electrets. 724-731. IEEE Press, New York, 1985a.

- , "Orientation Effects on Dielectric and Piezoelectric Properties of Polyvinylidene Fluoride Films," Proceedings of the IEEE 5th International Symposium on Electrets, 895-899. IEEE Press, New York, 1985b.
- , "Ferroelectric Polymers and Their Applications," Ferroelectrics, 40: 29-41. (1982)
- McAlpine, George A.. "Tactile Sensing," Sensors: 7-16. (April 1986)
- McKinney, J. E., G. T. Davis., and M. G. Broadhurst. "Plasma Poling of Poly (vinylidene Fluoride): Piezo- and Pyroelectric Response," Journal of Applied Physics, 51: 1676-1681. (March 1980). DTIC AD-A070750
- Omar, M. Ali. Elementary Solid State Physics: Principles and Applications. Reading, Massachusetts: Addison-Wesley, 1975.
- Pedotti, A., R. Assente, G. Fusi, D. De Rossi, P. Dario, and C. Domenici. "Multisensor Piezoelectric Polymer Insole for Pedobarography," Ferroelectrics, 60: 163-174 (1984).
- Prest, Jr., W. M., and D. J. Luca. "The Morphology and Thermal Response of High-temperature-crystallized Polyvinylidene Fluoride," Journal of Applied Physics, 46: 4136-4143 (October 1975).
- Scheinbeim J. I. and K. T. Chung. "The Poling Field and Draw Dependence of the Piezoelectric and Pyroelectric Response of Pressure-Quenched, Phase I Poly(vinylidene Fluoride) Films," Journal of Applied Physics, 52: 5983-5987 (October 1981).
- Seippel, Robert G. Transducers, Sensors, and Detectors. Reston, Virginia: Reston Publishing, 1983.
- Shuford, Richard J., Anthony F. Wilde, John J. Ricca, and George R. Thomas. "Characterization and Piezoelectric Activity of Stretched and Poled Poly(Vinylidene Fluoride). Part I: Effect of Draw Ratio and Poling Conditions," Polymer Engineering and Science, 16: 25-35 (January 1976).
- Solvay & Cie. "Tables of Chemical Resistance of Solef" (February 1986).
- Solvay & Cie. "Properties of Solef Piezoelectric Sheets, Preliminary Data," Solvay Piezo News: 4 pages (1983).

van der Ziel, Aldert. "Chapter 21, Piezoelectric and Ferroelectric Effect," Solid State Physical Electronics (Second Edition). Englewood Cliffs, New Jersey: Prentice-Hall, 1968.

Wada, Yasaku and Reinosuke Hayakawa. "A Model Theory of Piezo- and Pyroelectricity of Polyvinylidene Fluoride," Ferroelectrics, 32: 115-118 (1981).

-----, "Piezoelectricity and Pyroelectricity of Polymers," Japanese Journal of Applied Physics, 15: 2041-2057 (November 1976).

Wang, T. T. and Heinz von Seggern. "High Electric Field Poling of Electroded Poly(vinylidene Fluoride) at Room Temperature," Journal of Applied Physics, 54: 4602-4604 (August 1983).

Wang, T. T., H. von Seggern, J. E. West and H. D. Keith. "High Field Poling of Poly(vinylidene Fluoride) Films Using a Current Limiting Circuit," Ferroelectrics, 61: 249-256 (1984).

VITA

Captain David G. Pirolo was born 12 July 1958 in Milwaukee, Wisconsin. He graduated from high school in Largo, Florida, in 1977 and attended the University of South Florida, from which he received the degree of Bachelor of Science in Engineering in August 1982. His engineering major was in electrical engineering. While attending the University, he was a cooperative education student with the Tampa Electric Company for 2-1/2 years. He joined the United States Air Force in his last year (1981) at the University under the College Senior Education Program. After graduation, he attended Officer Training School from August through November 1982. He served in the Advance Seeker Division of the Air Force Armament Laboratory, Eglin Air Force Base, Florida as an electrical engineer and program manager from December 1982 to May 1986. At the end of May 1986, he entered the School of Engineering, Air Force Institute of Technology.

Permanent address: 531 Lake Hill Lane

Largo, Florida 34641

VITA

REPORT DOCUMENTATION PAGE

Form Approved
OMB No. 0704-0188

1. REPORT SECURITY CLASSIFICATION UNCLASSIFIED			1b. RESTRICTIVE MARKINGS		
2a. SECURITY CLASSIFICATION AUTHORITY			3. DISTRIBUTION / AVAILABILITY OF REPORT		
2b. DECLASSIFICATION / DOWNGRADING SCHEDULE			Approved for public release; distribution unlimited.		
4. PERFORMING ORGANIZATION REPORT NUMBER(S) AFIT/GE/ENG/87D-52			5. MONITORING ORGANIZATION REPORT NUMBER(S)		
6a. NAME OF PERFORMING ORGANIZATION School of Engineering		6b. OFFICE SYMBOL (if applicable) AFIT/ENG		7a. NAME OF MONITORING ORGANIZATION	
6c. ADDRESS (City, State, and ZIP Code) Air Force Institute of Technology Wright-Patterson AFB OH 45433-6583			7b. ADDRESS (City, State, and ZIP Code)		
8a. NAME OF FUNDING / SPONSORING ORGANIZATION		8b. OFFICE SYMBOL (if applicable)		9. PROCUREMENT INSTRUMENT IDENTIFICATION NUMBER	
8c. ADDRESS (City, State, and ZIP Code)			10. SOURCE OF FUNDING NUMBERS		
			PROGRAM ELEMENT NO.	PROJECT NO.	TASK NO.
			WORK UNIT ACCESSION NO.		
11. TITLE (Include Security Classification) PIEZOELECTRIC POLYMER TACTILE SENSOR ARRAYS FOR ROBOTICS (UNCLASSIFIED)					
12. PERSONAL AUTHOR(S) David George Pirolo, B.S.E., Captain, USAF					
13a. TYPE OF REPORT Masters Thesis		13b. TIME COVERED FROM TO		14. DATE OF REPORT (Year, Month, Day) 1987 December	
15. PAGE COUNT 235					
16. SUPPLEMENTARY NOTATION					
17. COSATI CODES			18. SUBJECT TERMS (Continue on reverse if necessary and identify by block number)		
FIELD	GROUP	SUB-GROUP	Piezoelectric Materials, Piezoelectric Transducers, Sensors		
09	01				
19. ABSTRACT (Continue on reverse if necessary and identify by block number)					
Thesis Chairman: Edward S. Kolesar, Jr., Major, USAF Associate Professor of Electrical Engineering					
<p>Abstract: This study resulted in the design and fabrication of 16 piezoelectric polymer tactile sensor arrays (PPTSAs) for robotics. Six of these PPTSAs were evaluated for piezoelectric activity. Two of the six were thermal poled and evaluated again for piezoelectric activity. Each PPTSA contained a 5 x 5 array of identical, (3 mm x 3 mm) discrete sensors. Polyvinylidene fluoride (PVDF) was the piezoelectric polymer used in this study. The PVDF was in two film thicknesses (25 and 40 microns) and in two forms (unmetallized and vendor metallized). The PVDF film had inherent chemical and temperature limitations. Two electrode-structure fabrication processes were developed to accomodate these limitations.</p>					
20. DISTRIBUTION / AVAILABILITY OF ABSTRACT			21. ABSTRACT SECURITY CLASSIFICATION		
<input checked="" type="checkbox"/> UNCLASSIFIED/UNLIMITED <input type="checkbox"/> SAME AS RPT. <input type="checkbox"/> DTIC USERS			UNCLASSIFIED		
22a. NAME OF RESPONSIBLE INDIVIDUAL Edward S. Kolesar, Jr., Major, USAF			22b. TELEPHONE (Include Area Code) (513) 255-3576		22c. OFFICE SYMBOL AFIT/ENG

Approved for public release: IAW AFR 180-1.
LYNN E. WOLAVEN
Dean for Research and Professional Development
Air Force Institute of Technology (AFIT)
Wright-Patterson AFB OH 45433

END

DATE

FILMD

3-88

DTIC